CZECH TECHNICAL UNIVERSITY IN PRAGUE
Faculty of Nuclear Sciences and Physical Engineering
Department of Physics

DISSERTATION

Study of Jet Properties in Au+Au Collisions at RHIC

Prague 2024

Ing. Robert Líčeník

Bibliografický záznam

Autor	Ing. Robert Líčeník České vysoké učení technické v Praze Fakulta jaderná a fyzikálně inženýrská Katedra fyziky
Název práce	Studium vlastností jetů ve srážkách Au+Au na urychlovači RHIC
Studijní program	Aplikace přírodních věd
Studijní obor	Jaderné inženýrství
Školitel	doc. RNDr. Jana Bielčíková, Ph.D. Akademie věd ČR Ústav jaderné fyziky Oddělení jaderné spektroskopie
Akademický rok	2023/2024
Počet stran	187
Klíčová slova	kvantová chromodynamika, jety, kvark–gluonové plazma, srážky těžkých iontů, experiment STAR, urychlovač RHIC, dekonvoluce

Bibliographic Entry

Author	Ing. Robert Líčeník Czech Technical University in Prague Faculty of Nuclear Sciences and Physical Engineering Department of Physics
Title of Dissertation	Study of Jet Properties in Au+Au Collisions at RHIC
Degree Programme	Applications of Natural Sciences
Field of Study	Nuclear Engineering
Supervisor	doc. RNDr. Jana Bielčíková, Ph.D. Czech Academy of Sciences Nuclear Physics Institute Department of Nuclear Spectroscopy
Academic Year	2023/2024
Number of Pages	187
Keywords	quantum chromodynamics, jets, quark–gluon plasma, heavy-ion collisions, STAR experiment, RHIC, unfolding

Abstract

Jets serve as a final-state approximation of high-energy partons. Jet quenching in central nucleus–nucleus collisions at high-energy has long been one of the key evidences of quark–gluon plasma formation, which is a state of matter thought to exist in the very early universe. Studying jet production inside the quark–gluon plasma and comparing it to a vacuum reference can therefore provide valuable information about this exotic state of matter.

This work presents the first analysis of inclusive fully-reconstructed jet spectra in Au+Au collisions at center-of-mass energy per nucleon–nucleon pair $\sqrt{s_{\mathrm{NN}}} = 200$ GeV at RHIC. Reconstructed jets contain both charged and neutral particles, as measured by the STAR experiment. Several techniques are employed in order to reduce the effects of the large and fluctuating background – especially in central Au+Au collisions – and the spectra are also fully corrected for the effects caused by the limited efficiency and resolution of the experimental systems using state-of-the-art unfolding techniques. Fully corrected spectra are reported up to $p_{\mathrm{T,jet}} =$ 60 GeV/c in central Au+Au collisions, significantly extending the reach of similar measurements for jets containing only charged particles at RHIC kinematics and allowing for direct comparison with results from experiments at the LHC. The thesis also presents and discusses various biases imposed on the presented spectra.

The results show significant jet yield suppression in central Au+Au collisions compared to p+p collisions simulated by the PYTHIA Monte-Carlo event generator. The obtained values $R_{\mathrm{AA}} \sim 0.2 - 0.3$ indicate large energy losses of the highly-energetic partons inside the quark–gluon plasma with slight dependence on the jet transverse momentum. The magnitude of suppression is consistent with the results published by the ALICE experiment and with the prediction of theoretical calculations which incorporate jet quenching. The R_{AA} in peripheral Au+Au collisions is consistent with unity within uncertainties, indicating the small or negligible effects of cold nuclear matter on jet production.

Finally, this thesis also contains a short report on other contributions by the author, including the ongoing tracking efficiency uncertainty study conducted alongside the main analysis as a STAR service task.

Abstrakt

Jety slouží jako pozorovatelné přiblížení vysokoenergetických partonů. Zhášení jetů v centrálních srážkách těžkých iontů při vysokých energiích již dlouho slouží jako jeden z hlavních důkazů vytváření kvark–gluonového plazmatu, stavu hmoty, o kterém se předpokládá, že existoval ve velmi raném vesmíru. Studium produkce jetů v kvark–gluonovém plazmatu a její porovnávání s referenční produkcí ve vakuu tedy může přinést cenné informace o tomto exotickém stavu hmoty.

Tato práce přináší výsledky první analýzy spekter inkluzivních plně rekonstruovaných jetů ve srážkách Au+Au při těžišťové energii na nukleon–nukleonový pár $\sqrt{s_{\mathrm{NN}}} = 200$ GeV na urychlovači RHIC. Zrekonstruované jety obsahují jak nabité, tak i neutrální částice změřené v experimentu STAR. V analýze je použito několik metod redukce vlivu velkého a fluktuujícího pozadí – především v centrálních Au+Au srážkách – a spektra byla plně opravena na vlivy způsobené omezenou účinností a rozlišením jednotlivých součástí experimentu pomocí moderních metod dekonvoluce. Plně korigovaná spektra jsou prezentována až do $p_{\mathrm{T,jet}} = 60$ GeV/c, čímž je významně rozšířen dosah předchozích měření s jety obsahujícími pouze nabité částice v podmínkách RHIC a umožněno přímé srovnání s výsledky experimentů na urychlovači LHC. Tato práce také diskutuje faktory, které prezentovaná spektra ovlivňují.

Výsledky práce ukazují významné potlačení produkce jetů v centrálních Au+Au srážkách v porovnání s výsledky z p+p srážek, které byly nasimulovány pomocí Monte-Carlo generátoru PYTHIA. Zjištěné hodnoty $R_{\mathrm{AA}} \sim 0.2-0.3$ indikují velké energetické ztráty vysokoenergetických partonů v kvark–gluonovém plazmatu s mírnou závislostí na příčné hybnosti jetů. Velikost potlačení je konzistentní s výsledky publikovanými experimentem ALICE a s předpověďmi teoretických výpočtů, které zahrnují zhášení jetů. Hodnota R_{AA} v periferních Au+Au srážkách je v rámci chyb rovna jedné, což indikuje malý či zanedbatelný vliv studené jaderné hmoty na produkci jetů.

Finální součástí práce je také krátké shrnutí ostatních příspěvků autora, například studie zabývající se přesným určením nejistoty efektivity rekonstrukce drah částic, která byla provedena souběžně s hlavní analýzou jako služba pro experiment STAR.

Acknowledgement

My deepest thanks definitely go to my supervisor, doc. Jana Bielčíková, who has guided me throughout the long and challenging process of finishing this thesis. Thank you for all the material and scientific support, and for creating an excellent working environment for myself and my colleagues. I want to thank you for always keeping me as motivated and as focused as possible, and also for all the pieces of life advice I received during our meetings. Finally I want to thank you for reading this thesis many times and providing a very valuable feedback.

Thank you, Dr. Peter Jacobs, for initiating this analysis and for pulling it out of mud whenever we thought it was stuck there. Thanks for your invaluable advice and for allowing me to visit you numerous times in Lawrence Berkeley National Laboratory to learn from one of the best scientists.

Thanks to Dr. Jan Rusňák for helping me transition into the jet analysis in the beginning of my PhD studies.

I would also like to thank doc. Jaroslav Bielčík for his support of my work and the life in our department in general.

Another round of thanks goes to my colleagues and friends who have provided help of any kind when I needed it.

Last, but definitely not least, I would like to sincerely thank my family and my wife for their infinite love and support. I would not have accomplished anything without you.

Declaration

I hereby declare that this thesis is the result of my own work and all the sources I used (literature, projects, software, etc.) are in the list of references. I have no objection against the use of this work in compliance with the act §60 Law No. 121/2000 Coll. (Copyright Act), and with the rights connected with the copyright act including the changes in the act.

In Prague, June 2024 Ing. Robert Líčeník

Contents

Introduction

Jets are products of hard (large–Q^2 transfer, high energy) scattering of quarks and gluons – collectively known as partons. Therefore, they serve as a final-state approximation of those partons and their kinematics. Jet production occurs early in collisions of ultrarelativistic particles and can be calculated using perturbative quantum chromodynamics (pQCD), making it a useful tool to test the validity of the theory of the strong interaction. The suppression of jet yields at high transverse momentum (p_{T}) in nucleus–nucleus collisions compared to a vacuum reference – known today as jet quenching – was first proposed by J. Bjorken in 1982 [1] as a clear signature of the formation of a new state of matter containing deconfined color charges, called the quark–gluon plasma (QGP). The basic idea is that as the parton traverses the medium, it loses energy via radiation, induced by the free color charges, and via ellastic collisions with other partons. Therefore, combined with the steeply falling shape of the parton spectrum, one would expect to find fewer jets at a given p_{T} when the QGP is present. The mechanisms contributing to jet quenching will be discussed later in the text.

Jet quenching has first been conclusively observed in central Au+Au collisions at $\sqrt{s_{\mathrm{NN}}} = 200$ GeV by the experiments at the Relativistic Heavy Ion Collider (RHIC) as a suppression of high–p_{T} charged hadron yields [2] and as the disappearance of the recoil peak in dihadron correlation measurements [3], substantially contributing to the announcement of the QGP discovery in 2004 [4]. The experiments at the Large Hadron Collider (LHC) have confirmed those results while significantly extending the kinematic reach and precision of such measurements [5, 6]. Since high–p_{T} hadrons carry only limited information into the jet quenching picture, actual jets need to be reconstructed in order to obtain deeper understanding of the underlying physics of jet quenching. Reconstructed jets are also well-suitable for direct comparisons to theoretical calculations. Therefore, there is a strong physics motivation for the analysis conducted as the main goal of this thesis: the reconstruction of inclusive jet spectra in Au+Au collisions. The results from systems which contain nuclear matter, but where the QGP is not expected to be produced, such as the proton–nucleus (p+A) collisions are also important, since they help distinguish between the various contributions to the modification of jet yields in nucleus–nucleus (A+A) collisions.

The thesis is organized as follows: Chapter 1 introduces the Standard Model with focus on elementary particles and the strong interaction. Chapter 2 describes the physics of relativistic heavy-ion collisions from variables used in high-energy physics to collision evolution with special emphasis on the QGP and finally to the main objective of the heavy-ion program – the QCD phase diagram. Chapter 3 focuses on jets as understood from both theoretical and experimental point of view, which are not quite the same and need not to be treated as such, and also contains an overview of jet measurements, both historically significant and selected recent results from RHIC and the LHC experiments, relevant to the topic of the thesis. Chapter 4 then presents the overview of the experimental facilities which provide the data used in this thesis, namely the RHIC accelerator complex and the STAR experiment. Chapter 5 describes in detail the analysis, which was conducted as the main part of this thesis. It presents the first reconstruction of inclusive fully-reconstructed jets in Au+Au collisions at $\sqrt{s_{\mathrm{NN}}} = 200$ GeV. Chapter 6 then contains and discusses the main results obtained from this analysis and their physics interpretation. Chapter 7 presents the results of the service task conducted in parallel with the main analysis, which aimed to carefully assess and potentially reduce the uncertainty of tracking efficiency estimation at STAR. Chapter 8 provides a brief overview of additional contributions of the author to STAR publications and operations. The final Chapter summarizes the contents of this thesis and outlines several possibilities for the future.

Chapter 1

Standard Model

The Standard Model (SM) of particle physics is currently the most advanced theory of the elementary particles and the fundamental interactions[1] of the known universe. The road towards the SM began in a broad sense in around 5th century BCE when the ancient Greek[2] philosophers (now known as the atomists) such as Leuccipus and Democritus speculated that all matter is composed of small, everlasting, and indivisible particles called atoms[3]. The properties of different substances were determined by the shape and arrangement of these particles. However, their ideas had no basis in experimental work and therefore remained just one of many philosophical thoughts until the 19th century. During his experiments at that time, John Dalton discovered that pure chemicals always decompose into the same elements and that their ratios also remain identical [7]. Combined with the observed law of conservation of mass, this led Dalton to formulate the atomic theory, which states that there are discrete, smallest, and indivisible parts of matter. He called them atoms, linking his observations to the ancient idea. However, since no atoms were directly observable, his theory, although scientifically sound, was not universally accepted at the time. There was some indirect evidence supporting the existence of atoms, such as the Brownian motion, where a light particle (such as a dust grain) is constantly moving when floating in water.

The atoms were considered the smallest particles until 1897, when J. J. Thomson discovered the electron. In his experiments with cathode rays, he observed that they are deflected by an electric field, implying that the rays are not the light. Instead, the rays are composed of negatively charged particles [8]. By measuring the charge-to-mass ratio, it became clear that these particles are almost 2000 times lighter than the lightest atom, hydrogen. Therefore, the electron became the first known subatomic particle and the pudding model of the (now divisible) atom was born [9]. The pudding model, where negatively-charged electrons travel through the positively-charged atoms, was quickly disproved after the famous Geiger-Marsden experiments [10] under the supervision of E. Rutherford. They bombarded a golden foil with alpha particles and observed that a small fraction of the alpha particles scattered at very large angles, inconsistent with the pudding model. Rutherford concluded that the atom is essentially an empty sphere, where most of its mass and all of its positive charge is concentrated in a very small center (nucleus) [11]. Rutherford also discovered that hydrogen nuclei are produced during the bombardment of nitrogen by alpha particles and conlcuded that the hydrogen nucleus is the simplest positively-charged particle, the proton. The Rutherford model of the atom, which assumed electrons orbiting a small nucleus, had its problems as well. Charged particles moving in a curved path emit energy through radiation and therefore

---

[1] Three out of four. The non-inclusion of gravity is discussed below.

[2] There were also probably Indian philosophers with similar ideas at the same time. However, the sources from this time period are limited.

[3] "atomos" = "indivisible" in ancient Greek

electrons should soon collide with the nucleus and cease to exist. Soon afterwards, N. Bohr incorporated the findings of M. Planck, A. Einstein and others and proposed the quantum-mechanical model of the atom, where electrons can change energy only via the emission or absorption of a quantum with discrete energy amount, corresponding to moving up or down to different orbits [12]. The work of L. de Broglie, E. Schrödinger, W. Heisenberg, W. Pauli and others in the 1920s and 1930s [13] led to the formulation of the modern model of the atom, where electrons do not have precise position and trajectory. Instead, they can be found anywhere with varying probability and the regions of high probability are called orbitals.

During his experiments with alpha particles bombarding a beryllium target in 1932, J. Chadwick discovered a particle that was very similar in mass to the proton, but had no electric charge [14]. This particle was named the neutron and together with the proton they form all known[4] nuclei and therefore are known together as nucleons. In the same year, the first antiparticle (positron) was discovered in a cloud chamber by C. Anderson [15], followed by his co-discovery of the muon in 1936 [16]. On the theory frontier, E. Fermi formulated his theory of the three-body neutron decay, the first description of the weak interaction [17] in 1934. One year later, H. Yukawa presented the first theory [18] describing the interactions between nucleons and predicted the existence of an exchange particle - the pion, discovered in 1947 [19]. This was the birth of the theory of the strong interaction. Since the strong interaction is the dominant force in the physics studied in this thesis, it is described in more detail in Sec. 1.1. The following years, until the end of World War II, were fully dedicated to the advancements in nuclear fission, both moderated and unmoderated.

Shortly afterwards, the rapid advancement in particle accelerator performance led to the discovery of many species of hadrons (massive particles interacting via the strong interaction), creating a so-called particle zoo (see for example [20] for a comprehensive review). These particles (and antiparticles) were similar in mass to nucleons and therefore were also considered elementary. This became sort of an aesthetics problem, because the overall sentiment of the community was that all matter should be composed of only a few elementary particles. This led to new theoretical and experimental advancements which completely changed the picture. Independently of each other, M. Gell-Mann and G. Zweig published the quark model[5] in 1964 [21,22]. The quark model proposes that all hadrons are bound states of elementary particles with fractional elementary charge. Baryons are composed from three quarks and mesons from one quark and one antiquark. Three kinds of quarks were necessary - the up (u), down (d) and strange (s) - and the corresponding quantum number is called "flavor", forming an approximate SU(3) flavor symmetry. Quarks were experimentally confirmed in deep inelastic scattering experiments performed at the Stanford Linear Accelerator Center (SLAC) in 1968 [23,24].

Around the same time, advancement in the electroweak theory (developed by S. Weinberg, A. Salam and S. Glashow in an attempt to unify electromagnetism with the weak force), namely the Glashow-Iliopoulos-Maiani mechanism [25], which predicted the (observed) suppression of flavor-changing neutral currents, created the necessity for a fourth quark flavor. The discovery of the charm (c) quark is one of the most fascinating stories in particle physics. Two teams, one at SLAC - headed by B. Richter - and the second at the Brookhaven National Laboratory (BNL) - led by S. Ting - used inverse processes to arrive at the same result at the same time. The BNL team used $p + \mathrm{Be} \rightarrow J/\psi \rightarrow e^+ + e^-$ to explore the dielectron invariant mass spectrum over a broad range, while the SLAC team used the highly precise $e^+ + e^- \rightarrow J/\psi \rightarrow X$ channel, but were initially limited by the kinematic range. Both teams announced

---

[4] At the time. Today, there are rare exceptions, with hypernuclei being produced in high-energy experiments and strange matter possibly existing in cores of neutron stars.

[5] "Quarks" is the name given by Gell-Mann, while Zweig proposed the name "aces". Since the name "quark" is now prevalent, it will be used throughout the text.

the discovery of the new particle[6] on November 11 1974 [26, 27], sparking the so-called November revolution as many discoveries were made shortly afterwards. The J/ψ particle was soon identified as a bound state of $c\bar{c}$ and is studied to this day. Even before the discovery of the c quark, M. Kobayashi and T. Maskawa proposed two additional quark flavors [28] in order to explain the charge-parity (CP) violation, observed in neutral kaon weak decay in 1964. The bottom/beauty (b) quark was discovered in 1977 by the E288 experiment team led by L. Lederman at the Fermi National Accelerator Laboratory (Fermilab) [29]. Meanwhile, the τ lepton was discovered in 1975 at SLAC by M. Perl *et al.* [30], completing the massive lepton part of the puzzle.

The strong force exchange particle, the gluon, was observed in tri-jet events by the experiments at the Positron–Electron Tandem Ring Accelerator (PETRA) in 1979 [31]. Experiments at the European Commission for Nuclear Research (CERN), led by C. Rubia and S. van der Meer, discovered the weak bosons[7] $W^{\pm}$ and Z^0 around 1983 and later measurements of the Z^0 decay width fixed the expected number of quark and lepton generations at three. Therefore, only the top (t) quark remained undetected until 1995, when the D0 and CDF collaborations at Tevatron announced the observation of an elementary particle with mass around 175 GeV/c^2 [32, 33], comparable to large atoms.

When the tau neutrino ν_τ was observed by the DONUT collaboration in 2001 [34], there was only one missing particle predicted by theory – the Higgs boson, which is the manifestation of the Higgs field through which all massive particles acquire their mass. The final piece of the puzzle was discovered in 2012 when the ATLAS and CMS collaborations at the LHC announced the observation of a particle consistent with the Higgs boson prediction [35,36]. The current picture of all known elementary particles can be seen in Fig. 1.1.

Although self-consistent, the SM is unable to explain all the phenomena observed in the present-day universe and a few key examples follow. Remarkably, it does not describe the gravitational interaction (explained with great success by the general theory of relativity), since there is no successful theory of quantum gravity and the expected force carrier – the graviton – has not yet been observed. There is no explanation for the excess of matter over antimatter observed today throughout the universe, even though A. Sakharov formulated three conditions necessary to create the imbalance [37] already in 1967. The SM operates with massless neutrinos, but the neutrino experiments in Japan [38] and Canada [39] discovered neutrino oscillations around the year 2000, implying that neutrinos must have non-zero mass[8]. The SM also does not describe dark matter particles, nor can it explain the expansion of the universe caused by the dark energy. Despite these shortcomings, the SM has been remarkably successful in predicting various phenomena in particle physics and it is not clear when or even if there will be the next breakthrough discovery hinting at some beyond-the-Standard-Model physics.

1.1 Strong Interaction

The strong interaction is one of the four currently recognized fundamental interactions, along with gravity, the electromagnetic interaction and the weak interaction. As its name suggests, it is the strongest of the four, strong enough to hold together positively-charged protons inside the nucleus. The strength

---

[6] The BNL team named the particle J while the SLAC team named the particle ψ. Since there was no overwhelming preference in the community, both names were accepted. To this day, J/ψ is the only particle to have two names.

[7] In simple terms, a boson is a particle with integer spin which does not follow the Pauli exclusion principle, while a fermion has half-integer spin and does obey the Pauli exclusion principle.

[8] More precisely, at least one neutrino flavor must have non-zero mass in order to facilitate the oscillations. The neutrinos which participate in weak interactions are linear combinations of the three mass states.

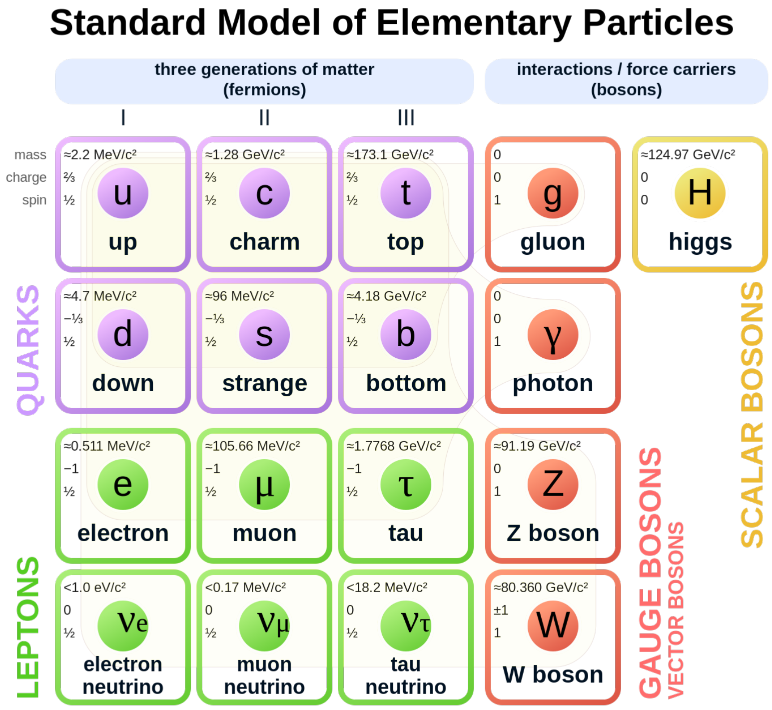

Figure 1.1: Table of all known elementary particles with their properties. Different types of particles are represented by different colors and (hardly visible) lines represent the coupling of fermions to bosons. Taken from public domain, made by user "Cush".

of each interaction is represented by the value of the corresponding coupling constant[9]. For comparison, under normal circumstances, the strong coupling constant has a relative value $\alpha_s \approx 1$, while for the electromagnetic interaction $\alpha = \frac{1}{137}$, the weak interaction $\alpha_w \sim 10^{-7}$ and the gravitational interaction merely $\alpha_g \sim 10^{-39}$. The weak interaction is mediated via the exchange of heavy bosons with short lifetime ($\sim 10^{-25}$ s) and therefore is very short-ranged. The strong force is also short-ranged, even though the force mediators (gluons) are massless. This effect is known as confinement and is discussed later in Subsec. 1.1.2. The electromagnetic force has unlimited range, because the photon is also massless, but since the universe is electrically neutral at macroscopic scales, it is in the end the gravitational interaction which dominates the universe as it is experienced by all massive particles. At large energies[10], the electromagnetic and the weak interacitons can be unified in the electroweak theory and therefore are regarded as different manifestations of the same force. The attempts to unify the electroweak and strong interactions are still incomplete within the SM[11], while gravity is completely ignored in the SM. The strong interaction is described within the framework of quantum chromodynamics (QCD), presented in Subsec. 1.1.1. The coupling constant and its "non-constantness" is discussed in Subsec. 1.1.3, leading

---

[9] Each coupling constant can be expressed in terms of fundamental constants related to the given interaction. For example, the fine structure constant $\alpha = \frac{e^2}{4\pi\epsilon_0\hbar c}$, where e is the elementary charge, ϵ_0 is the vacuum permitivity, $\hbar$ is the reduced Planck constant and c is the speed of light in vacuum.

[10] The electroweak scale is around 246 GeV, well within the reach of the LHC.

[11] This effort is known as the Grand Unified Theory (GUT) and the unification is expected at energies $\sim 10^{16}$ GeV, unfortunately unreachable by current or near-future accelerators.

to the interesting phenomenon known as the asymptopic freedom (Subsec. 1.1.4).

1.1.1 Color Charge and QCD Lagrangian

In order to participate in the strong interaction, a particle needs to have a non-zero quantum number called the color charge. Baryons are composed of three quarks, each carrying different color[12], while mesons are composed of a quark and an antiquark, with the quark carrying one color and the antiquark the corresponding anticolor, making the hadrons color neutral on the outside. The need for these new degrees of freedom arose with the discovery of the Δ^{++} (uuu), Δ^{-} (ddd), and Ω^{-} (sss) particles, which contain three valence quarks of the same flavor and therefore should not exist due to the Pauli exclusion principle. This means that flavor is not the correct symmetry. The quantum chromodynamics is a non-abelian gauge theory in the SU(3) group with exact local symmetry defined by the color charges and has an approximate flavor symmetry (exactness violated due to different quark masses). The Lagrangian of QCD is given by

$$L = \sum_{q} \bar{\psi}_{q,a} \left(i\gamma^{\mu} \left[\partial_{\mu}\delta_{ab} - i g_s T^{C}_{ab} A^{C}_{\mu} \right] - m_q \delta_{ab} \right) \psi_{q,b} - \frac{1}{4} F^{A,\mu\nu} F_{A,\mu\nu}, \tag{1.1}$$

where q runs over the 6 quark flavors, ψ is a Dirac spinor representing the quark field, a and b are the indices representing the 3 colors, γ^{μ} are the Dirac gamma matrices, $\partial_{\mu}\delta_{ab} - i g_s T^{C}_{ab} A^{C}_{\mu}$ is the gauge covariant derivative, where g_s is the coupling strength, T are the generators of the SU(3) group constructed from Gell-Mann matrices, C is the index of the 8 gluon fields A_{μ}, m is the quark mass and δ is the Kronecker delta. $F_{\mu\nu}$ is the gluon field strength tensor defined as

$$F^{A}_{\mu\nu} = \partial_{\mu} A^{A}_{\nu} - \partial_{\nu} A^{A}_{\mu} - g_s f_{ABC} A^{B}_{\mu} A^{C}_{\nu}, \tag{1.2}$$

where f_{ABC} are the structure constants of the SU(3) group. The definition is analogous to quantum electrodynamics (QED), but the key difference is the last term, which is not present in the QED Lagrangian and which represents the self-interaction of gluons. Gluons, as the mediators of the strong interaction, also carry the color charge[13], in contrast with photons. This is the reason why the strong interaction is only short-ranged (~ 1 fm $= 10^{-15}$ m).

1.1.2 Confinement

There is no analytically derived form of a quark-antiquark pair potential $V(r)$, but the following empirical formula

$$V(r) = -\frac{4}{3}\frac{\alpha_s}{r} + \sigma r, \tag{1.3}$$

where r is the distance and σ is the string stiffness parameter, is frequently used within the string model [40]. The first term is the repulsive Coulomb interaction, which dominates at small distances, but as the two quarks get separated, the gluon field forms a narrow flux tube (string), the second term rises and the string tension between the two quarks increases until the energy is sufficient to create a new quark-antiquark pair from vacuum, releasing the tension. The newly created quarks reduce the quark-antiquark distance and create new colorless hadrons. This phenomenon is called (color) confinement and is the reason we cannot observe quarks as free particles[14].

---

[12] The colors are usually called red, green and blue and the anticolors antired, antigreen and antiblue. There is no physical meaning behind the colors.

[13] There are 8 independent color charge combinations, each equivalent to one Gell-Mann matrix, and one color singlet.

[14] The only exception is the top quark, which decays so fast ($\tau_t \sim 10^{-25}$ s) that it does not form hadrons.

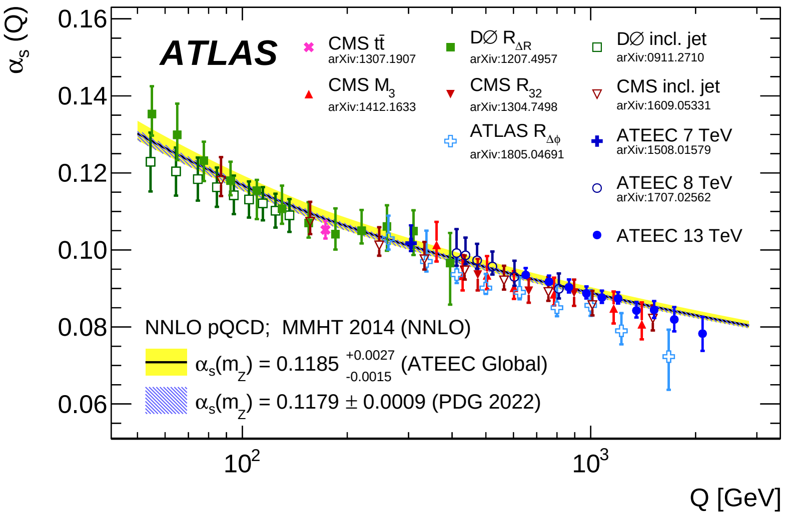

Figure 1.2: Dependence of the strong coupling constant α_s on the scale Q as measured by the ATLAS collaboration (blue filled circles). Different symbols represent earlier measurements by ATLAS as well as other experiments (references in figure). The black line represents the next-to-next-to-leading-order pQCD fit to the data while the shaded area represents the previous fit to world average data. Taken from [41].

1.1.3 Running Coupling Constant

QCD can be renormalized in order to avoid infinities caused by higher-order quantum loops. However, this causes α_s to not behave as a constant anymore, but to depend on the energy scale (also called virtuality) of the studied process $Q^2 \equiv -q^2$, where q^2 is the four-momentum transfer squared. If the energy of the process is larger or the time/distance is smaller, more virtual particles apear as a consequence of the uncertainty principle and contribute to the screening of the color charge, effectlively reducing the interaction strength. Therefore, α_s is decreasing with increasing Q^2 and this property is called the running of the coupling constant. It is not exclusive to QCD, as the fine structure constant α of QED is also dependent on the scale of the process with energy, but the self interaction of gluons makes the change in α_s more rapid. Fig. 1.2 shows the current status of α_s measurements done by ATLAS, and the comparison with previous measurements. The running of α_s is clearly visible with value at the Z boson mass $\alpha_s(m_Z) = 0.1185^{+0.0027}_{-0.0015}$, consistent with the world average and almost 10 times lower than under normal circumstances. For comparison $\alpha(m_Z) \approx \frac{1}{127}$, meaning that α grows slowly with the energy scale.

The evolution of $\alpha_s(Q^2)$ is given by

$$\alpha_s(Q^2) = \frac{12\pi}{(33 - 2N_f)\ln\left(\frac{Q^2}{\Lambda^2_{\mathrm{QCD}}}\right)}, \tag{1.4}$$

where $N_f = 6$ is the number of quark flavors and $\Lambda_{\mathrm{QCD}} \approx 220$ MeV is the typical QCD scale, which effectively serves as an infrared cutoff for the applicability of the perturbation theory, which requires

$\alpha_s \ll 1$, therefore $Q^2 \gg \Lambda_{\text{QCD}}$. Since most of the problems within QCD cannot be solved analytically, the applicability of perturbative QCD is almost always welcome[15].

1.1.4 Asymptotic Freedom

The implication of the running coupling constant α_s is clear. If the energy increases enough or at sufficiently short distances, the strong interaction becomes too weak to hold quarks and gluons together, $Q^2 \to +\infty \implies \alpha_s \to 0$, and they behave as quasi-free particles. This behavior is called the asymptotic freedom and was predicted by D. Gross, F. Wilczek and H. Politzer in 1973 [42, 43]. The only available process that can generate enough temperature to "melt" nucleons into a soup of deconfined quarks and gluons are relativistic collisions of heavy atomic nuclei, discussed in the next chapter.

---

[15] The pQCD utilizes the perturbation theory techniques which consider a system with known solution and add small corrections, in pQCD expressed as terms of powers of α_s, in order to describe a more complex system.

Chapter 2

Relativistic Heavy-Ion Collisions

Analyzing collisions of (ultra)relativistic heavy atomic nuclei is an excellent way to study the nuclear matter. It is also the only process which can generate the QGP, that is available to humans. Compared to collisions of small hadronic systems ($p + p$, $p/d/$He+A) at the same beam energy, the A+A collisions generate much higher energy density in the collision region due to large number of nucleon–nucleon interactions occuring at the same time. The history of heavy-ion collisions dates from the 1980s when it was proposed that such collisions can generate temperatures higher than the transition temperature from hadronic matter to the QGP [44]. These collisions were studied at lower energies by experiments at the Alternating Gradient Synchrotron (AGS) in BNL and at the Super Proton Synchrotron (SPS) in CERN with the latter observing phenomena indicating the formation of a new state of matter [45]. When RHIC became operational in 2000, it marked the true breaking point in heavy-ion physics and the LHC also conducts heavy-ion runs yearly since the beginning of its physics operations in 2010.

The first section 2.1 introduces several key variables used to describe the processes happening during relativistic heavy-ion collisions. Section 2.2 describes collision centrality, a key measure of the "violentness" of the event[1]. The full time–space evolution of a typical central A+A collision is described in Sec. 2.3. The most violent events can produce an exotic state of matter consisting of quasi-free quarks and gluons, the quark–gluon plasma (described in Sec. 2.4.). The QCD phase diagram (Sec. 2.5) contains different phases of matter composed of quarks and gluons and its description is one of the main goals of today's particle physics. Collisions of heavy ions at different energies can help complete this puzzle.

2.1 Variables

2.1.1 Spatial Coordinates

The standard spatial coordinates are the cartesian x, y and z. In circular collider experiments, z is usually defined along the beam axis, x points to the center of the accelerator ring and y goes upwards. However, the choice of these axes is somewhat arbitrary. Because there is no natural preference in the $x - y$ plane, most detectors of heavy-ion collisions have approximately cylindrical symmetry around the z axis and therefore it is convenient to use cylindrical coordinates. The azimuthal angle is defined in the $x - y$ plane and usually called ϕ. The polar angle (usually called θ) is the angle in the $z - y$ plane and is measured from the beam line. However, since the collisions and processes are relativistic, variables

---

[1] An event corresponds to one collision of accelerated particles

which have convenient properties for Lorentz transformations, such as rapidity and pseudorapidity, are usually used instead of the polar angle.

2.1.2 Rapidity

For a particle with energy E and longitudinal component of its momentum p_z, its rapidity y can be defined[2] as

$$y = \frac{1}{2} \ln \frac{E + p_z}{E - p_z}. \tag{2.1}$$

Rapidity is additive with respect to Lorentz transfromation, yielding

$$y' = y + y_{\mathrm{CM}}, \tag{2.2}$$

where y' is the particle rapidity in the laboratory frame, y is the rapidity in the center-of-mass frame and y_{CM} is the rapidity of the center of mass in the laboratory frame. Regions of high $|y|$ are referred to as forward regions [3], while the region with $|y|$ close to 0 is called mid-rapidity. There is no specific value of y which divides the space into forward and mid-rapidity sections, but it is usually a matter of convention at each experiment. For example, at STAR the mid-rapidity region is usually understood as the region with $|y| < 1$, which is fully covered by the main detector systems (see Chapter 4 for details).

2.1.3 Pseudorapidity

Pseudorapidity η measures the polar angle θ of the particle relative to the beam axis. It is defined as

$$\eta = -\ln\left(\tan\left(\frac{\theta}{2}\right)\right), \tag{2.3}$$

and is also additive under Lorentz transformation. Pseudorapidity converges to rapidity in the ultrarelativistic limit $m \approx 0 \implies E \approx p \implies \eta \approx y$, which is applicable for pion production at high-energy experiments. Pseudorapidity is often preferred, since it does not depend on the particle energy, but only on its polar angle. There is one additional reason why η and y are preferred to the polar angle: particle production has been found to be approximately constant as a function of these variables [46]. A purely angular distance between two particles can be calculated as $\Delta R = \sqrt{(\Delta\eta)^2 + (\Delta\phi)^2}$ and is often used in collider experiments.

2.1.4 Transverse Momentum

Particle momentum is usually stored as a three-vector $\vec{p} = (p_x, p_y, p_z)$. As mentioned before, there is no natural preference for physical processes regarding the azimuthal angle in the plane transverse to the beam axis. Therefore, the p_x and p_y are often combined, and the transverse momentum p_{T} is defined as

$$p_{\mathrm{T}} = \sqrt{p_x^2 + p_y^2}. \tag{2.4}$$

Using p_{T}, one can express the cartesian momenta as

$$\begin{aligned} p_x &= p_{\mathrm{T}} \cos\phi, \\ p_y &= p_{\mathrm{T}} \sin\phi, \\ p_z &= p_{\mathrm{T}} \sinh\eta. \end{aligned} \tag{2.5}$$

---

[2] Throughout this thesis, the convention $c = \hbar = k_{\mathrm{B}} = 1$ is used, unless specified otherwise.

[3] Where relevant, the region of large negative y is called backward rapidity, usually in asymmetric collision systems.

Transverse momentum is invariant with respect to Lorentz boosts in (pseudo)rapidity, which is again very convenient. The main physics importance of using p_T is that before the collision $p_\mathrm{T} \simeq 0$ regardless of the beam energy, thus if a high-p_T object is observed in the detector, it is a clear proof of a rare high-energy process occuring during the collision.

2.2 Collision Centrality

The result of a collision of two heavy ions largely depends on how much the nuclei actually overlap during the collision. If more nucleons participate in the event, they deposit more energy and increase the chance of a rare hard process occurring. Figure 2.1 shows a sketch of a typical heavy-ion collision. The nucleons which participate in the collision are called participants and the rest are called spectators, beacause they emerge from the collision largely unaffected. The impact parameter b, defined as the transverse distance between the centers of the two nuclei, is used to parametrize the overlap. It is obvious from simple geometry that the head-on collisions are very rare. In reality, during most of the collisions the two nuclei overlap by a very small part[4].

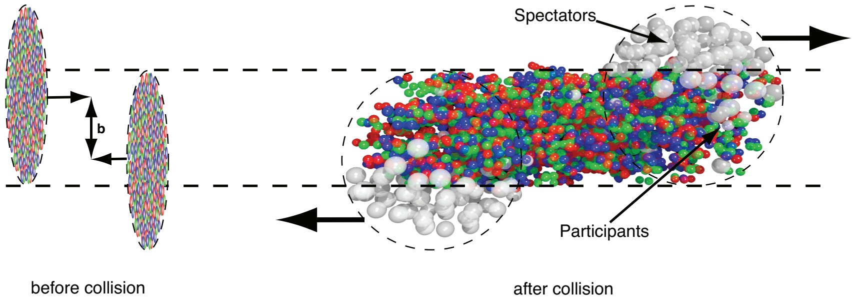

Figure 2.1: Illustration of a typical heavy-ion collision depicting the situation before (left) and after (right) the collision. Participants and spectators are noted as well as the impact parameter. Taken from [47].

Collisions can be sorted into three broad categories based on the value of b. If $b \sim 0$, we are talking about central collisions, for $0 < b < R_A + R_B$, where $R_{A,B}$ are the radii of both nuclei, the events are classified as peripheral collisions and in the case of $b > R_A + R_B$ the ultraperipheral collisions occur[5]. The physics of ultraperipheral collisions is very distinct from the other two types of collisions and lies beyond the scope of this thesis. There is no way to experimentally determine the value of b, so the concept of collision centrality was developed to classify each event. Events are classified depending on the value of some global variable expected to scale with b. There are multiple such variables. Experiments with focus on tracking, such as STAR and ALICE, usually use the total number of charged particles (multiplicity) within a defined region of the detector, while calorimetry-based experiments (ATLAS, CMS) measure the total transverse energy E_T deposited in one of their calorimeter systems. Figure 2.2 shows a STAR measurement of the uncorrected track multiplicity $N_\mathrm{ch}^\mathrm{raw}$ within $|\eta| < 0.5$ with the requirement of the primary vertex being within $|V_z^{TPC}| < 6$ cm, as measured in Au+Au collisions at $\sqrt{s_\mathrm{NN}} = 200$ GeV by the STAR Time Projection Chamber (TPC, details in Subsec. 4.2.1). This multiplicity is called the reference multiplicity and is used as a standard to determine the collision centrality at STAR. The distribution of the reference multiplicity is split into quantiles of the total inelastic cross section, since

---

[4] Even more common is, of course, that the nuclei don't interact at all during the beam crossing.

[5] In the case of ultraperipheral collisions, the nuclei interact only electromagnetically via the exchange of a virtual photon.

the highest reference multiplicity corresponds on average to events with the largest overlap of the nuclei. For example, the 0–5% centrality bin contains exactly 5% of all events and these are the events which produce the most charged-particle tracks, corresponding to the lowest values of b. The data are fit with the Monte Carlo (MC) Glauber model [47] and it is clear that the model describes the distribution very well, except for the lower end of the distribution (very peripheral events). This deviation is caused by the inefficiency of the Vertex Position Detector (VPD, details in Subsec. 4.2.3), used as the minimum-bias trigger, and is accounted for in STAR analyses.

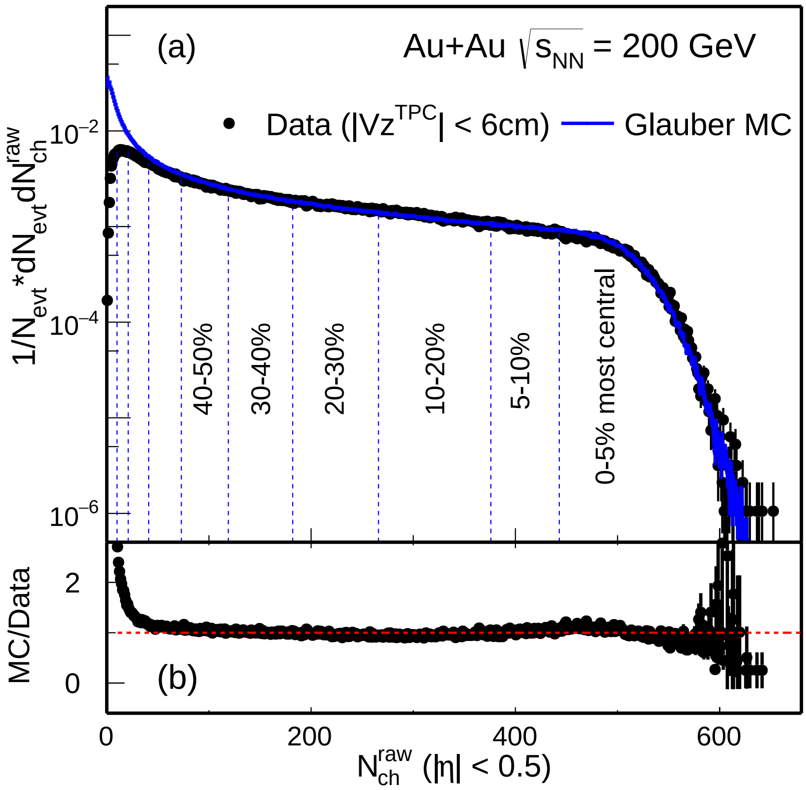

Figure 2.2: Centrality measurement at STAR. In the upper pannel, the black points represent the uncorrected number of charged-particle tracks $N_{\mathrm{ch}}^{\mathrm{raw}}$ per Au+Au event at $\sqrt{s_{\mathrm{NN}}} = 200$ GeV and the blue line represents the MC Glauber model fit to the high end of the spectrum. Centrality bins are highlighted by dashed lines. The bottom panel shows the ratio of model/data. Taken from [48].

2.3 Time-space Evolution of Relativistic Heavy-Ion Collisions

The typical central relativistic heavy-ion collision undergoes an evolution through several stages. Figure 2.3 shows the entire time-space evolution of such collision.

Before the collision, the nuclei approach as Lorentz-contracted pancakes. When the nuclei collide, individual nucleons participate in binary collisions, each assumed to be independent of the others. In each such collision, the partons inside the nucleons can scatter with high momentum transfer (hard scattering) and the system is not in a thermal equilibrium. The matter undergoes a phase transition into the QGP

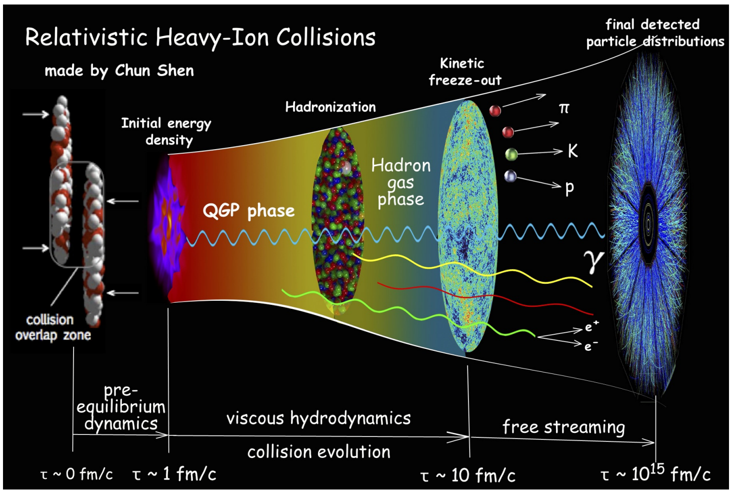

Figure 2.3: Sketch of a relativistic heavy-ion collision evolution with key phases highlighted. Taken from [49].

phase, creating a fireball. Once the matter thermalizes, the fireball expands and cools down in time τ as

$$T = T_0 \left(\frac{\tau_0}{\tau} \right)^{-1/3}, \tag{2.6}$$

where T_0 is the temparature at the thermalization time $\tau_0 \sim 1$ fm/c after the collision starts. The system evolves following the laws of hydrodynamics for a low-viscosity fluid until the time τ_C when the temperature drops below the critical temperature T_C and a transition into the hadron-gas phase begins. The process of hadronization is still not fully understood within the QCD framework (it is a soft process) and lasts until $\tau_\mathrm{H} \sim 10$ fm/c, where all quarks and gluons are once again confined inside hadrons. This boundary is called the chemical freeze-out, because the hadronic composition is fixed from this point on. The hadrons can still interact via ellastic collisions until the kinetic freeze-out, when the probability of such collisions becomes negligible. After the kinetic freeze-out, unstable particles decay while the stable particles continue largely unaffected towards the particle detectors. The only particles which have sufficient mean decay length so that they can effectively reach a typical detector system are the hadrons $\pi^\pm, K^\pm, K^0_\mathrm{L}, p, \bar{p}, n$ and $\bar{n}$, the leptons $e^\pm, \mu^\pm$, and γ. This evolution is very similar to the evolution of the early universe[6], making the study of the heavy-ion collisions extremely important even from the cosmological point of view. In a nutshell, we are creating thousands of small Big Bangs in a laboratory every second during the RHIC or the LHC heavy-ion runs.

2.4 Quark–Gluon Plasma

The creation and study of the quark–gluon plasma is the alpha and omega of high-energy heavy-ion research. From the theory stand point, the history of QGP dates from the 1960s when R. Hagedorn calculated that the mass spectra of particles rise exponentially, indicating a limiting temperature of hadronic matter [50,51]. After the prediction of the asymptotic freedom in 1973, two independent groups [52,53]

---

[6] On much larger timescales, of course. The QGP phase is believed to have occured approximately ~ 1 µs after the Big Bang, while the recombination of electrons and nuclei (analogous to kinetic freeze-out), which produced the Cosmic Microwave Background, occured when the universe was approximately 379 000 years old.

interpreted the Hagedorn temperature as an onset of a phase transition from hadronic matter to a deconfined state in 1975. Currently, the state-of-the-art lattice QCD (lQCD) calculations estimate the transition (critical) temperature at $T_c \sim 150 - 175$ MeV [54], depending on the quark properties used in the calculations. Experimentally, the first hints of QGP existence were announced by the SPS experiments in 2000 [55]. The QGP discovery was officially announced in 2004 [4], followed by all four experiments at RHIC presenting overwhelming evidence for a new deconfined medium consisting of free quarks and gluons [56–59]. Later measurements have provided additional information. One surprising finding was that the QGP behaves as a strongly-coupled liquid with very low viscosity to entropy ratio, which is in contrast with the naïve expectation that it would behave similarly to an ideal gas [60]. The QGP has also many extreme properties, even compared to other real-life extreme examples. For example, its temperature, which reaches around $T \sim 10^{12}$ K, is several orders of magnitude larger than the temperature in the core of the Sun ($T \simeq 15 \times 10^6$ K) or vorticity, which was measured to be $\omega \sim 10^{21}$ s^{-1}, shattering the previous record of superfluid helium nanodroplets with $\omega \sim 10^7$ s^{-1} [61].

Since the QGP exists only for a tiny fraction of a second and is confined to a very small volume, it is impossible to determine its properties directly. Fortunately, there are many processes which can be measured and which probe the QGP. These probes can be roughly divided into three main categories. The soft probes (for example flow and strangeness) utilize the collective behavior of the deconfined medium. The hard probes (such as jets[7] and quarkonia) emerge from hard partons which are created before the QGP forms and their modification can be interpreted (at least partially) as the effects of the medium. The electromagnetic probes (e. g. direct photons) are highly penetrating inside the medium and provide us with otherwise inaccessible information from the very core of the QGP droplet. The abovementioned probes are briefly introduced in the following subsections. For more detailed reviews of historical and current status of the QGP physics see for example [62] or [63].

2.4.1 Flow

The anisotropic flow is a measure of the azimuthal anisotropy of particles in an event. It is usually parametrized by the flow coefficients v_n appearing in the Fourier decomposition of the particle spectrum [64]:

$$E\frac{\mathrm{d}^3N}{\mathrm{d}^3p} = \frac{1}{2\pi}\frac{\mathrm{d}^2N}{p_\mathrm{T}\mathrm{d}p_\mathrm{T}\mathrm{d}\eta}\Big(1 + 2\sum_{\mathrm{n}=1}^{\infty} v_\mathrm{n}\cos[\mathrm{n}(\phi - \Psi_\mathrm{RP})]\Big), \tag{2.7}$$

where Ψ_RP is the reaction plane of the collision, defined as the angle between the beam line and the line connecting the centers of the two nuclei in the transverse plane. The flow coefficients are then defined as

$$v_\mathrm{n} = \langle\cos[n(\phi - \Psi_\mathrm{RP})]\rangle, \tag{2.8}$$

where the angle brackets represent mean value. The most important component is the elliptic flow v_2. Elliptic flow arises as a consequence of the initial spatial anisotropy of the collision. In a peripheral collision, the overlap region of the two nuclei has an approximate almond shape (illustrated in Fig. 2.4) and the difference in pressure gradients translates into the final-state momentum anisotropy.

This picture is of course valid only under the assumption that the medium created during the collision behaves hydrodynamically. Therefore, the observation of large positive v_2 of both inclusive hadrons and identified particles in Au+Au collisions at RHIC experiments, as shown in Fig. 2.5, was one of the key arguments for the existence of the QGP as a strongly-coupled liquid [66, 67].

---

[7] Jets, as the main topic of this thesis, are discussed in detail separately in Chapter 3.

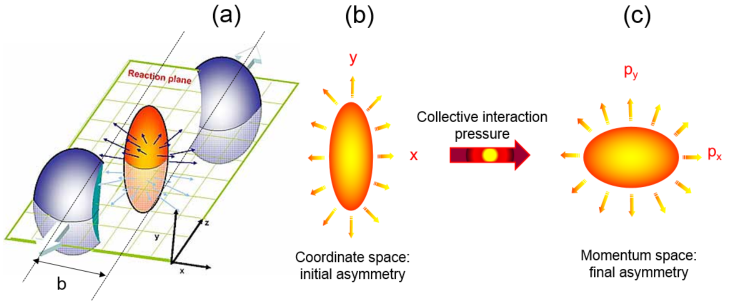

Figure 2.4: Illustration of the origin of the elliptical flow. Panel (a) depicts the reaction plane and the almond shape overlap region after the collision. Panel (b) shows the initial spatial anisotropy which translates into (c) the final-state momentum anisotropy. Taken from [65].

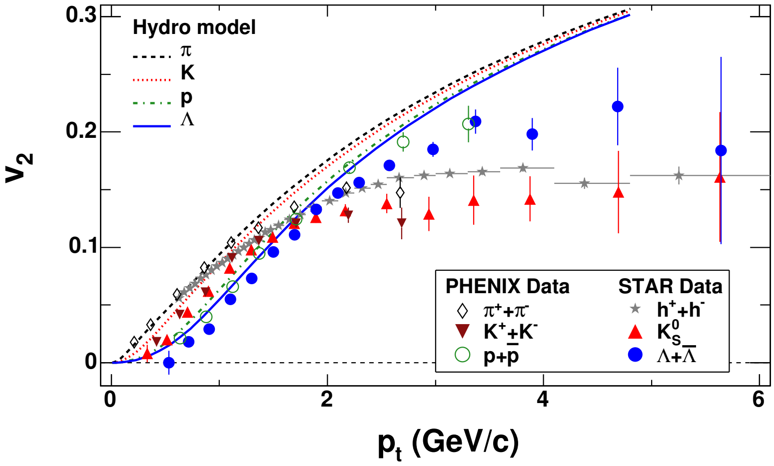

Figure 2.5: Elliptic flow coefficient v_2 as a function of particle p_T from minimum bias Au+Au collisions at $\sqrt{s_{NN}} = 200$ GeV at RHIC. Different symbols represent different particle species and lines represent corresponding calculations from hydrodynamical models. Taken from [67].

The higher flow coefficients were also measured in heavy-ion collisions [68, 69], further supporting the hydrodynamic nature of the QGP. In recent years, there have been surprising results from the high-multiplicity p+p collisions at the LHC, which indicate collective behavior even in systems where no QGP is expected [70, 71]. The search for flow in these small systems is an active field of research today, but unfortunately lies beyond the scope of this thesis.

2.4.2 Strangeness

Strangeness, in particular the enhancement of strange particle production in heavy-ion collisions, has been one of the earliest proposed signatures of QGP production [72]. The net strangeness ($S = N_{\bar{s}} - N_s$) is a conserved quantity and is zero in the initial state. In the hadronic picture, strange hadrons can be produced in reactions such as

$$p + p \to p + \Lambda + K^+, \tag{2.9}$$

where the threshold of such reaction is around $m_\Lambda + m_{K^+} - m_p \simeq 672$ MeV. The situation changes when we have quarks as the degrees of freedom, here the s quarks can be produced for example in the following way:

$$q + \bar{q} \rightarrow s + \bar{s}, \tag{2.10}$$

where q represents light flavor quarks (u, d), with threshold $2m_s - 2m_q \simeq 200$ MeV. Therefore, it is much easier to produce strange particles inside the deconfined medium and the enhancement of the yield of strange particles is expected. Strangeness enhancement has been observed by the experiments at the SPS, RHIC and the LHC [73–75]. As an example, the centrality dependence of multi-strange baryon enhancement can be seen in Fig. 2.6. The strangeness enhancement increases with collision centrality – with hints of saturation in the most central collisions – and also with the strangeness content of the particles. The enhancement is significantly lower at the LHC than observed at the SPS and RHIC.

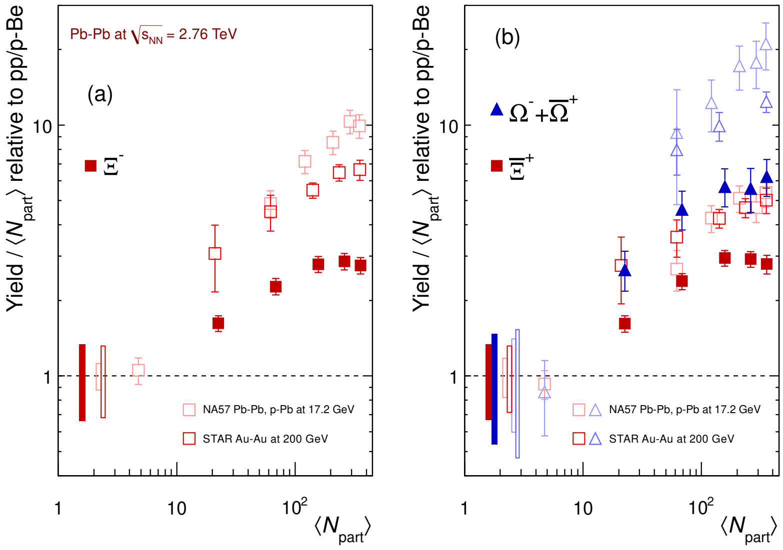

Figure 2.6: Yield enhancement (relative to p+p collisions/p+Be collisions) of the multistrange baryons Ξ^- (a) and $\overline{\Xi}^+$ and $\Omega^- + \overline{\Omega}^+$ (b) as a function of the mean number of participants $\langle N_{\mathrm{part}} \rangle$ measured by the NA57 collaboration in Pb+Pb and p+Pb collisions at $\sqrt{s_{\mathrm{NN}}} = 17.2$ GeV, the STAR collaboration in Au+Au collisions at $\sqrt{s_{\mathrm{NN}}} = 200$ GeV and the ALICE collaboration in Pb+Pb collisions at $\sqrt{s_{\mathrm{NN}}} = 2.76$ TeV. Taken from [75].

2.4.3 Quarkonia

Quarkonia are bound states of $Q\bar{Q}$ pairs, where Q represents either c or b quark. These quarks are heavy and therefore their production occurs only during the initial hard parton scattering. This means that the quarkonium experiences the entire evolution of the system (see Sec. 2.3). The heavy quarks are bound by the Cornell potential, defined in Eq. 1.3. When the quarkonium is in the medium with free color charges, it experiences Debye-like screening of the potential which causes the two quarks to stop "feeling" each other's presence. This phenomenon is known as quarkonium melting and was first proposed in 1986 by T. Matsui and H. Satz [76] for J/ψ as a signature of the QGP formation. The effective distance of the potential is temperature-dependent, because the higher the temperature, the more color charges can contribute to the screening. Some quarkonia are more tightly bound than others, meaning that the distance of the $Q\bar{Q}$ pair is smaller and the quarkonium can survive in a higher-temperature medium. This leads to the idea of a quarkonium thermometer. By measuring various quarkonium states, one can determine the approximate medium temperature by observing, which quarkonium states survived and which did not. The left panel of Fig. 2.7 shows the measurement [77] of the dimuon invariant mass spectrum in p+p collisions at $\sqrt{s_{\mathrm{NN}}} = 5.02$ TeV with peaks corresponding to the three Υ meson ($b\bar{b}$) states clearly visible. The right panel of Fig. 2.7 shows the same region of the dimuon spectrum in Pb+Pb collisions at the same collision energy. The sequential suppression of all three Υ states, compared to yields in p+p collisions, is clearly visible, with the peak corresponding to $\Upsilon(3S)$ no longer observable. The $\Upsilon(1S)$ is the most tightly bound state and its suppression is caused mainly by the elimination of feed-down from the higher states[8], not by melting of the ground state itself. Many quarkonia-related measurements are conducted at all major high-energy experiments (for example STAR [79]), but discussion of these results lies beyond the scope of this thesis.

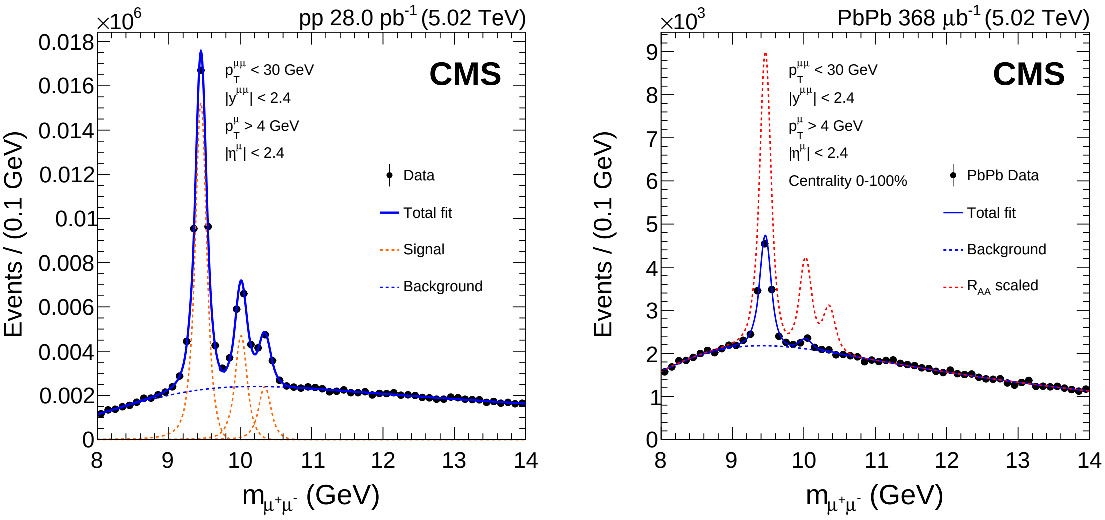

Figure 2.7: Dimuon mass spectrum from p+p (left) and Pb+Pb (right) collisions at $\sqrt{s_{\mathrm{NN}}} = 5.02$ TeV measured by the CMS experiment at mid-rapidity. Black markers represent data, the blue solid line represents the total fit to the data including background (also shown separately as blue dashed line). The red dashed line on the left represents the fit of the signal, while on the right it represents the shape of the p+p spectrum. Taken from [77].

2.4.4 Direct Photons

Direct photons can be produced in the QGP in the following processes:

$$\begin{aligned} q + \bar{q} &\rightarrow \gamma + \gamma, \\ q + \bar{q} &\rightarrow \gamma + g, \\ g + q &\rightarrow \gamma + q, \end{aligned} \tag{2.11}$$

---

[8] The decays of the higher states produce around 50 % of the ground states of Υ and J/ψ [78]. The observed suppression is therefore consistent with the elimination of the feed-down being responsible for the observed $\Upsilon(1S)$ suppression.

and they carry information about the medium at the point of their creation. The energy of the photons is linked to the medium temperature since the partons involved in the processes are thermalized within the medium and the photon energy is not further modified by the medium. There are many competing processes, inlcuding the initial parton scattering, the hadronic reactions:

$$\begin{aligned} \pi^+ + \pi^- &\rightarrow \gamma + \rho^0, \\ \pi^\pm + \pi^0 &\rightarrow \gamma + \rho^\pm, \end{aligned} \tag{2.12}$$

and resonance decays, such as

$$\pi^0 \rightarrow \gamma + \gamma, \tag{2.13}$$

making it difficult to distinguish between the direct photons created in the QGP and the background. Experimentally, direct thermal photons have been observed in both Au+Au collisions at $\sqrt{s_{\mathrm{NN}}} = 200$ GeV and Pb+Pb collisions at $\sqrt{s_{\mathrm{NN}}} = 2.76$ TeV as an excess of low-p_{T} photons in central A+A collisions compared to both the p+p spectrum and pQCD calculations [80, 81], yielding temperature estimates of $T \simeq 221$ MeV at RHIC and $T \simeq 297$ MeV at the LHC. As an example, the results by PHENIX are shown in Fig. 2.8.

2.5 QCD Phase Diagram

Similarly to well-known substances, such as water, the QCD matter can exist in multiple phases. Unlike water, the phase diagram of QCD matter is not completed and there are lots of unconfirmed phases and other features. The completion of the QCD phase diagram is one of the main goals of current research in not only the field of heavy-ion physics, but also in other fields, such as astrophysics. Figure 2.9 shows the current understanding of the QCD phase diagram in terms of temperature (T) and net baryon density (n, corresponding to the excess of baryons over antibaryons). At low values of both T and n, the quarks and gluons are confined inside hadrons. At near-zero n and high temperatures, accessible at the LHC and high RHIC energies and comparable to the conditions of the early universe, the system undergoes a phase transition into the QGP phase via a smooth crossover (mixed phase transition) as predicted by lQCD [82]. The theory also predicts a first-order phase transition above a certain value of n [83, 84]. This means that a critical point is expected to be located at the end of the first order-transition line in the diagram. RHIC has dedicated two periods of data taking (called the RHIC beam energy scan – BES I and BES II [85, 86]) at multiple low collision energies down to $\sqrt{s_{\mathrm{NN}}} = 3$ GeV, in order to search for the critical point. This very experimentally challenging task has yielded inconclusive results so far. Future high-luminosity, low-energy experiments should explore the region of intermediate n and low T, where the first-order phase transition is expected. These conditions will be similar to the cores of massive neutron stars, where the QGP is also predicted. At even more extreme values of n, several exotic phases, including the Color Super Conductor, are predicted [87, 88].

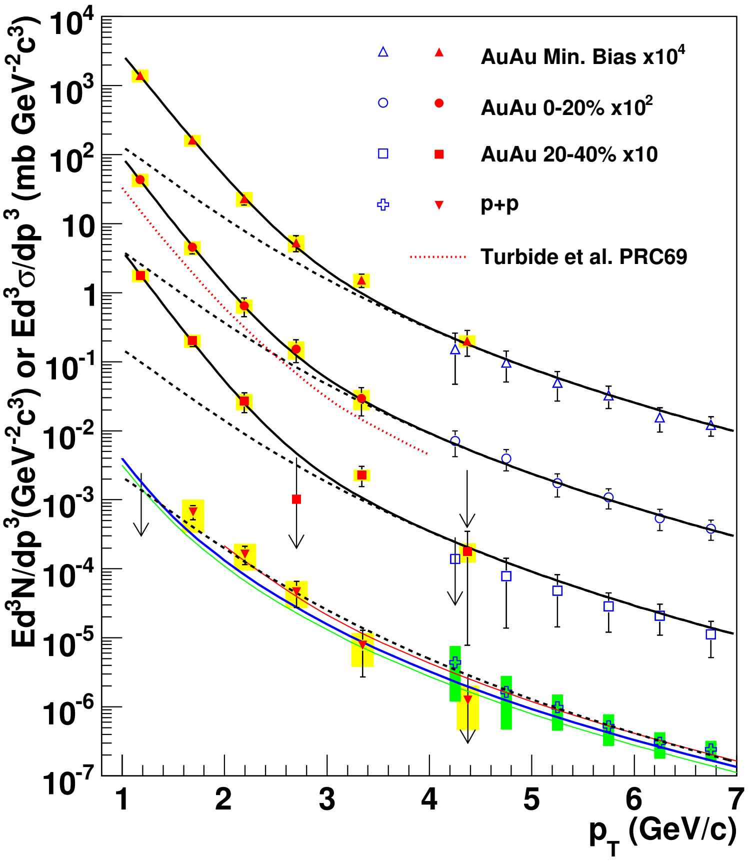

Figure 2.8: Direct photon spectra measured by the PHENIX experiment. The open crosses and inverse triangles represent data from p+p collisions at $\sqrt{s_{\mathrm{NN}}}$ = 200 GeV and the other symbols represent data from different centrality classes of Au+Au collisions at the same energy (scaled by powers of 10 for visibility). Error bars represent statistical uncertainties and the color bands represent systematic uncertainties and the arrows represent upper confidence limit. The three curves near the p+p data points represent NLO pQCD calculations, and the dashed curves show a power-law fit to the p+p data, scaled by the appropriate nuclear thickness function T_{AA}. The black curves represent exponential + power law fits to the data. The dotted red curve is a theory calculation for the 0–20% centrality class. Taken from [80].

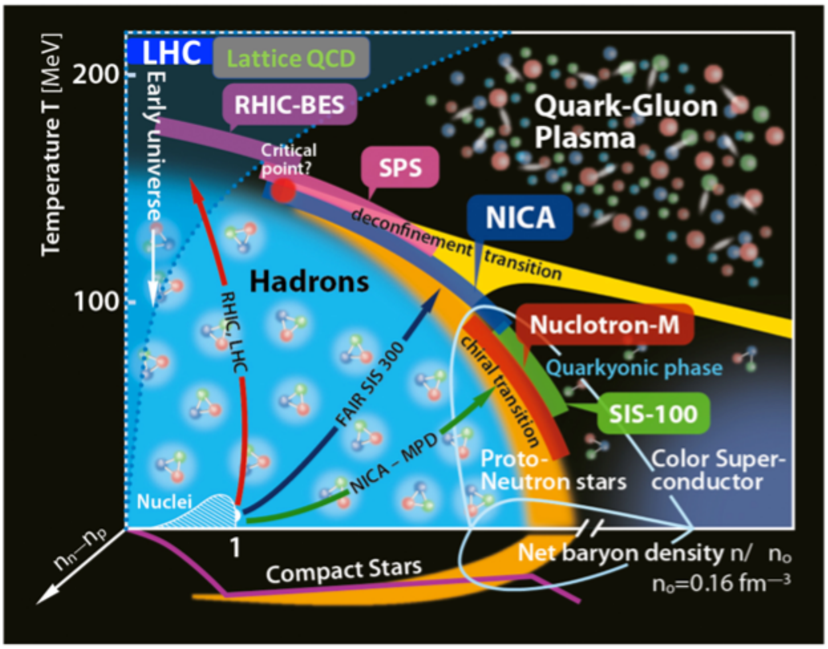

Figure 2.9: QCD phase diagram in terms of net baryon density *n*, normalized by standard nuclear density $n_0 = 0.16\ \text{fm}^{-3}$ and temperature T, with current and possible future measurements, and confirmed and hypothetic phases highlighted. Taken from [89].

Chapter 3

Jets in Theory and Experiment

As mentioned earlier, jets are one of the most important probes of the QGP and measuring their production in vacuum provides one of the best tests of the perturbative QCD theory. Jets serve as an observable approximation of a single parton, but the question "What is a jet?" is deeper than that and will be answered in Sec. 3.1. The mechanisms of jet evolution in vacuum without any additional effects are discussed in Sec. 3.2. If the jets are produced in the presence of the medium, their production and evolution will be modified by the presence of both cold and hot nuclear matter, these effects are summarized in Sec. 3.3. This modification is generally called jet quenching and was proposed in the early 1980s by J. Bjorken [1]. Experimentally, jet quenching was first observed at RHIC experiments, significantly contributing to the universally accepted discovery of the QGP. The following Sec. 3.4 presents the widely used jet reconstruction algorithms, necessary for both experimentalists and theorists. Section 3.5 contains the historical overview of jet quenching measurements from the high-p_{T} hadron suppression to full reconstructed jet measurements. Finally, Sec. 3.6 offers a smooth transition into the overview of recent results from experiments at RHIC and the LHC, focusing on current trends in jet physics.

3.1 Jet Definition

The answer to the question "What is a jet?" is far from trivial. The commonly presented statement "Jets are collimated sprays of hadrons.", is a little misleading and the real answer depends on the point of view. There are three levels at which one can observe a jet - the partonic level, the detector level and the analysis level. All three need to be taken into account when interpreting the results of jet measurements.

Parton level

At the parton level, a jet is a collection of partons produced during a partonic shower. When a parton obtains large momentum and virtuality Q during the hard scattering, it is knocked out of the original hadron. Since it cannot be free, as discussed in Subsec. 1.1.2, it tries to neutralize its color by radiating gluons which interact and can produce other partons, creating a shower of partons. The shower continues until the virtuality of the partons drops below a threshold ($Q \sim 1$ GeV) at which point the partons recombine to form color-neutral hadrons.

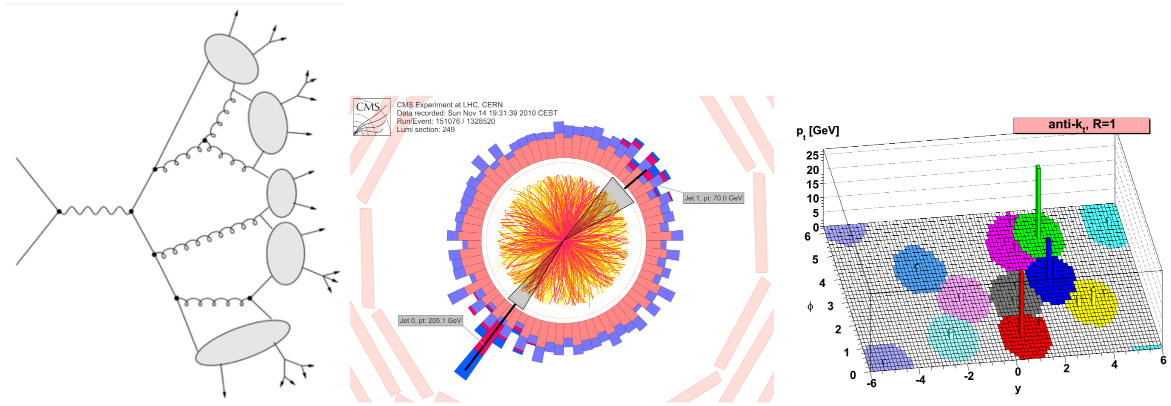

Figure 3.1: Illustration of jets at parton (left), detector (middle) and analysis (right) levels. Taken from [90–92], respectively.

Detector level

Once the hadronization is completed, the particles continue to move freely towards the detector, collectively containing the entire momentum of the original parton. As the angles of the gluon radiation are rather small, most of the particles are located in a narrow cone when reaching the detector. In the detector, jets are observed as large energy deposits consisting of many particles in a relatively small region. From this point of view, one can talk about the collimated sprays of hadrons.

Analysis level

Because of the background processes happening during the collision (underlying event, UE), it is impossible to distinguish between the energy deposited by the particles from the original parton and particles originating elsewhere. Therefore, jets in the experimental data analysis are defined by jet reconstruction algorithms (discussed in 3.4), which reconstruct jets from all particles (passing specific selection criteria) measured in the event. If only charged-particle tracks are considered, the reconstructed jets are called charged (or more precisely charged-particle) jets. If the neutral energy is also considered, one reconstructs full (or calorimetric) jets[1]. In simple terms, a jet is anything the jet algorithm reconstructs as a jet. Now it is clear why one needs to be careful when interpreting the results of jet measurements, since all the results are inherently algorithm-dependent and the background subtraction procedures are very challenging. Figure 3.1 shows an illustration of all three approaches to the definition of a jet.

3.2 Jets in Vacuum

The QCD factorization theorem [93] states that the total inclusive jet cross section calculation can be performed in steps, which correspond to different steps in the time evolution of the jet. The contributions to the jet production cross section are the intial conditions of the colliding systems, the hard scattering cross section and the parton fragmentation, described by the fragmentation function. Each step is described in more detail in this section. This only applies to jet evolution in vacuum[2], since the presence of the nuclear matter modifies the jet evolution significantly, as discussed in detail in Sec. 3.3.

---

[1] In this thesis, when discussing jets at the analysis level, full jets should be assumed, unless specified otherwise.

[2] The environment of $e^{-}+e^{+}$, $e^{-}+p$ or $p+p$ collisions is usually considered close enough to vacuum.

3.2.1 Initial Conditions

The current picture of the structure of a nucleon contains three real valence quarks and many virtual quark-antiquark pairs (sea quarks) and gluons, which mediate the strong interaction. The abundance of these virtual particles depends on the energy of the nucleon. Each parton carries a fraction of the total nucleon momentum, called (Bjorken-)$x = \frac{p_a}{p_N}$, where p_a is the momentum of parton a and p_N is the nucleon momentum. Bjorken-x is defined in terms of the nucleon four-momentum p and the four-momentum transfer q as

$$x \equiv \frac{Q^2}{2p \cdot q}, \tag{3.1}$$

which means that low-x values generally correspond to high-energy nucleons at fixed values of Q^2. The probability of finding a parton which carries a fraction x is given by the parton distribution functions (PDF) $f(x_a, Q^2)$, specific for each type of parton. The parton distribution functions cannot be calculated using pQCD and therefore have to be experimentally measured. The natural process for the measurements of the PDFs is the Deep Inelastic Scattering (DIS), where a highly energetic lepton interacts with a proton. Such measurements were conducted at the Hadron Electron Ring Accelerator (HERA) experiments H1 and ZEUS and yielded the now famous results shown in Fig. 3.2. The figure shows the x-scaled PDFs as a function of x. It can be seen that at high x, the proton consists mostly of 2 valence u quarks and 1 valence d quark. However, as x decreases, the number of sea quarks and mainly gluons rises dramatically and the gluon PDF dominates at the lowest accessible values of x, which means that a high-energy proton is mainly composed of gluons.

The results in Fig. 3.2 were evaluated at a factorization scale $Q^2 = \mu_t^2 = 10\ \mathrm{GeV}^2$. The factorization scale determines the low-Q^2 cutoff of the pQCD applicability. Above this scale, the Dokshitzer-Gribov-Lipatov-Altarelli-Parisi (DGLAP) equation [95–97] can be used to calculate the evolution in Q^2 of the PDF of parton a:

$$Q^2 \frac{\partial f_a(x, Q^2)}{\partial Q^2} = \sum_b \int_x^1 \frac{\mathrm{d}z}{z} \frac{\alpha_s}{2\pi} P_{ab}(z) f_b\left(\frac{x}{z}, Q^2\right), \tag{3.2}$$

where P_{ab} are the splitting functions describing the probability of parton b splitting into parton a with the momentum fraction z of the original parton b. The splitting functions depend on the type of the partons involved and can be calculated using pQCD in leading-order (LO) in terms of momentum fraction x as[3]:

$$\begin{aligned}
P_{qq}(x) &= P_{\bar{q}\bar{q}}(x) = \frac{4}{3}\left[\frac{1+x^2}{1-x}\right]_+, \\
P_{qG}(x) &= P_{\bar{q}G}(x) = \frac{1}{2}\left[x^2 + (1-x)^2\right], \\
P_{Gq}(x) &= P_{G\bar{q}}(x) = \frac{4}{3}\left[\frac{1+(1-x)^2}{x}\right], \\
P_{GG}(x) &= 6\left(\left[\frac{x}{1-x}\right]_+ + \frac{1-x}{x} + x(1-x) + \left(\frac{33-2N_f}{36} - 1\right)\delta(1-x)\right),
\end{aligned} \tag{3.3}$$

where N_f is the number of quark flavors and the distribution + is defined for any regular test function $f(x)$ via

$$\int_0^1 \frac{f(x)}{(1-x)_+}\mathrm{d}x = \int_0^1 \frac{f(x) - f(1)}{x-1}\mathrm{d}x. \tag{3.4}$$

---

[3] G is used instead of the traditional g for the gluon PDF for readability here.

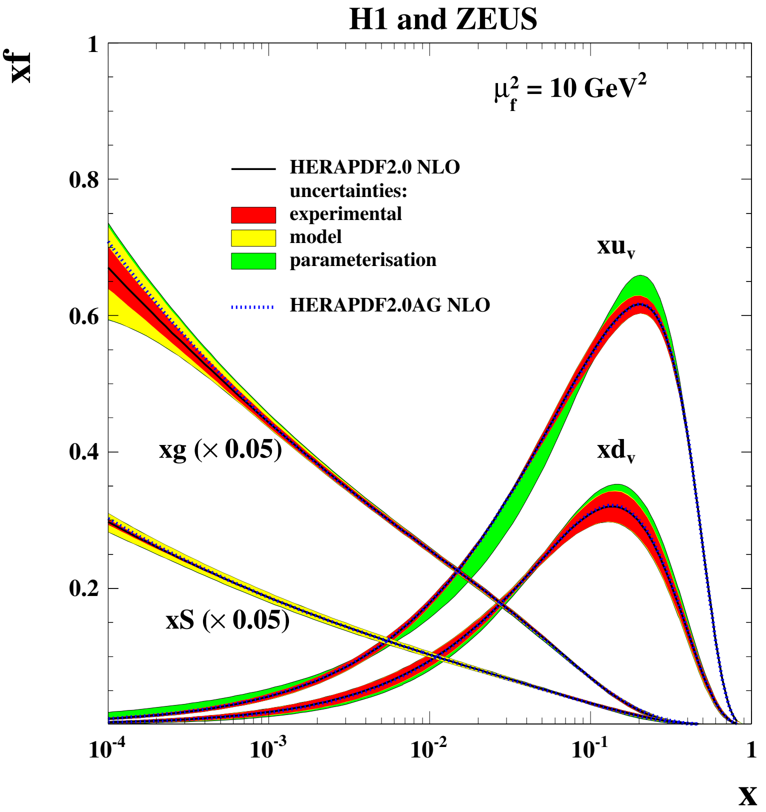

Figure 3.2: Parton distribution functions (scaled by x) for valence quarks u_v and d_v, sea quarks S, and gluons g, as a function of x, as measured by the H1 and ZEUS experiments. The S and g PDFs are down-scaled by a factor of 20 to fit in the figure. Taken from [94].

The splitting functions diverge for $x \to 0$ and $x \to 1$, which means that the most probable cases are the parton transfering almost none or almost all of its momentum during the splitting. There are currently several collaborations which aim to improve the calculation of PDFs by taking into account new data from experiments, by extending the calculation to higher orders of pQCD and by expanding the range of Q^2. These sets of PDFs are collected in the Les Houches Accord PDFs (LHAPDF) library [98] and can be used with modern MC generators.

3.2.2 Hard Scattering

The probability of a hard parton–parton scattering can be calculated using pQCD, yielding a simple formula for the cross section σ of an $a + b \to c + d$ process:

$$\left.\frac{\mathrm{d}\sigma}{\mathrm{d}t}\right|_{a+b\to c+d} = \frac{1}{16\pi s}\left|\mathcal{M}^2\right|, \tag{3.5}$$

where $t = (p_a - p_c)^2 = (p_d - p_b)^2$ and $s = (p_a + p_b)^2 = (p_c + p_d)^2$ are the Mandelstam variables and $\mathcal{M}$ is the scattering amplitude of the process, calculable directly from the corresponding Feynman diagrams. Figure 3.3 shows the relative contribution of elementary hard scattering processes to the total inclusive

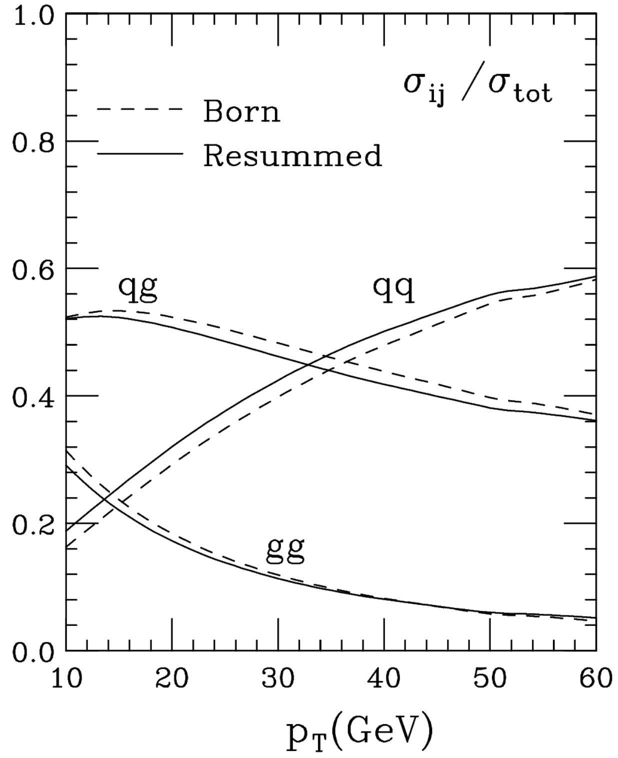

Figure 3.3: Relative contribution of elementary parton–parton scattering processes to the total inclusive jet cross section in p+p collisions at $\sqrt{s} = 200$ GeV as a function of p_T. The dashed line shows the Born-level calculation, while the solid line includes the resummed next-to-leading-logarithms (NLL) corrections. Taken from [99].

jet cross section in p+p collisions at RHIC energies. It can be seen that the main contributions are the $q+g$ and $q+q$ processes, the first dominant at low p_T while the other most important at high p_T.

3.2.3 Fragmentation Function & Hadronization

There are two mechanisms which contribute to the production of partons after the initial scattering. The first mechanism is the rapid radiation of gluons (gluonstrahlung), during the acceleration phase of the scattered parton. This occurs extremely fast ($t \sim 1/E \ll 1$ fm) and the gluons are radiated preferrably to small angles following

$$\frac{\mathrm{d}N_g}{\mathrm{d}\theta} \sim \frac{1}{\theta^2}, \tag{3.6}$$

where θ is the emission angle. The gluons can then split into $q\bar{q}$ pairs or radiate other gluons. Furthermore, the emission angle is getting smaller in subsequent splittings due to the interference of multiple Feynman diagrams, an effect known as angular ordering. The probabilities of such splittings are governed by the same splitting functions as introduced in Subsec. 3.2.1. When the distance between individual partons approaches the 1 fm threshold, the second mechanism starts to contribute. Due to the color confinement within QCD (as described in Subsec. 1.1.2), soon it becomes more energetically favorable to create new partons out of the vacuum in order to reduce the distance between individual partons, creating a narrow cascade of partons - the parton shower. The parton shower continues until the typical momentum transfers reach the Λ_{QCD} scale. At this point the partons form colorless hadrons. This process is called the hadronization and, since the pQCD is not valid anymore in this regime, is still not fully understood and relies on theoretical model description. One of these models is the Lund string model [100] which treats the gluons as narrow strings and is the basis for many MC event generators, such as the widely-used PYTHIA [101]. For the theoretical description of hadronization, one can introduce the parton fragmentation function (FF) $D_i^h(x, Q^2)$, which describes the probability of parton i hadronizing into hadron h with momentum fraction x. This is analogous to the PDF used to describe the initial conditions. The FF is parametrized at a fixed value of Q^2 called the initial energy scale[4] μ_0^2 as

$$D_i^h(x, \mu_0^2) = Nx^{\alpha}(1-x)^{\beta}\left(1+\gamma(1-x)^{\delta}\right), \tag{3.7}$$

where N is a normalization constant and $\alpha - \delta$ are free parameters. Values of all these parameters depend on the energy scale and also on the type of the parton a and hadron h and have to be extracted from experimental data from $e^- + e^+$, $e^- + h$ or $h + h$ collisions. The results from the measuremets of parton FF show [102] that quarks tend to fragment harder (creating fewer hadrons with higher momentum) than gluons of the same momentum.

3.3 Jets in Medium

As mentioned before, jets are an excellent probe of the medium created in the heavy-ion collisions, because they are created very early in the collision, before the QGP can be formed and therefore their production rate is not affected by the medium. They also have enough time to interact with the medium. Furthermore, the production rate is expected to scale with the number of binary nucleon–nucleon collisions, providing a simple normalization factor to compare the measurements from different collision systems. As will be shown in Sec. 3.6, pQCD is remarkably successful in predicting the jet production in p+p collisions. Therefore, any observed modification of jet yields in larger systems (p+A, A+A) must be a consequence of the presence of the nuclear matter. There are two general categories of nuclear matter effects. The Cold Nuclear Matter (CNM) effects do not require the deconfinement of nuclear matter and are studied in asymmetric collisions systems which involve one small and one large nucleus (i.e. p+A, d+A, ^{3}He+A). The effects of the deconfined (hot) matter are studied in collisions of large nuclei (A+A). The CNM effects are also present in the large system collisions to some degree and need to be evaluated before interpreting the results.

3.3.1 Cold Nuclear Matter

The initial conditions inside a nucleus are different from protons. At higher momenta, the number of gluons inside each nucleon rises. Since the nucleons are close to each other, the gluons start to interact with gluons from other nucleons. These gluons with low x can combine to form gluons with larger x leading to the deficit of gluons with low x (effect known as shadowing [103]) and the excess of large-x gluons (antishadowing). There are also additional effects, not all of them understood theoretically, but observed experimentally. These effects are accounted for by modifying the parton distribution function of the nucleon into the nuclear parton distribution function (nPDF). The ratio of the NLO nPDF set EPPS16, which includes the new data from the LHC p+Pb collisions, to nucleon PDF can be seen in Fig. 3.4, clearly showing the shadowing and antishadowing effects [104].

---

[4] Usually $\mu_0^2 \sim 1\mathrm{GeV}^2$ for light quarks and gluons and $\mu_0^2 \sim m_Q^2$ for heavy quarks)

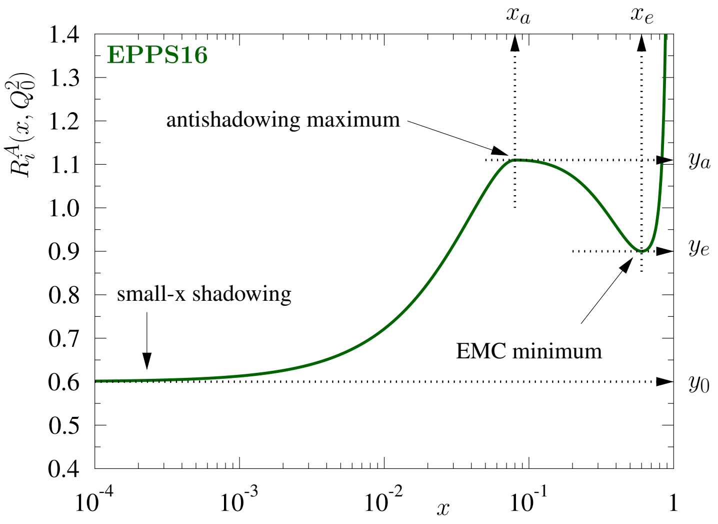

Figure 3.4: Ratio of nPDF to PDF $R_i^A(x, Q_0^2)$ as a function of momentum fraction x calculated by the EPPS16 collaboration with key features highlighted. Taken from [104].

Another modification observed in p+A collisions is the Cronin effect, which manifests as an excess of intermediate-p_{T} particles around $\sim$ 2 GeV. It is the consequence of the multiple scattering which happens inside the nucleus and the effect scales with the number of nucleons [105].

3.3.2 Hot Nuclear Matter

The effects caused by the deconfined matter containing free color charges can influence the jets in multiple ways. The main modification is called jet quenching and corresponds to the energy loss of the initial parton traversing the medium. There are two ways the parton can lose energy [106, 107]. First is the ellastic collision energy loss, initially suggested by Bjorken [1]. The parton scatters multiple times and the energy loss per unit length for a light quark or a gluon with energy E inside of a medium with temperature T can be calculated as

$$-\frac{\mathrm{d}E_{\mathrm{coll}}}{\mathrm{d}l} = \frac{1}{4} C_R \alpha_s(ET) m_D^2 \ln\left(\frac{ET}{m_D^2}\right), \tag{3.8}$$

where $C_R = 4/3$ (3) is a color factor for quarks (gluons) and $m_D^2 \simeq 4\pi\alpha_s T^2(1 + N_f/6)$, where N_f is the number of quark flavors, is the QGP Debye mass squared. The total energy loss depends only weakly on the initial parton energy and is linear with the medium thickness. Numerically, if one assumes $E = 20$ GeV and $T = 0.4$ GeV, a light quark loses around 2.3 GeV/fm. The second mechanism are the radiative energy losses caused by gluonstrahlung inside the QGP. There are two limiting cases based on the medium thickness length L compared to the radiation length λ. In the thin medium limit ($L \ll \lambda$), or the Bethe–Heitler regime, the total radiative energy loss can be calculated via

$$\Delta E_{\mathrm{rad}} \approx \alpha_s C_R \hat{q} L^2 \ln\left(\frac{E}{m_D^2}\right), \tag{3.9}$$

where $\hat{q} \equiv \frac{\langle q_t^2 \rangle}{\lambda}$ is the medium transport coefficient, which describes the properties of the medium, such as its temperature and viscosity, and $\langle q_t^2 \rangle$ is the square of the mean transverse momentum transferred to the medium. In the thick medium limit ($L \gg \lambda$), the parton enters the Landau–Pomeranchuk–Migdal (LPM) regime and for the radiative energy loss one gets

$$\Delta E_{\mathrm{rad}} \approx \alpha_s C_R \hat{q} L^2 B; B = \begin{cases} 1 & \omega < \omega_{\mathrm{c}}, \\ \ln\left(\frac{E}{\hat{q}L^2}\right) & \omega > \omega_{\mathrm{c}}, \end{cases} \tag{3.10}$$

where ω is the emitted gluon energy which further distinguishes between the soft gluon emission ($\omega < \omega_{\mathrm{c}}$) and hard gluon emission ($\omega > \omega_{\mathrm{c}}$), where $\omega_c = \frac{1}{2}\hat{q}L^2$ is the characteristic gluon energy. In this case, the energy loss is quadratically dependent on the path length (in contrast with QED, where the dependence is only $\propto L$). Assuming again $E = 20$ GeV, $L = 6$ fm and $\hat{q} = 2$ GeV^2/fm, one gets $\Delta E_{\mathrm{rad}} \sim 10$ GeV/fm in the LPM regime, which means that radiation is the dominant mechanism of parton energy loss inside the medium and the total energy loss inside the QGP is an order of magnitude larger than in cold nuclear matter [108]. The main experimental observables sensitive to jet quenching are the jet yield suppression, the dijet transverse momentum imbalance and the modification of jet shape or its inner structure. All these observables are discussed below.

Jet Yield Suppression

The energy losses described above lead to the suppression of high-p_{T} jet yield compared to yield in p+p collisions. The main observable of jet quenching is therefore the nuclear modification factor R_{AA}, defined as the ratio of the normalized jet yield in A+A collisions to the normalized jet yield in p+p collisions scaled by the mean number of binary collisions $\langle N_{\mathrm{coll}} \rangle$:

$$R_{\mathrm{AA}} = \frac{1}{\langle N_{\mathrm{coll}} \rangle} \cdot \frac{\frac{1}{N_{\mathrm{evt}}^{\mathrm{AA}}} \frac{\mathrm{d}^2 N_{\mathrm{AA}}^{\mathrm{jet}}}{\mathrm{d}p_{\mathrm{T,jet}}\mathrm{d}\eta}}{\frac{1}{N_{\mathrm{evt}}^{pp}} \frac{\mathrm{d}^2 N_{pp}^{\mathrm{jet}}}{\mathrm{d}p_{\mathrm{T,jet}}\mathrm{d}\eta}}, \tag{3.11}$$

where $N_{\mathrm{evt}}^{\mathrm{AA}/pp}$ is the number of analyzed[5] A+A or p+p collisions, respectively, or its alternative definition in terms of the cross section (σ^{jet}, usually used in p+p analyses):

$$R_{\mathrm{AA}} = \frac{\frac{1}{N_{\mathrm{evt}}^{\mathrm{AA}}} \frac{\mathrm{d}^2 N_{\mathrm{AA}}^{\mathrm{jet}}}{\mathrm{d}p_{\mathrm{T,jet}}\mathrm{d}\eta}}{T_{\mathrm{AA}} \cdot \frac{\mathrm{d}^2 \sigma_{pp}^{\mathrm{jet}}}{\mathrm{d}p_{\mathrm{T,jet}}\mathrm{d}\eta}}, \tag{3.12}$$

where T_{AA} is the nuclear thickness function, defined as the ratio of $\langle N_{\mathrm{coll}} \rangle$, determined from the Glauber model calculation [47], and the total inelastic cross section from p+p collisions.

$$T_{\mathrm{AA}} = \frac{\langle N_{\mathrm{coll}} \rangle}{\sigma_{\mathrm{pp}}^{\mathrm{inel.}}}. \tag{3.13}$$

The R_{AA} in the absence of nuclear matter effects has a value of 1, provided the $\langle N_{\mathrm{coll}} \rangle$ scaling holds.

---

[5] Since a trigger requiring a hard process is often required, the number of events should be the equivalent of the number of minimum bias events. This technicality is discussed in Chapter 5.

Dijet Transverse Momentum Imbalance

Due to the conservation of momentum, jets which are produced in qq scattering are created in pairs – dijets – which are back-to-back in the angular space and should have very similar transverse momentum. There is a slight smearing of the angle and the momentum balance, caused by fluctuations of the initial parton transverse momentum [109]. The jet with the highest p_{T} is called the leading (or trigger) jet, while the second is the subleading (recoil) jet. In the presence of the QGP medium, the picture changes based on where the dijet is formed. If the dijet is formed close to the edge of the fireball, the trigger jet will move away from it to vacuum, without losing significant amounts of energy. The recoil jet will travel through the medium, lose large amounts of energy (as shown in Eq. 3.10) and possibly be deflected to large angle relative to the expected angle $\phi_{\mathrm{recoil}} \simeq \pi - \phi_{\mathrm{trig}}$. The situation is illustrated in Fig. 3.5.

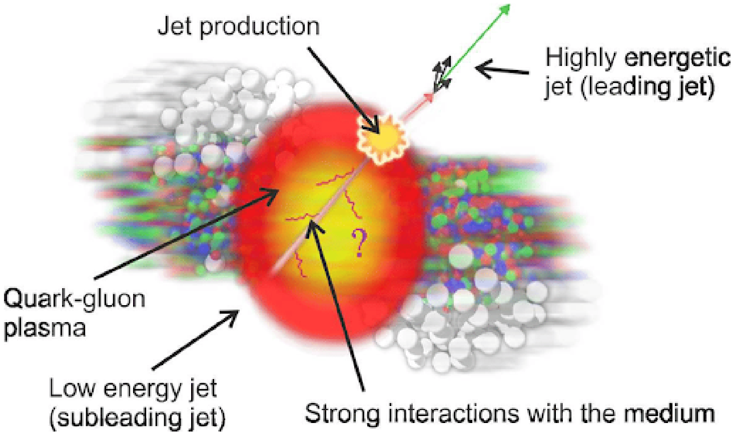

Figure 3.5: Illustration of a dijet event happening at the edge of the fireball. Cartoon made by Peter Jacobs.

The observable which describes the magnitude of jet quenching is the dijet transverse momentum imbalance A_{J}, defined as

$$A_{\mathrm{J}} = \frac{p_{\mathrm{T,jet}}^{\mathrm{lead}} - p_{\mathrm{T,jet}}^{\mathrm{sub}}}{p_{\mathrm{T,jet}}^{\mathrm{lead}} + p_{\mathrm{T,jet}}^{\mathrm{sub}}}, \tag{3.14}$$

or alternatively the transverse momentum balance

$$x_{\mathrm{J}} = \frac{p_{\mathrm{T,jet}}^{\mathrm{sub}}}{p_{\mathrm{T,jet}}^{\mathrm{lead}}}, \tag{3.15}$$

where $p_{\mathrm{T,jet}}^{\mathrm{lead}}$ is the leading jet transverse momentum and $p_{\mathrm{T,jet}}^{\mathrm{sub}}$ is the subleading jet transverse momentum. In the absence of medium effects, $A_{\mathrm{J}} \simeq 0$ and $x_{\mathrm{J}} \simeq 1$ is expected.

Modification of Jet Shape and Substructure

There are additional effects the QGP can have on jets. The QGP medium can influence the fragmentation of the initial parton, the presence of the free color charges induces radiation of soft gluons, which create hadrons at low p_{T}. Therefore, one would expect the spectrum of tracks inside the jet cone to be softer in p+p collisions than in A+A collisions. Due to the additional scattering inside the medium, the jet radiation is expected to be emitted into wider angles. Therefore, by comparing the measurements of jets with different size of the jet cone, one can estimate the magnitude of this effect. Very active field of research within jet physics is the study of jet substructure and its modification within the QGP medium according to the degree to which the jet is resolved by the medium. New techniques [110, 111] were developed to remove the soft, wide angle gluon radiation from the jet to focus on the hard splits into two prongs within the jets, introducing variables such as the groomed jet radius r_g, the angular distance between the constituents at the first hard split, or the groomed momentum fraction of the split

$$z_\mathrm{g} = \frac{p_{\mathrm{T},2}}{p_{\mathrm{T},1} + p_{\mathrm{T},2}}, \tag{3.16}$$

where $p_{\mathrm{T},1}$ is the transverse momentum of the hardest prong and $p_{\mathrm{T},2}$ is the transverse momentum of the second prong. Studying jet quenching as a function of jet substructure can shed light on the details of the quenching mechanisms.

3.4 Jet Reconstruction Algorithms

As mentioned earlier, jet reconstruction algorithms are a key ingredient to jet analyses, as they define what actually is a jet. Algorithms used to reconstruct jets should fulfill the following criteria:

- **Level independence:** The algorithm reconstructs the same jets at partonic and detector levels and also when reconstructing jets from MC particles.
- **Detector independence:** The algorithm works independently of the specifics of the experimental setup.
- **Infrared safety:** The algorithm is not sensitive to the addition of soft particles, so the number and shape of the jets remains the same.
- **Collinear safety:** The algorithm is not sensitive to collinear splitting of particles. It should for example reconstruct the same jets regardless of whether a particle deposits energy in one or two calorimeter towers.
- **High efficiency:** The algorithm reconstructs all significant jets in the event.
- **Low computing requirements:** The algorithm computation time does not increase too quickly with the number of particles N. The practical limit is $\sim \mathcal{O}\left(N^3\right)$.
- **Easy use:** The algorithm is easy to implement in frequently used coding languages and to use on experimental data.

The jet reconstruction algorithms can be classified into two categories, the cone algorithms and the sequential recombination (clustering) algorithms [112].

3.4.1 Cone Algorithms

The cone algorithms are the more intuitive of the two categories. A high-p_T particle (seed) is identified and a cone with a user-defined value of $R = \sqrt{\left(\Delta\phi^2_\mathrm{seed}\right) + \left(\Delta\eta^2_\mathrm{seed}\right)}$, where $\Delta\phi_\mathrm{seed}$ and $\Delta\eta_\mathrm{seed}$ are the angular distances relative to the seed position in the $\eta - \phi$ space, is formed around the seed particle. All particles inside the cone (usually above some p_T threshold) are declared as the (proto)jet constituents.

The jet energy and p_T is calculated as the sum of the constituent energy and p_T. All such protojets in the event are identified and those who do not intersect are declared final jets. The final momentum vector of the jet needs to be aligned with the cone axis. Such cones are called stable and if this is not the case, an iterative procedure called stabilization is needed in order to shift the axis in such way that the cone is stable. Because of the p_T threshold of the seed particles, this algorithm is not collinear safe. Therefore a seedless cone algorithm was invented and now is called the SISCone algorithm.

SISCone Algorithm

The Seedless Infrared-Safe Cone (SISCone) algorithm is the only current cone algorithm which is both collinear and infrared safe. It works in the following steps [113]:

1. Put the set of current particles equal to the set of all particles in the event.

   repeat

2. Find all stable cones of radius R for the current set of particles
3. For each stable cone, create a protojet from the current particles contained in the cone, and add it to the list of protojets.
4. Remove all particles that are in stable cones from the list of current particles.

   until no new stable cones are found, or one has gone around the loop N_pass times.

5. Run a split–merge procedure [114] on the full list of protojets, with overlap parameter f and transverse momentum threshold $p_\mathrm{T,min}$.

The computation speed of the SISCone algorithm is $O\left(N^2 \ln N\right)$, where N is the number of particles in the event.

3.4.2 Clustering Algorithms

In contrast with the cone algorithms, the clustering algorithms do not produce jets of a fixed conical shape. They start with one particle and sequentially add others which fulfill certain distance condition. This is also closer to the way jets are produced in reality. The idea of sequential clustering was proposed in the 1990s [115], but the real breakthrough came around the year 2005, when it was shown [116] that the k_T algorithm complexity can be reduced from $O\left(N^3\right)$ to $O\left(N \ln N\right)$, making it not only computationally viable, but also the fastest jet finding algorithm at the time. Currently, there are three main variations of the (infrared and collinear safe) k_T algorithm - the original [115], the anti-k_T algorithm [92] and the Cambridge/Aachen (C/A) algorithm [117].

k_T Algorithm

The k_T algorithm works in the following steps:

1. For each pair of particles i, j calculate the k_T distance

$$d_{i,j} = \min\left(p_\mathrm{T,i}^2, p_\mathrm{T,j}^2\right) \frac{\Delta R_{ij}^2}{R^2}, \tag{3.17}$$

where $p_{\mathrm{T,i}}$ and $p_{\mathrm{T,j}}$ are the transverse momenta of the particles,

$$\Delta R_{ij}^2 = (y_i - y_j)^2 + (\phi_i - \phi_j)^2, \tag{3.18}$$

where y_i and ϕ_i are the rapidity and azimuth of particle i. R is the jet radius parameter, sometimes also called the jet resolution or reconstruction parameter, since it resembles the cone size from the cone algorithms. Therefore, jets reconstructed with smaller values of R are called small jets and jets with large R large jets. Larger jets recover larger fraction of the original parton momentum, but also contain more background from the UE, making the corrections more difficult. The typical values of R in small-collision system environments are $0.5 - 0.7$, while for large systems $R = 0.2 - 0.4$ is common.

2. For each particle i also work out the beam distance $d_{iB} = p_{\mathrm{T},i}^2$.
3. Find the minimum d_{min} of all the d_{ij}, d_{iB}.
4. If $d_{\mathrm{min}} = d_{ij}$ merge particles i and j into a single particle, summing their four-momenta (this is the energy recombination scheme[6]). If $d_{\mathrm{min}} = d_{iB}$, then declare particle i to be a final jet and remove it from the list.
5. Repeat from step 1 until no particles are left.

Important feature is that the k_{T} algorithm starts from the softest particles (due to the exponent in Eq. 3.17), making it sensitive to the soft background and therefore is commonly used for background estimation.

Anti-k_{T} Algorithm

The anti-k_{T} algorithm differs from the k_{T} only in the exponent of the particle p_{T}. Therefore the steps are:

1. For each pair of particles i, j calculate the anti-k_{T} distance

$$d_{i,j} = \min\left(p_{\mathrm{T,i}}^{-2}, p_{\mathrm{T,j}}^{-2}\right) \frac{\Delta R_{ij}^2}{R^2}. \tag{3.19}$$

2. Calculate the beam distance $d_{iB} = p_{\mathrm{T},i}^{-2}$.
3. Find the minimum d_{min} of all the d_{ij}, d_{iB}.
4. If $d_{\mathrm{min}} = d_{ij}$ merge particles i and j into a single particle and if $d_{\mathrm{min}} = d_{iB}$, then declare particle i to be a final jet and remove it.
5. Repeat from step 1 until no particles are left.

Since the anti-k_{T} algorithm uses the inverse-square of the particle p_{T} as the weight, it starts the clustering from the hardest particles and is therefore not sensitive to soft background. The shape of the anti-k_{T} jets is also more regular, resembling jets from cone algorithms. Combined with the high computation speed, this makes the anti-k_{T} the most popular algorithm for true jet reconstruction among the community[7].

---

[6] The energy recombination scheme is the default way how to combine the particles. Other schemes exist – p_{T},p_{T}^2,E_{T},E_{T}^2 – see [118] for overview.

[7] Since the anti-k_{T} algorithm is used so frequently, its usage is sometimes implicitly assumed in scientific texts and is assumed in this thesis as well.

Cambridge/Aachen Algorithm

The Cambridge/Aachen (C/A) algorithm is the simplest of the three. It works in the following steps:

1. For each pair of particles i, j calculate the C/A distance
$$d_{i,j} = \frac{\Delta R_{ij}^2}{R^2}. \tag{3.20}$$
2. Find the minimum $d_{\text{min}} = \min\left(d_{ij}, 1\right)$.
3. If $d_{\text{min}} = d_{ij}$ merge particles i and j into a single particle and if $d_{\text{min}} = 1$, then particle i is a final jet and is removed.
4. Repeat from step 1 until no particles are left.

This algorithm differs from the (anti-)k_{T} algorithms in that it does not take into account the p_{T} of the particles at all, but clusters them on a purely angular basis. This algorithm is frequently used in jet substructure studies.

Since these three algorithms work identically, apart from the exponent in $p_{\text{T,i,j}}$, they can be considered special cases of the generalized k_{T} algorithm, where

$$d_{i,j} = \min\left(p_{\text{T,i}}^{2p}, p_{\text{T,j}}^{2p}\right)\frac{\Delta R_{ij}^2}{R^2}; d_{iB} = p_{\text{T},i}^{2p}, \tag{3.21}$$

where p is a weight parameter. When one sets $p = 1, -1, 0$ they recover the k_{T}, anti-k_{T} and C/A algorithms, respectively.

Figure 3.6 shows the comparison between the results of the three clustering algorithms (k_{T}, anti-k_{T} and C/A) along with the SISCone algorithm. The different jet reconstruction algorithms were ran on the same MC event with the same reconstruction parameter $R = 1$. It is clear that all four algorithms reconstruct all the jets in the event, that the k_{T} and C/A algorithms are sensitive to the soft background while the anti-k_{T} algorithm produces regular jet shapes, similar to the SISCone algorithm. All algorithms mentioned in this section are implemented in the FastJet package [118]. Specifically version 3.3 of FastJet was used for the analysis presented in this thesis.

3.5 History of Jet Quenching Measurements

From the time jet quenching was proposed as one of the key signatures of the QGP formation, the experimentalists have tried to observe it in high energy A+A collisions. Since full jet reconstruction is a very challenging task, high-p_{T} hadrons were proposed as an approximation of jets. Before the advent of RHIC, no jet quenching has been observed, even at the highest achievable SPS energies for Pb+Pb collisions [119]. When RHIC delivered the first Au+Au collisions at $\sqrt{s_{\text{NN}}} = 130$ GeV in 2000, the suppression of high-p_{T} hadrons was observed, indicating significant medium effects [120] later confirmed at the top RHIC energy for heavy ions, $\sqrt{s_{\text{NN}}} = 200$ GeV [2]. However, it was still not clear whether these effects can be explained by cold nuclear matter or whether deconfinement is needed. The breakthrough occured when the RHIC experiments also measured d+Au collisions where the CNM effects are present, but no QGP is expected to form. Figure 3.7 shows the nuclear modification factor R_{AA} (defined

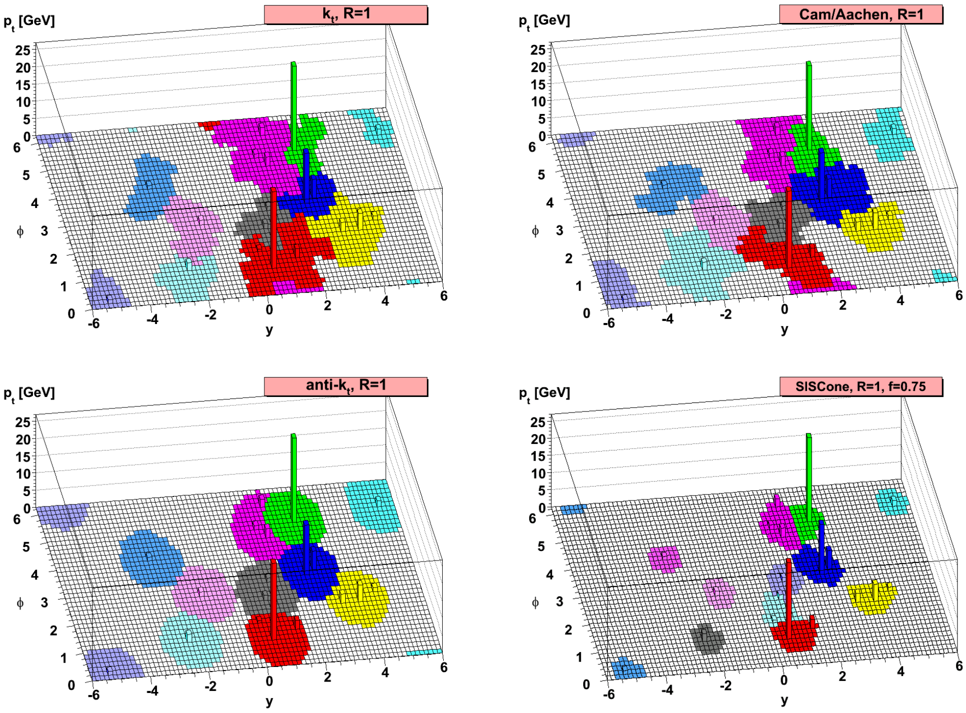

Figure 3.6: Jets reconstructed from a single MC event by the k_T (top, left), C/A (top, right), anti-k_T (bottom, left) and SISCone (bottom, right) algorithms with $R = 1$. The SISCone algorithm was run with overlap parameter $f = 0.75$. Each uniquely colored area in the $y - \phi$ plane represents one jet. Taken from [92].

in Eq. 3.12) of inclusive particles as a function of p_{T} from central Au+Au and central and minimum bias (MB) d+Au collisions at $\sqrt{s_{\mathrm{NN}}} = 200$ GeV measured by the STAR experiment. The nuclear modification factor shows high suppression of the particle yield in the central Au+Au collisions while in d+Au collisions (even the most central) an enhancement of particle yield is observed. The Cronin effect is visible in all three cases as a peak at intermediate p_{T}. This measurement provided the first evidence that the observed suppression of high-p_{T} particles is a consequence of the deconfined medium effects, strongly supporting the QGP formation hypothesis.

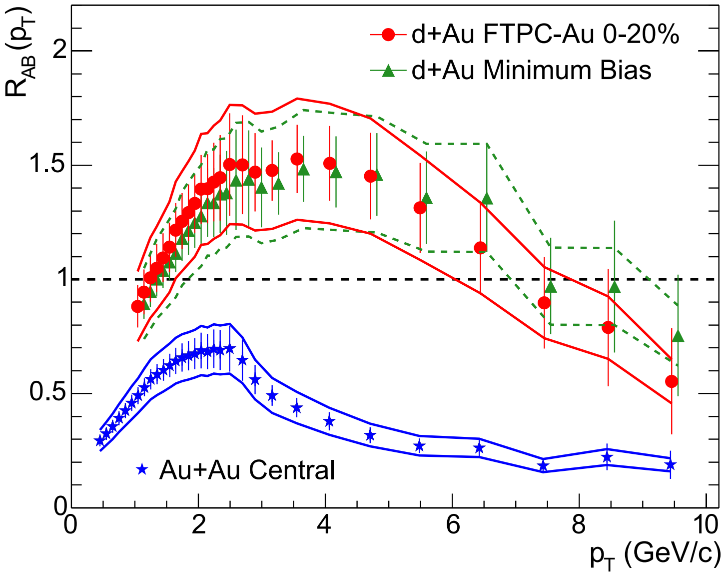

Figure 3.7: Nuclear modification factor R_{AB} of inclusive particles as a function of p_{T} from central Au+Au (blue stars), central d+Au (red circles) and MB d+Au (green triangles) collisions at $\sqrt{s_{\mathrm{NN}}} = 200$ GeV measured by the STAR experiment. The error bars represent statistical uncertainties while solid/dashed lines represent systematic uncertainties. Taken from [121].

Further evidence came from the complementary measurements of the correlations between two high-p_{T} charged hadrons. Figure 3.8 shows the azimuthal correlations of dihadrons where the trigger particle was required to have $p_{\mathrm{T}}^{\mathrm{trig}} > 4$ GeV/c and the recoil particle was selected with $p_{\mathrm{T}} > 2$ GeV/c. Compared are the results from central Au+Au and d+Au and MB p+p collisions, all showing a peak at $\Delta\phi \sim 0$. This is an expected result, corresponding to selecting both hadrons from the same jet. More interesting is the behavior at the recoil side $\Delta\phi \sim \pi$, where the recoil peak (hadron selected from the recoil jet) is observed in p+p collisions and also in central d+Au collisions while there is no peak in central Au+Au collisions. This corresponds to the situation illustrated in Fig. 3.5 where the trigger jet (represented by the trigger particle) goes through vacuum while the recoil jet has to go through significant path inside the medium, losing a large amount of energy.

In later years, both STAR and the Pioneering High Eenergy Nuclear Interaction eXperiment (PHENIX) have measured the nuclear modification factor for many species of identified particles. A collection of PHENIX results is shown in Fig. 3.9. The figure demonstrates several key features. The first is that the direct γ, which are not affected by the medium, do not show any modification from unity, proving that the binary collision scaling works as expected, while all strongly interacting particles (except protons) show varying levels of suppression at $p_{\mathrm{T}} > 2$ GeV/c. The neutral mesons (π^0, η, ω) show the highest

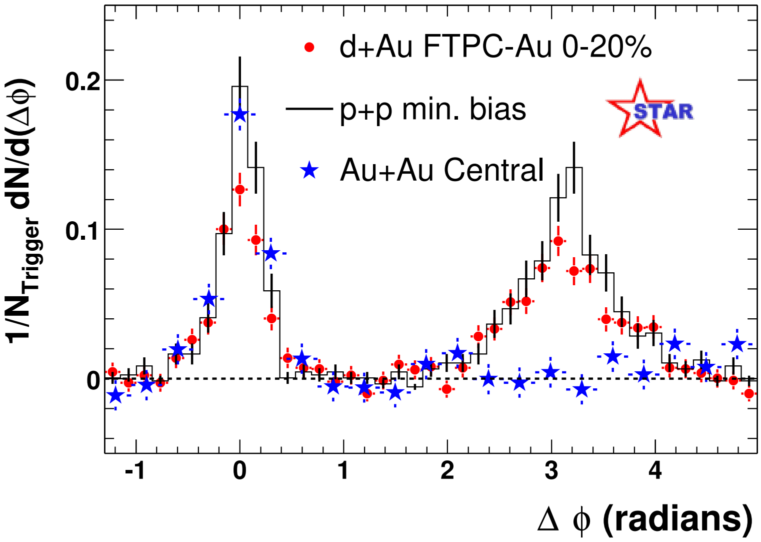

Figure 3.8: Per-trigger yield of charged dihadrons as a function of the azimuthal angle difference from the trigger particle $\Delta\phi$ for central Au+Au (blue stars), central d+Au (red circles) and minimum bias p+p collisions (black line) at $\sqrt{s_{\mathrm{NN}}}$ = 200 GeV measured by STAR. Error bars represent statistical uncertainties. Taken from [58].

level of suppression, reaching $R_{\mathrm{AA}} \sim 0.2$. The strange particles (K^+, ϕ) show lower levels of suppression, confirming the strangeness enhancement inside the QGP. The proton R_{AA} is close to unity at high p_{T}, demonstrating the baryon anomaly. Since the particle p_{T} spectra are steeply falling, it is easier to produce a baryon from three softer quarks than a meson from a harder $q\bar{q}$ pair at fixed p_{T}. All hadrons experience the Cronin effect at intermediate p_{T}. The behavior at low-p_{T} is dominated by soft QCD processes and not easily interpretable. The charmed J/ψ and electrons produced in heavy flavor decay show approximately the same level of suppression as light flavors meaning that the dead cone[8] effect [122] is not observed at RHIC energies.

With the LHC delivering the highest-energy collisions to date in 2010 a new era of jet quenching studies began. The LHC experiments also measured the high-p_{T} hadron suppression in central Pb+Pb collisions at $\sqrt{s_{\mathrm{NN}}}$ = 2.76 TeV compared to p+p collisions at the same collision energy. Figure 3.10 shows the compilation of nuclear modification factor measurements from SPS to LHC energies. The WA98 results of neutral pion production from 0–7% most central Pb+Pb collisions at $\sqrt{s_{\mathrm{NN}}}$ = 17.3 GeV do not show suppresison at high p_{T}, in contrast with the PHENIX results from 0–10% most central Au+Au collisions at $\sqrt{s_{\mathrm{NN}}}$ = 200 GeV. Both CMS and ALICE results of charged hadron production from 0–5% most central Pb+Pb collisions at $\sqrt{s_{\mathrm{NN}}}$ = 2.76 TeV show a similar level of suppression as the neutral pions at PHENIX and significantly higher than STAR charged hadrons from 0–5% most central Au+Au collisions at $\sqrt{s_{\mathrm{NN}}}$ = 200 GeV in the overlap p_{T} region. It needs to be said that the level of suppression does not depend only on the energy loss, but also on the shape of the spectra. The spectra at LHC are flatter than at RHIC and therefore, by observing a similar level of suppression, one can conclude that the energy losses at LHC are significantly higher. Data are compared to several theoretical

---

[8] In simple terms, the dead cone is an angular area where gluon radiation of a parton is prohibited. This angle depends on the parton mass. Therefore, the massive c and b quarks are expected to lose energy less rapidly than light flavor quarks.

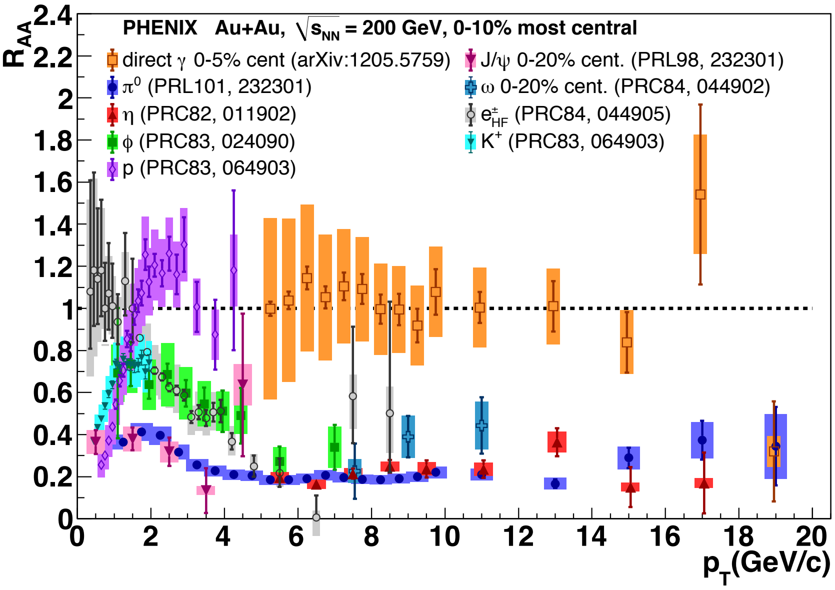

Figure 3.9: Nuclear modification factor R_{AA} as a function of p_{T} for many identified particle species from central Au+Au collisions at $\sqrt{s_{\mathrm{NN}}}$ = 200 GeV measured by PHENIX. Error bars represent statistical uncertainties while color boxes represent systematic uncertainties. Taken from [123], further references in figure.

calculations which incorporate jet quenching effects and most of them qualitatively describe the data, capturing the rising trend at high p_{T}.

The two calorimeter-based experiments (ATLAS and CMS) were designed for full jet reconstruction, extending the kinematic reach of jet measurements by at least one order of magnitude compared to RHIC and provided high statistical and systematic precision. The ALICE experiment, in design closer to STAR[9], with focus on charged-particle tracking was able to reconstruct charged-particle jets with smaller bias on jet constituents at much lower momenta, allowing potential comparison with RHIC. The nuclear modification factor for inclusive jets from the three LHC experiments in Pb+Pb collisions at $\sqrt{s_{\mathrm{NN}}}$ = 2.76 TeV is shown in Fig. 3.11. Although there are some differences between the jet populations analyzed by the three collaborations, the level of suppression is consistent among them within uncertainties with $R_{\mathrm{AA}} \approx 0.3 - 0.6$ with weak p_{T} dependence accross the studied p_{T} range, indicating strong energy losses even for highly-energetic partons.

One of the first jet quenching results at the LHC was the ATLAS measurement of the dijet transverse momentum imbalance A_{J} (defined in Eq. 3.14) and the dijet angular separation $\Delta\phi$ in Pb+Pb collisions at $\sqrt{s_{\mathrm{NN}}}$ = 2.76 TeV, shown in Fig. 3.12. It can be seen that in peripheral collisions both the A_{J} and $\Delta\phi$ distributions copy the shape from p+p collisions and the simulation where PYTHIA [125] provides the parton scattering and the Heavy Ion Jet INteraction Generator (HIJING, [126]) simulates the background of heavy-ion collisions. The A_{J} peaks at 0, indicating balance between the dijet p_{T} and the angular separation peaks near $\Delta\phi \sim \pi$ confirming that the dijets are mostly produced back-to-back. The situation changes in central collisions, especially in the 0–10% centrality bin, where there is a peak at $A_{\mathrm{J}} \sim 0.5$, indicating significant quenching of the recoil jets. The jets are still mainly back-to-back, but a slight

---

[9] Detailed description of the STAR experiment is in Sec. 4.2.

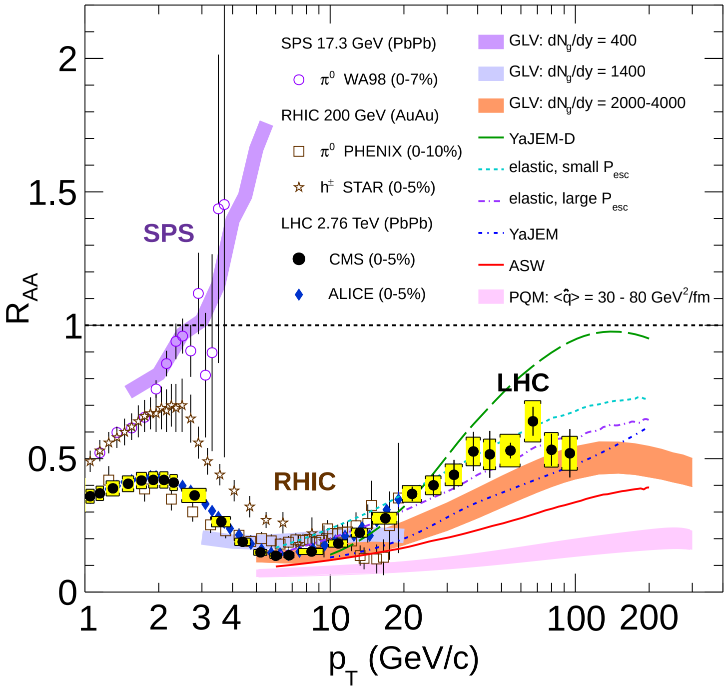

Figure 3.10: Nuclear modification factor R_{AA} as measured at SPS (open purple circles - WA98), RHIC (brown open squares - PHENIX and brown stars - STAR) and LHC (filled black circles - CMS and blue diamonds - ALICE) as a function of p_{T} for neutral pions and charged hadrons in central collisions (systems defined in figure). Compared to several theoretical calculations shown as colored bands and dashed lines. Taken from [5], see original publication and reference therein for details on analysis and theoretical calculations.

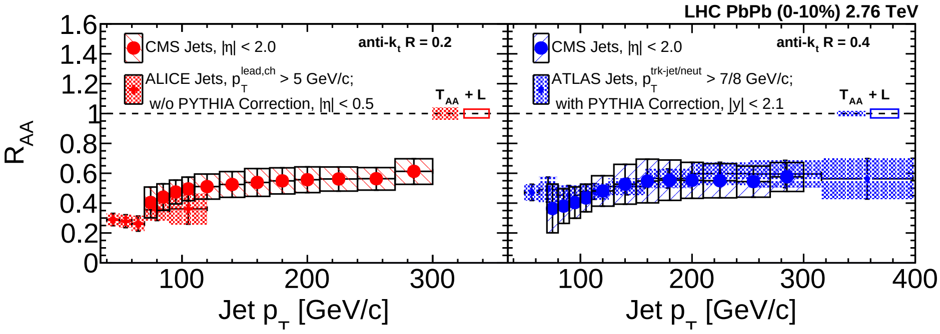

Figure 3.11: Nuclear modification factor R_{AA} as a function of jet p_{T} for inclusive anti-k_{T} jets reconstructed with (left) $R = 0.2$ by the CMS (red circles) and ALICE (red diamonds) experiments and (right) $R = 0.4$ by CMS (blue circles) and ATLAS (blue diamonds) in 0–10% most central Pb+Pb collisions at $\sqrt{s_{\mathrm{NN}}} = 2.76$ TeV. Error bars represent statistical and shaded boxes systematical uncertainties. Taken from [124], see original publication (with references therein) for further discussion on analysis details.

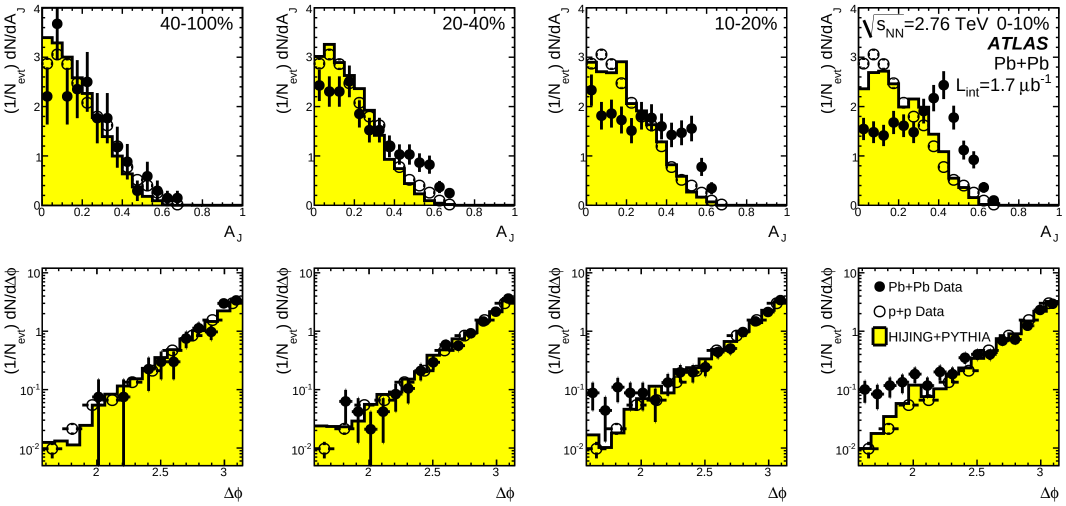

Figure 3.12: Distributions of dijet transverse momentum imbalance A_J (top) and angular separation $\Delta\phi$ (bottom) as a function of collision centrality (increasing from left to right) in Pb+Pb collisions at $\sqrt{s_\mathrm{NN}} = 2.76$ TeV measured by ATLAS. Taken from [128].

enhancement of jets being deflected from the recoil jet axis is observed. The CMS collaboration has confirmed these observations shortly afterwards [127].

Figure 3.13 shows later STAR measurements of the A_J, which have confirmed the dijet imbalance for jets with high-p_T constituents, but have shown that the balance is restored when including also soft constituents (see [129] for details of the jet reconstruction and matching procedures), for jets reconstructed with $R = 0.4$, while the balance is not fully recovered for $R = 0.2$ jets.

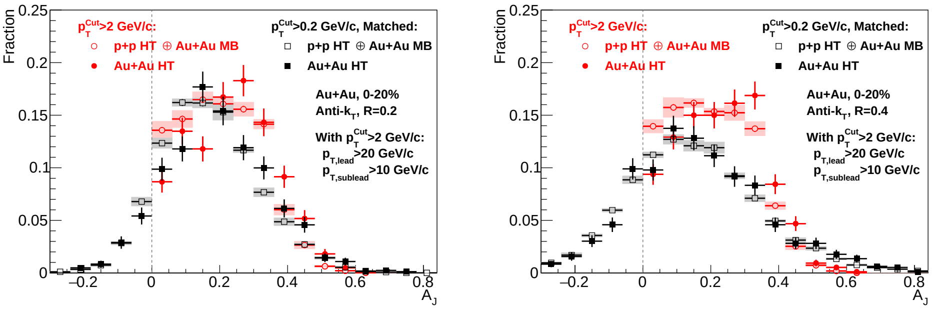

Figure 3.13: Normalized A_J distribution for anti-k_T jets reconstructed with $R = 0.2$ (left) and $R = 0.4$ (right) in 0-20% most central Au+Au collisions selected by the high tower trigger (filled symbols) and p+p collisions at $\sqrt{s_\mathrm{NN}} = 200$ GeV embedded into MB Au+Au collisions. Data for jets with the high-p_T constituent cut $p_\mathrm{T}^\mathrm{Cut} > 2$ GeV/c are shown in red color, while jets which include constituents with $p_\mathrm{T}^\mathrm{Cut} > 0.2$ GeV/c are represented with black color. Statistical errors are represented by the error bars while the shaded boxes represent systematic uncertainties. Taken from [129].

In order to confirm that the observed jet quenching is a result of the QGP formation, jet production was also studied in p+Pb collisions at $\sqrt{s_\mathrm{NN}} = 5.02$ TeV by the LHC experiments. The results from the

ATLAS and CMS collaborations, shown in Fig. 3.14, demonstrate that the nuclear modification factor $R_{p\mathrm{Pb}}$ for MB event selection, and jets produced at mid-rapidity and reconstructed with $R = 0.3$ at CMS and $R = 0.4$ at ATLAS, is consistent with unity within the uncertainties across the measured kinematic range, with possible hints of enhancement at $p_{\mathrm{T}} < 200$ GeV/c.

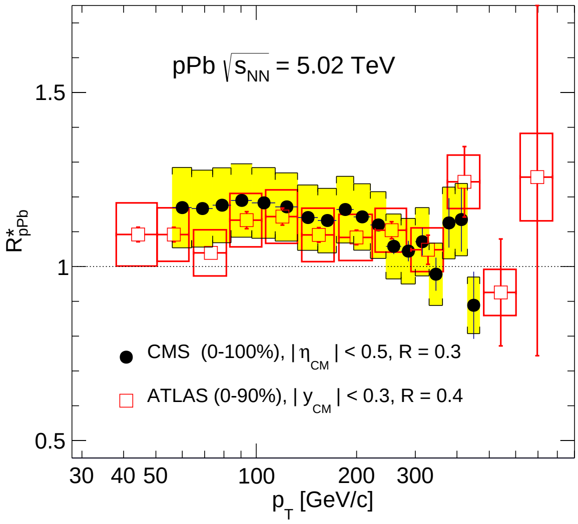

Figure 3.14: Nuclear modification factor $R^{*}_{p\mathrm{Pb}}$ (the $*$ indicates extrapolated p+p reference) for minimum bias p+Pb collisions at $\sqrt{s_{\mathrm{NN}}} = 5.02$ TeV of jets reconstructed at mid-rapidity with $R = 0.3$ (CMS, black circles) and $R = 0.4$ (ATLAS, red open circles). Error bars represent the statistical uncertainties while boxes represent the systematic uncertainties. Taken from [130], see original publications for details of differences between the analyses.

The last historical milestone regarding jet quenching discussed here is the inclusive charged-particle jet production published by STAR in 2020 [131]. Figure 3.15 shows the nuclear modification factor $R_{\mathrm{AA}}^{\mathrm{PYTHIA}}$, which compares the yield in 0–10% most central Au+Au collisions to the PYTHIA 6 p+p baseline. The results show strong suppression of the charged-particle jet yield with weak (if any) dependence on $p_{\mathrm{T,jet}}$ or the jet radius. The theoretical models which include jet quenching all describe the data and higher kinematic reach and systematic precision is needed in order to discriminate between these models. The predictions also assume full jets instead of charged-particle jets, increasing the need for a full jet analysis at STAR, which would also extend the kinematic reach.

3.6 Recent Results from RHIC and LHC

This section covers selected recent results from jet measurements at RHIC and the LHC. The results are grouped in subsections according to the system size.

3.6.1 p+p Collisions

The main motivation behind jet measurements in p+p collisions is to test the pQCD predictions of jet production cross section and to provide a baseline for similar measurements in the collisions of larger

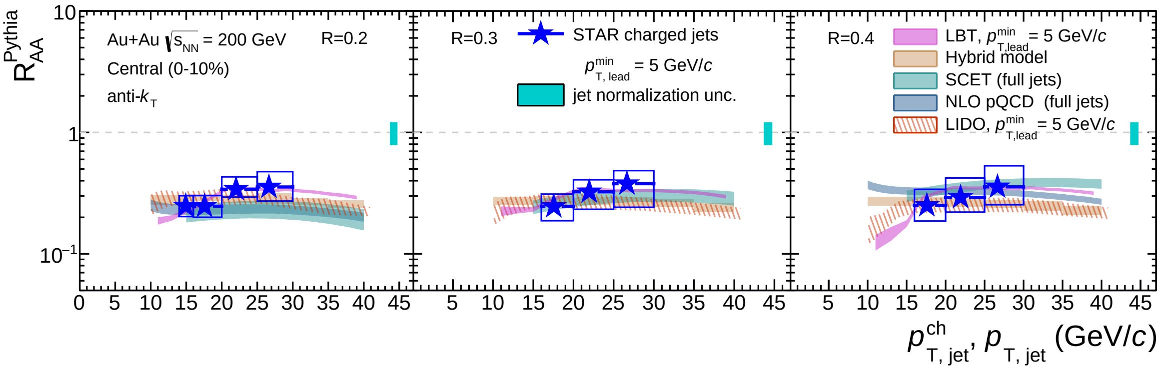

Figure 3.15: Nuclear modification factor R_{AA}^{PYTHIA} as a function of $p_{T,jet}$ of charged-particle jets reconstructed with anti-k_T algorithm with $R = 0.2$ (left), $R = 0.3$ (middle) and $R = 0.4$ (right) in 0–10% most central Au+Au collisions at $\sqrt{s_{NN}} = 200$ GeV measured by the STAR experiment (blue stars). Jets were required to contain at least one track with $p_T^{lead} > 5$ GeV/c. PYTHIA was used to simulate the p+p baseline at $\sqrt{s} = 200$ GeV. Error bars (not visible at this scale) represent statistical uncertainties while boxes represent systematic uncertainties. Colored bands represent theoretical predictions (see original publication for details). Taken from [131].

systems. The STAR collaboration has published the preliminary results of the inclusive jet cross section in p+p collisions at $\sqrt{s} = 200$ GeV. Figure 3.16 shows the double differential cross section as a function of jet p_T. The comparison with theoretical predictions indicates tension between both the NLO pQCD calculation [132], which over-predicts the data and the PYTHIA 6 MC generator, which was tuned to describe single particle spectra at STAR (STAR tune, [133]), and which underpredicts the data, especially at lower jet p_T. The final results (expected soon) are needed in order to confirm or disprove this tension. Furthermore, since the R_{AA}depends on the results from p+p collisions as the baseline, the publication of these results is crucial for finalizing the main analysis of this thesis.

The ALICE collaboration has published their results of inclusive jet production in p+p collisions at $\sqrt{s} = 5.02$ TeV in 2019 for jets reconstructed with $R = 0.1 - 0.6$ (Fig. 3.17, left). The right panel of Fig. 3.17 contains the ratios of the theory/data with theoretical predictions from NLO pQCD with NLL and non-perturbative (NP) corrections and the POWHEG+PYTHIA 8 MC generator tuned for ALICE. The ratios of both predictions to data for all R and all $p_{T,jet}$ bins are consistent with unity, indicating great understanding of pQCD at the NLO in the studied kinematic range.

The upper panel of Fig. 3.18 shows the ratio of inclusive jet spectra reconstructed with different R in p+p collisions at $\sqrt{s} = 5.02$ TeV to the spectrum of jets reconstructed with $R = 1.0$. The first observation is that larger jets contain more energy of the initial parton, as evidenced by the R−ordering. The difference between small and large jets gets smaller at high $p_{T,jet}$ supporting the argument that high-p_T jets fragment more collinearly, resulting in narrower cones. Both PYTHIA 6 and PYTHIA 8 predict these trends of the data, with PYTHIA 8 being generally quantitatively closer to the data (more visible in the lower panel of Fig. 3.18 for $R = 0.2$ and $R = 0.4$ jets).

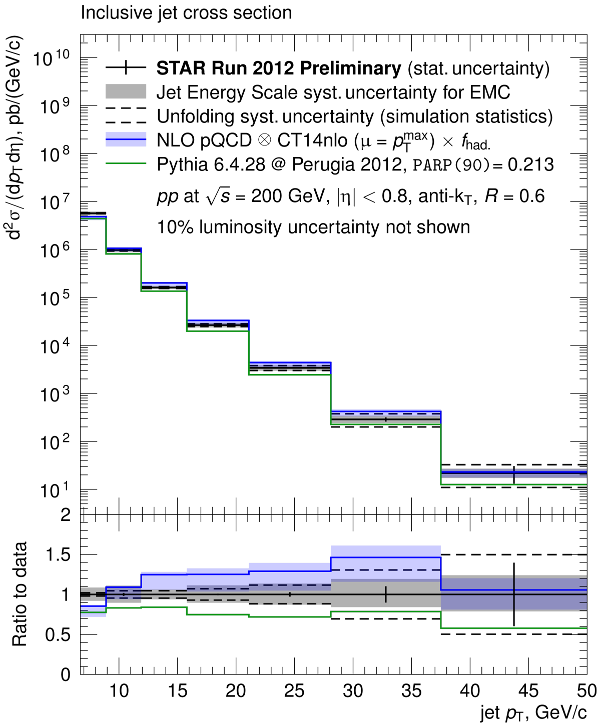

Figure 3.16: Inclusive anti-k_T, $R = 0.6$, jet cross section $d^2\sigma/dp_T d\eta$ in p+p collisions at $\sqrt{s} = 200$ GeV (black lines) as a function of jet p_T, measured by the STAR experiment (preliminary) at mid-rapidity. Vertical lines represent statistical and dashed lines systematic uncertainties. Blue line and shaded area represents NLO pQCD prediction with the CT14nlo PDFs and the green line represents the PYTHIA 6 STAR tune. Taken from [134].

3.6.2 p/d+A Collisions

The main motivation behind the jet measurements in p/d+A collisions is to study the effects of CNM on observed jet production, so the effects of QGP can be more precisely determined. There is also an ongoing effort to measure jet quenching in p+A collisions, especially in very violent p+Pb collisions at the LHC energies. The ALICE collaboration has recently published their results of search for jet quenching in p+Pb collisions at $\sqrt{s_{NN}} = 5.02$ TeV. Figure 3.19 shows the comparison of the nuclear modification factor $R_{p\mathrm{Pb}}$ as a function of $p_{T,\mathrm{jet}}$ for charged-particle jets reconstructed with $R = 0.4$ with $R_{p\mathrm{Pb}}$ of full jets reconstructed by ATLAS, $R = 0.3$ full jets reconstructed by CMS (all in the same collider configuration) and $R_{d\mathrm{Au}}$ of $R = 0.3$ full jets measured at PHENIX in d+Au collisions at $\sqrt{s_{NN}} = 200$ GeV. All data points are consistent with unity across the measured kinematic range and with each other in the overlap regions within uncertainties, with CMS and ATLAS data hinting possible enhancement around $p_{T,\mathrm{jet}} \sim 100$ GeV/c.

Figure 3.20 shows the dijet transverse momentum balance x_J (defined in Eq. 3.15) distribution in p+Pb collisions at $\sqrt{s_{NN}} = 5.02$ TeV as a function of event activity (EA) as determined by the total E_T deposited in the forward calorimeter systems at the CMS experiment. The data are compared to a PYTHIA prediction simulating p+p collisions and a PYTHIA+HIJING simulation which considers the underlying event in p+Pb events, but does not include jet quenching effects. The data do not show any significant shape differences from the predictions and no significant dependence on the total forward

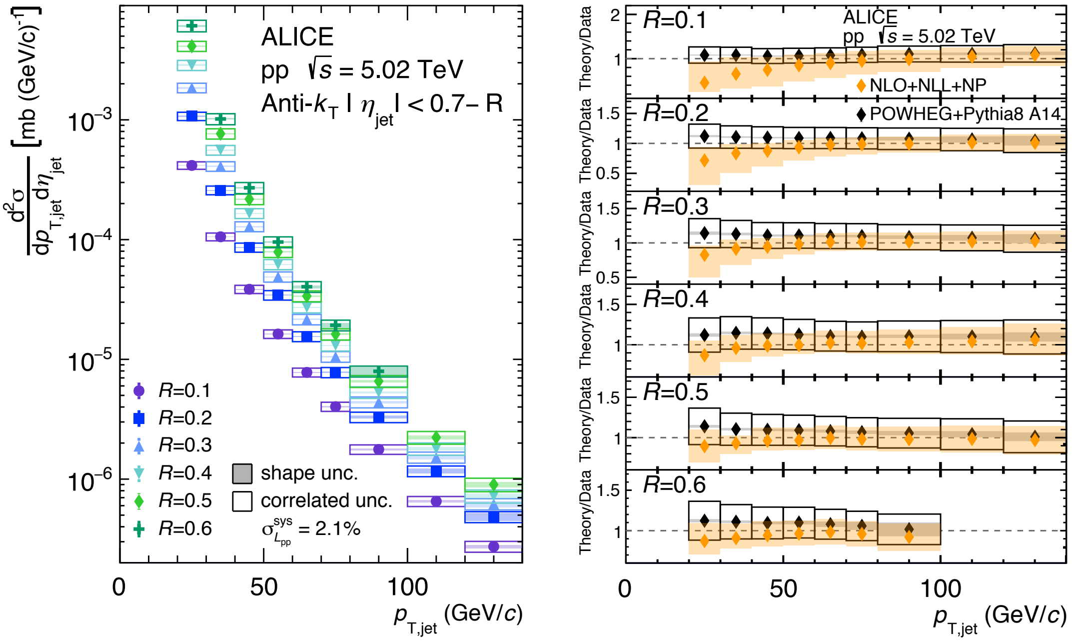

Figure 3.17: (Left) Inclusive anti-k_T jet cross section $d^2\sigma/dp_T d\eta$ as a function of jet transverse momentum $p_{T,jet}$ as measured by the ALICE collaboration in p+p collisions at $\sqrt{s} = 5.02$ TeV at mid-rapidity. Different symbols represent different values of R used for jet reconstruction. Shape systematic uncertainties are shown as shaded boxes, while correlated systematic erros are shown as empty boxes. Statistical errors are not visible at this scale. (Right) Ratios of theory/data for $R = 0.1 - 0.6$, where black diamonds represent the POWHEG+PYTHIA8 MC generator and the orange diamonds represent the NLO pQCD calculation with NLL and NP corrections. Boxes represent systematic uncertainties and are summed in quadrature from data and theory. Taken from [135] - see original publication for details on theoretical predictions.

E_T in the event, consistent with the absence-of-jet-quenching picture in p+A systems.

3.6.3 A+A Collisions

The rich heavy-ion programs of RHIC and LHC experiments focus mainly on studying jet qunching as a signature of the QGP formation. Recently, the focus of the field advanced towards more differential measurements of jet production, including focus on extending the reach of current measuremets, studying large jets and exploring the jet substructure. These measurements can provide finer tools to study jet quenching and in consequence the QCD in general. In 2021, the CMS collaboration has published the results of jet measurements with jets reconstructed with R up to 1, an unprecedented feat in the heavy-ion collision environment. Figure 3.21 shows the nuclear modification factor as a function of jet p_T in central Pb+Pb collisions at $\sqrt{s_{NN}} = 5.02$ TeV for six different values of jet reconstruction parameter R. The data show significant suppression for jets up to $p_{T,jet} = 1$ TeV/c and for all values of R which shows that the medium-induced gluon radiation is very wide-angled. The JEWEL [139] and PYQUEN [140] models, incorporating jet quenching, are shown for comparison. The JEWEL version without recoil severely underpredicts the data, while including the medium response brings the prediction closer to data, making

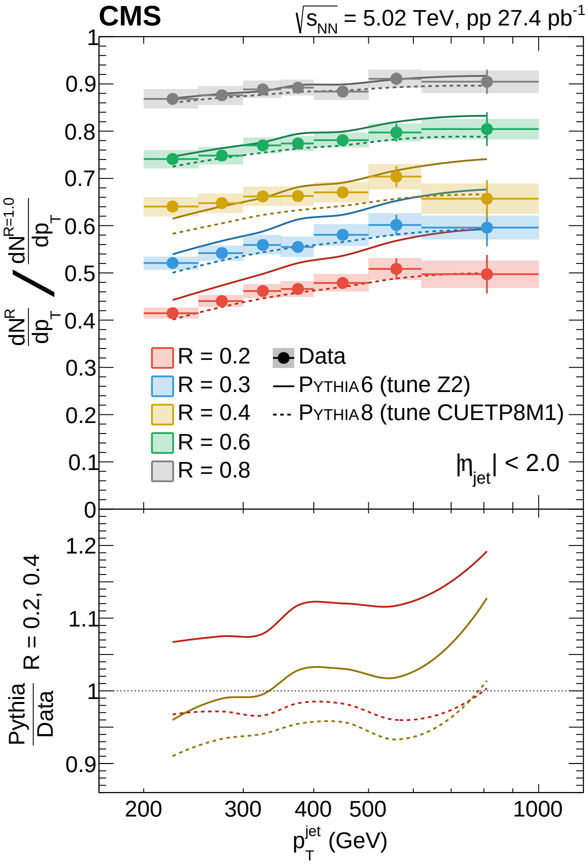

Figure 3.18: Ratio of inclusive jet spectra for jets of different R, represented by different colors, to spectrum of jets reconstructed with $R = 1.0$ at mid-rapidity by the CMS collaboration in p+p collisions at $\sqrt{s} = 5.02$ TeV as a function of jet transverse momentum $p_{\mathrm{T,jet}}$ (upper panel). Error bars represent the statistical uncertainties and boxes represent the systematic errors. Solid line represents the PYTHIA 6 prediction and dashed line represents the PYTHIA 8 prediction. (Lower panel) Double ratio of PYTHIA/Data for $R = 0.2$ and $R = 0.4$. Taken from [136].

it consistent for large jets. The default PYQUEN prediction overpredicts the data, especially at low $p_{\mathrm{T,jet}}$, while including the wide angle radiation brings the prediction down, closer to the data points. These results show that the medium effects play a significant role.

More recently, at the 2023 Quark Matter conference, the ALICE collaboration has shown [141] the preliminary results of their novel approach of background subtraction based on the mixed-event technique, yieldng a spectrum of $R = 0.3$ charged-particle jets, unbiased within $13.5 < p_{\mathrm{T,jet}} < 100$ GeV/c in 0–10% most central Pb+Pb collisions at $\sqrt{s_{\mathrm{NN}}} = 5.02$ TeV, significantly extending the reach in the low-p_{T} part of the spectrum. For the first time, the charged-particle jet R_{AA} is directly comparable between RHIC and the LHC. The data points are constistent in the overlap region within uncertainties. However, since the R_{AA} is affected by both energy loss and the spectrum shape, which is much harder at the LHC than at RHIC and also has different mixture of quark and gluon jets contributing, one should be careful in interpreting the results as they do not suggest that the energy loss in the RHIC and LHC medium is identical.

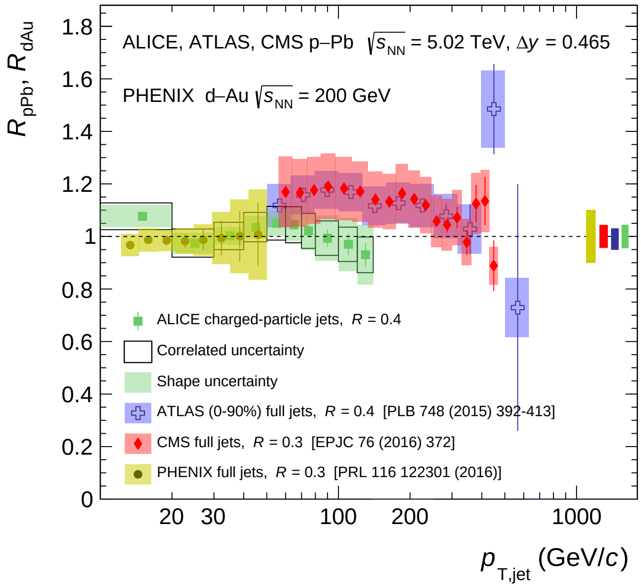

Figure 3.19: Nuclear modification factor $R_{p\mathrm{Pb}}$ as a function of $p_{\mathrm{T,jet}}$ for charged-particle jets reconstructed with $R = 0.4$ measured by ALICE (green squares), compared to $R_{p\mathrm{Pb}}$ of full jets reconstructed by ATLAS (blue crosses), $R = 0.3$ full jets reconstructed by CMS (red diamonds), all measured in p+Pb collisions at $\sqrt{s_{\mathrm{NN}}} = 5.02$ TeV, and $R_{d\mathrm{Au}}$ of $R = 0.3$ full jets measured at PHENIX (yellow circles) in d+Au collisions at $\sqrt{s_{\mathrm{NN}}} = 200$ GeV. Statistical errors are represented by error bars and systematic errors are shown as boxes and shaded areas. Taken from [137] and references in figure.

The STAR collaboration has published new results from jet quenching measurements using the semi-inclusive distribution of charged-particle jets recoiling from a neutral pion (π^0) or direct photon (γ_{dir}) trigger [142, 143]. This measurement is sensitive to color charge and in-medium path length dependence of jet energy loss mechanisms in the QGP. The γ_{dir} are not affected by the medium and (at LO) balance the initial momentum of the scattered parton in the $qg \to \gamma_{\mathrm{dir}}q$ process, dominant at RHIC energies. The hadronic trigger interacts with the medium and therefore preferentially selects events which occur near the edge of the fireball, in contrast with the γ_{dir} trigger. Figure 3.23 shows the ratio of trigger-normalized jet yields in 0-15% most central Au+Au collisions and p+p collisions both at $\sqrt{s_{\mathrm{NN}}} = 200$ GeV, I_{AA}. The data for both triggers show similar level of suppression for both $R = 0.2$ and $R = 0.5$ jets, with larger jet production being less suppressed than for smaller jets. Since the spectrum of recoil jets is steeper in p+p collisions for γ_{dir} than for π^0, the data indicate larger energy loss for the π^0-triggered jets. Theoretical predictions from the Jet-fluid, the Soft Collinear Effective Theory (SCET), the LBT, the Coupled LBT+hydro (CoLBT-hydro) and two options of the Hybrid Model (see [143] for model overview) are compared to the data. All models capture the overall trends of the data with varying level of success. Within the current precision, the data cannot discriminate between the models regardless of whether they include the medium response (LBT, CoLBT-hydro and Hybrid with wake) or not.

The ATLAS collaboration has published two interesting results in 2023. The first is the measurement of jet quenching dependence on the jet transverse momentum balance x_{J} [144]. The left panel of Fig. 3.24 shows the absolutely normalized x_{J} distribution for jets reconstructed with $R = 0.4$ in various centrality classes of Pb+Pb collisions at $\sqrt{s_{\mathrm{NN}}} = 5.02$ TeV and p+p collisions at the same energy. The leading jet was required to have $100 < p_{\mathrm{T}} < 112$ GeV. In this case of low-p_{T} (by ATLAS standards)

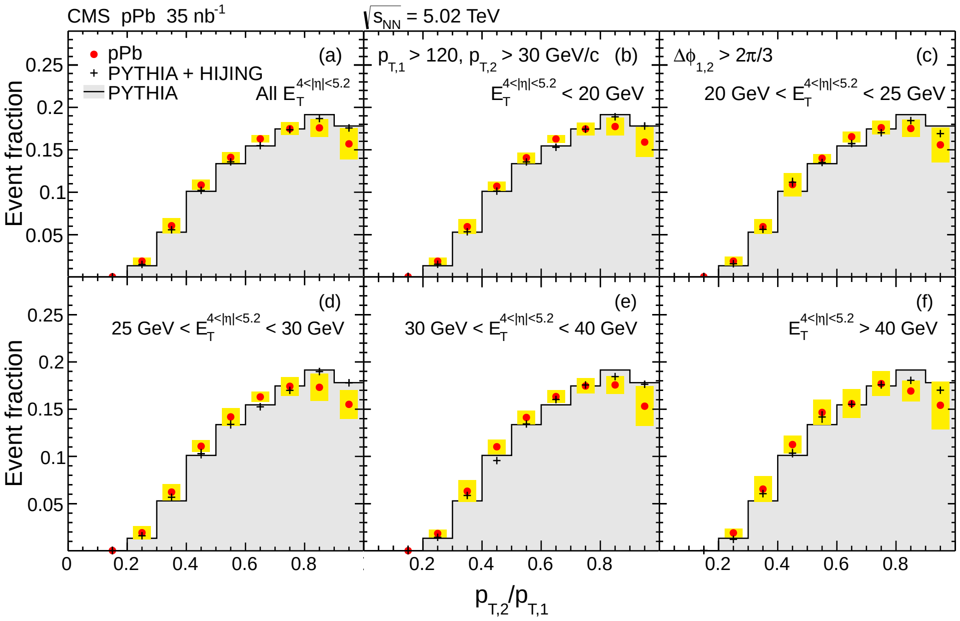

Figure 3.20: Dijet transverse momentum balance distribution as a function of forward E_T, measured by the CMS experiment (red circles) in p+Pb collisions at $\sqrt{s_{NN}}$ = 5.02 TeV. Panel (a) shows the inclusive EA bin, while panels (b) – (f) show bins with increasing EA. Statistical errors are invisible at this scale and systematic errors are represented by the yellow boxes. Predictions from MC generators are shown as black crosses (PYHTIA) and black shaded area (PYTHIA+HIJING). Taken from [138].

jets, the balanced dijets are suppressed significantly more in central Pb+Pb collisions, when compared to $p+p$ collisions, than imbalanced jets, leading to a peak structure around $x_J \sim 0.6$. The depletion of balanced dijets is observable even in more peripheral events, although smaller in magnitude. The difference between Pb+Pb and $p+p$ collisions is significantly smaller for high-p_T leading jets, as seen in the right panel of Fig. 3.24.

The second result by ATLAS is their measurement of the substructure-dependent jet quenching [145]. Figure 3.25 shows the nuclear modification factor R_{AA} as a function of $p_{T,jet}$ in 0–10% most central Pb+Pb collisions at $\sqrt{s_{NN}}$ = 5.02 TeV for different classes of the jet groomed radius r_g. A strong dependence of R_{AA} on r_g is observed with the yield of narrow-splitting jets being significantly less suppressed than jets with wide-angle hard splitting, with weak dependence on $p_{T,jet}$. The predictions from JETSCAPE [146] which combines the jet quenching from MATTER [147] and Linearized Boltzmann Transport (LBT, [148]) models are able to describe the r_g dependence of the R_{AA}, with the exception of the narrow jets with $0.00 < r_g < 0.02$, where JETSCAPE overestimates the data.

The STAR collaboration has also recently published results of jet substructure observables [149]. The groomed jet radius R_g and groomed momentum fraction z_g distributions are shown in Fig. 3.26 for both dijets with high-constituent-p_T requirement (HardCore jets) and inclusive dijets (Matched jets) reconstructed with R = 0.4. The results from 0–20% most central Au+Au collisions, selected using a high-energy trigger particle, at $\sqrt{s_{NN}}$ = 200 GeV are compared with results from $p+p$ collisions at the same energy emedded into 0–20% most central Au+Au collisions selected with the MB trigger to account for the high-multiplicity environment, providing a baseline without jet quenching effects. No significant difference between the Au+Au and baseline distributions is observed for either trigger or recoil jets

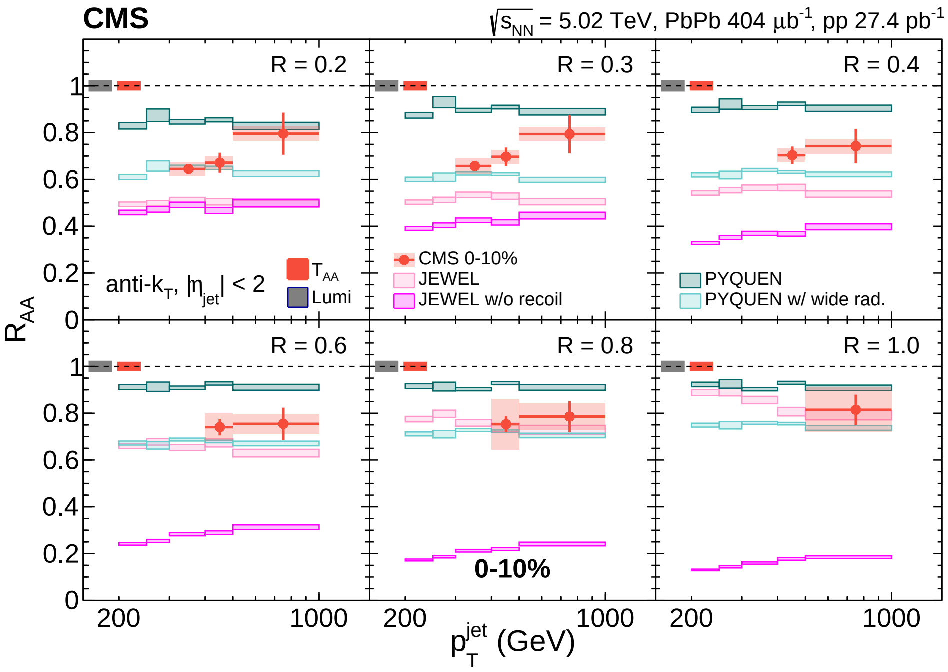

Figure 3.21: Nuclear modification factor R_{AA} as a function of $p_{\mathrm{T,jet}}$ and the jet radius R as measured by the CMS experiment at mid-rapidity in 0–10% most central Pb+Pb collisions at $\sqrt{s_{\mathrm{NN}}} = 5.02$ TeV (red points). The error bars represent statistical errors while systematic errors are shown as red boxes. The colored boxes represent JEWEL without recoil (magenta), JEWEL default (pink), PYQUEN default (teal) and PYQUEN with wide angle radiation (turquoise) model predictions. Taken from [136].

and for both HardCore and Matched jets, while there is a significant difference between HardCore and Matched jets in the R_{g} shape for both trigger and recoil jets. This difference is caused by the HardCore jets not being affected by the combinatorial background and shows that the R_{g} observable is sensitive to the underlying event.

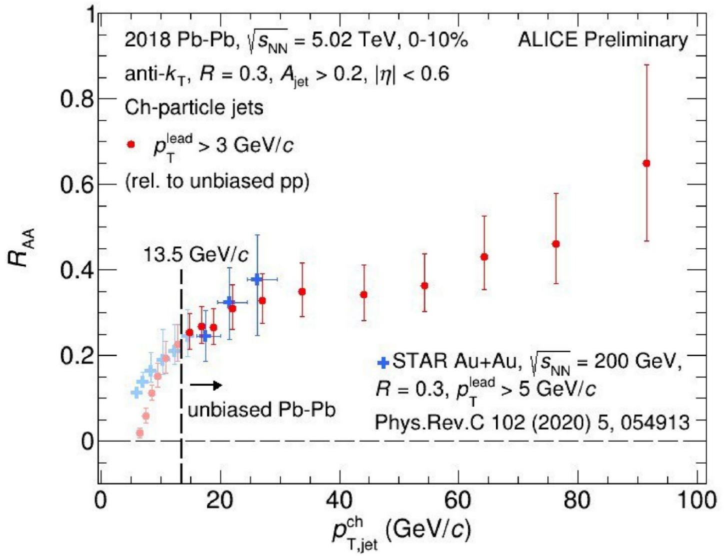

Figure 3.22: Preliminary nuclear modification factor R_{AA} as a function of $p_{\mathrm{T,jet}}^{\mathrm{ch}}$ for charged-particle jets with $p_{\mathrm{T}}^{\mathrm{lead}} > 3$ GeV, reconstructed by ALICE in 0–10% most central Pb+Pb collisions at $\sqrt{s_{\mathrm{NN}}} = 5.02$ TeV at mid-rapidity (red points). The blue crosses represent previous STAR data (reference in figure) from central Au+Au collisions at $\sqrt{s_{\mathrm{NN}}} = 200$ GeV. Only statistical errors are included. The unbiased region is marked by the dashed vertical line. Taken from [141].

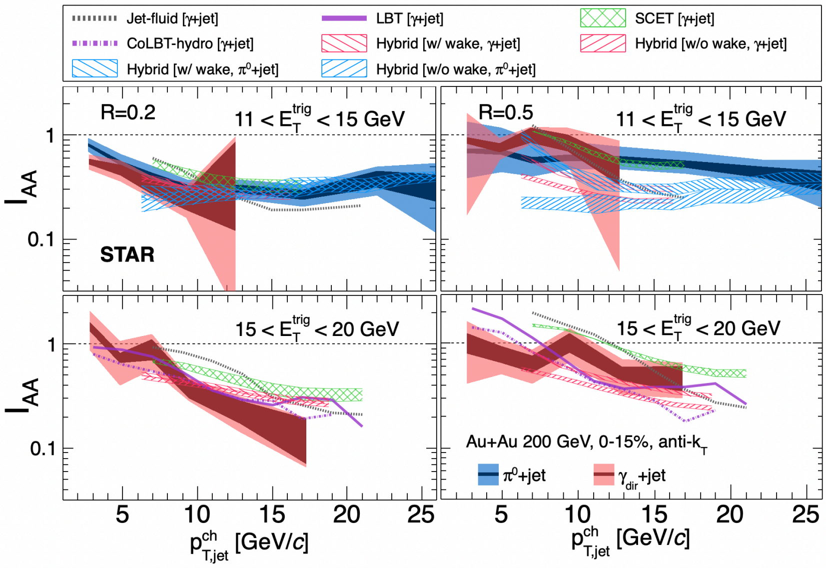

Figure 3.23: Recoil-jet yield ratio I_{AA} in 0–15% most central Au+Au and p+p collisions at $\sqrt{s_{\mathrm{NN}}} = 200$ GeV, for γ_{dir} (red bands) and π^0 (blue bands) triggers with $11 < E_{\mathrm{T}}^{\mathrm{trig}} < 15$ GeV (top) and $15 < E_{\mathrm{T}}^{\mathrm{trig}} < 20$ GeV (bottom, γ_{dir} only), of jets reconstructed with $R = 0.2$ (left) and $R = 0.5$ (right). Dark band width represents the statistical uncertainty and light band width represents systematic uncertainty. Theoretical calculations are represented by dashed lines and bands. Taken from [142].

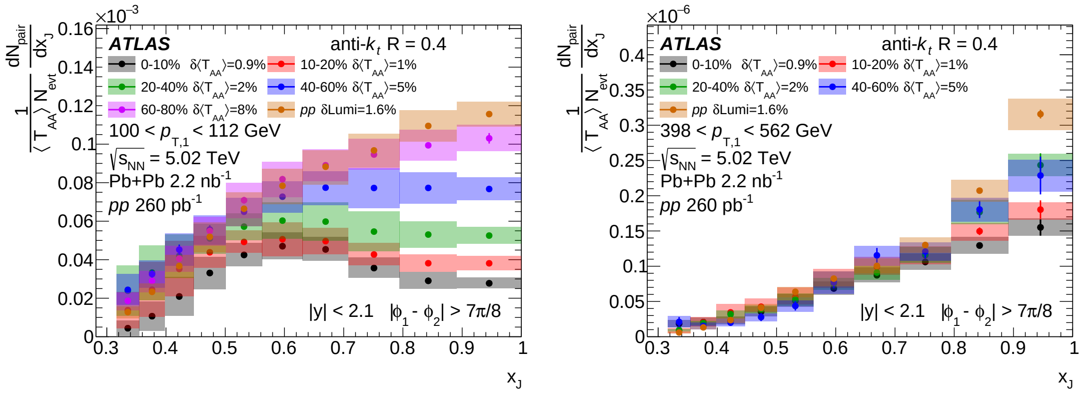

Figure 3.24: Absolutely normalized x_J distribution for jets reconstructed with $R = 0.4$. Different colors represent different centrality classes of Pb+Pb collisions at $\sqrt{s_{NN}} = 5.02$ TeV and p+p collisions at the same energy (orange), measured by ATLAS at mid-rapidity. The leading jet was required to have $100 < p_T < 112$ GeV (left) or $398 < p_T < 562$ GeV (right). Error bars represent statistical errors while systematic errors are shown as boxes. Taken from [144].

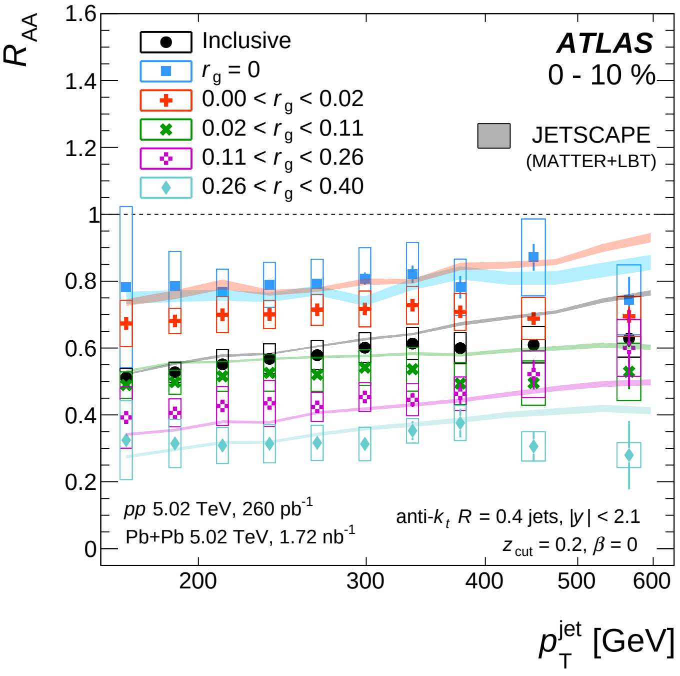

Figure 3.25: Nuclear modification factor R_{AA} as a function of $p_{T,jet}$ in 0–10% most central Pb+Pb collisions at $\sqrt{s_{NN}} = 5.02$ TeV as measured by the ATLAS experiment at mid-rapidity. Different symbols and colors represent different intervals of the groomed radius r_g with black circles representing the inclusive distribution. Shaded color bands represent the JETSCAPE prediction for the corresponding interval. Statistical errors are represented by error bars and systematic errors are shown as boxes. Taken from [145].

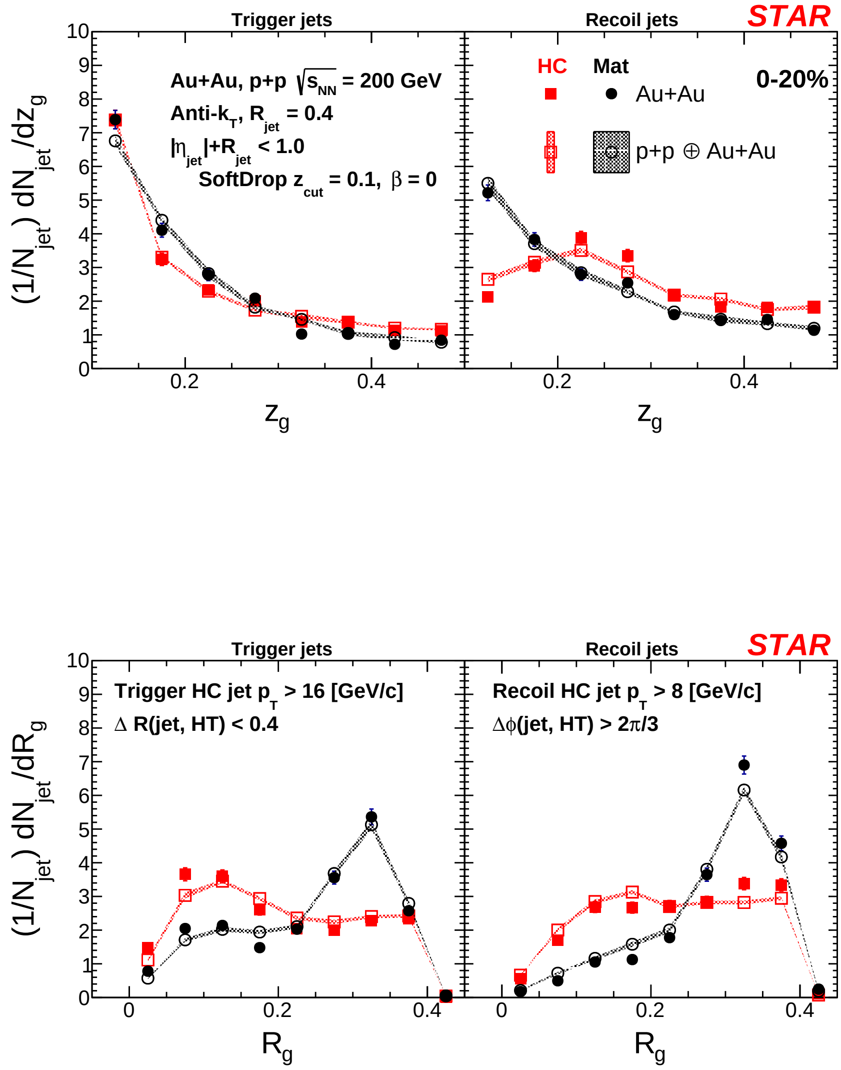

Figure 3.26: Distributions of jet substructure observables z_g (top) and R_g (bottom) for HardCore (red) and Matched (black) trigger (left) and recoil (right) jets reconstructed with $R = 0.4$ at mid-rapidity in 0–20% most central Au+Au collisions at $\sqrt{s_{NN}} = 200$ GeV (solid markers) and in p+p collisions at the same energy embedded into central Au+Au collisions (open markers). Vertical lines represent statistical uncertainties (invisible for most points) and shaded areas represent systematic uncertainties. Taken from [149].

Chapter 4

RHIC and STAR

This chapter describes the experimental facilities used to obtain the data used for the analyses presented in the following chapters, namely the RHIC accelerator (Sec. 4.1) and the STAR detector (Sec. 4.2). Since BNL is expecting major upgrades in the near future, the prospects of high energy physics at BNL are also discussed in Sec. 4.3.

4.1 RHIC

The Relativistic Heavy Ion Collider (RHIC) is the main accelerator of the BNL accelerator complex (described in Subsec. 4.1.1), located on Long Island, NY, USA. RHIC is one of only two operational high-energy heavy-ion colliders in the world, along with the LHC in CERN. In contrast with the LHC, whose main program is the physics at the highest energy frontier achieved in p+p collisions, the main physics goals of RHIC focus on heavy ion collisions. RHIC is a remarkably versatile collider, having successfully collided 12 disctinct systems at various energies. Figure 4.1 shows the average store luminosity L_{NN} for beams of all collided systems, each of them serving a specific physics goal. The large system collisions (Au+Au, U+U) explore the QCD phase diagram, while the p/d+Au collisions focus on studying the cold nuclear matter effects. The isobar (Zr+Zr and Ru+Ru) collisions were carefully studied during the search for the elusive chiral magnetic effect, with negative results [150]. Other small nuclei collisions serve as complementary to the Au+Au program. The p+p collisions serve as a baseline for the heavy-ion collisions and also enable unique studies of the spin of the proton, since RHIC is the only collider in the world capable of colliding polarized protons.

The two RHIC storage rings (called blue and yellow) have a diameter of around 1220 m, making RHIC one of the largest particle accelerators to ever exist. Four superconducting radiofrequency (RF) cavities, each operating at 28.15 MHz are used for the acceleration and 10 storage cavities with a frequency of 197 MHz help maintain the beams at the maximum energy, which is 255 GeV for a proton beam and 100 AGeV for a heavy-ion beam, throughout the beam storage which usually lasts around 10 hours[1]. The acceleration in RF cavities works in the following way: the antenna excites the electric field inside the cavity, which is designed to trap the field inside. Since the input frequency is the same as the intrinsic frequency of the cavity (determined by its shape), a standing wave of high-intensity electric field is formed due to the resonance inside the cavity. As the charged particles inside the bunch pass through the cavity, they are accelerated by this electric field. The oscillations of the standing wave are tuned in

---

[1] As the two beams pass through each other repeatedly and the particles collide, the quality of the beam gradually decreases. The average storage time is determined by the time it becomes more efficient to discard the beams and fill new ones. In case of accidents, the beams are dumped immediately into a designated space.

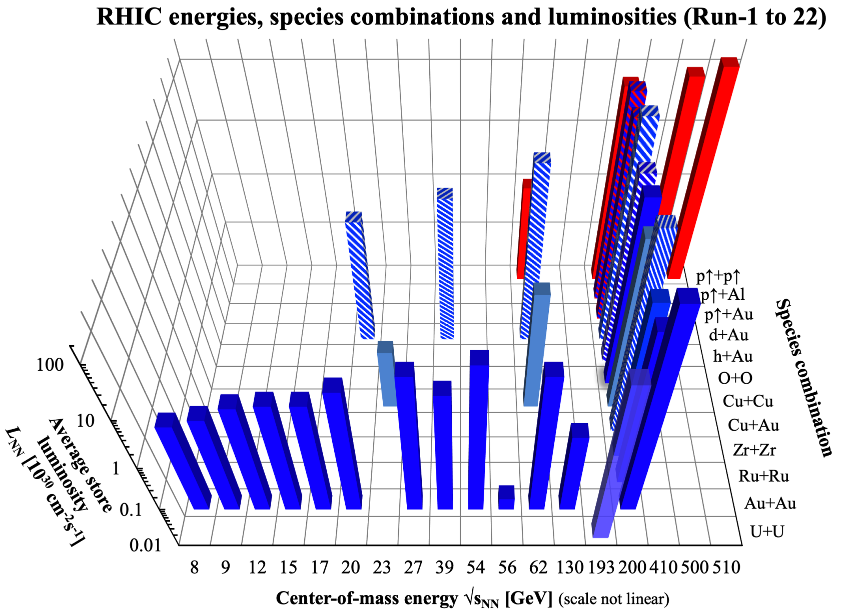

Figure 4.1: Summary of the delivered luminostity of the major collision systems and the corresponding center-of-mass energies at RHIC. Taken from [151].

such way that the particles which arrive in the front of the bunch are accelerated less than those who arrive later, therefore maintaining the compactness of each bunch and also the bunch spacing. Dipole 3.5 T magnets are used to maintain the circular[2] trajectory of the beams while quadrupole magnets are used for focusing the beam. The magnets are superconducting, as they have to withstand a current in excess of 5 kA flowing through the conductors. The two rings intersect at 6 interactions points, each labeled by the clock position. Four experiments have been placed at these interaction points. The PHOBOS experiment, which completed its program in 2005, was located at the 10 o'clock position. The BRAHMS experiment at 2 o'clock completed its program in 2006. The two major experiments are the STAR experiment at the 6 o'clock position, which has been running successfully for over 23 years and is described in detail in Sec. 4.2, and the sPHENIX experiment at the 8 o'clock intersection point. The sPHENIX experiment (still in the commisioning phase in 2023) is the successor of the PHENIX detector, which finished the data taking in 2016, and will focus mainly on the physics of hard probes, studying for example jet production and the Υ meson decays [152]. The technical specifications of RHIC are summarized in Tab. 4.1 and for the full RHIC design overview see [153].

4.1.1 Pre-Accelerators at BNL

RHIC is the final accelerator in the BNL accelerator complex. The journeys of protons and heavy nuclei are slightly different. Let's start with a Au nucleus, which is the most commonly accelerated kind of heavy nuclei. The Au nucleus starts its journey at the Laser Ion Source[3] [154], where a pulsed laser extracts individual atoms from a target foil with +1 charge. The atom is then transfered to the Electron Beam Ion Source (EBIS, [155]), which replaced the older Tandem Van De Graaf generator

---

[2] Both RHIC storage rings actually have approximately hexagonal shape.

[3] The Laser Ion Source at BNL is abbreviated as LION, while in general a laser ion source is abbreviated as LIS. Both abbreviations are used interchangibly.

Circumference	3 834 m
No. of dipole magnets	2 × 396
No. of quadrupole magnets	2 × 492
Operating magnetic field	3.5 T
Operating current	5.1 kA
Maximum beam energy	protons 255 GeV
	heavy ions 100 AGeV
No. of interaction points	6
Nominal storage time	10 h

Table 4.1: RHIC technical design specifications. Taken from [153] and [151].

system, where it is ionized to a Au^{32+} state by an electron beam and accelerated to 2 AMeV. The nucleus, along with around $3.4{\times}10^9$ others in the same pulse, is transfered to the Booster Synchrotron and further accelerated to 95 AMeV. The ions are organized into 24 bunches which pass through stripping foils and are now ionized to a Au^{77+} state and injected into the Alternating Gradient Synchrotron (AGS). The AGS accelerates the ions to 10.8 AGeV and reorganizes them into 4 bunches. The nuclei are also fully ionized (Au^{79+}) and transferred to RHIC via the AGS-to-RHIC (AtR) beam pipe. Before entering RHIC, the bunches are divided into smaller bunches of $\sim 10^9$ ions and injected into one of the two RHIC storage rings by an electromagnetic switch. In RHIC, the bunches enter the final stage of the acceleration, up to 100 AGeV. In total, 112 bunches can circulate inside RHIC at the same time. RHIC is continuously upgraded and now exceeds its design luminosity many times [151, 153]. Polarized protons are produced in the optically pumped polarized proton source [156], and are accelerated in the 200 MeV proton linear accelerator (LINAC) before being injected to the Booster and following the journey of the heavy ions from then on. The polarization of the protons is maintained by the siberian snake magnets. The aerial view of the BNL accelerator complex with key components highlighted can be seen in Fig. 4.2.

4.2 STAR

The Solenoidal Tracker at RHIC (STAR) is one of the two currently operating experiments at RHIC, along with sPHENIX, and the only one who has participated in every Run[4] since RHIC became operational in 2000. Historically, STAR focused on the measurements of the properties of the QGP created in high-energy Au+Au collisions. In order to measure multiple QGP signatures simultaneously, it has an approximate cylindrical symmetry with full azimuthal coverage at mid-rapidity and uses precise charged-particle tracking and particle identification (PID) as its main tools. This is in contrast with sPHENIX, which focuses mainly on calorimetry, making STAR and sPHENIX complementary experiments. STAR combines information from multiple subdetector systems which are continuously upgraded in order to maximize its scientific potential. The analysis presented in Chapter 5 uses data collected in the year 2014. Therefore, the description of STAR is based on its state in that year with special focus on detectors used in the analysis, including the TPC (Subsec. 4.2.1), the BEMC (Subsec. 4.2.2), the VPD (Subsec.

---

[4] By Run we mean one data-taking period lasting usually several months.

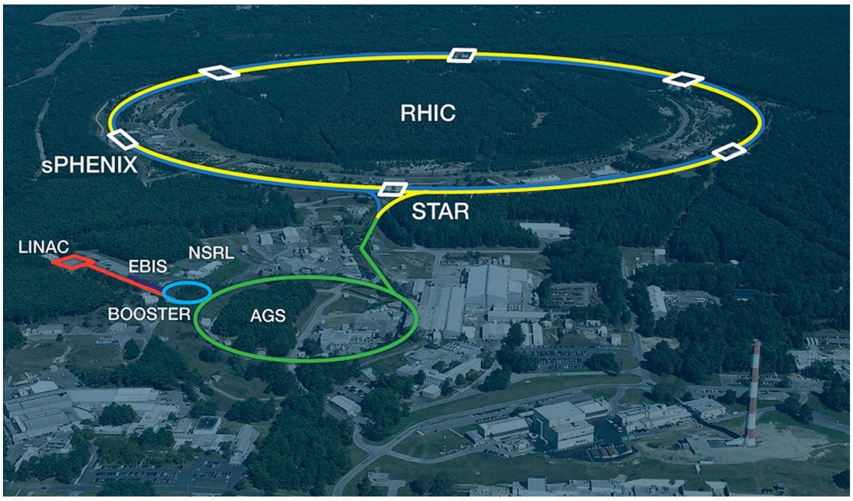

Figure 4.2: Aerial view of the BNL accelerator complex. Key accelerators and the STAR and sPHENIX experiments are highlighted. Taken from [157].

4.2.3) and the BBC (Subsec 4.2.4). The current status of STAR, including the upgrades since the year 2015, is presented in Subsec. 4.2.6. Important part of STAR is the 1100 ton room-temperature magnet, which produces 0.5 T solenoidal field which bends the trajectories of charged particles, allowing precise momentum measurements [158]. Kindly refer to [159] for a complex overview of the STAR experiment. A 3D model of the STAR experiment (from year 2014) can be seen in Fig. 4.3.

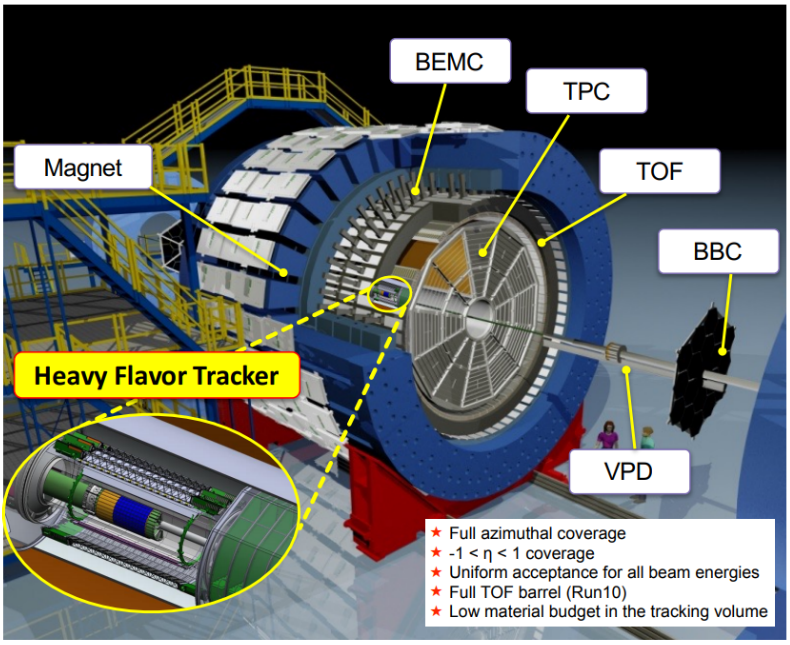

Figure 4.3: 3D model of the STAR detector from year 2014 with the magnet and key detectors highlighted. Originally made by Maria and Alex Schmah.

4.2.1 TPC

The Time Projection Chamber (TPC) [160] is the heart of the STAR experiment. It is a 420 cm long cylinder with the outer diameter of 400 cm and inner diameter of 100 cm. The TPC is filled with a P10 gas mixture. The mixture consists of 90 % argon for ionization and 10 % methane for quenching and is kept 2 mbar above the atmospheric pressure. The TPC has a full azimuthal coverage and allows full tracking in the pseudorapidity range of $|\eta| < 1.0$. It is divided into two halves by a conductive cathode membrane kept at 28 kV. The anodes are located at the end caps and kept at ground level, producing a uniform electric field $E = 135$ V·cm^{-1}. The end caps are divided into 12 sections, each split into the inner and outer sectors. Each of the 24 sectors contains a read-out system based on the Multi Wire Proportional Chamber (MWPC). A 3D model of the STAR TPC can be seen in Fig. 4.4.

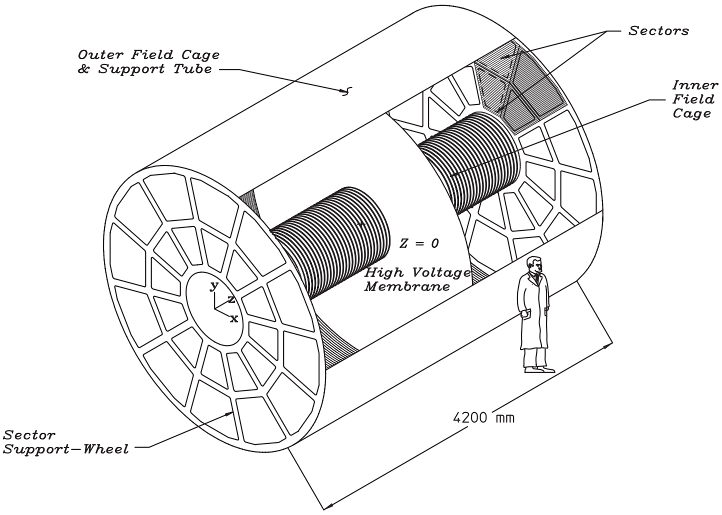

Figure 4.4: Sketch of the STAR TPC with the key features highlighted. Taken from [160].

When a charged particle passes through the TPC, it interacts with the gas and loses energy via the ionization of the gas. The free electrons then drift towards the end caps, where they are amplified by a factor of 1000-3000 to create signal which can be detected. This signal is called a TPC hit and its $x - y$ position is given by the position of the wires. The z component of the particle hit position is determined from the drift time of the electrons. The typical electron drift velocity is about 5.45 cm/μs and is frequently measured and calibrated at STAR. One charged particle usually creates multiple such hits, with maximum being 45 at the STAR TPC. An algorithm is then used to fit all the points with a helix, creating a track corresponding to one charged particle. This track is called a global track. If the track has sufficient quality and passes close to the Primary Vertex[5] (PV), the PV position is added as an additional (very precise) point and the tracks are refit. The tracks which also include the PV are then called primary tracks. From the track curvature, the TPC can determine the particle momentum. The procedure described above is called tracking and is done simultaneously for all charged particles in one

---

[5] The primary vertex is the place where the collision most likely actually happened. It is reconstructed by a specific software, called the vertex finder, by locating the intersections of different tracks. Throughout this thesis, the primary vertex should be understood as reconstructed by the TPC, unless specified otherwise.

event, sometimes generating several thousand tracks at once. The TPC therefore creates a snapshot of each event, similarly to a 3D camera in photography. Figure 4.5 shows a typical central Au+Au collision at $\sqrt{s_{\mathrm{NN}}} = 200$ GeV, with each colored curve representing one reconstructed track, demonstrating the impressive tracking abilities of the STAR TPC.

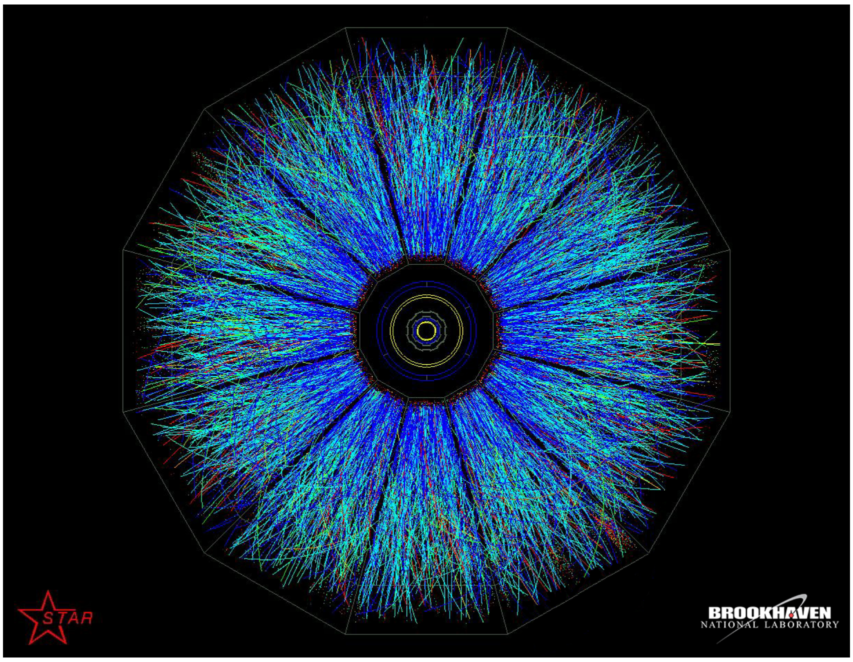

Figure 4.5: Event display for a central Au+Au collision at $\sqrt{s_{\mathrm{NN}}} = 200$ GeV as reconstructed by the STAR TPC. View from the beam direction. Taken from [161].

The TPC can measure the particle momentum with relative resolution down to ~ 2 %. Particles with momentum lower than 100 MeV/c will not reach the TPC volume because their trajectories will be bent too much by the magnetic field while particles above 30 GeV/c will be almost straight lines, making momentum measurements impossible. The TPC can also identify the particles via the measurements of their ionization energy loss $\mathrm{d}E/\mathrm{d}x$. Every kind of particle has a specific mean energy loss dependence on its momentum $\langle \mathrm{d}E/\mathrm{d}x \rangle_{\mathrm{th}}$ which can be calculated using the Bichsel functions [162], a modified version of the Bethe-Bloch formula. For each track, its measured energy losses are compared to the theoretical prediction for all common particle species and the number of standard deviations from the prediction is calculated as

$$n_\sigma^a = \frac{\ln \frac{\mathrm{d}E/\mathrm{d}x}{\langle \mathrm{d}E/\mathrm{d}x \rangle_{\mathrm{th}}^a}}{R_{\mathrm{d}E/\mathrm{d}x}}, \tag{4.1}$$

where a represents particle species and $R_{\mathrm{d}E/\mathrm{d}x}$ is the TPC energy loss resolution. For example, if a track has $n_\sigma^\pi = 1$, $n_\sigma^K = 2$ and $n_\sigma^p = 10$, it is most likely a pion, but can also be identified as a kaon. The chance of it being a proton is negligible. The STAR measurement of ionization energy loss as a function of particle momentum along with the theoretical predictions can be seen in Fig. 4.6. Separation between protons and pions is possible up to 1 GeV/c. The main disadvantage of the TPC is the slowness of the readout, caused mainly by the slow drift speed of the electrons. This makes the TPC sensitive to pile-up, which happens when the TPC reconstructs parts of multiple events as one. This is a problem mainly in

p+p collisions where the collision rate is much higher than for Au+Au collisions. For more technical details of the STAR TPC and its performance refer to [160].

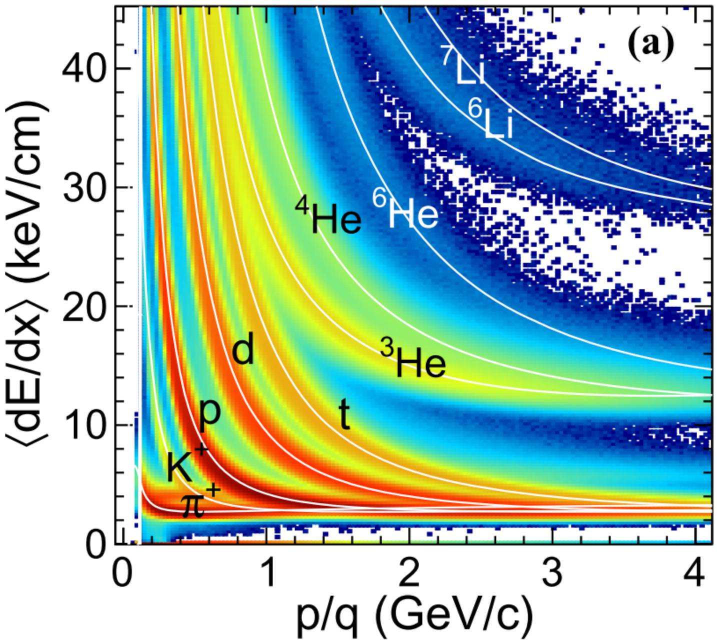

Figure 4.6: Mean energy loss ⟨dE/dx⟩ as a function of particle momentum p (divided by charge q) as measured by the STAR TPC. The solid white lines represent the Bichsel function predictions for each kind of measured particles. Taken from [163].

4.2.2 BEMC

The STAR Barrel Electromagnetic Calorimeter (BEMC, [164]) is a cylindrical detector with inner radius 223.5 cm and outer radius 263 cm, located between the TPC and the magnet coils. The BEMC has a full azimuthal coverage and covers the pseudorapidity range $|\eta| < 1$, matching the TPC coverage. A 3D model of the BEMC can be seen in Fig. 4.7. It is composed out of 120 modules, each further divided into 40 towers. The towers are the basic cells of the calorimeter. In total, there are 4800 towers, each covering 0.05×0.05 in $\Delta\eta\times\Delta\phi$ and is composed of 20 layers of lead (5 mm thick) and 21 layers of plastic scintillator. One BEMC module can be seen in Fig. 4.8, showing the projective nature of the towers. When a particle hits a lead layer, it will produce a shower of particles which are then detected by the scintillator. The calorimetric towers therefore measure the total deposited energy. However, one particle can deposit energy into multiple towers and multiple particles can deposit energy into a single tower. The energy resolution of the BEMC is about 17 % for 1.5 GeV electrons and about 10 % for 3 GeV electrons in the most central Au+Au events, demonstrating a typical calorimetric behavior where the resolution improves with larger energy deposits[6] as $\propto 1/\sqrt{E}$. Since electrons lose energy inside material much easier than heavier particles, they will deposit almost all of their energy inside the BEMC. The BEMC can therefore be used for electron identification via the E/p measurement, where E is the energy

---

[6] This is in contrast with the TPC momentum resolution, which worsens approximately linearly with increasing particle momentum.

measured by the BEMC and p is the momentum measured by the TPC. Electrons will have $E/p \sim 1$, while other charged particles will deposit only a fraction of their energy. In addition, the BEMC is used to detect neutral particles, mainly direct γ and π^0, which produce an electromagnetic shower, fully contained inside the calorimeter. Since the BEMC is a fast detector (especially compared to the TPC), it can be used as a trigger, selecting events where a rare hard process has occured. Therefore, the BEMC is an essential detector for the measurements of jets and heavy flavor production. For more details on the BEMC refer to [164].

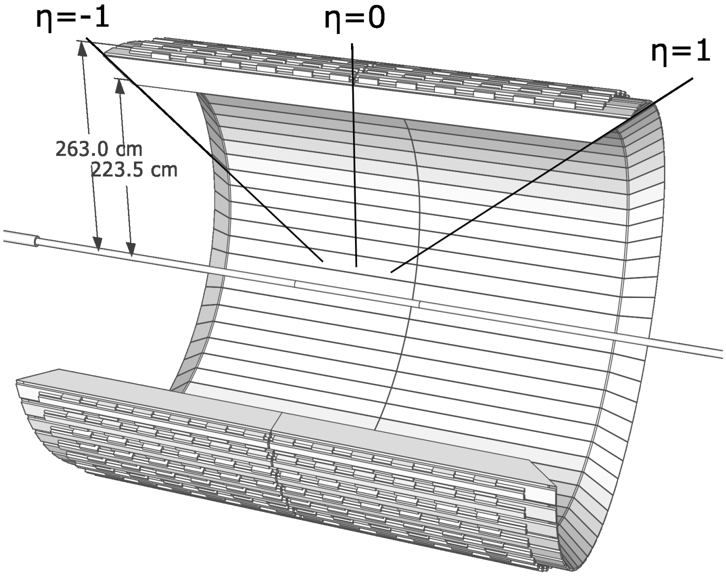

Figure 4.7: 3D model of the STAR BEMC. Taken from [164].

4.2.3 VPD

The STAR Vertex Position Detector (VPD, [165]) is a very fast detector composed of two identical scitillator arrays behind a lead convertor, each located at one side of the STAR experiment, approximately 5.7 m from the nominal center of the STAR detector and close to the beampipe. Each assembly contains 19 lead-scintillator sectors. A cross-sectional view and a photo of one such sector can be seen in Fig. 4.9. During heavy-ion collisions at high energy, many π^0 mesons are created. These mesons decay almost immediately to photon pairs which can then travel along the beam line at the speed of light. When the photons reach the lead convertor, they create an electromagnetic shower which can be detected by the scintillators. This signal provides the timestamp of each collision, which can then be also used by other detector systems. The event start time is calculated by

$$T_{\text{start}} = \left(T_{\text{east}} + T_{\text{west}}\right)/2 - L/c, \tag{4.2}$$

where T_{east} and T_{west} are the times obtained from each of the VPD assemblies and L is the distance from the center of the STAR experiment. The resolution of the event start time measurements is of around 20 ps for high energy Au+Au collisions and around 80 ps for p+p collisions. The VPD also measures the position of the primary vertex along the z axis, which can be calculated from the following equation:

$$V_z^{VPD} = c\left(T_{\text{east}} - T_{\text{west}}\right)/2, \tag{4.3}$$

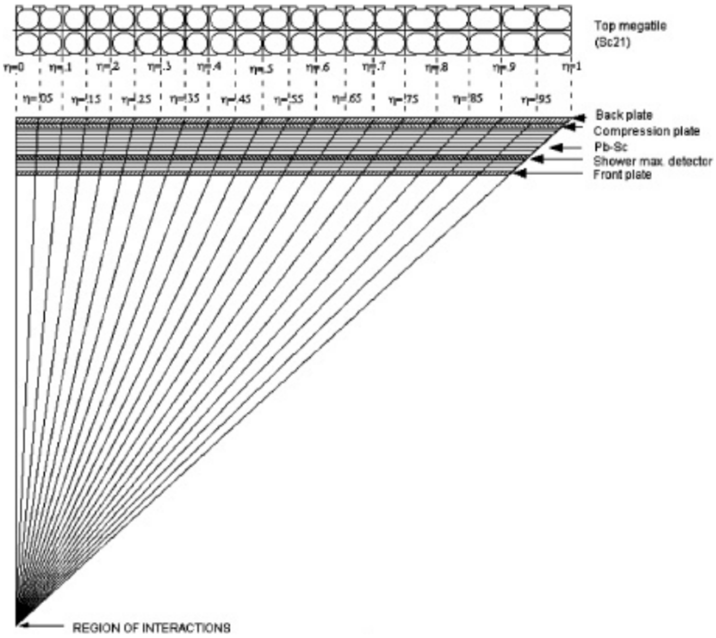

Figure 4.8: Side view of one module of the STAR BEMC, showing the projective nature of the towers. Taken from [164].

and the resolution of the V_z^{VPD} is around 1 cm. The VPD is also used as a minimum-bias trigger for Au+Au collisions, selecting multiple classes of events based on the vertex position. For more technical details on the VPD and its performance see [165].

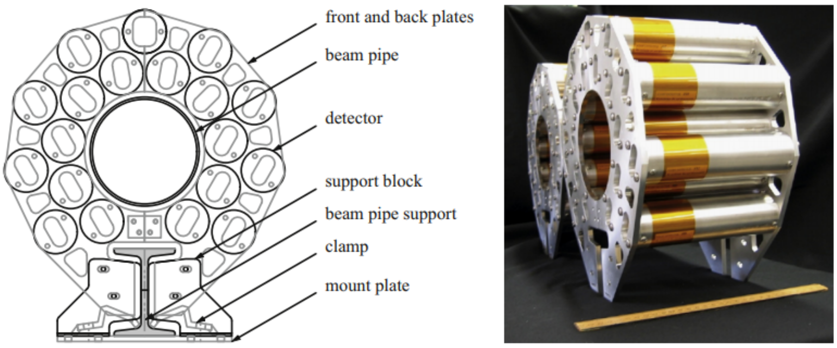

Figure 4.9: Cross-sectional view of one VPD assembly (left) and a photo of the VPD assemblies with a one-foot ruler shown for comparison (right). Taken from [165].

4.2.4 BBC

The Beam-Beam Counter (BBC, [166]) at STAR is a set of hexagonal scintillator tiles located near the beampipe in the pole tips of the STAR magnet. There are 18 small inner tiles and 18 larger outer tiles at both east and west sides of the BBC. Figure 4.10 contains a schematic view of the BBC setup.

The BBC detects forward-going charged particles and can be used to measure event activity[7], which is proportional to the detected signal. The BBC also serves as a minimum bias trigger in p+p collisions, where a coincidence between the east and west parts of the BBC is required. The BBC beam crossing rate can also be used to determine the luminosity of RHIC.

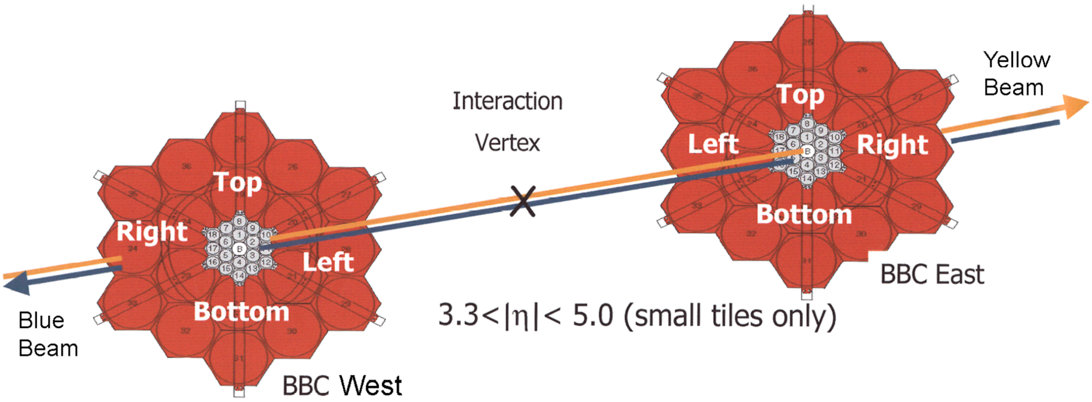

Figure 4.10: Schematic view of the BBC setup, Red tiles are the outer part and white tiles are the inner part. Taken from [166].

4.2.5 Other Detectors

There were additional detectors at STAR in 2014, but since they are not used in the analysis presented as a part of this thesis, their description will be limited. The Zero Degree Calorimeter (ZDC, [167]) system consists of two calorimeters around 20 m away from the STAR center covering a near-zero angle around the beampipe and focuses on measuring the energy of the neutral fragments released during the Au+Au collisions. The ZDC can be used as a minimum-bias trigger, provides basic event classification and its coincidence rate is used to determine the luminosity of the collisions at RHIC.

The Time-of-Flight detector (TOF, [168]) was fully installed in 2010, snadwiched between the TPC and the BEMC. It improves particle identification at high momentum by detecting charged particles in multi-gap resistive plate chambers.

The Heavy Flavor Tracker (HFT, [169]) was installed between 2014-2016. It was a 4-layer silicon detector with excellent spatial resolution which enabled the reconstruction of the secondary vertices coming from decays of open-charmed particles.

The Muon Telescope Detector (MTD, [170]) was installed in 2014 as the outermost layer of the STAR detector, outside the magnet. As its name suggests, its main objective is the detection of muons, which are the only charged particles which can pass through the dense BEMC and magnet layers. This detector enables precise measurements of quarkonium production.

The Endcap Electromagnetic Calorimeter (EEMC, [171]) is installed at the western tip of the STAR magnet and is used in a similar way as the BEMC for forward-going particles. The Shower Maximum Detectors (BSMD, ESMD) are integrated within both calorimeter systems and are used for the discrimination between γ and π^0.

---

[7] Event activity is a concept similar to centrality in smaller systems.

4.2.6 Current Status

The STAR experiment has received multiple upgrades since 2014, with most upgrades allowing STAR to perform measurements in the forward region. The Event Plane Detector (EPD, [172]) was installed in 2018 as the replacement of the BBC and allows precise determination of the event plane of heavy-ion collisions, crucial for the anisotropic flow measurements. The GMT detector, based on the Gas Electron Multiplier (GEM) technology was added to improve the corrections and calibrations of the TPC tracking [173]. The STAR TPC has received an upgrade of the inner sectors which extend its acceptance to $|\eta| < 1.7$. This upgrade is called the inner TPC (iTPC, [174]) and became fully operational in 2019. The Forward Tracking System (FTS) was installed in 2021 and consists of two detectors, the Forward Silicon Tracker (FST) and the small-strip Thin Gas Chamber (sTGC) which together provide excellent tracking in the forward region, necessary for precise spin physics [175]. Together with the FTS, a Forward Calorimeter System (FCS, [176]), consisting of both electromagnetic and hadronic calorimeters, covering the pseudorapidity range $2.5 < \eta < 4.5$, was installed to detect highly energetic particles in the forward region. STAR is also testing an endcap Time Of Flight (eTOF) module, which will be used at the future Compressed Baryonic Matter (CBM) experiment at the Facility for Antiproton and Ion Research (FAIR) in Darmstadt (Germany), to help with particle identification in the forward region [177].

4.3 Future of High Energy Physics at BNL

BNL has been the home of high energy physics experiments since 1952 when the Cosmotron became the first accelerator to achieve energies above 1 GeV. The AGS was also the highest-energy accelerator in the world, when it became operational in 1960. In 2000, RHIC became the world's premier heavy-ion accelerator and the only accelerator capable of colliding polarized protons. The BES-II phase of RHIC program was successfully completed in 2022 and the year 2023 was again dedicated to top-energy Au+Au collisions and sPHENIX commissioning. The STAR and sPHENIX experiments will continue taking data until 2025. The main focus will be as usual on Au+Au collisions at $\sqrt{s_{\mathrm{NN}}} = 200$ GeV to study the QGP and p+p collisions at the same energy to provide baseline measurements. Assuming the success of these two programs, a p+Au program lasting several weeks is expected in 2024. Despite the limited time, thanks to the luminosity upgrades to RHIC and the detectors, these three years will yield more data than the previous two decades combined, assuring productive science by both collaborations for the near future. After the RHIC shuts down in 2025, the preparations for the Electron-Ion Collider (EIC, [178]) will begin immediately. It will be the first collider of its kind and will provide unprecedented insight into the structure of the atoms. The electron-Proton/Ion Collider (ePIC) collaboration [179] is currently being established (via the merger of the proposed ECCE and ATHENA proto-collaborations) in order to build the first detector at the interaction point where STAR is currently situated, with a second detector being a possibility in case of sufficient funds.

Chapter 5

Analysis of Inclusive Jet Production in Au+Au Collisions

This chapter describes the analysis of inclusive jet production in central and peripheral Au+Au collisions at $\sqrt{s_{\mathrm{NN}}} = 200$ GeV. The first Section 5.1 introduces the analyzed dataset, including the event selection process. Section 5.2 describes the jet reconstruction process. The following Sec. 5.3 contains the steps taken in order to correct the jet yield for the effects of the large and fluctuating background effects. The next Sec. 5.4 focuses specifically on the correction technique known as unfolding, widely used in jet measurements to account for the residual background and instrumental effects. The Sec. 5.5 discusses the various contributions to the total systematic uncertainty of the measurements. The following Sec. 5.6 presents the validation of the correction techniques and the final Sec. 5.8 discusses the bias imposed by the online event selection. The physics results are presented and discussed separately in Chapter 6. This analysis follows the same overall strategy as the analysis of inclusive charged-particle jets [131, 180] while the inclusion of the BEMC information presents major additional challenges and opportunities. Unless stated otherwise, all steps in the analysis were performed individually by the author.

5.1 Dataset

The STAR experiment recorded a high-quality and large-statistics dataset of Au+Au collisions at $\sqrt{s_{\mathrm{NN}}} = 200$ GeV during the RHIC Run 14 period. The dataset is stored in the picoDst format, which is the smallest centrally-produced data file format, the final step in the STAR data production chain. The STAR data production is run in 3 steps, the first is the raw data file production where the signal from the detectors is fully digitized. The MuDst files, which contain ROOT [181] trees with information from the detector subsystems, are then produced with specific version of the STAR software. The MuDst files are finally converted into the picoDst files, again using a specific set of libraries, compressing and reducing the stored information in order to save disk space and speed up the data-reading process. The used data files were produced in the P18ih production series with the SL20d picoDst reproduction, which fixed the matching of TPC tracks to the BEMC towers (such matching is crucial for this analysis). The HFT, a major upgrade for this Run, was not included in the tracking during this production, since these data files were produced specifically for jet analyses[1]. Since the ultimate goal of the analysis is to experimentally

---

[1] Jets are produced in the primary vertex from the initial parton scattering, so the spatial resolution provided by the HFT is not needed and including it would only lower the tracking efficiency. In addition, HFT tracking is not very well described

observe the effects of the QGP on inclusive jet production, the central (0–10%) and peripheral (60-80%) collisions are studied separately. The centrality is determined as described in Sec. 2.2, using the reference multiplicity distribution of tracks reconstructed by the TPC within $|\eta| < 0.5$, corrected for the VPD inefficiency, the $z-$position of the PV and for the beam luminosity. The VPD inefficiency is corrected for by a centrality-dependent weight factor which is $\simeq 1$ in central collisions and up to 2.5–3 in peripheral collisions. The dataset is divided into four classes of beam luminosity (pre-split early runs, low, mid and high), as determined by the ZDC crossing rate. The high-luminosity part of the dataset was not considered because of the missing centrality definition.

5.1.1 Bad Run Selection

During each Run, when the RHIC beams are stable and the STAR detector is ready for data taking, the data are being collected in ~30 min periods called runs. When some problems occur during individual runs, the run is marked as bad either online by the Shift Leader[2] – usually when one or more detector subsystems malfunctions are noticed – or later during the offline Quality Assurance (QA) study. The offline QA is done by an individual analyzer and is specific for each dataset. The offline QA checks the run-by-run distributions of variables which should be independent of the specific run and significant deviations from the mean values signal a bad run, which is then excluded from the analysis. These distributions include the number of recorded events, the PV position V_z and $V_r = \sqrt{V_x^2 + V_y^2}$, the ZDC coincidence rate, the reference multiplicity, the mean track p_{T} and the BEMC tower firing rate[3]. In total, 360 runs were excluded, amounting to around 13 % of all runs and 8 % of all events. The bad run list for this analysis has been provided by the Physics Working Group (PWG) which focuses on hard probes. The bad run IDs are listed in App. A.

5.1.2 Online Event Selection

Events are selected online using the High Tower (HT) trigger, which requires a large energy deposit recorded by at least one BEMC tower, combined with a standard minimum-bias trigger. Specifically, the HT2*VPDMB30 trigger (IDs 450202 and 450212) configuration was used. The HT2 trigger is fired when the read-out of a tower records a signal higher than a certain value. However, each tower has a specific noise energy (called pedestal), which needs to be taken into account. The precise energy threshold of this trigger is therefore tower-dependent, but generally $E_{\mathrm{trig}} \approx 4.2$ GeV. In addition, the PV position is required to lie within 30 cm from the center of STAR along the beampipe as measured by the VPD detector. This trigger preferentially selects central events with hard processes, such as jet production. Due to the nature of the STAR BEMC, which is an electromagnetic calorimeter, most trigger particles are either direct photons or neutral pions (which decay into photon pairs). The total recorded integrated luminosity of this trigger is 5.2 nb^{-1}.

5.1.3 Offline Event Selection

Event selection is further carried out offline with selection criteria (cuts) requiring the PV as reconstructed by the TPC to lie within 30 cm of the TPC center along the z axis ($|V_z| < 30$ cm) and within 2 cm in the radial direction ($V_r < 2$ cm) assuring that the central detectors will have sufficient coverage of the particles produced in the particular event. To exclude pile-up events, an agreement between the

---

within the STAR simulation software, causing additional difficulties.

[2] The Shift Leader is the person in charge of operations in the STAR control room during usual data-taking periods.

[3] The tower activity criterion is specific for full jet analyses, and is discussed in Subsec. 5.2.2 in more detail.

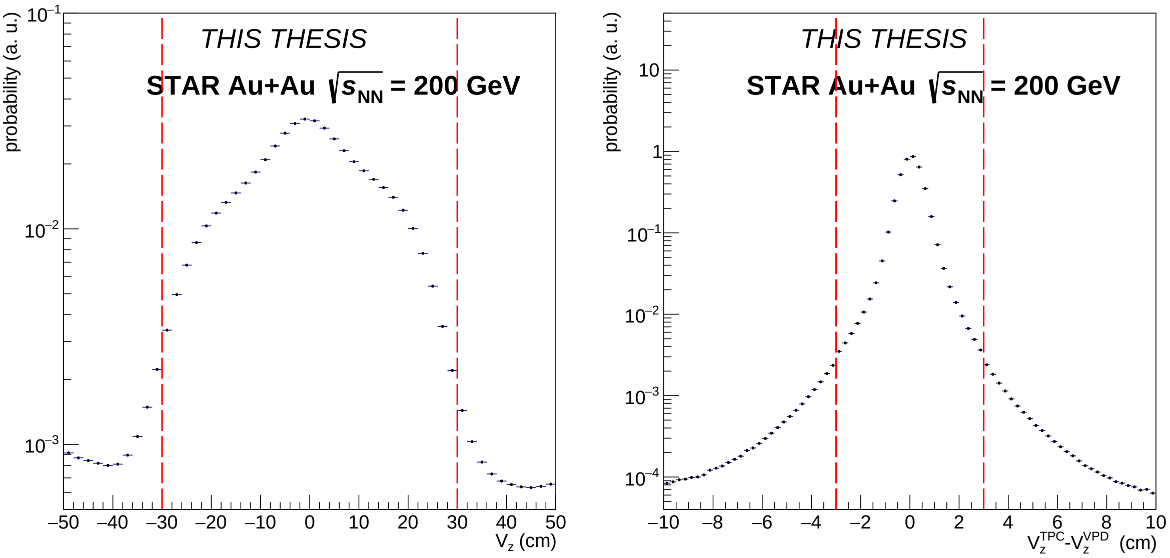

Figure 5.1: Probability distributions of the PV position along the z axis V_z (left) and the difference in the position reconstructed by the TPC and the VPD $V_z - V_z^{VPD}$ (right). The red dashed lines represent the cut values and events which lie in between these lines were accepted.

PV position (as reconstructed separately by the TPC and VPD detectors) is required, $|V_z - V_z^{VPD}| < 3$ cm. The V_z and $V_z - V_z^{VPD}$ distributions can be seen in Fig. 5.1.

Figure 5.2 shows the cummulative effect of event selection criteria on the total number of events. It is clear that the run and trigger selections are the major contributions. In total, 14 046 975 central and 733 496 peripheral events were accepted for the analysis.

5.2 Jet Reconstruction

Jets are reconstructed from both charged-particle tracks reconstructed by the TPC and the energy deposited in the BEMC towers. The selection procedures are described in Subsec. 5.2.1 and 5.2.2, respectively. In order to avoid double-counting of the charged-particle energy, a technique called the hadronic correction, described in Subsec. 5.2.3, is employed. The particles are clustered together using the anti-k_T algorithm, as implemented in the FastJet package (version 3.3.0) [118], with the standard energy recombination scheme and the reconstruction parameter $R = 0.2,\ 0.3$ and 0.4. The algorithm is described in Sec. 3.4. As discussed in Sec. 3.1, the jets reconstructed by FastJet contain a mixture of real products of QCD fragmentation and combinatorial background. The techniques used to correct the obtained jet yield are described in Sec. 5.3 and Sec. 5.4.

5.2.1 Track Selection

The charged part of the jet energy is recovered from primary tracks [4]. The primary tracks are accepted if they fullfill the following criteria:

- Number of fit points $N_{\mathrm{fit}} > 14$, to provide tracks with sufficient quality. The distribution of N_{fit} of accepted tracks can be seen in the left panel of Fig. 5.3.

---

[4] As defined in Subsec. 4.2.1.

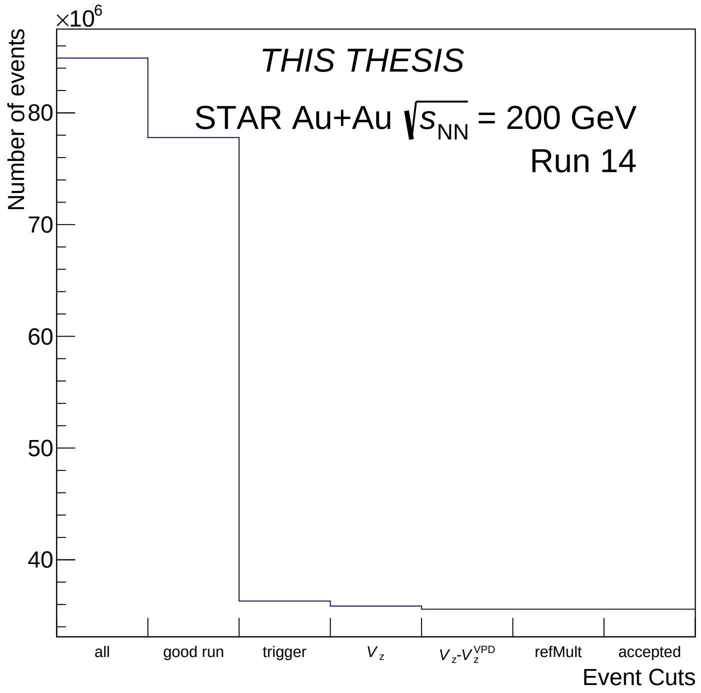

Figure 5.2: The cummulative effect of different cuts on the total number of accepted events from Run 14 Au+Au collisions at $\sqrt{s_{\rm NN}} = 200$ GeV.

- Ratio of the numbers of fit points and the maximum number of fit points $N_{\rm fit}/N_{\rm fit}^{\rm max} > 0.52$, in order to avoid tracks which have split into multiple sub-tracks.
- The distance of closest approach (DCA) of the track to the PV $DCA < 1$ cm, to assure that the track originates from the center of the collision and not from a decay or pile-up. The DCA distribution of accepted tracks can be seen in the right panel of Fig. 5.3.
- Track pseudorapidity $|\eta_{\rm trk}| < 1$, to make sure that the track is within the full TPC acceptance. The η–ϕ distribution of accepted charged-particle tracks is shown in the left panel of Fig. 5.4.
- Track transverse momentum $0.2 < p_{\rm T,trk} < 30.0$ GeV/c. Tracks of transverse momentum lower than 200 MeV/c curve too much in the magnetic field and they do not generate enough signal in the TPC. Tracks with transverse momentum higher than 30 GeV/c are essentially straight lines which makes precise measurement of their momentum impossible. Since the presence of such tracks can disrupt tracking in general, whole events are discarded if they contain tracks with $p_{\rm T,trk} > 30$ GeV/c. However, these tracks are extremely rare at RHIC energies. The charged track $p_{\rm T}$ spectrum can be seen in the left panel of Fig. 5.5.

There is no PID involved in the analysis and the tracks are inserted into the jet finder using massless approximation.

5.2.2 Tower Selection

The neutral part of the jet energy is recovered from BEMC towers. The key difference between towers and tracks is that while tracks correspond to individual particles, whose position changes event

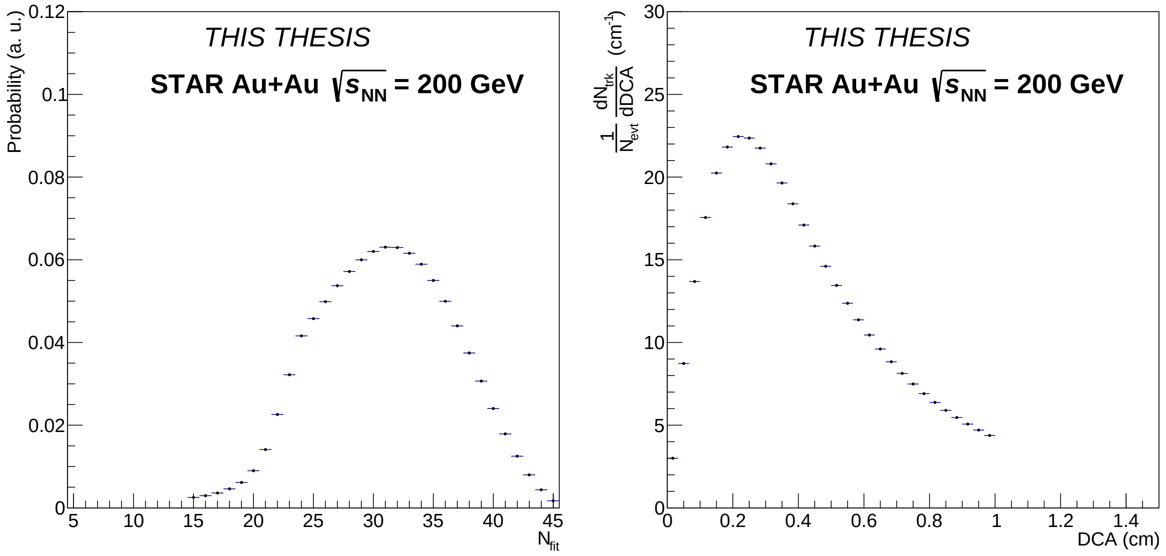

Figure 5.3: Distribution of the number of fit points N_{fit} (left) and the track DCA (right).

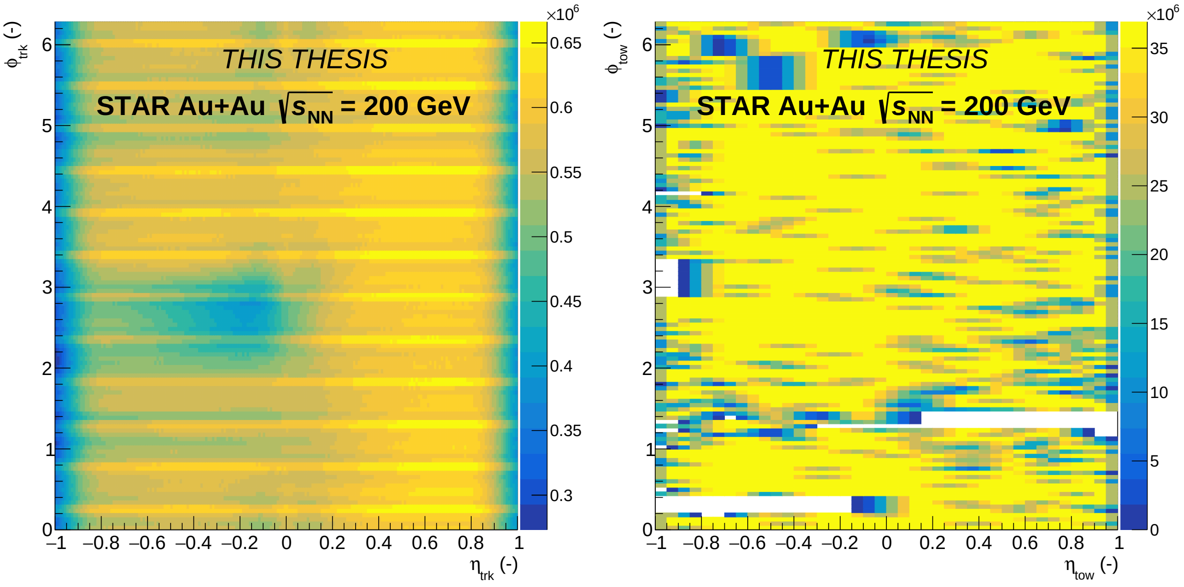

Figure 5.4: Spatial η–ϕ distribution of accepted charged-particle tracks (left) and towers (right).

by event, the towers are always located at the same place within the detector and detect energy from all particles which pass through the tower sensitive volume. Some towers of the BEMC do not record signal at all or at a low rate and are considered dead, while some towers are firing at an exceptional rate and these are considered hot. Additionally, some towers are not mapped correctly due to both software and hardware errors which have accumulated over the many years of the detector lifetime. All such cases of irregular tower behavior are excluded from the analysis on a tower-by-tower basis. If the number of such towers in a specific run was exceedingly high, all events from this run were excluded from the dataset.

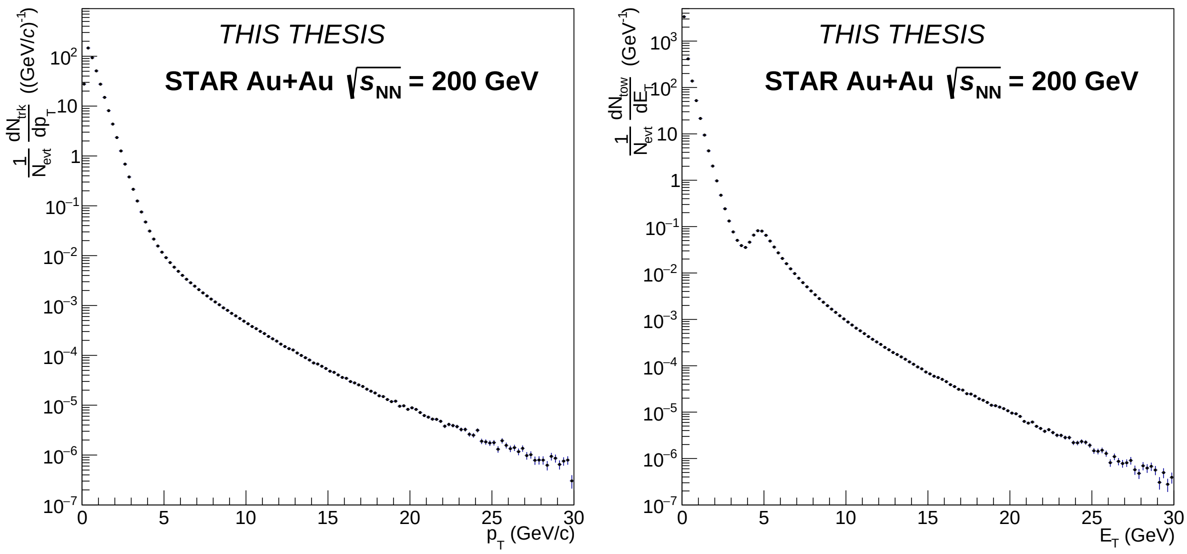

Figure 5.5: Charged-particle track p_{T} spectrum (left) and BEMC tower E_{T} spectrum after hadronic correction (right).

Therefore, the definition of a bad tower is mutually dependent on the definition of a bad run. One can consider two cases – the loose bad tower selection, resulting in more holes in the BEMC coverage, but preserving more runs and therefore higher statistics; or the tight bad tower selection, which preserves a more complete coverage of the BEMC at the cost of reduced statistics. For this analysis, the loose bad tower selection is used, permanently removing 822 towers from the analysis, resulting in lowering the BEMC coverage by around 17 %[5]. This choice was made in order to preserve the high statistics of the recorded dataset, and also because the effect of missing towers is somewhat mitigated by the fact that jets are generally objects with size exceeding the size of a single tower (0.05×0.05 in η–ϕ). The list of removed towers was provided by the Hard Probes PWG and can be found in App. B. Since the BEMC towers are projective to the nominal center of the STAR experiment, the η of the towers needs to be recalculated event-by-event to take into account the displacement of the PV along the z axis. The spatial distribution of towers in the η–ϕ space is shown in the right panel of Fig. 5.4, clearly showing the holes in the BEMC coverage and the smearing caused by the η correction.

5.2.3 Hadronic Correction

The BEMC towers record energy from all particles entering it, both charged and neutral. However, the BEMC does not offer full calorimetric capabilities and the towers therefore do not contain the full energy of some particles and one cannot use only the BEMC towers for jet reconstruction. Furthermore, the momentum resolution of charged particles is much more precise in the TPC for vast majority of the particles. On the other hand, the simple addition of track and tower energy would result in double–counting some of the charged-particle energy. The natural solution to this problem is to project the TPC tracks to the BEMC, and subtract a fraction f of the sum of tracks momentum from each BEMC tower a with matched global tracks,

---

[5] For comparison, the tight bad tower selection would result in 433 bad towers, or 9 %.

$$E^{\rm corr}_{{\rm tow},a} = E_{{\rm tow},a} - f \cdot \sum_{\rm trk} p_{{\rm trk},a}. \tag{5.1}$$

In case of $E^{\rm corr}_{{\rm tow},a} < 0$, we set $E^{\rm corr}_{{\rm tow},a} = 0$ and discard this unphysical object from the analysis. The parameter f represents the assumed fraction of momentum which the charged particles leave in the BEMC. Since the value of f is unknown, we set $f = 1$ in this analysis, a 100% hadronic correction, and a variation of this parameter is used to estimate the systematic uncertainty of the measurement. The graphic in Fig. 5.6 illustrates this technique.

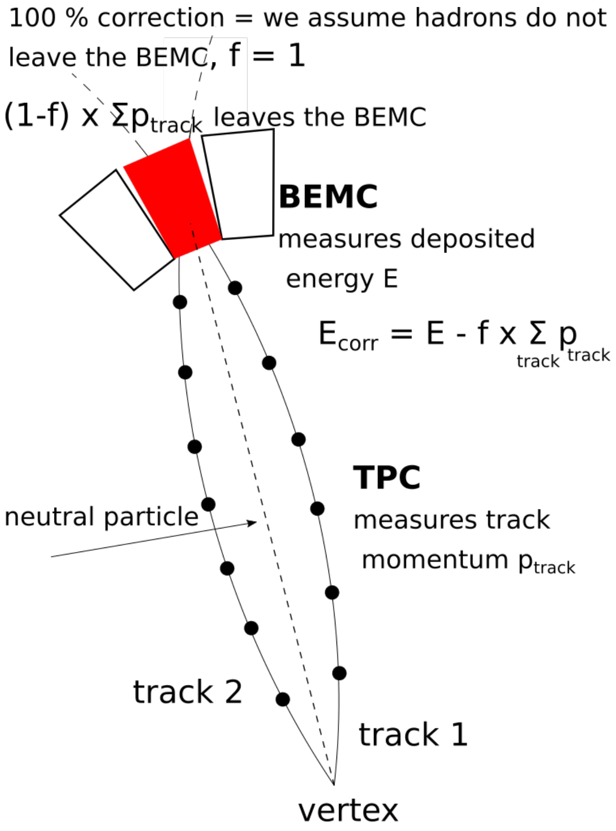

Figure 5.6: Illustration of the hadronic correction technique. Two TPC tracks (hadrons) and one neutral particle from the primary vertex enter one BEMC tower. Hadrons deposit a part (we assume 100 %) of their energy in the tower. The momentum of the tracks is then subtracted from the tower energy.

An extensive data-driven study of the hadron energy deposition in the BEMC has been conducted. In order to study the dependence on the calorimeter cell size, we consider three cases of BEMC clustering – single tower (no clustering), 2×2 purely geometrical clustering (using BEMC with decreased granularity) and 3 × 3 physical clustering around a high-energy seed tower. The study then defines the value $R_{\rm corr}$, which measures how much energy does a hadron deposit inside the BEMC, defined as:

$$R_{\rm corr} = \frac{E_{\rm tow/cl} - E^{\rm corr}_{\rm tow/cl}}{\sum p_{\rm trk}}, \tag{5.2}$$

where the denominator is equal to the sum of momentum of all tracks matched to the tower or cluster in question. The probability distributions of R_{corr} in sparse events[6] can be seen in Fig. 5.7 for two cases – one is $\sum p_{\mathrm{trk}} < 1$ GeV/c and the other for $4 < \sum p_{\mathrm{trk}} < 5$ GeV/c. The truncation near $R_{\mathrm{corr}} = 1$ corresponds to the case of hadrons depositing their entire energy inside the BEMC. It can be seen that the clustering has significant effect on the distributions and also that the 3×3 clustering leads to a larger fraction of hadron energy being deposited.

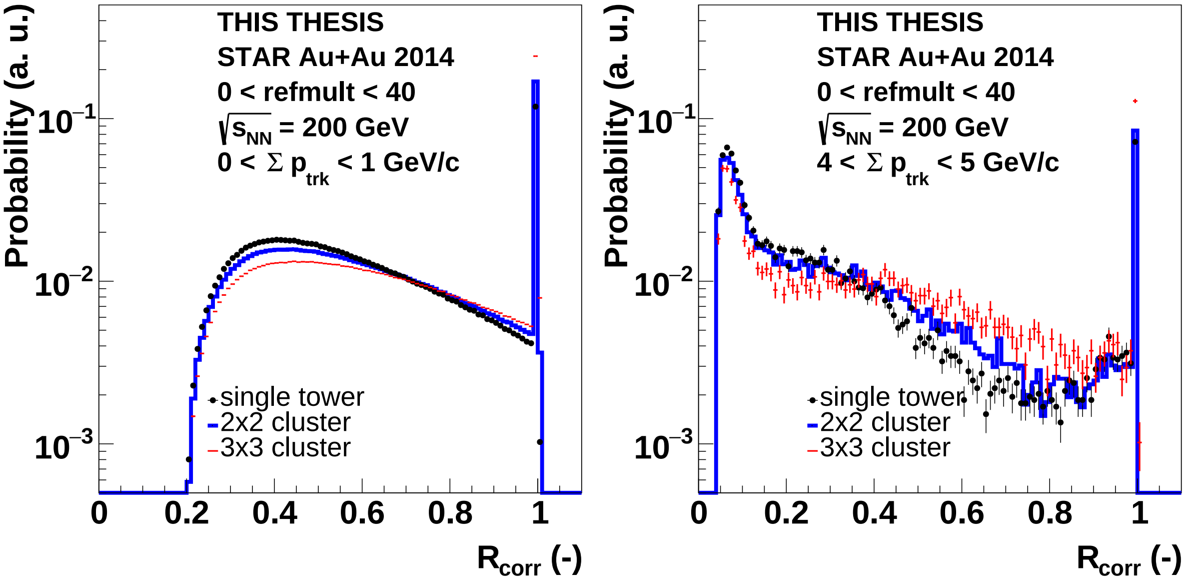

Figure 5.7: Probability distribution of the R_{corr} variable in sparse Au+Au events at $\sqrt{s_{\mathrm{NN}}} = 200$ GeV for $\sum p_{\mathrm{trk}} < 1$ GeV/c (left) and $4 < \sum p_{\mathrm{trk}} < 5$ GeV/c (right). The black points represent distribution for no clustering, the blue line for 2×2 geometrical clustering and the red points represent distribution for 3×3 physical clusters.

It would seem intuitive to only subtract the momentum of the tracks used for jet finding. However, the BEMC records energy of all particles, including secondary tracks and low-quality primary tracks. Since the track selection criteria are rather loose (except for the DCA cut), the contribution of low-quality tracks is not expected to be significant, since these tracks usually carry low momentum and do not reach the calorimeter. The contribution of global tracks, that do not originate from the PV, to the cluster energy needs to be estimated. In the top panel of Fig. 5.8, one can see the distribution of the difference between the sum of global and primary track momenta deposited in the same cluster $\delta \sum p = \sum p_{\mathrm{glob}} - \sum p_{\mathrm{prim}}$. The distribution has a very sharp peak around the central value of 0 GeV/c (all matched tracks are primary). The tail observed for $\delta \sum p \gtrsim 0.2$ GeV/c arises from the contribution of secondary tracks and its contribution can be seen in the bottom panel of Fig. 5.8, which represents the cumulative distribution. It can be seen that with a 90 % confidence level, the undersubtraction of the track momenta from the BEMC is less than 0.7 GeV/c and is less than 0.4 GeV/c within 68 % confidence level. We did not observe large dependence of $\delta \sum p$ on the total energy deposited in the cluster.

The undersubtraction effect is, however, not negligible and therefore global tracks are used for the hadronic correction. In order to suppress the contribution of fake and pile-up tracks, the same track quality criteria as for the main analysis track selection (Sub. 5.2.1) are chosen, with the exception of DCA

---

[6] Events with reference multiplicity < 40, roughly corresponding to the 60–80% centrality bin. This minimizes the effects of the π^0-decay photons pile-up.

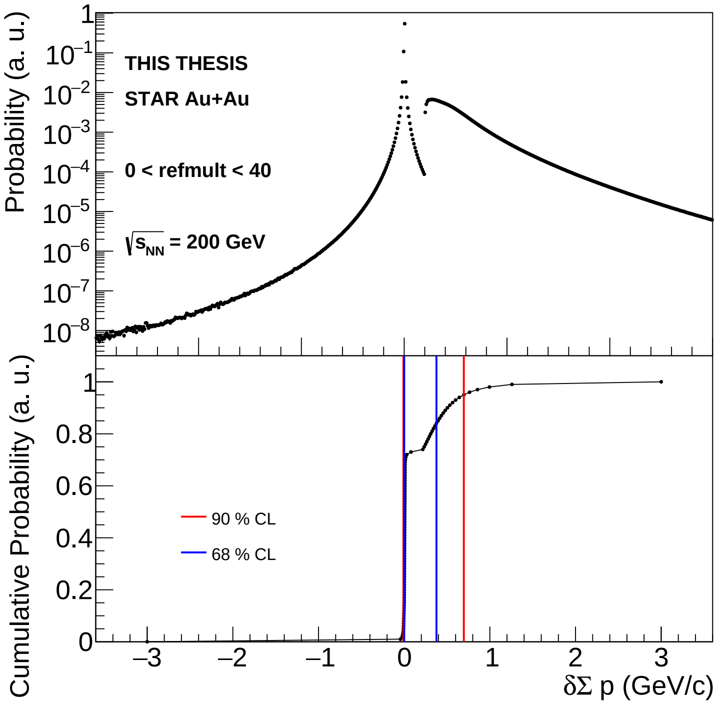

Figure 5.8: Distribution of the difference between the sum of global and primary track momenta deposited in the same cluster $\delta\Sigma p$ (top) and its cumulative distribution (bottom). The solid lines represent the 90% (red) and 68% (blue) confidence levels around the central value.

to primary vertex. For these global tracks, we choose to cut only on DCA in the $z-$direction, motivated by the pile-up rejection. This is demonstrated in Fig. 5.9, which compares the DCA_z distribution in case of low and high beam luminosity. It can be seen that the two distributions overlap in the central region, while the tails are more significant in the high-luminosity case, showing the effect of pile-up. The distributions start to significantly deviate at around 3 cm and that is the value chosen for the DCA_z cut.

Based on this study, the physical clusters seem like the best input to the jet finder, since the hadronic correction is more precise than when using smaller calorimetrical objects. However, the spectrum of clusters, especially in central collisions, is very much different from the spectrum of individual particles (tracks), mainly due to the pile-up from neutral particles. The comparison of transverse energy E_T, where $E_\mathrm{T} = E^{\mathrm{corr}}_{\mathrm{tow/cl}} / \cosh(\eta_{\mathrm{tow/cl}})$, spectra for individual towers and clusters can be seen in Fig. 5.10 along with the p_T spectra of global tracks in central and peripheral collisions. Therefore, individual towers were chosen for the analysis, since they have better correspondence to individual particles, essential for later stages of the analysis (Subsec. 5.3.4).

Towers are accepted for the analysis if they fulfill the following condition after the hadronic correction: $0.2\ \mathrm{GeV} < E_\mathrm{T} < 30.0\ \mathrm{GeV}$, and were combined with charged-particle tracks as an input to the jet finding algorithm. The lower limit is chosen to eliminate noise towers and the upper limit is motivated mainly for the consistency with the track selection, because the BEMC energy resolution is naturally good for high-energy particles. The transverse energy spectrum of towers after the hadronic correction can be seen in the right panel of Fig. 5.5. Overall, the spectrum of towers is softer than the spectrum of tracks, which is caused by the fact that the towers are not able to contain the entire energy of most

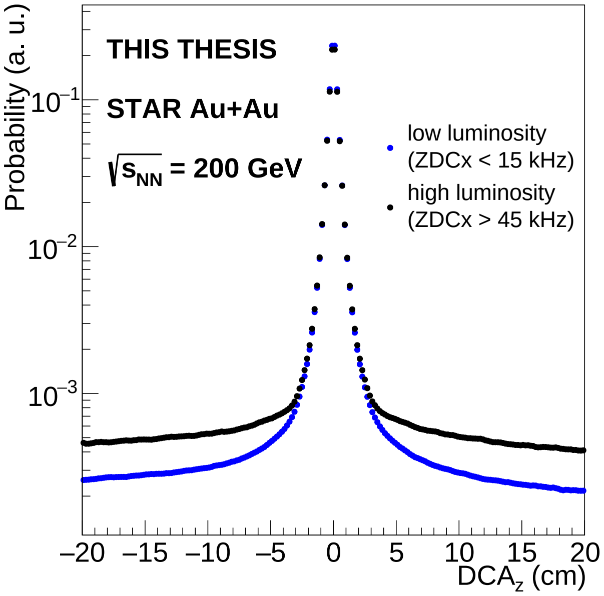

Figure 5.9: Distribution of global track DCA to the primary vertex in the z–direction DCA_z for low (blue) and high (black) luminosity classes.

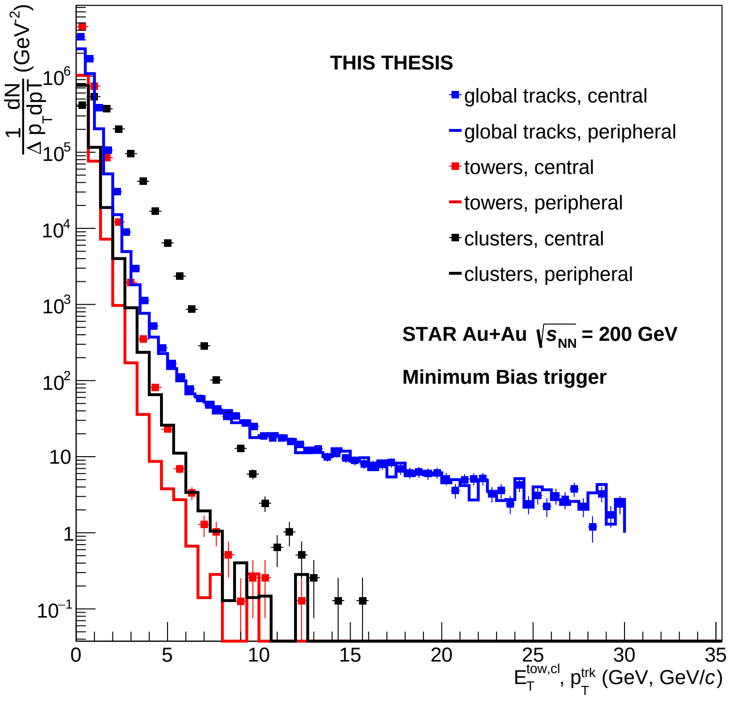

Figure 5.10: Transverse energy E_T spectra of towers (red) and 3 × 3 physical clusters (black) and transverse momentum p_T spectra of global tracks (blue) in central (markers) and peripheral (lines) minimum bias Au+Au collisions at $\sqrt{s_{NN}} = 200$ GeV.

particles. The spectrum features a significant peak around $E_\mathrm{T} \sim 5$ GeV which is a result of the trigger turn-on beyond the HT2 trigger threshold. The presence of the trigger towers brings up an interesting question. Whether or not require the jets to contain the trigger tower? This is an important decision, which will be further discussed in Sec. 5.8. At this point, both approaches are considered.

5.3 Corrections for Underlying Event Background

Objects obtained from the jet finder are referred to as jet candidates. Jet candidates were accepted if they are fully located within the fiducial acceptance of the STAR detector. The acceptance is dependent on the jet reconstruction parameter R and is set to $|\eta_\mathrm{jet}| < 1 - R$, where η_jet is the pseudorapidity of the jet axis. It is not possible to fully distinguish between real jets and combinatorial jets and also which jet constituents are the product of the initial hard-parton scattering and which are added by the jet-finding algorithm from the underlying event. Therefore, several correction techniques, described in this section, are employed in order to reduce the effects of the UE on the measured jet population.

5.3.1 Jet Area

The area of jet candidates can be calculated using a variety of methods. Three calculation methods were proposed by the FastJet authors [182], the active ghost method, the passive ghost method and the Voronoi area method. The active ghost area calculation method, which uniformly places many extremely soft particles – ghosts – to the event and adds them to the clustering, was chosen for the analysis. The area of a given jet is then proportional to the number of ghosts it contains. The presence of the ghosts (with $p_\mathrm{T} \sim 10^{-100}$ GeV/c) does not affect the jet reconstruction because of the IR safety of the anti-k_T algorithm. Jets reconstructed with a given value of R generally tend to have similar areas. Cuts on the jet area were applied to reject combinatorial jets which are more likely to have unreasonably small areas. The cuts are R–dependent:

$$\begin{aligned} R = 0.2 &\implies A > 0.07,\\ R = 0.3 &\implies A > 0.2, \\ R = 0.4 &\implies A > 0.4. \end{aligned} \tag{5.3}$$

The cut values were motivated by embedding studies [180], where simulated single-particle jets were embedded into real events and their area was reconstructed. The area distributions for jet candidates can be seen in the right panel of Fig. 5.12 for different values of R.

5.3.2 Median Background Density

While it has been established that it is nearly impossible to subtract the UE background on a jet-by-jet basis, the so-called median background density subtraction method is used on an event-by-event basis instead (as recommended by the FastJet authors). As the first step, the median background density ρ is calculated:

$$\rho = \mathrm{med}\left\{\frac{p^i_\mathrm{T,jet}}{A_i}\right\}, \tag{5.4}$$

where the index i runs over all jet candidates reconstructed in the event with the k_T algorithm and $R_{BG} = 0.3$. The k_T algorithm is used because of its sensitivity to soft particles which are mostly background. In order to avoid biasing the background density estimation by real jets, the hardest jet in peripheral collisions and two hardest jets in central collisions are removed from the calculation. The calculation of ρ slightly depends on R_{BG}. However, this dependence should be corrected for by the unfolding procedure. In order to take into account any residual effects, the value of the reconstruction parameter used for ρ calculation is subject to variation for the systematic uncertainty estimation. Figure 5.11 shows the dependence of ρ on event centrality, represented by the reference multiplicity (defined in 2.2). A strong positive correlation is observed, however, the smearing (mainly due to the neutral pile-up) is also rather large. This highlights one of the difficulties of this analysis – jets created in central collisions acquire additional energy of the order of tens GeV/c from the UE.

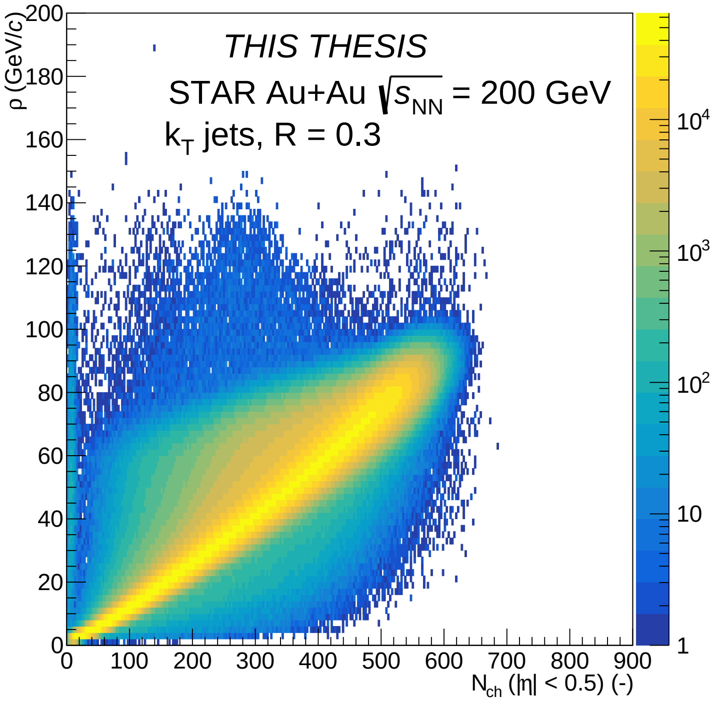

Figure 5.11: The median background density ρ as a function of event reference multiplicity N_{ch}, calculated from tracks reconstructed within $|\eta| < 0.5$. Jets were reconstructed using the k_{T} algorithm with $R = 0.3$ in Au+Au collisions at $\sqrt{s_{\mathrm{NN}}} = 200$ GeV.

Once ρ is estimated, it is then subtracted from the raw jet candidate transverse momentum $p_{\mathrm{T,jet}}^{\mathrm{raw}}$ via

$$p_{\mathrm{T,jet}}^{\mathrm{reco}} = p_{\mathrm{T,jet}}^{\mathrm{raw}} - \rho \cdot A, \tag{5.5}$$

where A is the jet area. The reconstructed jet transverse momentum $p_{\mathrm{T,jet}}^{\mathrm{reco}}$ distribution correlation with jet area can be seen in the left panel of Fig. 5.12. It can be seen that the jet area changes with increasing $p_{\mathrm{T,jet}}^{\mathrm{reco}}$ and the distribution is narrow in the high-p_{T} region. The area distribution is wider for jets reconstructed with larger R than smaller jets. It can be seen that certain jets acquire negative values of $p_{\mathrm{T,jet}}^{\mathrm{reco}}$. This might look surprising at first, but it can happen since ρ was shown to be large. The true jet p_{T} needs – of course – to be positive and this is taken into account. This feature is discussed later in the text.

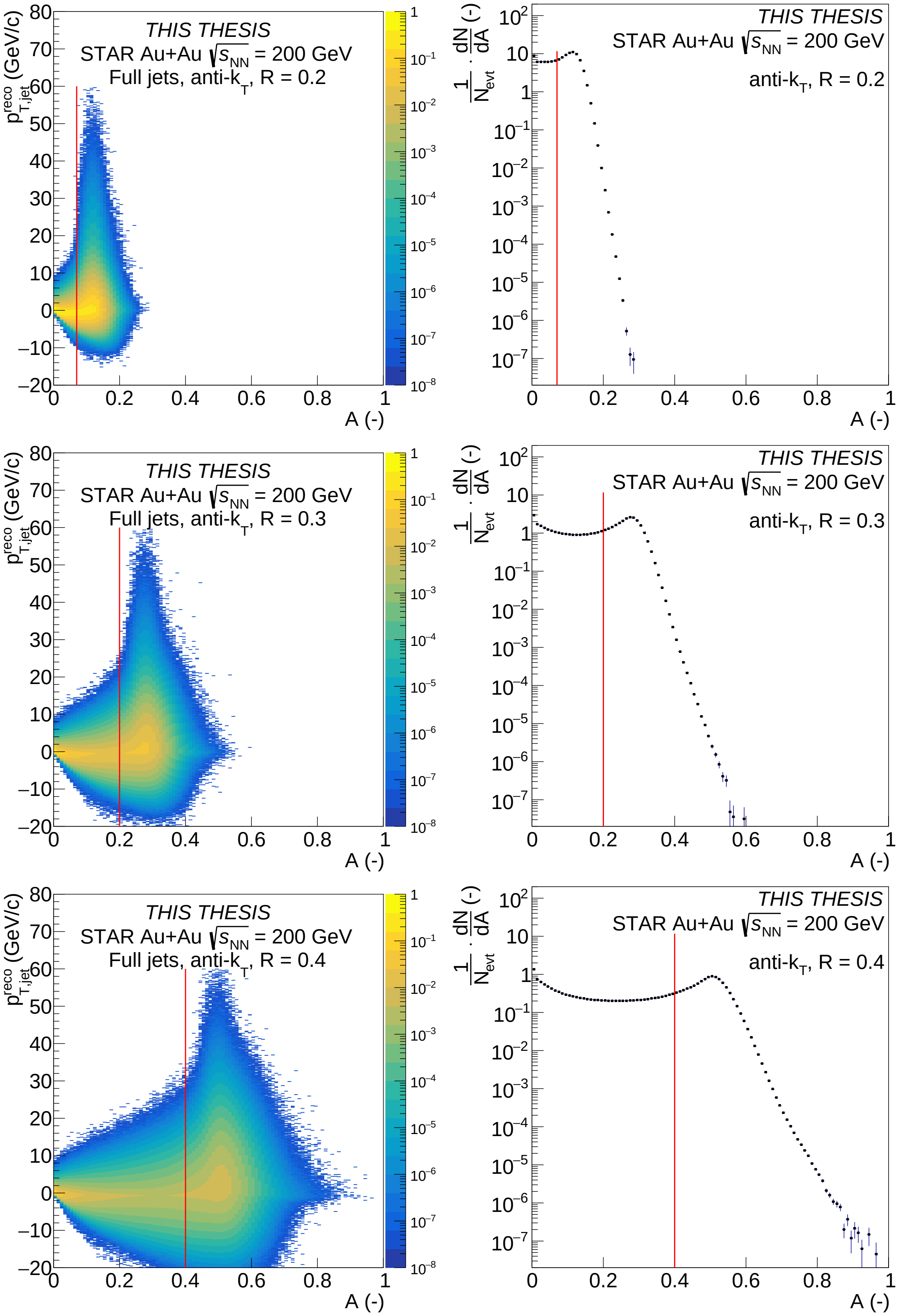

Figure 5.12: Jet area correlation with reconstructed jet transverse momentum $p_{\mathrm{T,jet}}^{\mathrm{reco}}$ (left) and jet area distributions (right) for jet candidates reconstructed with $R = 0.2$ (top), $R = 0.3$ (middle) and $R = 0.4$ (bottom). Red lines represent the cut values.

5.3.3 Jet Neutral Energy Fraction

Since QCD is largely indifferent to the charge of particles, one would expect jets to be composed from roughly 1/3 neutral particles and 2/3 charged particles. In a large jet sample, the energy fraction carried by neutral particles should also approach 1/3. Due to the inherent nature of the calorimeter to pick-up energy from background and π^0-decay photons (neutral pile-up), the jet neutral energy fraction NEF, defined as

$$\mathrm{NEF} = \frac{\sum_{\mathrm{tow}} E_{\mathrm{T,tow}}}{p_{\mathrm{T,jet}}^{\mathrm{raw}}}, \tag{5.6}$$

where the numerator takes into consideration all towers which are the constituents of the particular jet, is expected to rise. Additionally, the HT2 trigger preferentially selects events where a jet containing a hard neutral particle was created, further increasing the average NEF. This behavior can be seen in Fig. 5.13. In central collisions, the NEF peaks around 0.7 for all three values of R with larger jets having a sharper peak. In peripheral collisions, the distributions show less dependence on R and a very broad peak between NEF $\sim 0.3 - 0.5$, a significantly lower value than in the central collisions.

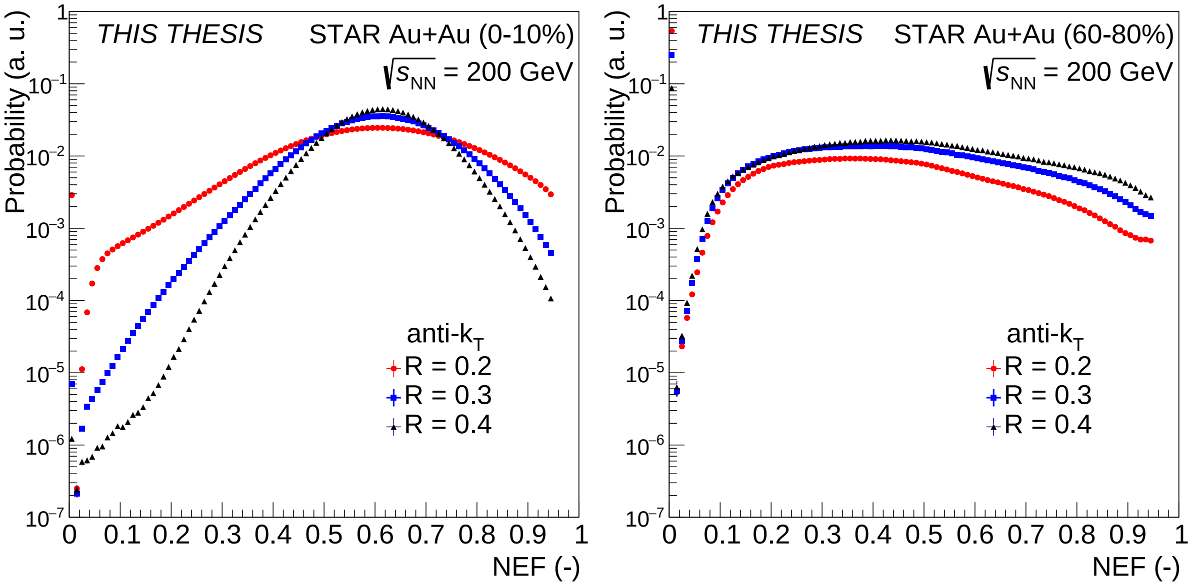

Figure 5.13: Jet neutral energy fraction of jets reconstructed with $R = 0.2$ (red circles), $R = 0.3$ (blue squares) and $R = 0.4$ (black triangles) in central (left) and peripheral (right) Au+Au collisions at $\sqrt{s_{\mathrm{NN}}} = 200$ GeV.

In order to avoid jets generated by the neutral pile-up, jets were accepted if NEF < 0.95. After these cuts, the jet $p_{\mathrm{T,jet}}^{\mathrm{reco}}$ spectra dependence on R can be seen in Fig. 5.14 in both central and peripheral collisions. The spectra in central collisions show a significant dependence on R, since the larger jets typically contain more background. It can also be seen that a large portion of the spectrum has negative p_{T} values. This is caused by the ρ calculation, which takes the median value of the background energy density. The situation in peripheral collisions is significantly simpler as the smearing due to the background presence is much smaller.

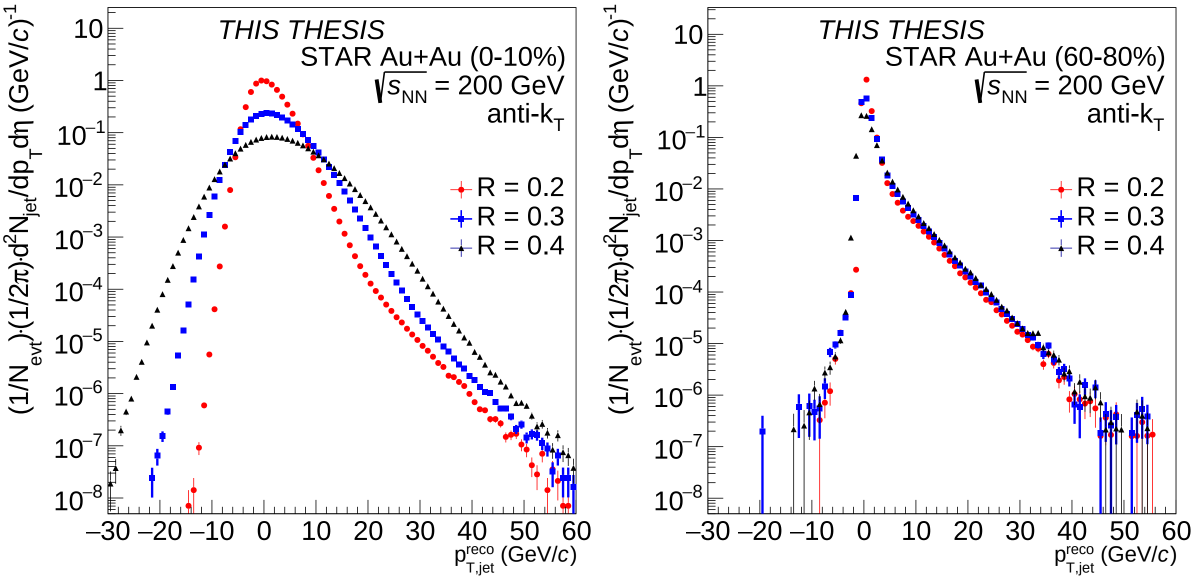

Figure 5.14: Reconstructed transverse momentum $p_{\mathrm{T,jet}}^{\mathrm{reco}}$ spectra of anti-k_{T} jets reconstructed with $R = 0.2$ (red circles), $R = 0.3$ (blue squares) and $R = 0.4$ (black triangles) in central (left) and peripheral (right) Au+Au collisions at $\sqrt{s_{\mathrm{NN}}} = 200$ GeV.

5.3.4 Leading Hadron Transverse Momentum

As discussed before, the reconstructed spectra contain a large population of combinatorial jets, especially in the soft part of the spectrum. Even the application of the area and NEF cuts is not sufficient to effectively suppress the background. Background could in principle be suppressed further by requiring a high-p_{T} cut on individual jet constituents. This requirement would, however, introduce a large bias into this measurement with regards to jet fragmentation and therefore would make the jet quenching studies extremely complicated. Therefore, a sort of middle–ground approach is employed. The cut is applied only on the transverse momentum of the most energetic (leading) jet constituent, $p_{\mathrm{T}}^{\mathrm{lead}}$. The leading particle can be either a track or a tower. This cut strongly suppresses the contribution of the soft combinatorial jets while still keeps a large portion of true jets containing mainly soft constituents, which are essential for the jet quenching studies. However, by imposing this requirement, the jet reconstruction can become collinearly unsafe and therefore the effects of the $p_{\mathrm{T}}^{\mathrm{lead}}$ cut have to be carefully estimated.

The jet distributions as a function of $p_{\mathrm{T,jet}}^{\mathrm{reco}}$ and $p_{\mathrm{T}}^{\mathrm{lead}}$ can be seen in Fig. 5.15 for different cases of R and collision centrality. The effect of the $p_{\mathrm{T}}^{\mathrm{lead}}$ cut is immediately observable as the suppression of the jet population (by orders of magnitude), especially in the low-$p_{\mathrm{T,jet}}^{\mathrm{reco}}$ region, while at high $p_{\mathrm{T,jet}}^{\mathrm{reco}}$, the distributions generally overlap. This means that most of the real jets are kept while the background is severely suppressed.

There is still some residual negative-$p_{\mathrm{T,jet}}^{\mathrm{reco}}$ population, especially for larger jets in central collisions. This region still contains valuable information about the true jet population which can be explored, and therefore it is kept in the analysis. This is in contrast with many jet analyses, which consider this population to be unphysical and discard it. The spectra in peripheral collisions contain a bump feature around mid-$p_{\mathrm{T,jet}}^{\mathrm{reco}}$ caused by the interplay between the trigger and the $p_{\mathrm{T}}^{\mathrm{lead}}$ cut. This feature is not visible in central collisions because it is masked by the large and fluctuating background. Overall, the plots in

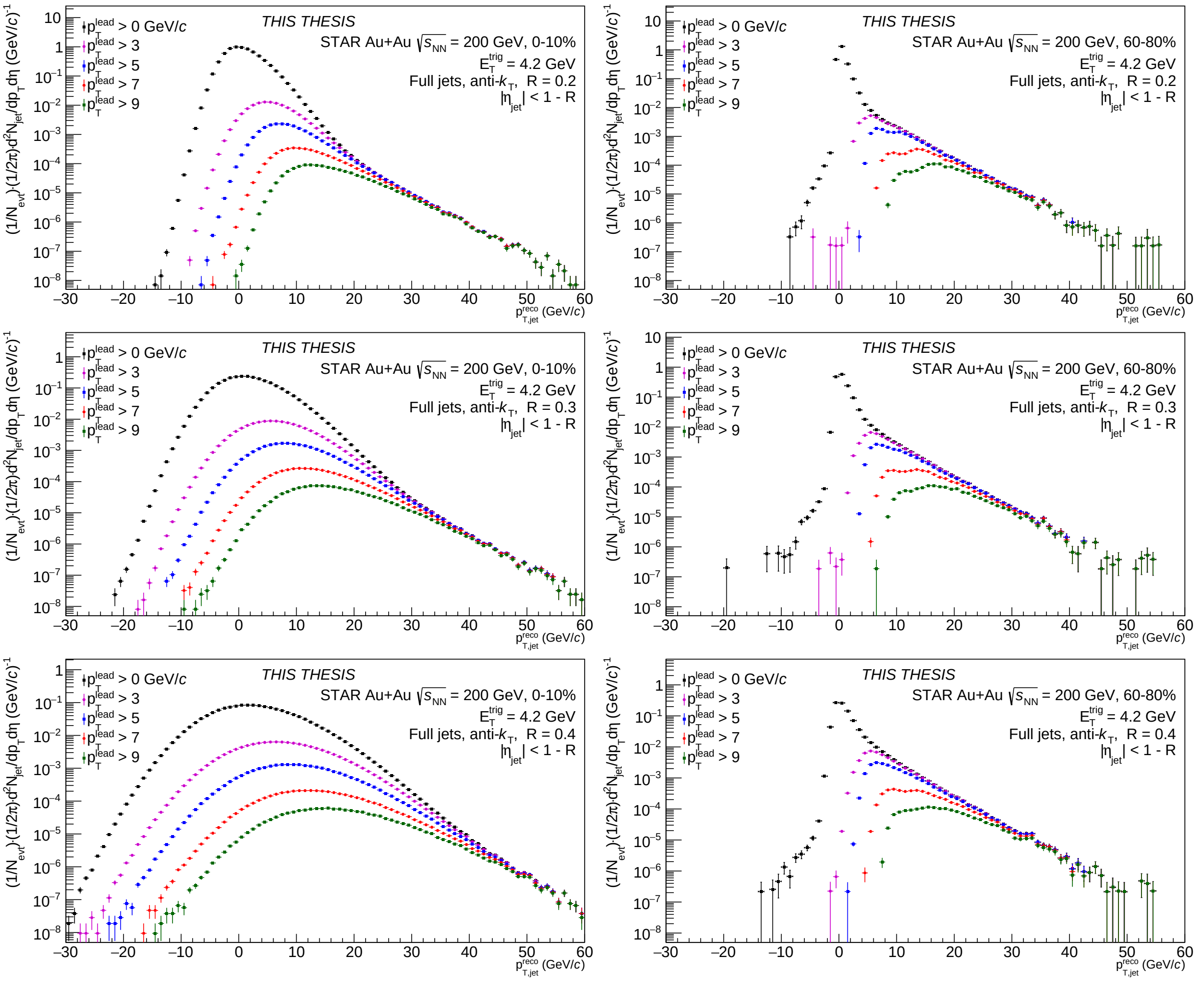

Figure 5.15: Reconstructed transverse momentum $p_{\mathrm{T,jet}}^{\mathrm{reco}}$ spectra of anti-k_{T} jets reconstructed with R = 0.2 (top), R = 0.3 (middle) and R = 0.4 (bottom) in central (left) and peripheral (right) Au+Au collisions at $\sqrt{s_{\mathrm{NN}}}$ = 200 GeV. Black markers represent the unbiased distribution ($p_{\mathrm{T}}^{\mathrm{lead}}$> 0 GeV/$c$), while other colors of markers represent different values of the $p_{\mathrm{T}}^{\mathrm{lead}}$ cut: 3 GeV/c (purple), 5 GeV/c (blue), 7 GeV/c (red) and 9 GeV/c (green). Error bars represent statistical uncertainties only.

this figure demonstrate both the very promising kinematic reach of this measurement and the challenges associated with obtaining it.

The spectra still need to be corrected for the residual background contributions, for instrumental effects and for the trigger bias before any physics conclusions can be made.

5.4 Corrections for Residual Background and Detector Effects

The previous section presented the correction procedures done on a jet-by-jet or event-by-event basis. It has also been established that these corrections are insufficient for removing the background effects fully and they do not take into account the detector effects, such as acceptance, efficiency, noise and non-linear response to signal. This section therefore focuses on the procedure which corrects for both detector effects and the residual background effects by modifying the jet spectra as a whole. Also, since jets are complex objects composed of many particles, a simple bin-by-bin reconstruction efficiency correction is infeasible due to the interplay of detector effects causing large count migration between bins.

Compared to the previous inclusive charged-particle jet analysis at STAR [131], this analysis takes advantage of the embedding technique, described in Subsec. 5.4.1, which improves the description of the detector effects and also considers the background effects at the same time. Subsection 5.4.2 focuses on the construction of the response matrix, a key ingredient for the corrections presented in this section. The set of techniques which use the response matrix to obtain the true spectrum from the measured one is called the unfolding of the measured spectrum and its basic concepts are introduced in Subsec. 5.4.3. The final Subsec. 5.4.4 compares the performance of various unfolding techniques.

5.4.1 Embedding

Embedding is the name of a simulation technique where a single particle or a whole p+p event, simulated using a MC generator such as PYTHIA, is embedded inside a real event and reconstructed together with the data using the same reconstruction software as real data. The information which particle comes from the simulation is stored in the output files along with the percentage of hits which are associated to the particular MC particle. This simulation then contains information about the effects of pile-up and the multiplicity of the environment and therefore is a crucial ingredient for most analyses which require corrections for the effects of the detector and the event background. Embedding is necessary, because no simulator of full nucleus – nucleus collision evolution, capable of describing such collisions in sufficient detail, is currently available.

Embedding at STAR is usually done centrally by the embedding team where the experts have sufficient knowledge about the simulator settings in order to correctly simulate the detector response. The embedding is usually produced in a small sample and given out to the collaboration for Quality Assurance (QA) studies. Once approved, the full embedding sample is produced and released to the collaboration. However, in case of rarely used datasets or studies which require specific simulation tuning, STAR collaborators also produce (after a discussion with the experts) their private embedding samples.

In this analysis, a sample of p+p events generated by PYTHIA 6.428, Perugia 2012 version, further tuned[7] to match STAR single-particle spectra (STAR tune [133]) was embedded into MB Au+Au collisions at $\sqrt{s_{\mathrm{NN}}} = 200$ GeV and then reconstructed using a full GEANT 3 [183] simulation of particle propagation and interaction with the components of the STAR experiment corresponding to the year 2014. This embedding sample then combines the instrumental effects and the background effects on the generated spectra. The author of this thesis was involved in producing the picoDst files of the embedding sample for the entire Physics Working Group (PWG) which focuses on hard probes.

In order to access the hard part of the jet spectrum and avoid generating hundreds of million unbiased PYTHIA events, the MC spectrum is instead generated in 11 bins of parton – parton scattering transverse momentum transfer $\hat{p}_{\mathrm{T}}$. The bin edges are (3, 5, 7, 9, 11, 15, 20, 25, 30, 40, 50, -1), where -1 represents no limit on $\hat{p}_{\mathrm{T}}$. Each bin then contains 100 000 – 1.5 million generated events. The resulting spectrum would be unphysical and therefore, before combining the bins, each of them is scaled by a weight factor w,

$$w = \frac{\sigma_{\hat{p}_{\mathrm{T}}}}{N_{\mathrm{evt}}}, \tag{5.7}$$

---

[7] The tuning was done by modifying the PARP(90) parameter from 0.24 to 0.213. The PARP(90) parameter represents the power of the energy-rescaling term of two scale parameters $p_{\mathrm{T,min}}$ and $p_{\mathrm{T,0}}$. Both parameters represent the scale, below which the perturbative cross section is assumed vanishing or severely suppressed.

$\hat{p}_{\mathrm{T}}$ (GeV/c)	3-5	5-7	7-9	9-11	11-15	15-20	20-25	25-30	30-40	40-50	50+
$\sigma_{\hat{p}_{\mathrm{T}}}$ (μb)	1616	136	23	5.5	2.2	0.34	0.047	$8.5{\cdot}10^{-3}$	$2.2{\cdot}10^{-3}$	$1.2{\cdot}10^{-4}$	$6.9{\cdot}10^{-6}$
N_{evt} ($\cdot 10^5$)	10.2	15.3	12.8	10.2	10.2	10.2	10.2	7.7	5.1	3.1	1.0

Table 5.1: Cross section $\sigma_{\hat{p}_{\mathrm{T}}}$ and number of events N_{evt} for the used $\hat{p}_{\mathrm{T}}$ bins in simulated p+p collisions at $\sqrt{s}$ = 200 GeV by PYTHIA.

where $\sigma_{\hat{p}_{\mathrm{T}}}$ is the cross section of a particular $\hat{p}_{\mathrm{T}}$ bin given by PYTHIA and N_{evt} is the number of generated PYTHIA events in the same $\hat{p}_{\mathrm{T}}$ bin. Table 5.1 summarizes the cross section and number of events in each $\hat{p}_{\mathrm{T}}$ bin.

Since the embedding is into MB Au+Au collisions, the reconstructed events are subject to the same selection criteria and centrality weighting as in the case of real data. In order to simulate the effect of the HT2 trigger, events were accepted if they contain a tower with $E_{\mathrm{tow}} > 4.2$ GeV (before hadronic correction). Combining the jet spectra from weighted finite-size samples is prone to high-weight fluctuations, because there can be a count where a sub-count probability value is expected. These fluctuations manifest themselves as large-error spikes in the otherwise smooth combined spectrum. For this reason, jets with $p_{\mathrm{T,jet}} > 1.5 \cdot \hat{p}_{\mathrm{T}}{}^{\mathrm{max}}$, where $\hat{p}_{\mathrm{T}}{}^{\mathrm{max}}$ represents the upper edge of a given $\hat{p}_{\mathrm{T}}$ bin, were discarded. Figure 5.16 shows the reconstructed MC jet spectrum for small and large jets and it can be seen that the spectra are smooth.

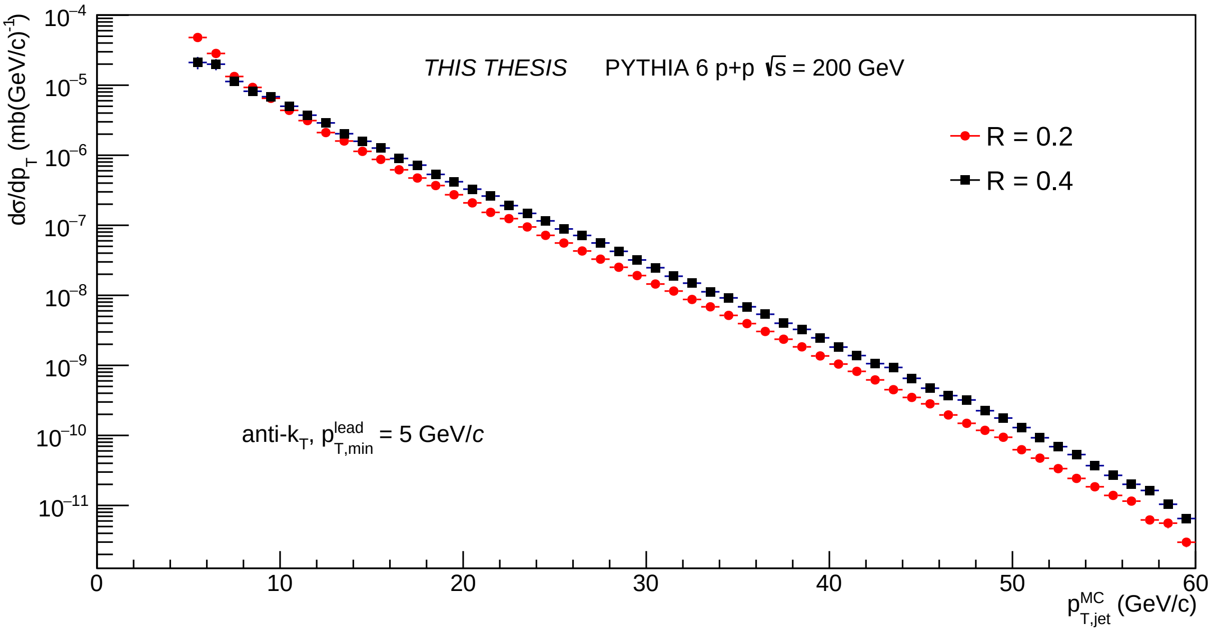

Figure 5.16: Spectrum of MC jets reconstructed with R = 0.2 (red circles) and R = 0.4 (black squares) and $p_{\mathrm{T,min}}^{\mathrm{lead}}$ = 5 GeV/c from p+p events at $\sqrt{s}$ = 200 GeV generated by PYTHIA 6.

5.4.2 Response Matrix

The response matrix is a key ingredient for the unfolding procedure, since it contains information about the effects of the detectors and background fluctuations on the true jet p_{T} spectrum. It is constructed by matching jets which are reconstructed from MC particles – called interchangibly particle-level jets or MC jets – generated by PYTHIA 6 STAR tune, which are not affected by the detector response simulation, and jets reconstructed from the combination of simulated and real tracks and towers in the event – called detector-level jets.

There is not one particular method for jet matching. In this analysis, the jet matching procedure works in the following steps:

1. MC particles with $|\eta_{\mathrm{trk}}^{\mathrm{MC}}| < 1$, $p_{\mathrm{T}}^{\mathrm{MC}} > 0.2$ GeV/c, and which are associated with the primary vertex of the MC event are selected. Neutrinos and muons are discarded since they are not expected to leave significant signal in the detector and they are usually not associated with jet production.

2. MC jets are reconstructed from the selected MC particles.

3. Detector-level jets are reconstructed using the same procedure as described in Sec. 5.2.

4. Each MC jet is matched to the closest detector-level jet in $r = \sqrt{\left(\eta_{\mathrm{jet}}^{\mathrm{MC}} - \eta_{\mathrm{jet}}^{\mathrm{det}}\right)^2 + \left(\phi_{\mathrm{jet}}^{\mathrm{MC}} - \phi_{\mathrm{jet}}^{\mathrm{det}}\right)^2}$, under the condition $r < 0.6\,R$ (motivated by [184]).

5. If the particle-level jet is outside the fiducial acceptance $|\eta_{\mathrm{jet}}^{\mathrm{MC}}| < 1 - R$ or contains only charged particles, the pair is discarded.

6. If the detector level jet is outside the fiducial acceptance $|\eta_{\mathrm{jet}}^{\mathrm{det}}| < 1 - R$, or fails to fulfill the same jet area or NEF selection criteria as the data analysis, the pair is discarded.

7. The $p_{\mathrm{T}}^{\mathrm{lead}}$ of the pair is taken as $\min\left(p_{\mathrm{T}}^{\mathrm{lead,MC}}, p_{\mathrm{T}}^{\mathrm{lead,det}}\right)$, and the $p_{\mathrm{T}}^{\mathrm{lead}}$ cut is applied.

8. The corresponding bin of the response matrix R_{ij}, where i is the $p_{\mathrm{T,jet}}^{\mathrm{MC}}$ and j is the $p_{\mathrm{T,jet}}^{\mathrm{det}}$ is incremented.

A different approach for jet matching in step 4 was also considered. In this approach, a detector-level jet is matched to the MC jet, which shares the largest fraction (p_{T} –wise) of reconstructed tracks matched to the MC tracks inside the MC jet. This alternative approach yields results consistent with the default procedure.

The response matrix is filled in fine binning, and is later rebinned into wider bins, because the binning has an effect on the unfolding procedure. The top panel of Fig. 5.17 shows the response matrix used for unfolding in central and peripheral collisions for jets reconstructed with $R = 0.3$. The matrix was normalized row–wise to 1, so the smearing of $p_{\mathrm{T,jet}}^{\mathrm{MC}}$by the detectors and residual background is visible. It can be seen that the smearing is much larger in central collisions, due to the larger UE fluctuations. The bottom panel of Fig. 5.17 shows the pior distribution (projection of the original matrix on the y axis) used as the input for the unfolding.

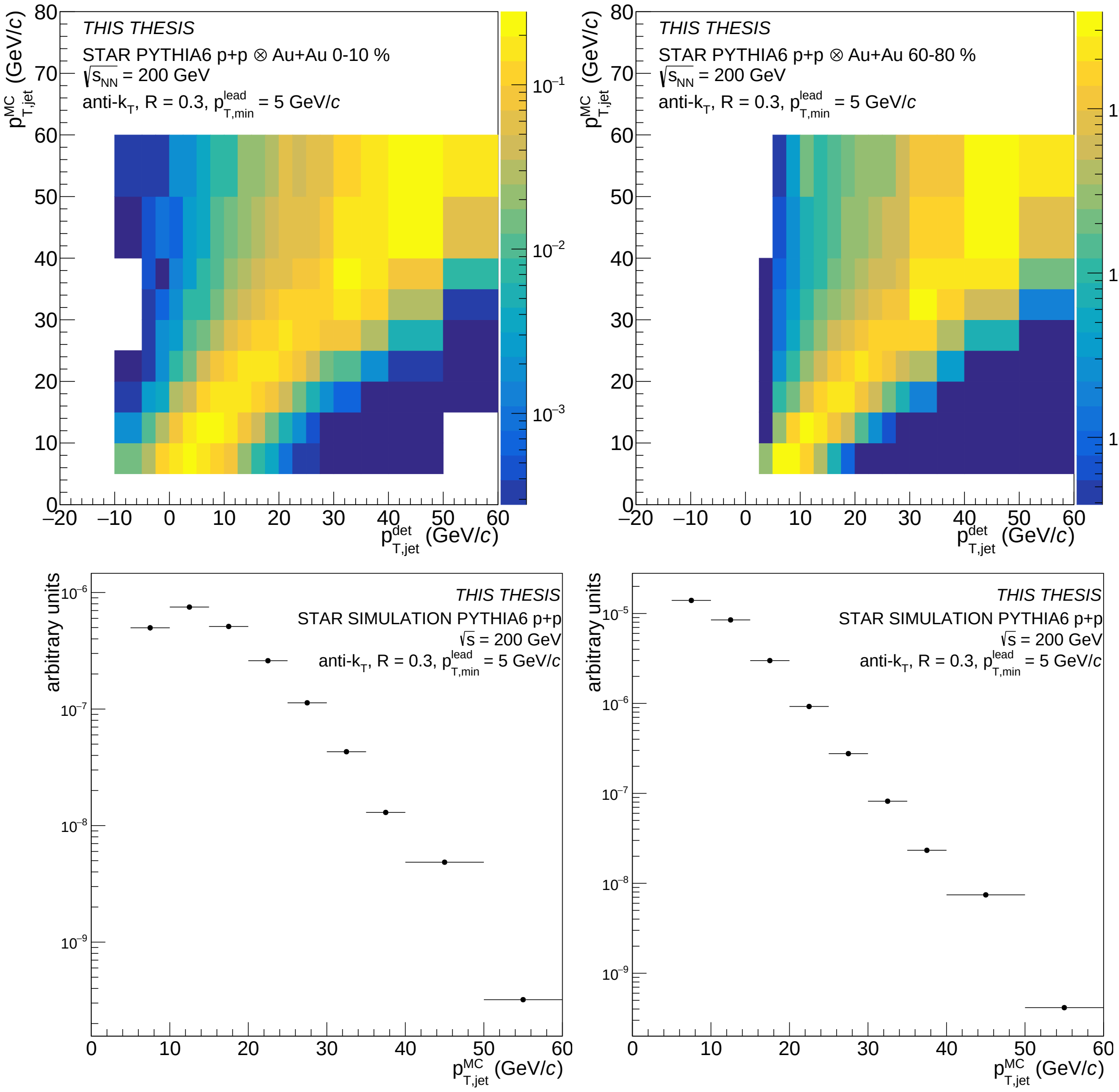

Figure 5.17: Response matrix (top) constructed from anti-k_T jets reconstructed with $R = 0.3$ in the embedding sample normalized row–wise to unity for visibility for central (left) and peripheral (right) collisions. The bottom panel shows the prior distributions (projection of the unnormalized matrix on the y axis) from p+p collisions simulated by PYTHIA 6 STAR tune.

Jet Matching Efficiency

Jet matching efficiency represents the probability of finding a match for each true jet in the event. Therefore, it can be defined as

$$\epsilon = \frac{\frac{\mathrm{d}N_{\mathrm{jet}}^{\mathrm{MC,\,match}}}{\mathrm{d}p_{\mathrm{T}}}}{\frac{\mathrm{d}N_{\mathrm{jet}}^{\mathrm{MC}}}{\mathrm{d}p_{\mathrm{T}}}}, \tag{5.8}$$

where the numerator is the p_{T} spectrum of MC jets which were matched to a detector-level jet during the matching procedure described above and the denominator is the p_{T} spectrum of all MC jets. The jet matching efficiency as a function of $p_{\mathrm{T,jet}}^{\mathrm{MC}}$, $p_{\mathrm{T}}^{\mathrm{lead}}$, R and centrality can be seen in Fig. 5.18. Overall, the efficiency has a similar shape for all the bins with a turn-on at low $p_{\mathrm{T,jet}}$ and the distribution flattening out at the high end, reaching values of around 90 %. The turn-on is significantly slower for larger jets in central collisions, which can possibly be attributed to the smearing of the jet axis due to the presence of the large background. The matching efficiency is slightly higher in peripheral collisions and for smaller jets. The effect of the $p_{\mathrm{T}}^{\mathrm{lead}}$ cut is observable in peripheral collisions at low $p_{\mathrm{T,jet}}$, while the distributions converge at high $p_{\mathrm{T,jet}}$. The jet matching efficiency is taken into account as a correction factor during the unfolding.

5.4.3 Introduction to Unfolding

When conducting a measurement of certain observable (such as jet p_{T}), we divide the continuous distribution into many bins and measure the counts in each bin. Due to limited detector acceptance, its inefficiency and non-linear response, background noise, and other effects, the measured count distribution $\vec{m}$ generally does not correspond to the true distribution $\vec{t}$ of that variable. In mathematical terms, this problem can be defined as

$$m_i = R_{ij} t_j, \tag{5.9}$$

where R_{ij} represents elements of the response matrix which contains all smearing effects. The response matrix can be fairly easily obtained from simulations using a known true distribution, producing the measured distribution. However, the truth is generally not known beforehand in experiments. The experiment obtains measured values and the smearing effects need to be corrected for before one can compare the results to theoretical predictions. Therefore, the common problem is the inversed version of the problem above:

$$t_i = R_{ij}^{-1} m_j. \tag{5.10}$$

In theory, calculating the inverse of the response matrix should be enough to solve the problem and obtain the true distribution from the measured one. In practice, due to the binning being commonly much finer than the detector resolution, the response matrix is not diagonal and the presence of the off-diagonal elements makes the matrix inversion outright impossible or burdened by very large statistical fluctuations (very nice simple example can be found in [185]).

Therefore, a number of methods has been proposed to modify the response matrix inversion procedure by introducing some bias into the procedure. Generally speaking, the stronger the bias the more stable are the results with respect to fluctuations, and therefore there is a trade-off between the introduced bias and the precision of the results, which is subject to analysis choice and discussion. These methods are collectively called unfolding, and several unfolding methods have been implemented in the RooUnfold C++ package [186], which is used in the analysis. The two most commonly used methods are the Singular Value Decomposition (SVD) method [187] and the iterative Bayesian method [188], which are described below.

Singular Value Decomposition

The singular value decomposition of the $m \times n$ response matrix R is its factorization

$$R = USV^T, \tag{5.11}$$

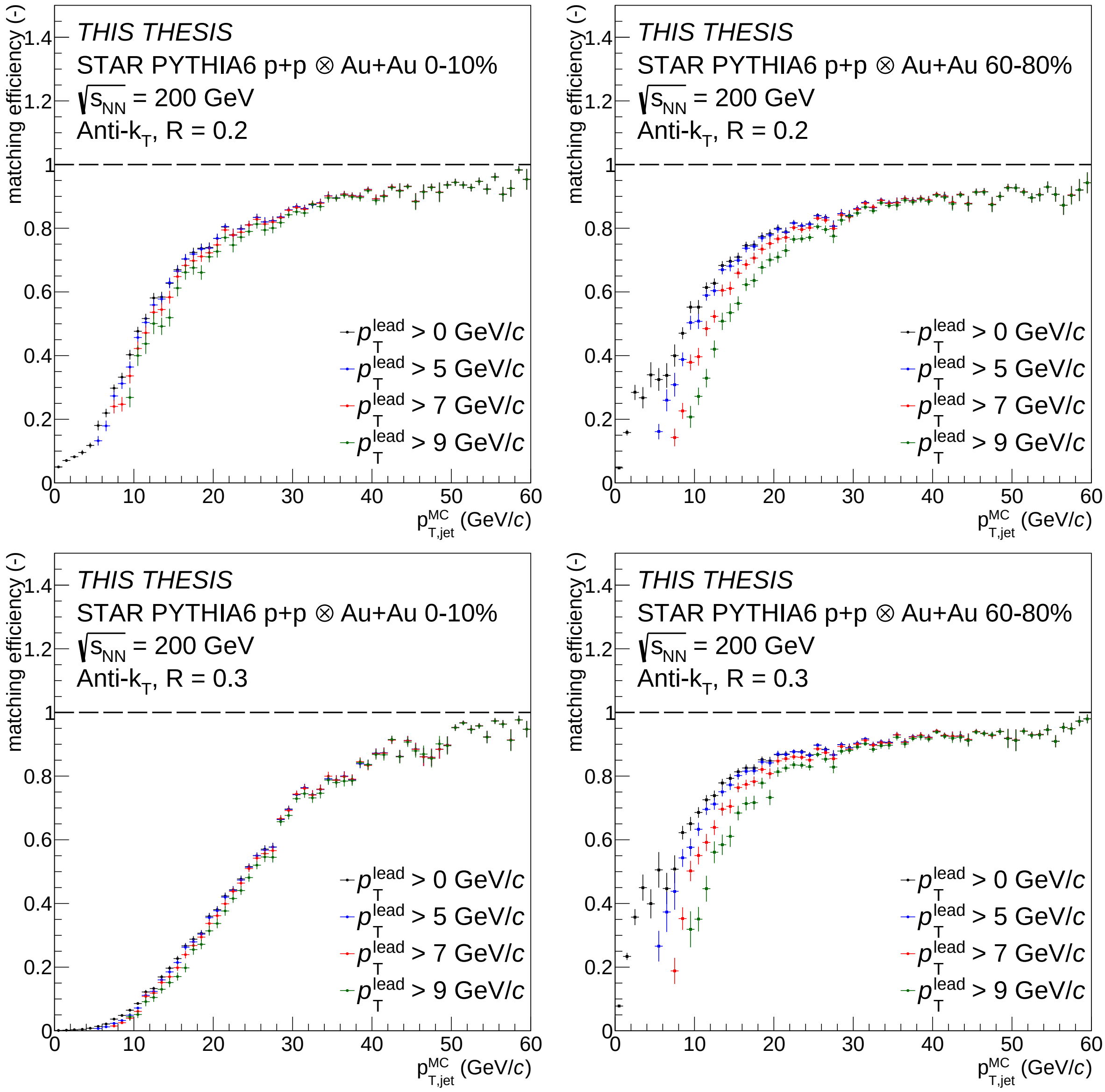

Figure 5.18: Jet matching efficiency as a function of jet transverse momentum $p_{\mathrm{T,jet}}^{\mathrm{MC}}$ for particle-level jets reconstructed by the anti-k_{T} algorithm with $R = 0.2$ (top) and $R = 0.3$ (bottom) from PYTHIA 6 STAR tune embedded into central (left) and peripheral (right) Au+Au collisions.

where U is an $m \times m$ orthogonal matrix, V is an $n \times n$ orthogonal matrix and S is an $m \times n$ diagonal matrix with non-negative diagonal elements $S_{ii} \equiv s_i$. The diagonal elements s_i are called the singular values of the response matrix and the columns of U and V are called the left and right singular vectors, respectively. Inserting 5.11 into 5.9, one gets

$$\vec{m} = USV^T\vec{t} \implies U^T\vec{m} = SV^T\vec{t}, \tag{5.12}$$

since U is orthogonal. If one then sets $\vec{z} \equiv V^T \vec{t}$ and $\vec{d} \equiv U^T \vec{m}$, one gets a set of equations

$$d_i = s_i z_i \implies z_i = \frac{d_i}{s_i}. \tag{5.13}$$

Solving for z_i and substituting back, one obtains the true distribution as

$$\vec{t} = V\vec{z}. \tag{5.14}$$

This method encounters problems for s_i equal to or close to zero as this can lead to large fluctuations and therefore errors. The original publication [187] suggests a regularization method to treat these problems. The regularization method then considers only k terms of the d vector decomposition, since additional terms should be statistically insignificant. The choice of the regularization parameter k is a subject to optimization.

Iterative Bayesian Method

The iterative Bayesian method is based on the Bayes' theorem, which states

$$P(\mathrm{A}|\mathrm{B}) = \frac{P(\mathrm{B}|\mathrm{A})P(\mathrm{A})}{P(\mathrm{B})}, \tag{5.15}$$

where $P(\mathrm{A}|\mathrm{B})$ and $P(\mathrm{B}|\mathrm{A})$ are the conditional probabilities P of event A happening when B happened and vice versa, and $P(\mathrm{A})$ and $P(\mathrm{B})$ are the likelihoods of events A and B happening, respectively. In the terms of unfolding, this theorem can be rewritten to calculate the probability of obtaining a measurement in bin i given a true event in bin j when we know the probability of such event producing that measurement:

$$P(t_j|m_i) = \frac{P(m_i|t_j)P_0(t_j)}{\sum_{l=1}^{n_t} P(m_i|t_l)P_0(t_l)}, \tag{5.16}$$

where n_t is the number of bins in the true spectrum. The left-hand side $P(t_j|m_i)$ is essentially the inverse response matrix and $P(m_i|t_j)$ is the response matrix constructed from simulation (see the Subsec. 5.4.1 for details), the denominator is a normalization constant and the last ingredient, $P_0(t_j)$ is a guess of the shape of the true spectrum (prior). This guess is the bias introduced in this method, since the true spectrum is not/should not be known before the unfolding. This method then estimates the new true spectrum $\hat{\vec{t}}$ as

$$\hat{\vec{t}} = \vec{m} \cdot P(t_j|m_i) = \vec{m} \cdot \frac{P(m_i|t_j)P_0(t_j)}{\sum_{l=1}^{n_t} P(m_i|t_l)P_0(t_l)}, \tag{5.17}$$

and one can get a new estimate $P_1(t_j)$ via

$$P_1(t_j) = \frac{\hat{t}_j}{N_t}, \tag{5.18}$$

where $N_t = \sum_{j=1}^{n_t} t_j$ is the estimated number of all true events, producing an iterative method which uses the k-th estimate $P_k(t_j)$ as the prior distribution for the $(k+1)$-th iteration. Increasing the number of iterations should therefore lead to less dependence on the initial guess. In theory, any initial guess should produce accurate results (in terms of being close to the truth) after a finite number of iterations. However, if the number of iterations is too large, it leads to instabilities of the method since the statistical fluctuations are propagated in each step. Therefore, the practical number of iterations is usually limited to the point where the results do not change much with subsequent iterations. This choice is subject to discussion.

Prior Distribution

Both SVD and Bayesian methods expect an initial guess of the true spectrum. In principle, any sufficiently well-behaved distribution, such as flat spectrum, should produce correct results. However, one can take advantage of the existing models and theoretical calculations to assume that the jet spectrum is steeply falling. Therefore, as a default choice, the p_{T} spectrum of matched jets which was generated by PYTHIA 6 for the response matrix is used as a prior.

5.4.4 Unfolding Performance

There are a few tests which can be used to determine, whether the unfolding procedure produces reliable and stable results. For the Bayesian unfolding, the main test is the convergence of the iterative procedure. Figure 5.19 shows the convergence test for Bayesian unfolding with PYTHIA 6 prior distribution as a function of jet p_{T}, centrality and $p_{\mathrm{T}}^{\mathrm{lead}}$. Figure 5.20 shows the same for jets reconstructed with $R = 0.3$. In all cases, it can be seen that the unfolding procedure converges as the ratios of successive iterations (bottom panels) tend towards unity with larger number of iterations, with change below 10 % in most bins after just a few iterations. In order to limit the statistical fluctuations, the spectra after 4 iterations were used as the nominal value and spectra after 5 iterations for systematic uncertainty estimation. As evidenced by the ratios shown in Fig. 5.21, the unfolding of jet spectra reconstructed with $R = 0.4$ in central collisions fails the convergence test. This can be attributed to the inability to accurately describe the background contained in such large objects. Therefore, spectra of $R = 0.4$ jets reconstructed in central Au+Au collisions are not reported in this thesis further.

For the SVD unfolding, one should not expect the spectra to "converge" with successive increasing of the regularization parameter k, because these spectra can have very different shapes. Instead, the correct value of k can be determined from the $d-$vector (as introduced in 5.4.3). The expected behavior is steeply falling values of $|d_k|$ with increasing k, until the values reach the end-point of statistical significance near $|d_k| = 1$. An example of the $d-$vector can be seen in Fig. 5.22 for jets reconstructed with $R = 0.2$ and $p_{\mathrm{T,min}}^{\mathrm{lead}} = 9$ GeV/c in central Au+Au collisions, from where it seems like $k = 5$ is the optimal value.

The validity of this choice can be justified when comparing the results of the SVD unfolding with the Bayesian unfolding results. Figure 5.23 shows such comparison for two cases of $R = 0.2$ jets. In both cases, one can see that both unfolding methods give consistent results. In ideal case, one would either choose one method as the nominal and use the other for systematic uncertainty estimation or report the average of both methods as the nominal result, and use the deviations of both methods from the average as the systematic uncertainty. However, since the SVD unfolding is not performing well for all considered combinations of jet R and $p_{\mathrm{T}}^{\mathrm{lead}}$, and collision centrality, only results obtained from the Bayesian unfolding are reported further.

Another test, which can determine whether the unfolding procedure is self-consistent, is the backfolding test, where the unfolded spectrum is smeared with the response matrix and then is compared to the measured spectrum. One expects the two distributions to be close, though not identical. This is because of the bias introduced by the prior distributions and also because of the propagation of statistical fluctuations. Figure 5.24 presents an example of the backfolding test for jets reconstructed with $R = 0.3$ with $p_{\mathrm{T,min}}^{\mathrm{lead}}= 5$ and 7 GeV/c in both central and peripheral Au+Au collisions. It can be seen that for most cases, the ratio of backfolded to measured spectra is consistent with unity within uncertainties, making the backfolding test successful.

These tests only confirm the mathematical correctness of the unfolding, but by themselves cannot assure that the obtained results contain the correct physics message. In order to really determine the correcntess of the unfolding, one needs to perform the closure test on simulated data resembling real

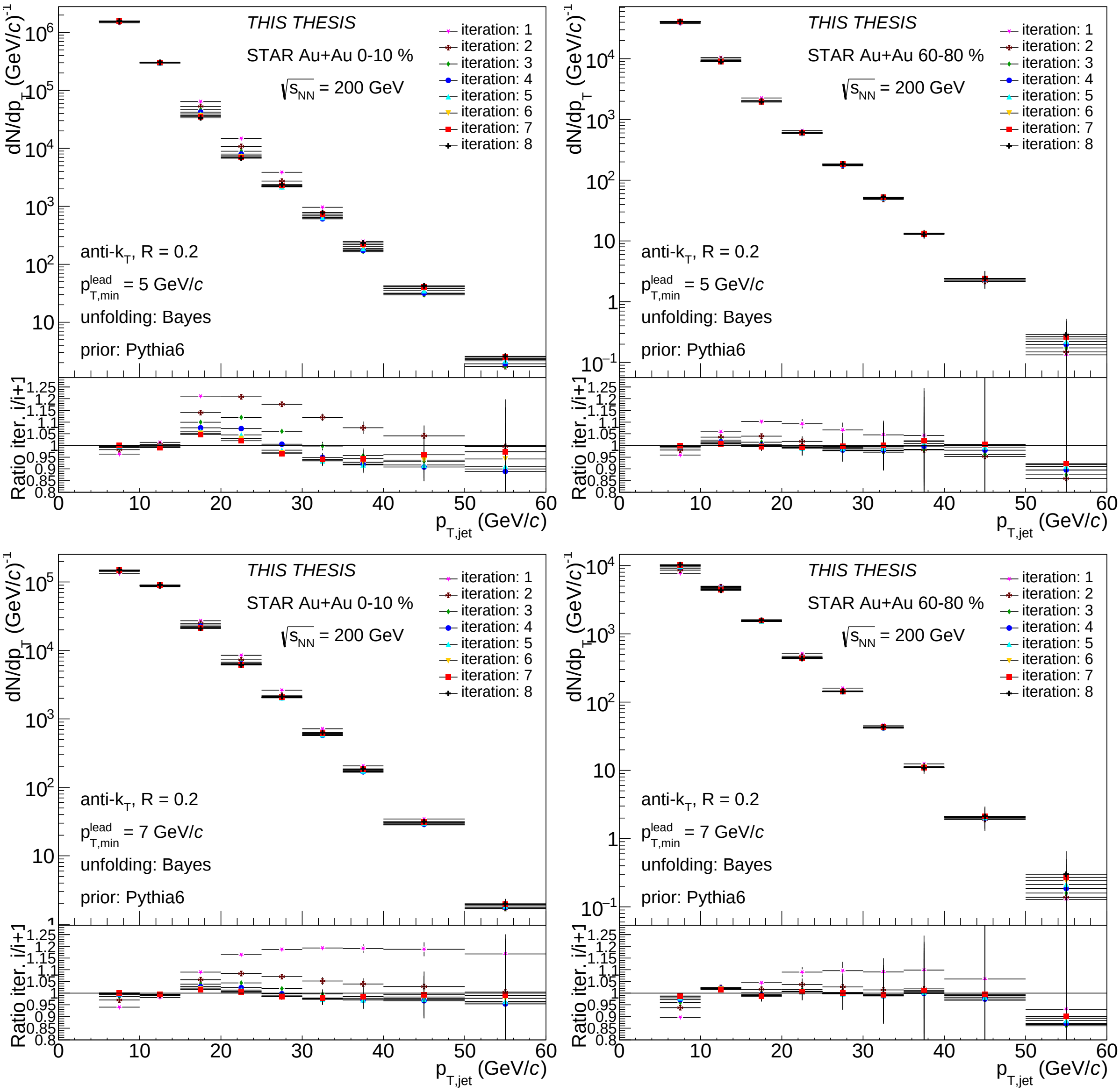

Figure 5.19: Bayesian unfolding convergence test for anti-k_T jets reconstructed with $R = 0.2$ and $p_{\mathrm{T,min}}^{\mathrm{lead}} = 5$ GeV/c (top) and $p_{\mathrm{T,min}}^{\mathrm{lead}} = 7$ GeV/c (bottom) in central (left) and peripheral (right) Au+Au collisions at $\sqrt{s_{\mathrm{NN}}} = 200$ GeV. Different symbols represent different iterations (top panels) and ratios of successive iterations (bottom panels), many symbols in each bin overlap. The error bars represent statistical uncertainties.

conditions of the data. However, before one can fully perform the closure test, the systematic uncertainties of the measurement have to be estimated.

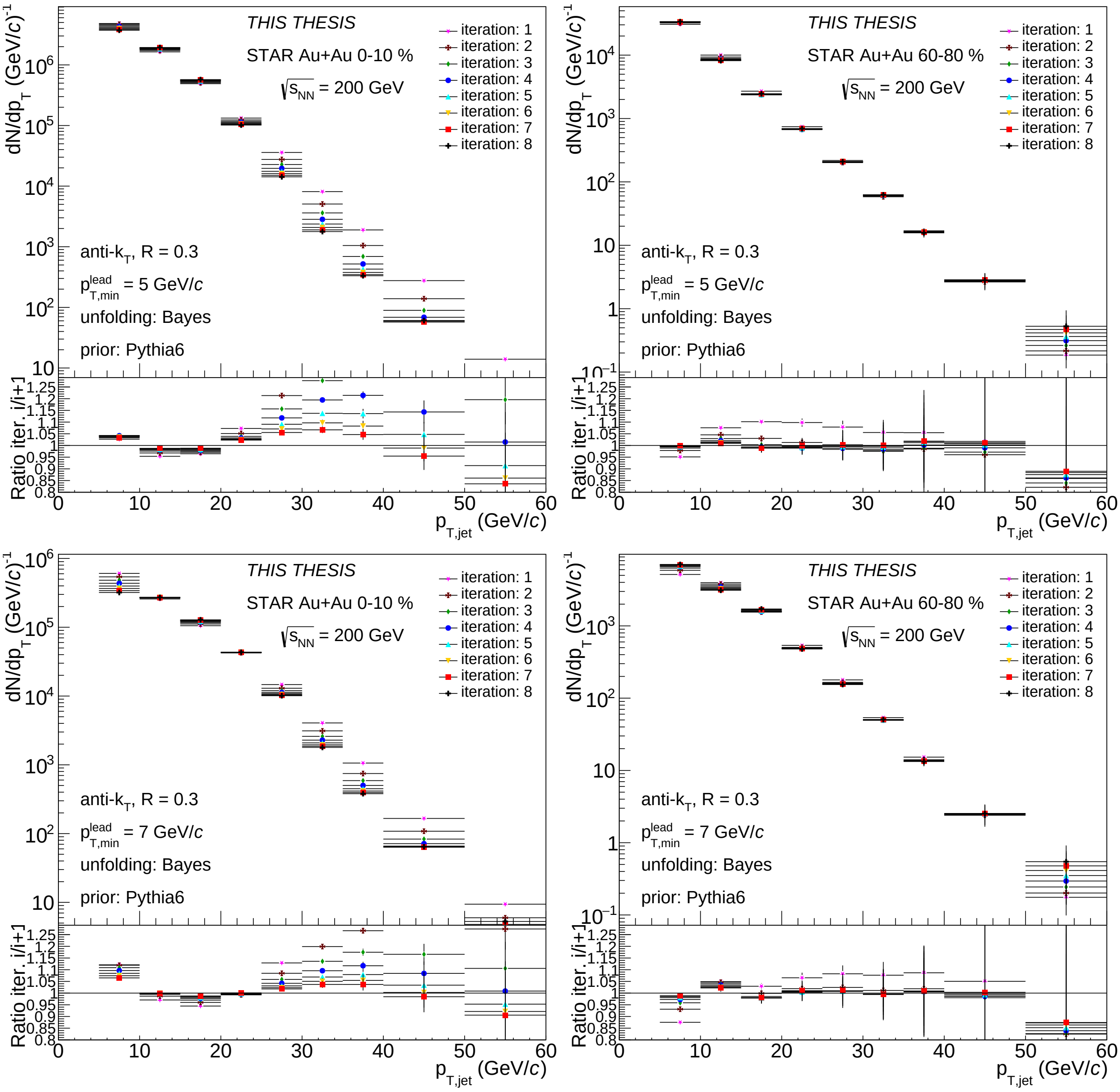

Figure 5.20: Bayesian unfolding convergence test for anti-k_T jets reconstructed with $R = 0.3$ and $p_{T,\mathrm{min}}^{\mathrm{lead}} = 5$ GeV/c (top) and $p_{T,\mathrm{min}}^{\mathrm{lead}} = 7$ GeV/c (bottom) in central (left) and peripheral (right) Au+Au collisions at $\sqrt{s_{\mathrm{NN}}} = 200$ GeV. Different symbols represent different iterations (top panels) and ratios of successive iterations (bottom panels), many symbols in each bin overlap. The error bars represent statistical uncertainties.

5.5 Systematic Uncertainties

The estimation of systematic uncertainties is a key ingredient in presenting any physics results. There are two general types of systematic uncertainties in this analysis. The first is the correlated systematic uncertainty with highly positive correlation among jet p_T bins. The second is the shape uncertainty which arises from applying the unfolding procedure and which changes the shape of the spectrum. These two types are therefore estimated separately in Subsec. 5.5.1 and Subsec. 5.5.2. In most cases, the

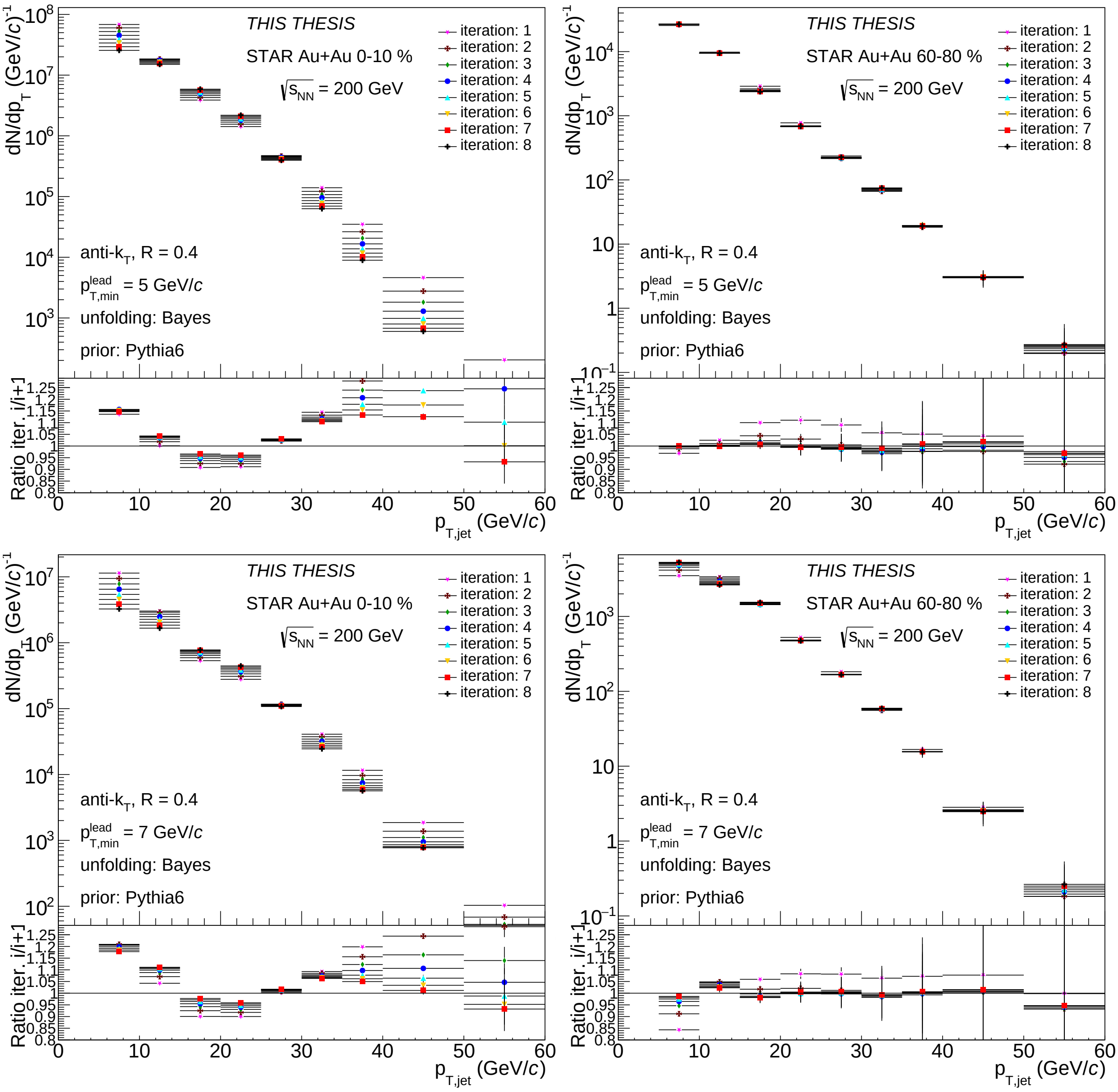

Figure 5.21: Bayesian unfolding convergence test for anti-k_T jets reconstructed with $R = 0.4$ and $p_{T,min}^{lead} = 5$ GeV/c (top) and $p_{T,min}^{lead} = 7$ GeV/c (bottom) in central (left) and peripheral (right) Au+Au collisions at $\sqrt{s_{NN}} = 200$ GeV. Different symbols represent different iterations (top panels) and ratios of successive iterations (bottom panels), many symbols in each bin overlap. The error bars represent statistical uncertainties.

uncertainties are also reported separately for the results. However, for the closure test, the correlated and shape uncertainties are added in quadrature and the total uncertainty $\sigma_{tot} = \sqrt{\sigma^2_{corr.} + \sigma^2_{shape}}$ is used instead.

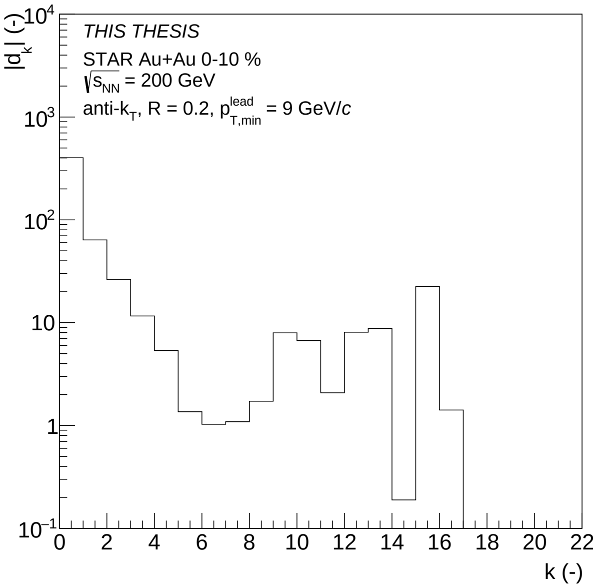

Figure 5.22: d–vector of anti-k_{T} jets reconstructed with R = 0.2 and $p_{\mathrm{T,min}}^{\mathrm{lead}}$ = 9 GeV/c in central Au+Au collisions at $\sqrt{s_{\mathrm{NN}}}$ = 200 GeV.

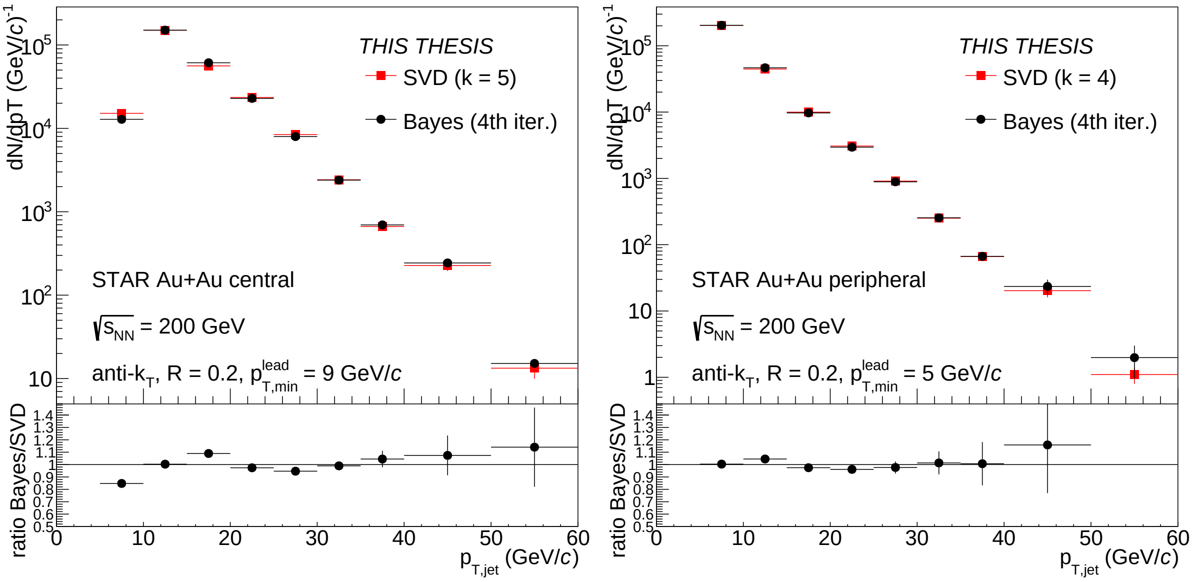

Figure 5.23: Comparison of SVD (red squares) and Bayesian (black circles) unfolding results for anti-k_{T}, R = 0.2 jets, reconstructed with $p_{\mathrm{T,min}}^{\mathrm{lead}}$ = 9 GeV/c in central (left) and with $p_{\mathrm{T,min}}^{\mathrm{lead}}$ = 5 GeV/c in peripheral Au+Au collisions at $\sqrt{s_{\mathrm{NN}}}$ = 200 GeV (right). The bottom panel shows the ratio of the spectra.

5.5.1 Correlated Uncertainty

There are several sources of the correlated systematic uncertainty:

- Tracking Efficiency - the uncertainty of the TPC tracking efficiency. Estimated by removing ad-

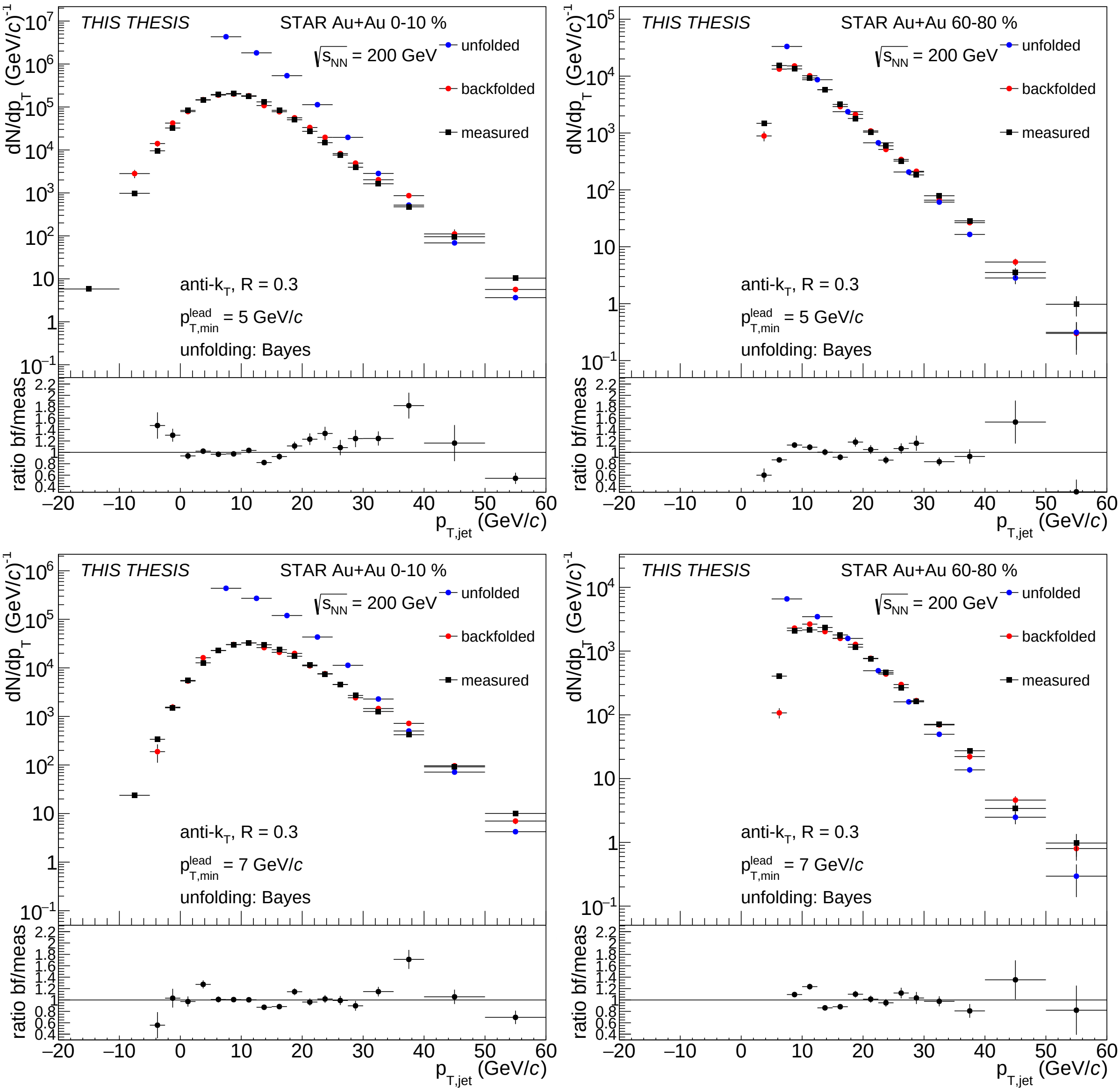

Figure 5.24: Bayesian unfolding backfolding test for anti-k_T jets reconstructed with $R = 0.3$ and $p_{T,min}^{lead} = 5$ GeV/c (top) and $p_{T,min}^{lead} = 7$ GeV/c (bottom) in central (left) and peripheral (right) Au+Au collisions at $\sqrt{s_{NN}} = 200$ GeV. (Top panels) Black squares represent the measured distribution while red circles represent the backfolded distribution. For comparison, the unfolded $p_{T,jet}$ spectrum is plotted as blue circles. (Bottom panels) Ratios of backfolded/measured jet spectra. The error bars represent statistical uncertainties.

ditional 5 % (relative) of accepted tracks from the embedding sample and repeating the unfolding procedure. Since it is impossible to add tracks into the embedding sample in any reasonable way, we assume that this uncertainty is symmetric.

- Tower Scale - the uncertainty of the BEMC tower energy scale. Estimated by increasing and reducing the energy of all towers in the embedding sample by 3.8 %.

- Hadronic Correction - the uncertainty of the fraction of momentum charged hadrons deposit inside the BEMC towers. Estimated by changing the hadronic correction to 50 % in both data analysis and embedding.
- R_{BG} - the dependence on R of the k_{T} jets during the median background ρ estimation. Estimated by changing R_{BG} to 0.4 in both data analysis and embedding.

All these sources are treated individually. After unfolding, the systematic uncertainty is then estimated as the absolute value of the difference between the resulting spectrum and the nominal spectrum obtained from the main analysis. Since these sources are assumed to be independent, these contributions are added in quadrature in order to obtain the total correlated uncertainty.

5.5.2 Shape Uncertainty

The shape uncertainty is estimated by changing the number of iterations in the Bayesian unfolding to 5 and taking the absolute difference between the resulting spectrum compared to the 4th iteration. As discussed in Subsec. 5.4.4, the SVD method has not proven to be reliable enough for this analysis to warrant full consideration for the systematic uncertainty estimation. In the few cases where the SVD unfolding produced results of reasonable quality, the difference between the Bayesian and SVD spectra was within a few percent in the relevant $p_{\mathrm{T,jet}}$ range.

Table 5.2 summarizes the contributions of all considered sources of systematic uncertainty for anti-k_{T} jets reconstructed with $R = 0.2$ and $p_{\mathrm{T,min}}^{\mathrm{lead}} = 5$ GeV/c in both central and peripheral Au+Au collisions at $\sqrt{s_{\mathrm{NN}}} = 200$ GeV. Figure 5.25 shows the contents of Tab. 5.2 for easier visualisation separately for central and peripheral collisions. It can be seen that the systematic uncertainty generally rises with $p_{\mathrm{T,jet}}$ and is of similar magnitude for central and peripheral collisions accross $p_{\mathrm{T,jet}}$, except for the last bin, where the vanishing statistical precision of the data manifests as large fluctuations of the results and therefore unreliable systematic uncertainty estimation. For this reason, the 50–60 GeV/c bin in peripheral collisions is not reported. The main sources of the systematic uncertainty are the tower scale uncertainty, the tracking efficiency uncertainty and the unfolding. The systematic uncertainty for other combinations of R and $p_{\mathrm{T,min}}^{\mathrm{lead}}$ can be found in App. C.

5.6 Closure Test

Once the systematic uncertainty has been estimated, the closure test can be performed. The motivation behind the closure test is to confirm that the unfolding procedure produces correct physics results, in our case the corrected jet p_{T} spectra. Therefore, one needs the following ingredients:

- the Truth - a known jet p_{T} spectrum, which should be independent of the unfolding output from real data. In our case, the jet p_{T} spectrum generated by the PYTHIA 6 STAR tune was used.
- the Test spectrum - a jet spectrum which is independent on the real raw data and the Truth, but has similar shape, statistical precision and contains similar effects of detector performance and background smearing. In our case, we use the jet $p_{\mathrm{T,jet}}^{\mathrm{reco}}$ spectra reconstructed from the embedding sample.
- the Response - a response matrix which takes into account both background presence in Au+Au collisions and the detector effects, and is used for unfolding of the Test spectrum. This response matrix has been constructed in the same way as in the main analysis.

Relative uncertainty (%)

	Central (0–10 %), R = 0.2, $p_{\mathrm{T,min}}^{\mathrm{lead}}$ = 5 GeV/c								
$p_{\mathrm{T,jet}}$ (GeV/c)	5-10	10-15	15-20	20-25	25-30	30-35	35-40	40-50	50-60
Tracking Efficiency	2.6	3.3	1.2	5.9	8.2	8.6	10.7	9.7	10.3
Tower Scale +	16.5	1.5	1.2	6.4	8.7	7.5	12.4	16.7	17.1
Tower Scale -	1.1	3.2	3.0	5.5	7.1	9.7	13.1	15.9	18.9
Hadronic Correction	6.4	4.7	5.0	0.9	2.6	2.2	1.8	2.3	1.5
R_{BG}	2.3	1.6	1.0	0.9	0.9	1.6	2.2	0.0	3.7
Total Correlated	18.0	6.9	6.1	10.4	14.2	15.2	21.1	25.1	27.7
Shape	0.4	0.5	7.5	7.2	0.6	5.1	8.0	9.2	11.1

	Peripheral (60–80 %), R = 0.2, $p_{\mathrm{T,min}}^{\mathrm{lead}}$ = 5 GeV/c								
$p_{\mathrm{T,jet}}$ (GeV/c)	5-10	10-15	15-20	20-25	25-30	30-35	35-40	40-50	50-60
Tracking Efficiency	1.9	5.2	4.4	6.1	8.6	10.6	13.3	13.0	–
Tower Scale +	0.3	0.9	7.9	9.6	10.7	12.0	11.3	15.3	–
Tower Scale -	0.2	7.8	4.6	7.3	10.0	11.5	14.0	14.3	–
Hadronic Correction	1.2	0.5	0.4	0.7	0.7	0.3	9.9	32.7	–
R_{BG}	0.8	0.4	0.2	2.4	1.2	2.8	0.3	0.6	–
Total Correlated	2.4	9.4	10.2	13.8	17.0	19.9	24.5	40.9	–
Shape	0.6	1.6	0.3	1.1	1.9	2.0	0.3	2.0	–

Table 5.2: Summary of the relative systematic uncertainty contributions (in %) from various sources along with the total correlated uncertainty and the shape uncertainty in the presented $p_{\mathrm{T,jet}}$ bins for jets reconstructed with $R = 0.2$ and $p_{\mathrm{T,min}}^{\mathrm{lead}} = 5$ GeV/c in central (top) and peripheral (bottom) Au+Au collisions at $\sqrt{s_{\mathrm{NN}}} = 200$ GeV. Note that values for the 50-60 GeV/c bin are not reported for peripheral collisions since they are dominated by statistical fluctuations.

If one would simply take the whole embedding sample, consider the MC spectrum as the Truth and the detector-level spectrum as the Test and use the same Response as in the main analysis, one would receive spectrum identical to Truth from the unfolding. This only again tests the self-consistency of the unfolding procedure, but does not constitute the closure test. In order to really perform the closure test, the Test and the Truth need to be completely independent of each other. Therefore, the embedding sample was split into two parts with similar statistical precision. One half was used to generate the Truth and the Response, while the Test spectrum was created from the other half. This assures independence of Truth and Test, and minimizes the difference in statistical precision. The unfolded Test spectrum should then be consistent with the Truth within the precision of the measurement. As an example, the results of the closure test for jets reconstructed with $R = 0.3$ and $p_{\mathrm{T,min}}^{\mathrm{lead}} = 5$ and 7 GeV/c can be seen in Fig. 5.26. Overall, the ratio of Truth and Test is consistent with unity across the $p_{\mathrm{T,jet}}$ range, demonstrating the

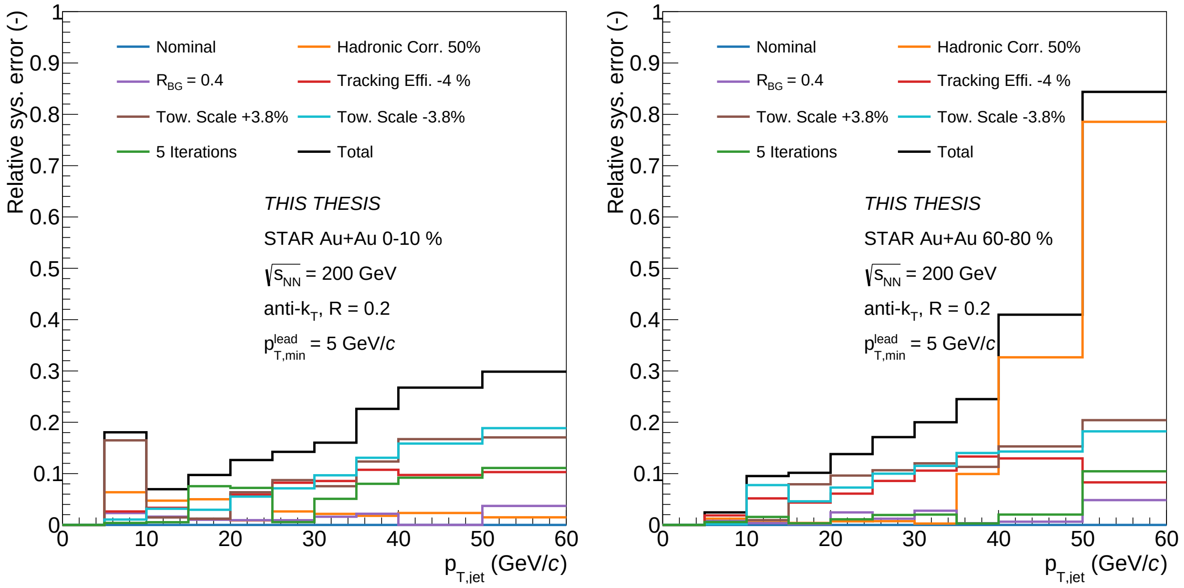

Figure 5.25: Contributions to the total systematic error from various sources (different colors). The black line represents the total uncertainty obtained by adding the sources in quadrature. Jets were reconstructed with $R = 0.2$ and $p_{\mathrm{T,min}}^{\mathrm{lead}} = 5$ GeV/c in central (left) and peripheral (right) Au+Au collisions at $\sqrt{s_{\mathrm{NN}}} = 200$ GeV.

success of the closure test. Other combinations of R and $p_{\mathrm{T}}^{\mathrm{lead}}$ demonstrate similar level of closure.

5.7 Bin–Width Correction

The jet p_{T} spectrum is represented by markers which are initially placed at the center of each bin with finite width. However, if one would fit these points with a reasonable function, the integral of the function would be higher than the total bin content of the histogram. The reason for this (undesired) behavior is the following. Because the spectrum is steeply falling, the integral inside each bin is higher to the left of the bin center than to the right. This effect is naturally larger in wider bins. Therefore, in order to correctly report the spectrum, one needs to either shift the bin centers to the left or down, in both cases reducing the integral of the fit function. We chose to shift the markers to the left – as is common in the field – using the following iterative method:

1. The spectrum is fitted with the Tsallis function:

$$f(p_{\mathrm{T}}) = A \cdot p_{\mathrm{T}} \left(1 + \frac{p_{\mathrm{T}}}{n \cdot T}\right)^{-n}, \tag{5.19}$$

   where A, n and T are free parameters.

2. For each bin with edges x_{min} and x_{max}, the integral of the fit to the left of the bin center $I_L = \int_{x_{\mathrm{min}}}^{x_0} f(p_{\mathrm{T}})\mathrm{d}p_{\mathrm{T}}$ and to the right $I_R = \int_{x_0}^{x_{\mathrm{max}}} f(p_{\mathrm{T}})\mathrm{d}p_{\mathrm{T}}$ of the bin center x_0 is computed.

3. The new bin center is calculated as $x_{\mathrm{new,\,i}} = x_{\mathrm{min}} + (x_0\text{-}x_{\mathrm{min}}) \cdot \frac{I_R}{I_L}$.

4. These steps then change the integral of the fit function and therefore are repeated 5 times, which assures the numerical convergence of the procedure.

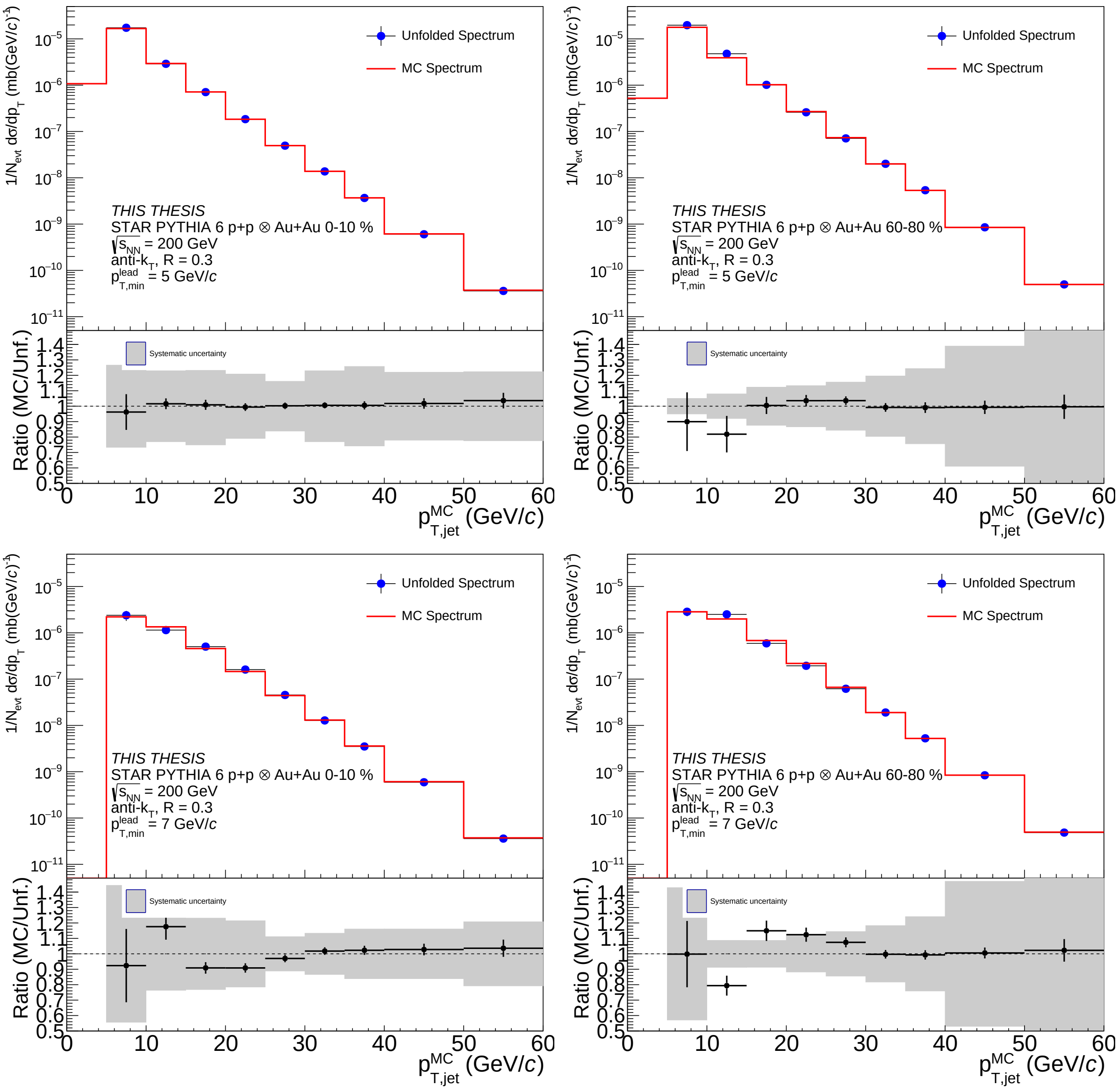

Figure 5.26: Closure test results for $R = 0.3$ jets reconstructed with $p_{\mathrm{T,min}}^{\mathrm{lead}} = 5$ GeV/c (top) and 7 GeV/c (bottom) in central (left) and peripheral (right) Au+Au collisions. The blue markers represent the unfolded Test spectrum while the red line represents the Truth MC spectrum. The bottom panels show the ratio between Truth and Test. The error bars represent statistical uncertainty and the grey area represents the total systematic uncertainty.

5.8 Trigger Bias

As discussed in Sec. 5.1, the data analyzed in this thesis were taken with the HT2 trigger and, therefore, the resulting spectra are biased by the trigger requirement. The biases arising as a consequence of the trigger are the following:

1. The **per-event jet yield is unphysically high**. Because the HT2 trigger preferentially selects events where jet production has occured, the cross section is overestimated.
2. The jet population is **biased towards more neutral jets**, since the HT2 trigger is more likely to be fired by a neutral particle.
3. The **neutral constituent spectrum is modified** by the presence of the trigger. This also creates a non-trivial interplay between the trigger and $p_{\mathrm{T}}^{\mathrm{lead}}$ biases.
4. The **centrality distribution is biased** towards more central collisions, because they are more likely to contain a trigger jet. Therefore, the 0–10 % centrality bin does not correspond to 10 % of the total cross section. Figure 5.27 shows the comparison between the centrality distribution in the HT2 and MB samples.
5. Related to 4, **distribution of $\langle N_{\mathrm{coll}} \rangle$ is also modified**, because each centrality bin is biased towards the upper edge. This is an important scaling factor for the ratios introduced in Sec. 3.3. Table 5.3 shows the comparison between the $\langle N_{\mathrm{coll}} \rangle$ for HT2 and MB in central and peripheral Au+Au collisions at $\sqrt{s_{\mathrm{NN}}} = 200$ GeV.

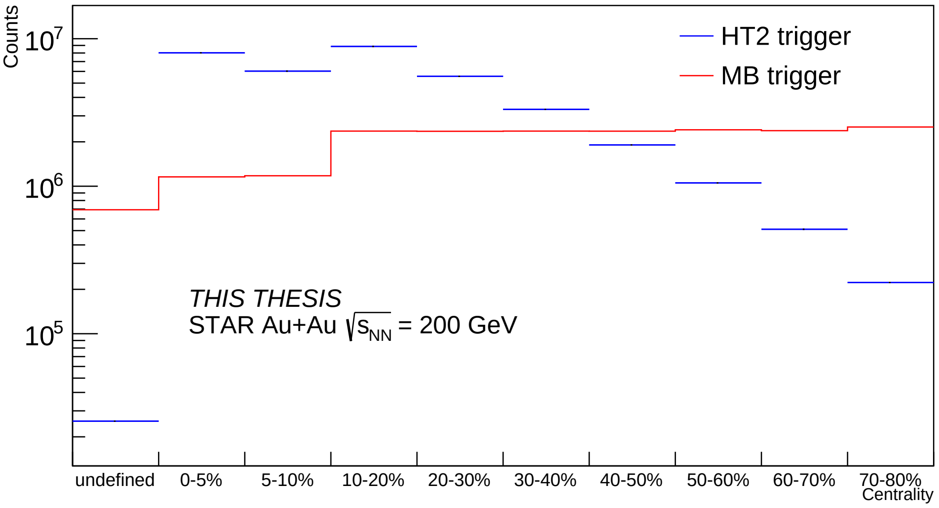

Figure 5.27: Comparison of centrality distribution between HT2 events (black) and MB events (red). Each bin represents different centrality interval, while events which do not have centrality properly defined are in the "undefined" bin.

Before obtaining any physics message from the reconstructed jet spectra, these biases need to be addressed. The main challenge is the first bias, and will be addressed later. The second bias is not expected to have large impact on the results of jet quenching studies, since from the QCD point of view, the electric charge of the constituents does not matter at the leading-order approximation. The third bias is expected to be corrected for during the unfolding, since the same bias is imposed when reconstructing jets from the embedding sample. The fourth and fifth biases can be accounted for somewhat by considering the event centrality definition with finer binning. STAR centrality definition provides 5% centrality intervals, but creating a special centrality definition which would better describe the HT2 dataset would be a possibility. The same can be said about the Glauber model calculation for the $\langle N_{\mathrm{coll}} \rangle$.

Centrality	$\langle N_{\text{coll}}^{\text{MB}} \rangle$	$\langle N_{\text{coll}}^{\text{HT}} \rangle$
0–10 %	959 ± 26	975 ± 26
60–80 %	22 ± 9	25 ± 10

Table 5.3: Mean number of binary nucleus–nucleus collisions $\langle N_{\text{coll}} \rangle$ in MB and HT2 Au+Au collisions at $\sqrt{s_{\text{NN}}} = 200$ GeV.

There are two possibilities of correcting the spectra in order to obtain the true jet cross section. The optimal way is to obtain the normalization factor for the spectra in the form of equivalent MB events. This process involves calculating the number of equivalent MB events from the number of HT2 events by taking into account run-by-run event statistics, the dead time of the trigger detectors and the pre-scale factors[8].

Furthermore, this process requires to take into account only the jets, which contain a trigger tower. Therefore, each HT2 event usually[9] contains only one such jet. Figure 5.28 shows the reconstructed spectra of jets which contain the trigger tower as a function of $p_{\text{T,jet}}^{\text{reco}}$, R and event centrality. It can be seen that the spectra overall follow the same trend as in the main analysis (Fig. 5.15), with the exception of the spectra reconstructed with $p_{\text{T}}^{\text{lead}} > 0$ GeV/c, which now practically overlap with the $p_{\text{T}}^{\text{lead}} > 3$ GeV/c spectra, since the trigger tower requirement essentially ensures a leading particle with $p_{\text{T}} \gtrsim 4.2$ GeV/c. Reconstruction of these spectra and performing the full correction procedure, including unfolding (which in this case is very demanding on the statistics of the embedding sample), constitutes a full separate complex analysis which – unfortunately – lies beyond the scope of this thesis.

The alternative way is to analyze MB events, perform all correction procedures, including the unfolding and find a normalization region. One would expect that the trigger bias changing the shape of the spectrum is negligible at high $p_{\text{T,jet}}$. Therefore, there should be a region where the ratio between the HT2 and MB spectra is approximately constant. This normalization constant then can be used to scale the HT2 spectra down in order to obtain the physical cross section. A data sample taken during the same run conditions as the HT2 dataset, but with the MB trigger (IDs 450010, 450020, 450008, 450018) was analyzed in the same way as described for the main analysis. This data sample contains around 2.3 million central and 4.9 million peripheral events, which by itself provides insufficient statistical precision (especially in peripheral events) for interesting physics results. However, one can at least attempt a rough estimation of the normalization factor for the HT2 trigger. The region of constant ratio of the spectra could not be easily identified with the available MB sample. The ratio was fit with a constant function between $p_{\text{T,jet}} = 10 - 28$ GeV/c. Because the spectra are steeply falling, the fit is dominated by the statistical precision of the first point. Instead of determining the uncertainty of this normalization factor from the fit, it is estimated by removing the first point ($p_{\text{T,jet}} = 10 - 15$ GeV/c) from the fit and taking the relative difference as the global systematic uncertainty of the measurement,

$$\sigma_{Norm} = \frac{R_4^{HT2/MB} - R_3^{HT2/MB}}{R_4^{HT2/MB}}, \tag{5.20}$$

---

[8] Some common triggers (such as MB) are pre-scaled by a certain factor x, which means that only every x-th event is recorded and reconstructed. This is a result of the limitations of the detectors (mainly the TPC at STAR) and the Data Acquisition (DAQ) systems. Rare-process triggers, such as the HT2 trigger, are ususally not pre-scaled

[9] Not always. The HT2 trigger can be fired by multiple towers, for example from a dijet event, and has no preference in such case.

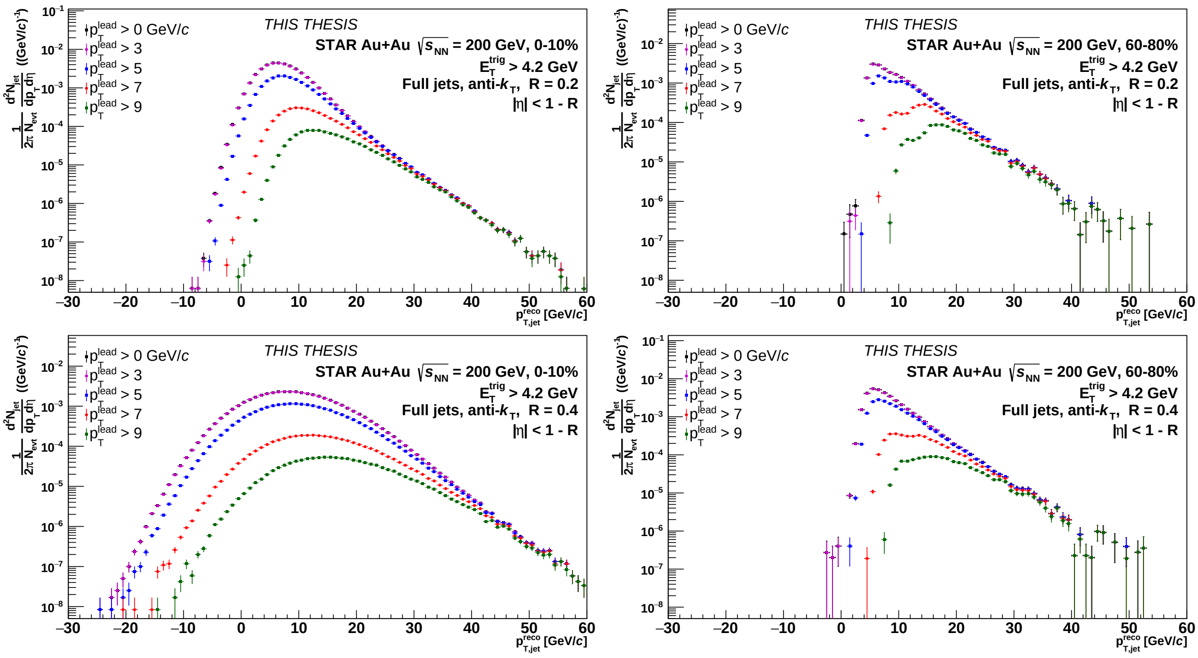

Figure 5.28: Reconstructed transverse momentum $p_{\mathrm{T,jet}}^{\mathrm{reco}}$ spectra of anti-k_{T} jets containing the trigger tower, reconstructed with $R = 0.2$ (top) and $R = 0.4$ (bottom) in central (left) and peripheral (right) Au+Au collisions at $\sqrt{s_{\mathrm{NN}}} = 200$ GeV. Black markers represent the unbiased distribution ($p_{\mathrm{T}}^{\mathrm{lead}} > 0$ GeV/c, practically overlapping with the purple points), while other colors of markers represent different values of the $p_{\mathrm{T}}^{\mathrm{lead}}$ cut: 3 GeV/c (purple), 5 GeV/c (blue), 7 GeV/c (red) and 9 GeV/c (green). Error bars represent statistical uncertainties only.

where the subscript represents the number of fit points. Table 5.4 summarizes the normalization factors obtained from the two regions and the calculated uncertainty. One can see that the bias in peripheral collisions is much larger than in central collisions, which is expected, since central MB collisions produce more jets per event than peripheral collisions. It can also be seen that this uncertainty is large for all bins and this needs to be taken into account when interpreting the results.

HT2/MB ratio	Central (0–10 %)			Peripheral (60–80 %)		
$p_{\mathrm{T,jet}}$ (GeV/c)	10-28	15-28	Rel. error (%)	10-28	15-28	Relative error (%)
R = 0.2, $p_{\mathrm{T,min}}^{\mathrm{lead}}$ = 5 GeV/c	85.3	110.8	29.9	1243.1	2163.9	74.1
R = 0.2, $p_{\mathrm{T,min}}^{\mathrm{lead}}$ = 7 GeV/c	73.1	101.5	38.9	1563.6	2159.8	38.1
R = 0.2, $p_{\mathrm{T,min}}^{\mathrm{lead}}$ = 9 GeV/c	64.2	94.8	47.7	1575.1	2240.6	42.6
R = 0.3, $p_{\mathrm{T,min}}^{\mathrm{lead}}$ = 5 GeV/c	493.8	797.7	61.5	1140.1	1877.5	64.7
R = 0.3, $p_{\mathrm{T,min}}^{\mathrm{lead}}$ = 7 GeV/c	291.3	486.2	66.9	1259.2	2234.9	77.5
R = 0.3, $p_{\mathrm{T,min}}^{\mathrm{lead}}$ = 9 GeV/c	175.5	336.4	91.8	1628.3	2135.8	31.2
R = 0.4, $p_{\mathrm{T,min}}^{\mathrm{lead}}$ = 5 GeV/c	-	-	-	1255.6	1548.6	23.3
R = 0.4, $p_{\mathrm{T,min}}^{\mathrm{lead}}$ = 7 GeV/c	-	-	-	1481.8	1853.2	25.1
R = 0.4, $p_{\mathrm{T,min}}^{\mathrm{lead}}$ = 9 GeV/c	-	-	-	1879.5	1868.8	0.6

Table 5.4: Ratios of jet spectra (multiple combinations of R and $p_{\mathrm{T}}^{\mathrm{lead}}$) obtained from the HT2 and MB datasets in central and peripheral Au+Au collisions at $\sqrt{s_{\mathrm{NN}}}$ = 200 GeV along with the associated relative systematic error in the two considered $p_{\mathrm{T,jet}}$ ranges.

Chapter 6

Results

This chapter contains the results obtained from the inclusive jet analysis described in the previous chapter. Although this analysis has been regularly presented to and discussed within the STAR Physics Working Group (PWG) which focuses on hard probes, the results have not yet been approved by STAR and accepted for publication. The results shown here are therefore for this thesis only. As mentioned before, these results are affected by the large uncertainty of the bias caused by the implementation of the HT2 trigger during the online event selection, which significantly alters the possibility of physics interpretation. Nevertheless, these results are still very valuable and demonstrate the feasibility of this challenging analysis, which paves the way for future improvements - including the precise determination of the inclusive jet cross section in Au+Au collisions.

The first results are the corrected $p_{\mathrm{T,jet}}$ spectra (Sec. 6.1). Section 6.2 discusses the effect of the $p_{\mathrm{T}}^{\mathrm{lead}}$ cut on the resulting spectra and the determination of the region of small bias. Section 6.3 presents the nuclear modification factor R_{AA} together with comparison to results from other analyses in A+A collisions at RHIC and the LHC. Sec. 6.4 shows the nuclear modification factor R_{CP} and discusses the comparison to other recent results from RHIC and LHC. Finally, the comparison of R_{AA} to theoretical predictions is discussed in Sec. 6.5.

6.1 Corrected Jet p_{T} Spectra

Figure 6.1 shows the spectra of fully reconstructed inclusive jets measured at STAR in central and peripheral Au+Au collisions at $\sqrt{s_{\mathrm{NN}}} = 200$ GeV. The corrected invariant yields are shown for $R = 0.2, 0.3$ and 0.4 (peripheral only), as a function $p_{\mathrm{T,jet}}$. Jets were reconstructed with $p_{\mathrm{T,min}}^{\mathrm{lead}} = 5$ GeV/c. The spectra are reported up to 60 GeV/c in central and up to 50 GeV/c in peripheral Au+Au collisions, which is a quarter of the maximum energy rechable in STAR heavy–ion runs. Figure 6.2 shows the same spectra for jets reconstructed with $p_{\mathrm{T,min}}^{\mathrm{lead}} = 7$ GeV/c and Fig. 6.3 for jets reconstructed with $p_{\mathrm{T,min}}^{\mathrm{lead}} = 9$ GeV/c. Note that the low $p_{\mathrm{T,jet}}$ values are strongly biased due to the $p_{\mathrm{T}}^{\mathrm{lead}}$ requirement and that the normalization uncertainty is not shown in the figures.

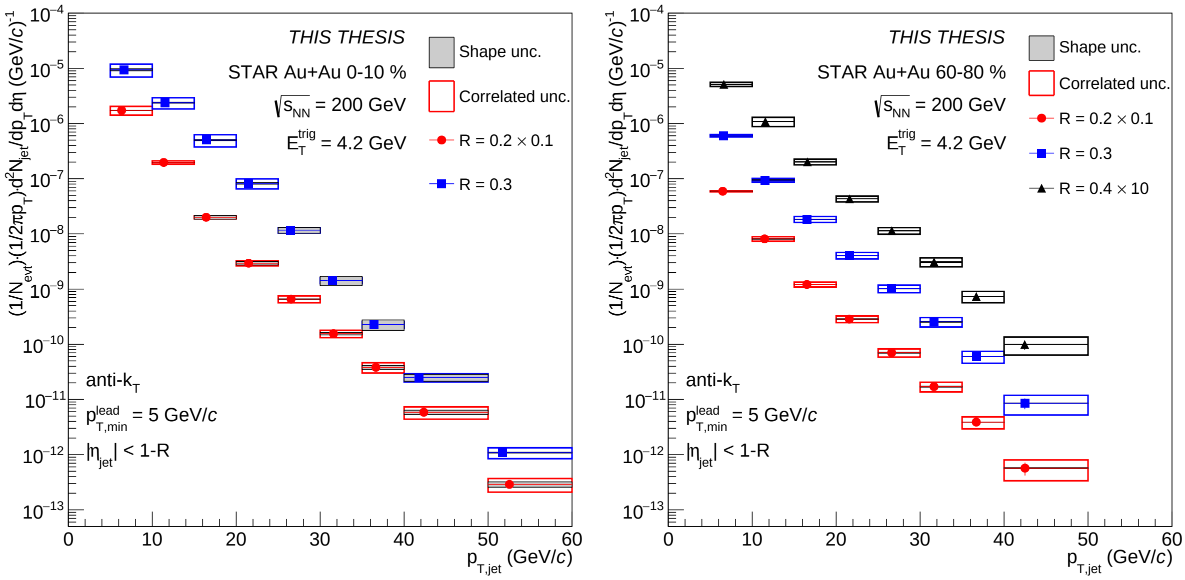

Figure 6.1: Spectra of inclusive anti-k_T jets reconstructed in central (left) and peripheral (right) Au+Au collisions at $\sqrt{s_{NN}}$ = 200 GeV with $p_{T,min}^{lead}$ = 5 GeV/c. Red circles represent jets reconstructed with R = 0.2 (scaled down by factor 10 for visibility), blue squares represent jets reconstructed with R = 0.3 and black triangles represent R = 0.4 jets (peripheral only, scaled up by factor 10 for visibility). Error bars represent statistical uncertainties while colored boxes represent correlated systematic uncertainty and shaded grey area represents the shape uncertainty.

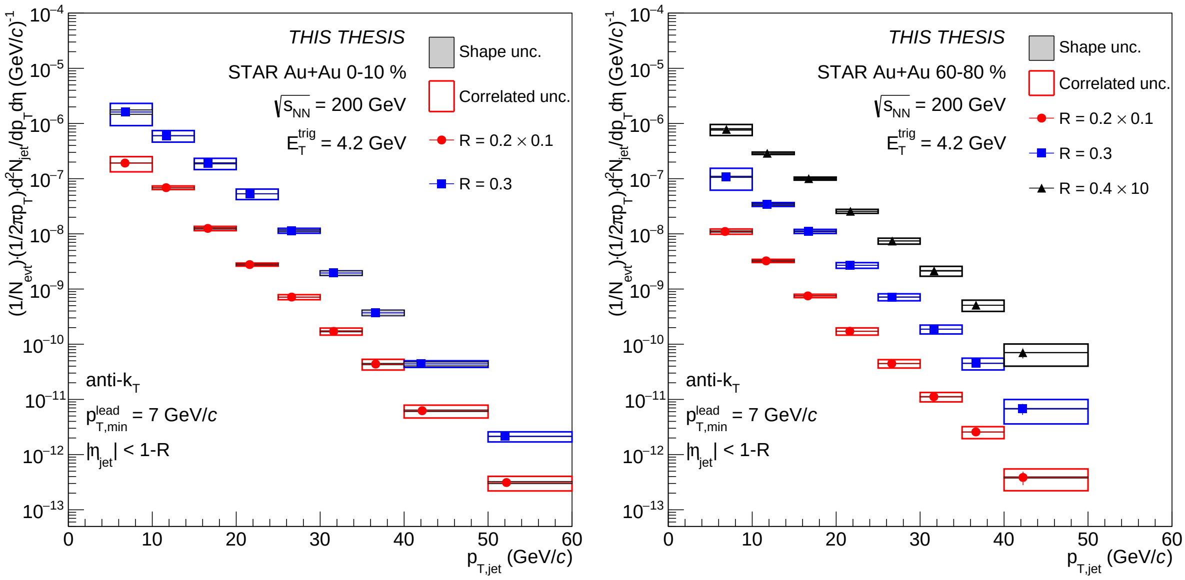

Figure 6.2: Spectra of inclusive anti-k_T jets reconstructed in central (left) and peripheral (right) Au+Au collisions at $\sqrt{s_{NN}}$ = 200 GeV with $p_{T,min}^{lead}$ = 7 GeV/c. Red circles represent jets reconstructed with R = 0.2 (scaled down by factor 10 for visibility), blue squares represent jets reconstructed with R = 0.3 and black triangles represent R = 0.4 jets (peripheral only, scaled up by factor 10 for visibility). Error bars represent statistical uncertainties while colored boxes represent correlated systematic uncertainty and shaded grey area represents the shape uncertainty.

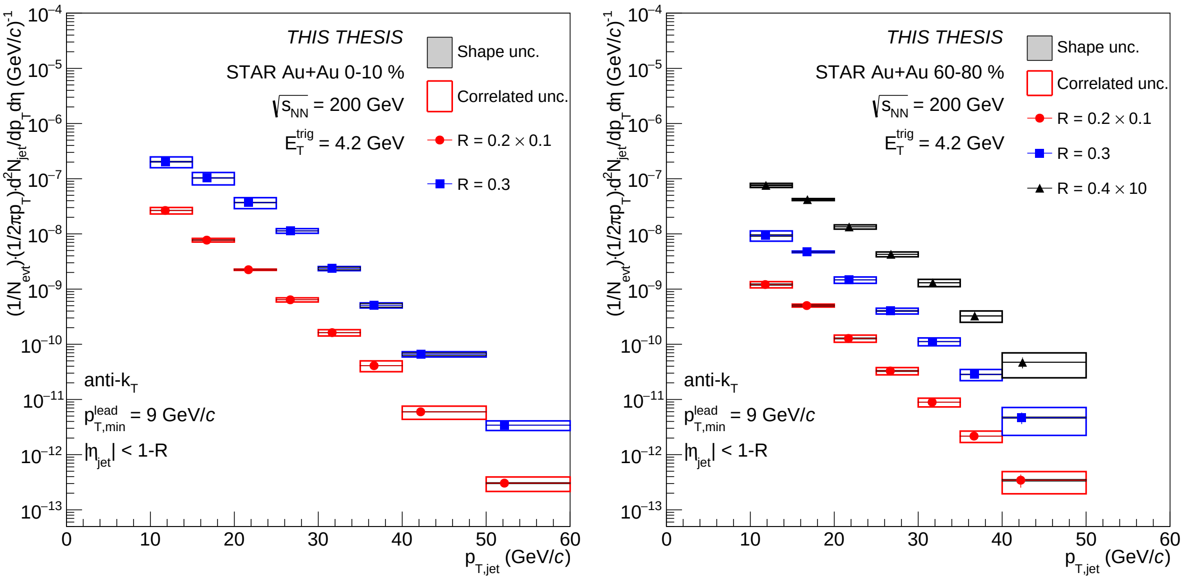

Figure 6.3: Spectra of inclusive anti-k_T jets reconstructed in central (left) and peripheral (right) Au+Au collisions at $\sqrt{s_{NN}} = 200$ GeV with $p_{T,min}^{lead} = 9$ GeV/c. Red circles represent jets reconstructed with $R = 0.2$ (scaled down by factor 10 for visibility), blue squares represent jets reconstructed with $R = 0.3$ and black triangles represent $R = 0.4$ jets (peripheral only, scaled up by factor 10 for visibility). Error bars represent statistical uncertainties while colored boxes represent correlated systematic uncertainty and shaded grey area represents the shape uncertainty.

6.2 Bias of Leading Particle p_T Cut

As discussed in Subsec. 5.3.4, the jet spectra are biased by the leading hadron transverse momentum requirement and it can be seen that the spectra for different values of the p_T^{lead} cut overlap at high $p_{T,jet}^{reco}$. This implies that there is a region where the bias is negligible. In order to find this region, one needs to compare the fully corrected spectra instead. Naturally, one would estimate this bias by comparing the spectra to the unbiased spectrum ($p_{T,min}^{lead} = 0$ GeV/c). However, such spectrum is not available, since the large background makes the correction procedure too difficult. The bias can be therefore estimated by looking at ratios of jet spectra reconstructed with different values of $p_{T,min}^{lead}$. Since the jet population with larger p_T^{lead} is a subset of the population with smaller p_T^{lead}, the ratio is expected to approach unity in the high-$p_{T,jet}$ region, where the bias should be small. In our case, the region, where the ratio is within uncertainties consistent with difference smaller than 10%, is considered and labeled as "~Unbiased".

It would be interesting to compare this behavior with results from p+p collisions at the same collision energy. Since there is no such reference available at STAR, the reference spectra were calculated using a PYTHIA 6 MC generator. Specifically, the STAR tune was used (see [133] for details and Subsec. 5.4.1 for a brief description). The relative uncertainty of the PYTHIA p+p reference has been estimated by generating the jet spectra using alternative tunes, each modifying certain parameter. Tune pairs 371 and 372 vary the magnitude of initial- and final-state radiation, tune 374 tests reduced color re-connection, tunes 376 and 377 modify longitudinal and transverse fragmentation, and tune 383 uses Innsbruck hadronization parameters. The uncertainty has been taken from the maximum deviation (tunes

371 and 372) from the nominal PYTHIA version (STAR tune). The uncertainty has a negligible dependence on $p_{\mathrm{T,jet}}$ and therefore is quoted as a global systematic uncertainty of 22 % for $R = 0.2$, 20 % for $R = 0.3$ and 18 % for $R = 0.4$ jets.

Figures 6.4 – 6.8 show the ratios of jet spectra $R\left(p_{\mathrm{T,min}}^{\mathrm{lead}} = 7\ \mathrm{GeV}/c \middle/ p_{\mathrm{T,min}}^{\mathrm{lead}} = 5\ \mathrm{GeV}/c\right)$ and also $R\left(p_{\mathrm{T,min}}^{\mathrm{lead}} = 9\ \mathrm{GeV}/c \middle/ p_{\mathrm{T,min}}^{\mathrm{lead}} = 7\ \mathrm{GeV}/c\right)$ for different jet R and collision centrality along with the p+p reference. In all cases, the ratios are consistent within uncertainties with the p+p reference. There seems to be a tension for the $R = 0.3$ jets in central collisions, where the ratio appears to be above unity at high $p_{\mathrm{T,jet}}$ for both combinations of $p_{\mathrm{T}}^{\mathrm{lead}}$. The ratio $R\left(p_{\mathrm{T,min}}^{\mathrm{lead}} = 9\ \mathrm{GeV}/c \middle/ p_{\mathrm{T,min}}^{\mathrm{lead}} = 7\ \mathrm{GeV}/c\right)$ is consistent with unity when taking into account the large normalization uncertainty. One can assume that the ratio in reality plateaus at unity and for this reason, one extra data point is taken out of the ~Unbiased region. For the $R\left(p_{\mathrm{T,min}}^{\mathrm{lead}} = 7\ \mathrm{GeV}/c \middle/ p_{\mathrm{T,min}}^{\mathrm{lead}} = 5\ \mathrm{GeV}/c\right)$ case, even the normalization uncertainty is not sufficient to fully explain the tension. Therefore, it suggests that the normalization factors between the two spectra are not fully correlated, as was assumed in this case. Since this analysis offers no way to determine the $p_{\mathrm{T}}^{\mathrm{lead}}$ bias for spectra reconstructed with $p_{\mathrm{T,min}}^{\mathrm{lead}} = 9$ GeV/c, physics results for these spectra should be taken as biased throughout the $p_{\mathrm{T,jet}}$ range.

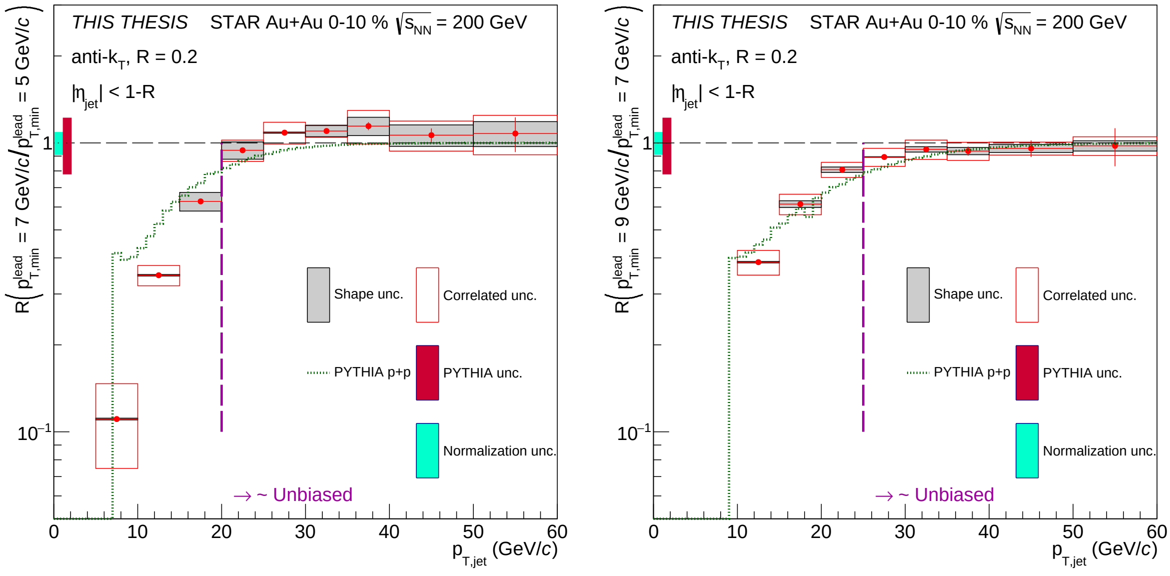

Figure 6.4: Ratio of anti-k_{T} jets reconstructed in central Au+Au collisions at $\sqrt{s_{\mathrm{NN}}} = 200$ GeV with $R = 0.2$ and $p_{\mathrm{T,min}}^{\mathrm{lead}} = 5$ and $p_{\mathrm{T,min}}^{\mathrm{lead}} = 7$ GeV/c (left) and $p_{\mathrm{T,min}}^{\mathrm{lead}} = 7$ and $p_{\mathrm{T,min}}^{\mathrm{lead}} = 9$ GeV/c (right) as a function of $p_{\mathrm{T,jet}}$. Error bars represent statistical uncertainties while colored boxes represent correlated systematic uncertainty and shaded grey area represents the shape uncertainty. The green dotted line represents PYTHIA 6 calculation, while the pink box represents its uncertainty. The teal box represents the normalization uncertainty. The ~Unbiased region lies to the right of the purple dashed line.

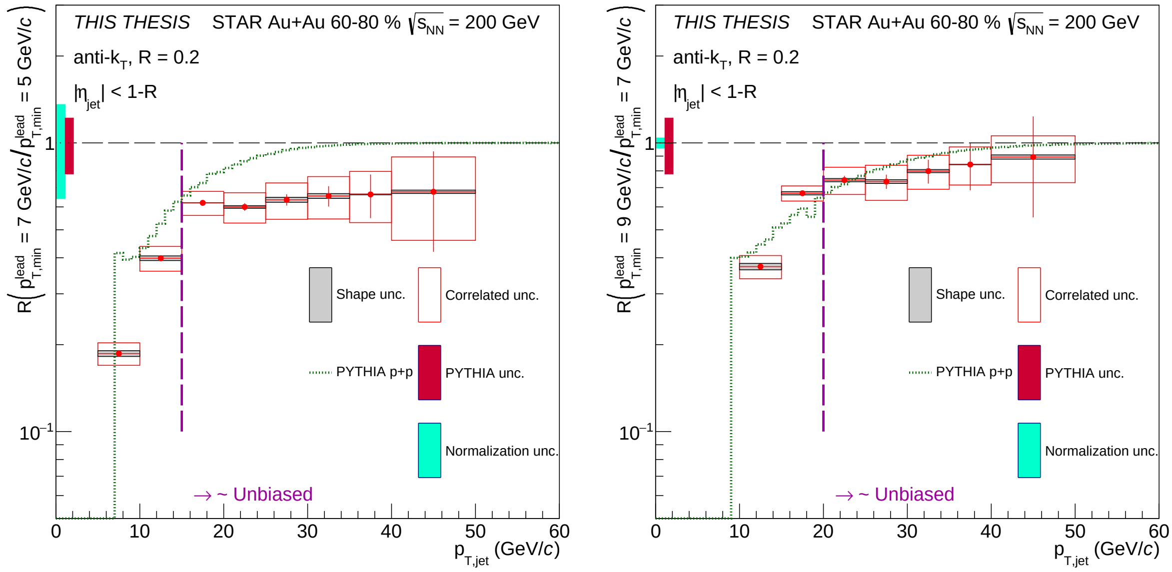

Figure 6.5: Ratio of anti-k_T jets reconstructed in peripheral Au+Au collisions at $\sqrt{s_{NN}} = 200$ GeV with $R = 0.2$ and $p_{T,min}^{lead} = 5$ and $p_{T,min}^{lead} = 7$ GeV/c (left) and $p_{T,min}^{lead} = 7$ and $p_{T,min}^{lead} = 9$ GeV/c (right) as a function of $p_{T,jet}$. Error bars represent statistical uncertainties while colored boxes represent correlated systematic uncertainty and shaded grey area represents the shape uncertainty. The green dotted line represents PYTHIA 6 calculation, while the pink box represents its uncertainty. The teal box represents the normalization uncertainty. The ~Unbiased region lies to the right of the purple dashed line.

6.3 Nuclear Modification Factor R_{AA}

The nuclear modification factor R_{AA} is the main observable of jet quenching, as it quantifies the jet yield suppression in heavy–ion collisions. By definition (3.12), the R_{AA} requires a baseline from p+p collisions at the same energy. As mentioned in Subsec. 3.6.1 and Sec. 6.2, there is currently no published measurement of inclusive jet cross section production at $\sqrt{s} = 200$ GeV at STAR which would serve as a baseline. Therefore, the same p+p PYTHIA 6 simulation, as introduced in Sec. 6.2, is used as the vacuum reference. The PYTHIA spectra were then scaled by the nuclear thickness function T_{AA}, which was calculated from the MC Glauber model [47] and has a value of $T_{AA} = 22.8 \pm 1.6$ mb^{-1} for central Au+Au collisions and $T_{AA} = 0.49 \pm 0.14$ mb^{-1} for peripheral Au+Au collisions at $\sqrt{s_{NN}} = 200$ GeV [131]. The relative uncertainties of the T_{AA} were assigned as a global systematic uncertainty of the R_{AA} results.

For each value of R, two spectra were reconstructed. The jets in the first spectrum were reconstructed without any requirement on the leading particle. The corresponding nuclear modification factor is denoted as $R_{AA}^{PYTHIA,UB}$, to clearly show that the baseline is simulated by PYTHIA and that the p+p spectrum is unbiased by the p_T^{lead} cut. Figure 6.9 shows the nuclear modification factor $R_{AA}^{PYTHIA,UB}$ for small jets as a function of $p_{T,jet}$, p_T^{lead} and centrality. For both values of p_T^{lead}, the $R_{AA}^{PYTHIA,UB} \simeq 0.2 - 0.3$ in central collisions, demonstrating strong jet yield suppression with weak $p_{T,jet}$ dependence in the region of small p_T^{lead} bias.

The results for jets reconstructed with $p_{T,min}^{lead} = 5$ GeV/c are consistent in the overlap $p_{T,jet}$ range with results from Pb+Pb collisions at $\sqrt{s_{NN}} = 5.02$ TeV [135] by ALICE. This however does not

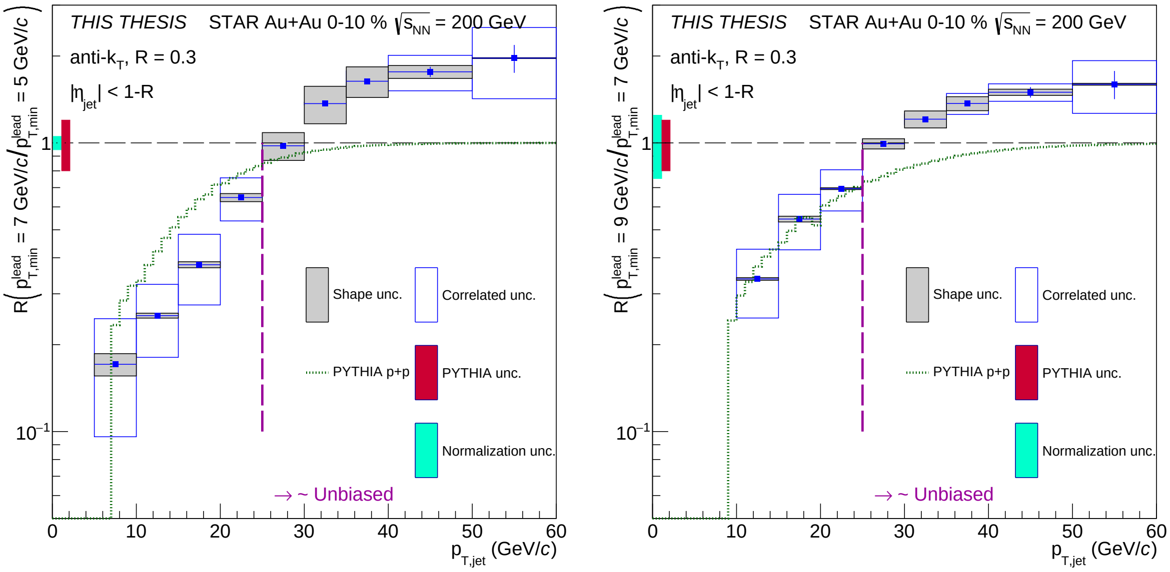

Figure 6.6: Ratio of anti-k_T jets reconstructed in central Au+Au collisions at $\sqrt{s_{NN}} = 200$ GeV with $R = 0.3$ and $p_{T,min}^{lead} = 5$ and $p_{T,min}^{lead} = 7$ GeV/c (left) and $p_{T,min}^{lead} = 7$ and $p_{T,min}^{lead} = 9$ GeV/c (right) as a function of $p_{T,jet}$. Error bars represent statistical uncertainties while colored boxes represent correlated systematic uncertainty and shaded grey area represents the shape uncertainty. The green dotted line represents PYTHIA 6 calculation, while the pink box represents its uncertainty. The teal box represents the normalization uncertainty. The ~Unbiased region lies to the right of the purple dashed line.

mean that the energy losses are of the same level at RHIC and LHC energies. Because the spectra at RHIC fall faster than at the LHC, similar level of suppression indicates larger energy loss in the central Pb+Pb collisions at the LHC. The $R_{AA}^{PYTHIA,UB}$ is significantly below the results from previous charged-particle jet analysis [131]. This difference can be explained by taking into account the normalization uncertainty and the fact that charged-particle jets do not recover the full energy of the original parton, unlike fully-reconstructed jets, and therefore the $p_{T,jet}$ of this measurement is not identical to the results from this thesis and ALICE. In peripheral collisions, the $R_{AA}^{PYTHIA,UB}$ is consistent with unity and with STAR charged-particle jet data within the uncertainties in the ~Unbiased region.

Figure 6.10 shows the $R_{AA}^{PYTHIA,UB}$ as a function of $p_{T,jet}$, p_T^{lead} and centrality for jets reconstructed with $R = 0.3$. Contrary to expectations, the results from central Au+Au collisions hint larger suppression and different $p_{T,jet}$ dependence than $R = 0.2$ jets. However, the reliability of these results can be questioned based on the large systematic uncertainties. The $R_{AA}^{PYTHIA,UB}$ in peripheral collisions is again consistent with unity within the measurement uncertainty. Once again, it needs to be mentioned that the normalization uncertainty in these bins is large.

Figure 6.11 shows $R_{AA}^{PYTHIA,UB}$ as a function of $p_{T,jet}$ and p_T^{lead} for jets reconstructed with $R = 0.4$ in peripheral Au+Au collisions. The $R_{AA}^{PYTHIA,UB}$ follows a similar trend as for smaller jets and is consistent with unity for smaller values of p_T^{lead}.

The second baseline which was calculated includes the same p_T^{lead} requirement as the jets from Au+Au collisions. The motivation for this is the assumption that the bias introduced by the p_T^{lead} requirement will at least partially cancel out. However, since there is no way to really quantify the magnitude of this effect, this spectrum should be regarded as double–biased, instead of unbiased. The corresponding

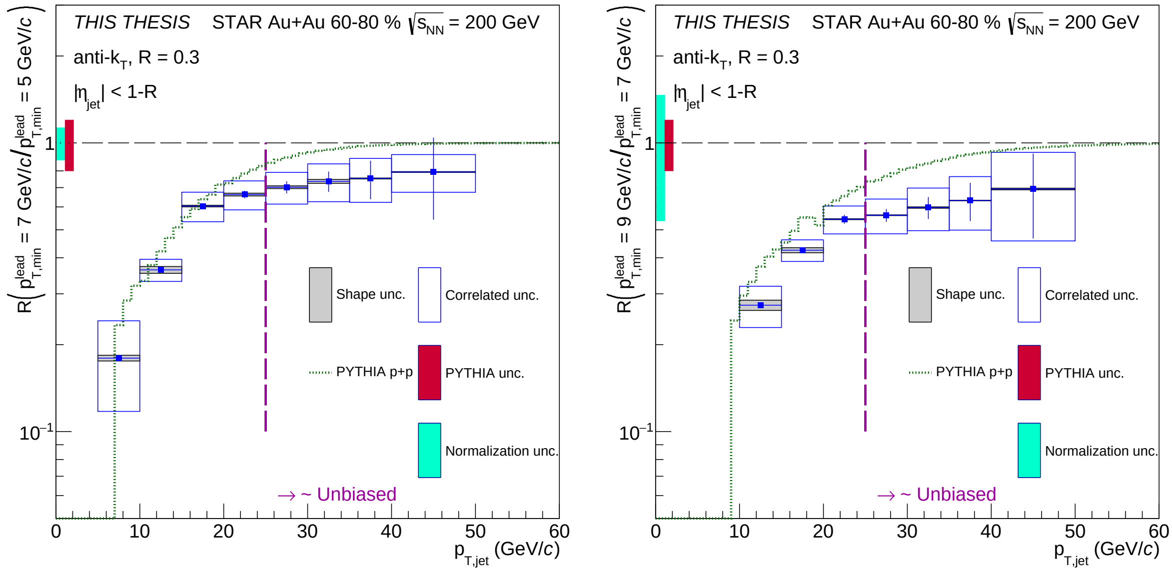

Figure 6.7: Ratio of anti-k_T jets reconstructed in peripheral Au+Au collisions at $\sqrt{s_{NN}} = 200$ GeV with $R = 0.3$ and $p_{T,min}^{lead} = 5$ and $p_{T,min}^{lead} = 7$ GeV/c (left) and $p_{T,min}^{lead} = 7$ and $p_{T,min}^{lead} = 9$ GeV/c (right) as a function of $p_{T,jet}$. Error bars represent statistical uncertainties while colored boxes represent correlated systematic uncertainty and shaded grey area represents the shape uncertainty. The green dotted line represents PYTHIA 6 calculation, while the pink box represents its uncertainty. The teal box represents the normalization uncertainty. The ~Unbiased region lies to the right of the purple dashed line.

nuclear modification factor is denoted $R_{AA}^{PYTHIA,p_T^{lead}}$. Figures 6.12–6.14 show the $R_{AA}^{PYTHIA,p_T^{lead}}$ as a function of $p_{T,jet}$,p_T^{lead}, R and centrality. It can be seen that the shape of $R_{AA}^{PYTHIA,p_T^{lead}}$ does not differ much from $R_{AA}^{PYTHIA,UB}$ in the high–$p_{T,jet}$ region in all cases and therefore the conclusions are the same. Additional $R_{AA}^{PYTHIA,UB}$ and $R_{AA}^{PYTHIA,p_T^{lead}}$ results can be found in App. D.

6.4 Nuclear Modification Factor R_{CP}

It is also interesting to look at the nuclear modification factor R_{CP} defined as the ratio of the spectrum from central collisions and peripheral collisions:

$$R_{CP} = \frac{\langle N_{coll}^{per} \rangle}{\langle N_{coll}^{cent} \rangle} \cdot \frac{\frac{1}{N_{evt}^{AA,cent}} \frac{d^2 N_{AA,cent}^{jet}}{dp_{T,jet} d\eta}}{\frac{1}{N_{evt}^{AA,per}} \frac{d^2 N_{AA,per}^{jet}}{dp_{T,jet} d\eta}}, \tag{6.1}$$

where $\langle N_{coll}^{per/cent} \rangle$ is the mean number of binary collisions in peripheral/central events. The values are taken from Tab. 5.3 (the version for HT events was used). The R_{CP} measurement takes advantage of the fact that it does not depend significantly on other analyses (or modelling) as in R_{AA} and can be obtained directly from the data. Additionally, some sources of systematic uncertainty – for example tracking efficiency – are highly correlated between the spectra and should cancel out.

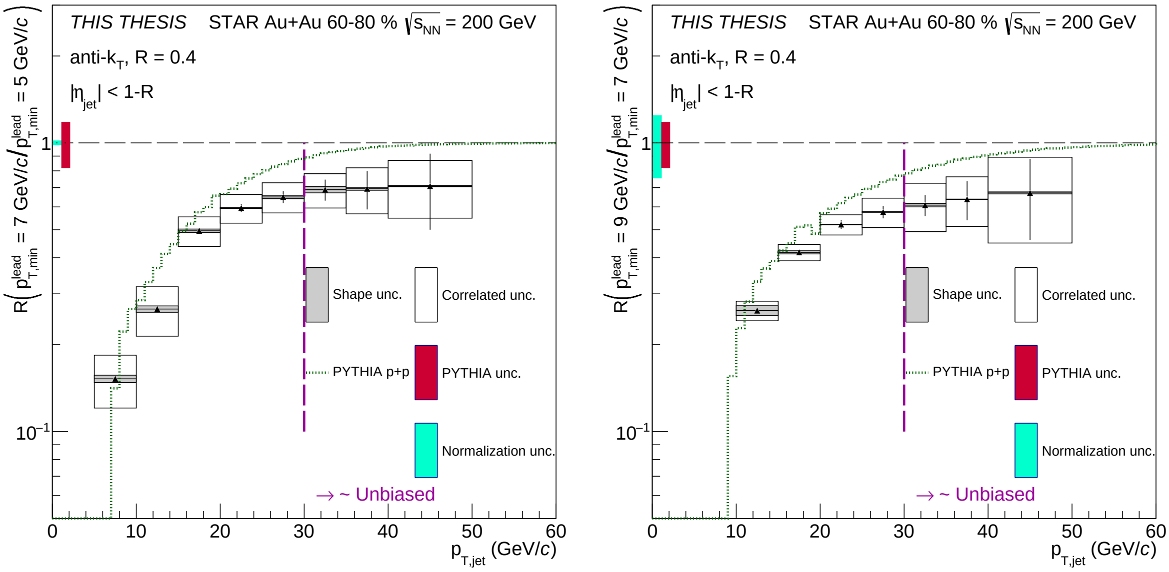

Figure 6.8: Ratio of anti-k_T jets reconstructed in peripheral Au+Au collisions at $\sqrt{s_{NN}} = 200$ GeV with $R = 0.4$ and $p_{T,min}^{lead} = 5$ and $p_{T,min}^{lead} = 7$ GeV/c (left) and $p_{T,min}^{lead} = 7$ and $p_{T,min}^{lead} = 9$ GeV/c (right) as a function of $p_{T,jet}$. Error bars represent statistical uncertainties while colored boxes represent correlated systematic uncertainty and shaded grey area represents the shape uncertainty. The green dotted line represents PYTHIA 6 calculation, while the pink box represents its uncertainty. The teal box represents the normalization uncertainty. The ~Unbiased region lies to the right of the purple dashed line.

The left panel of Fig. 6.15 shows the nuclear modification factor R_{CP} of small jets reconstructed with $p_{T,min}^{lead}$= 5 GeV/c as a function of $p_{T,jet}$. The ratio in the region with small p_T^{lead} bias is flat with respect to $p_{T,jet}$ with $R_{CP} \sim 0.3$. The ratio is consistent within uncertainties with ALICE results from charged-particle jet analysis in Pb+Pb collisions at $\sqrt{s_{NN}} = 2.76$ TeV [189]. The results from charged-particle jet analysis in Au+Au collisions at $\sqrt{s_{NN}} = 200$ GeV at STAR [131] show larger value of R_{CP} in the ~Unbiased region, however, the statistical and mainly systematical precision of both measurements is not sufficient to determine the nature of the tension between the two measurements. The right panel shows the same ratio for jets reconstructed with $p_{T,min}^{lead}$= 7 GeV/c and the ratio is flat in $p_{T,jet}$ and reaches values of around $R_{CP} \sim 0.4$. However, the uncertainties of this measurement are large as well. The normalization uncertainty for larger jets is too large to produce any reliable estimation of R_{CP} and therefore those are not reported in this thesis.

6.5 Comparison of R_{AA} with Theoretical Predictions

The results from this thesis are compared to two theoretical calculations, which incorporate jet quenching. The next-to-leading-order pQCD calculation (labeled "NLO", [190]) takes into account initial-state nuclear effects and predicts inclusive $R = 0.2$ jet $R_{AA} \sim 0.2$ based on collisional parton energy loss. This calculation was validated by providing a good description of the inclusive jet cross section for $R = 0.4$ jets in p+p collisions at $\sqrt{s} = 200$ GeV [191]. The Soft-Collinear Effective Theory (labeled "SCET" [192], [193]) includes initial-state effects, such as dynamical nuclear shadowing, Cronin effect, and initial-state parton energy loss. This theory describes well the measurement of charged-hadron

$R_{\rm AA}$ at the LHC (i. e. [194]). There are multiple implementations of this model and the version with slightly larger Cronin effect and smaller energy loss is used. Neither model includes any $p_{\rm T}^{\rm lead}$ requirement for the calculated $R_{\rm AA}$. Please note that the reach of the model predictions is limited only because the predictions have been made for [131], where the kinematic reach of the measurement was known to be limited. For the final publication of fully reconstructed jets, once approved by the STAR collaboration, we will ask the respective theorists to extend the $p_{\rm T}$ reach of their prediction to match our data. We would also like to include more model predictions for the final publication.

Figure 6.16 shows the comparison of STAR $R_{\rm AA}^{{\rm PYTHIA},p_{\rm T}^{\rm lead}}$ results to both models for jets reconstructed with $R = 0.2$ in central Au+Au collisions at $\sqrt{s_{\rm NN}} = 200$ GeV. Both models predict very similar level of suppression and very weak $p_{\rm T,jet}$ dependence up to 40 GeV/c. The data, in contrast, show a slightly rising trend and extend to larger values of $p_{\rm T,jet}$. In the overlap region of $p_{\rm T,jet}$ where the $p_{\rm T}^{\rm lead}$ bias of our data is small, the data agree with the model predictions within uncertainties confirming significant energy loss in central Au+Au collisions at top RHIC energy.

Figure 6.17 shows the comparison of $R_{\rm AA}^{{\rm PYTHIA},p_{\rm T}^{\rm lead}}$ for jets reconstructed with $R = 0.3$ with the SCET prediction. It can be seen that the data are significantly below the prediction, but the normalization uncertainty prohibits any strong conclusions from being made.

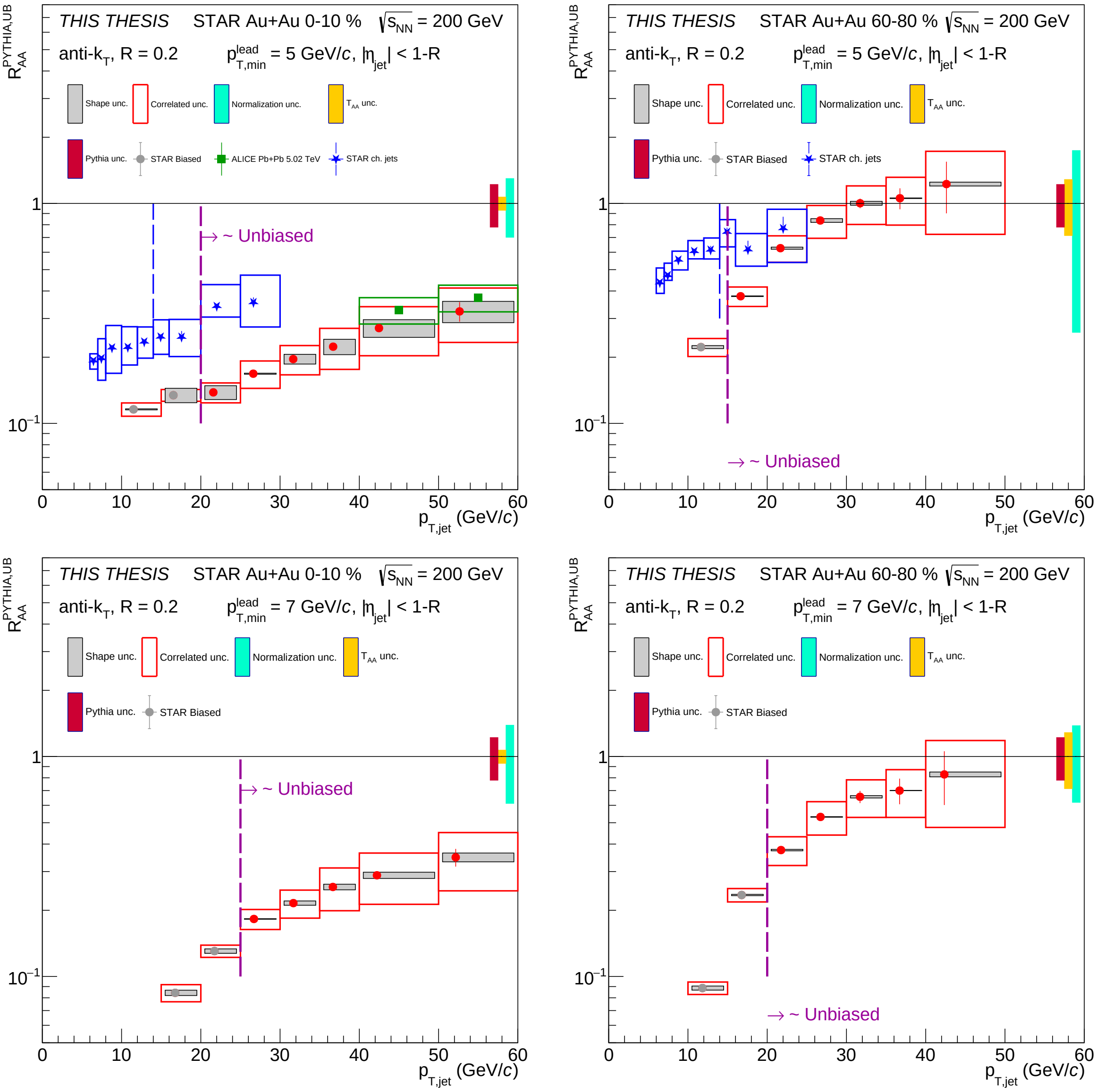

Figure 6.9: Biased nuclear modification factor $R_{AA}^{PYTHIA,UB}$ (red circles) of anti-k_T jets reconstructed with $R = 0.2$ and $p_{T,min}^{lead} = 5$ (top) and $p_{T,min}^{lead} = 7$ (bottom) GeV/c in central (left) and peripheral (right) Au+Au collisions at $\sqrt{s_{NN}} = 200$ GeV as a function of $p_{T,jet}$. The colored boxes around markers represent correlated systematic uncertainty, while gray-shaded areas represent shape systematic uncertainty. The boxes around unity represent global systematic uncertainties – normalization of the spectra (teal), T_{AA} (orange) and the PYHTIA p+p baseline (pink). The gray circles represent points biased by p_T^{lead} requirement. The purple dashed line represents the start of the region where the p_T^{lead} bias is small. The blue stars ($p_{T,min}^{lead} = 5$ GeV/c only) represent STAR data from charged-particle jet analysis in the same collision system and energy and the blue dashed line represents the start of the "~Unbiased" region for these results. The green squares (central, $p_{T,min}^{lead} = 5$ GeV/c only) represent ALICE results from Pb+Pb collisions at $\sqrt{s_{NN}} = 5.02$ TeV. Only points in the overlap $p_{T,jet}$ range are plotted and systematic errors of this measurement were added in quadrature.

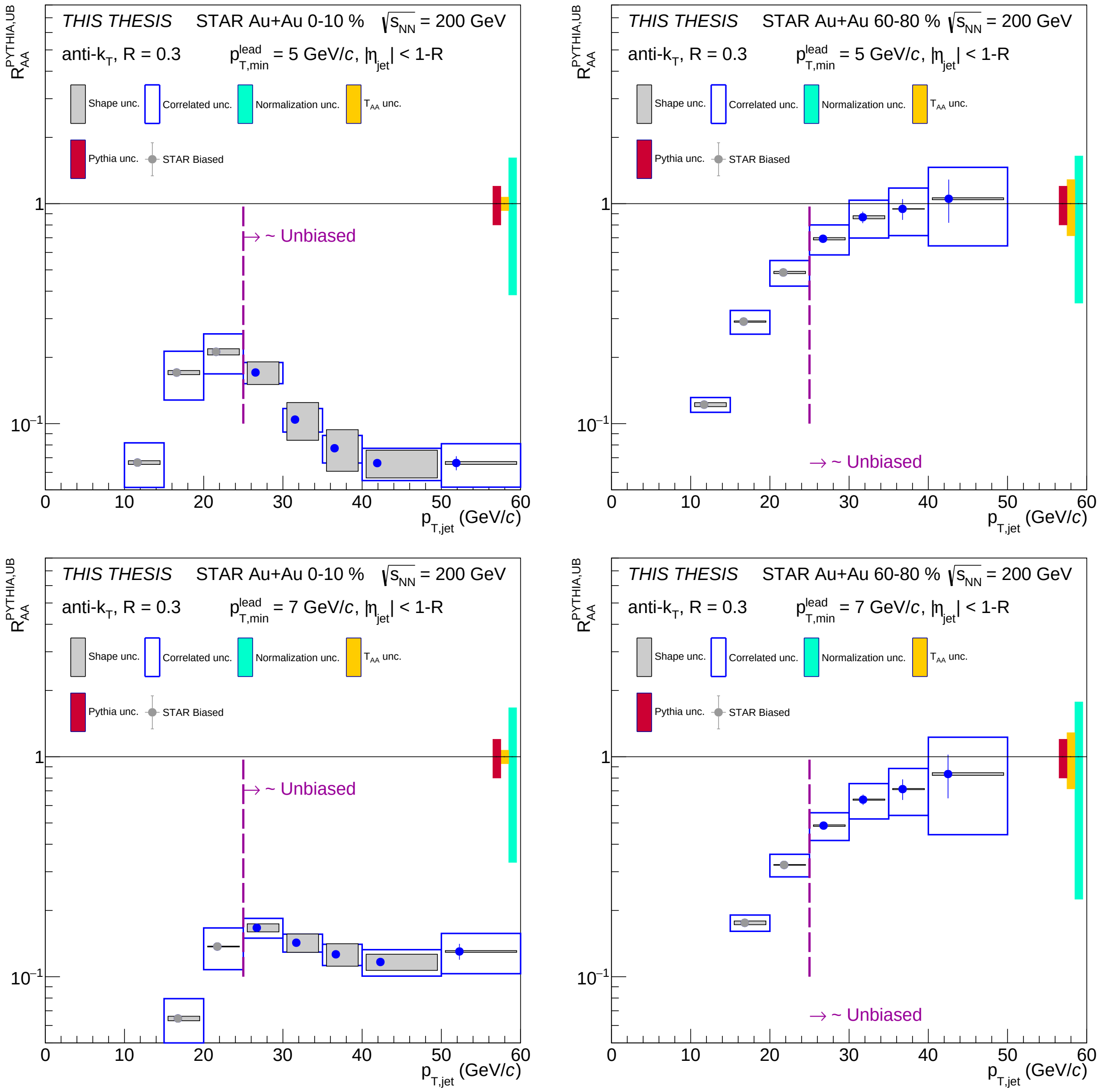

Figure 6.10: Biased nuclear modification factor $R_{\mathrm{AA}}^{\mathrm{PYTHIA,UB}}$ (blue circles) of anti-k_{T} jets reconstructed with $R = 0.3$ and $p_{\mathrm{T,min}}^{\mathrm{lead}} = 5$ (top) and $p_{\mathrm{T,min}}^{\mathrm{lead}} = 7$ (bottom) GeV/c in central (left) and peripheral (right) Au+Au collisions at $\sqrt{s_{\mathrm{NN}}} = 200$ GeV as a function of $p_{\mathrm{T,jet}}$. The colored boxes around markers represent correlated systematic uncertainty, while gray-shaded areas represent shape systematic uncertainty. The boxes around unity represent global systematic uncertainties – normalization of the spectra (teal), T_{AA} (orange) and the PYHTIA p+p baseline (pink). The gray circles represent points biased by $p_{\mathrm{T}}^{\mathrm{lead}}$ requirement. The purple dashed line represents the start of the region where the $p_{\mathrm{T}}^{\mathrm{lead}}$ bias is small.

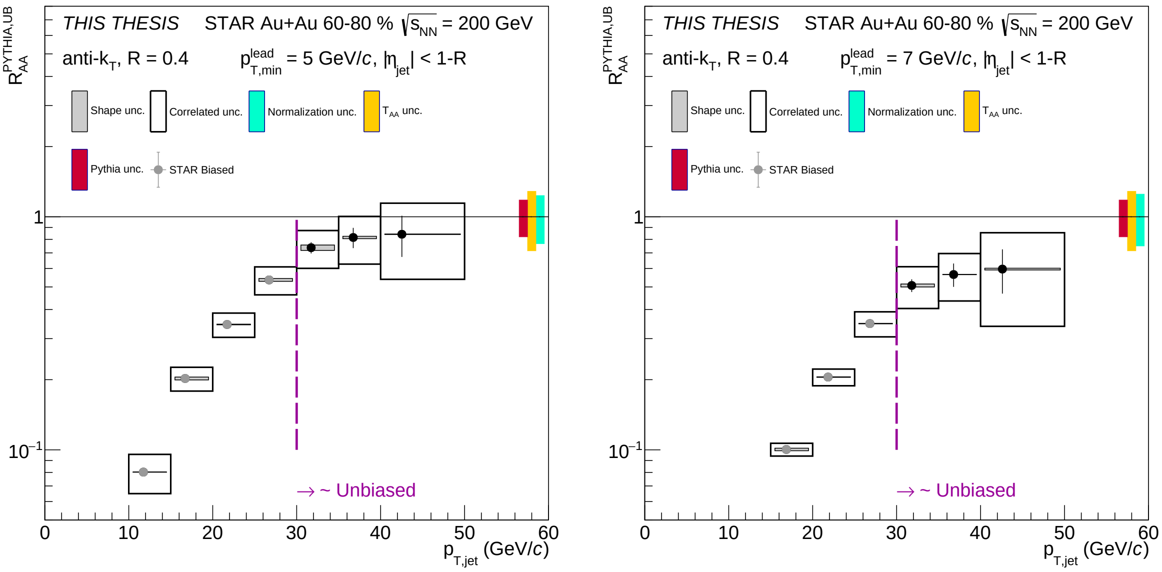

Figure 6.11: Biased nuclear modification factor $R_{AA}^{\text{PYTHIA,UB}}$ (black circles) of anti-k_T jets reconstructed with $R = 0.4$ and $p_{T,\min}^{\text{lead}} = 5$ (left) and $p_{T,\min}^{\text{lead}} = 7$ GeV/c (right) in peripheral Au+Au collisions at $\sqrt{s_{NN}} = 200$ GeV as a function of $p_{T,\text{jet}}$. The colored boxes around markers represent correlated systematic uncertainty, while gray-shaded areas represent shape systematic uncertainty. The boxes around unity represent global systematic uncertainties – normalization of the spectra (teal), T_{AA} (orange) and the PYHTIA p+p baseline (pink). The gray circles represent points biased by p_T^{lead} requirement. The purple dashed line represents the start of the region where the p_T^{lead} bias is small.

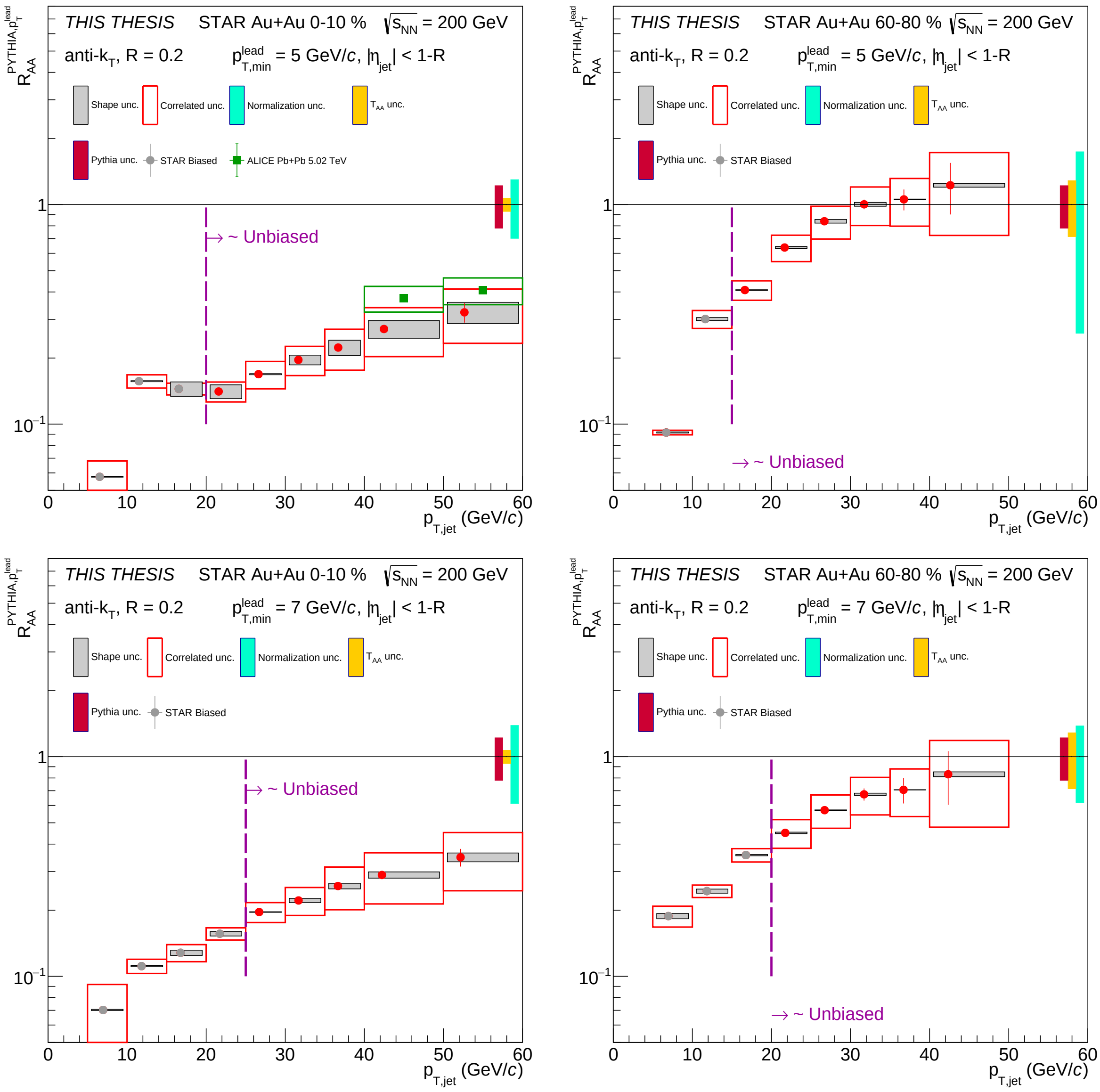

Figure 6.12: Double–biased nuclear modification factor $R_{AA}^{PYTHIA,p_T^{lead}}$ (red circles) of anti-k_T jets reconstructed with $R = 0.2$ and $p_{T,min}^{lead} = 5$ (top) and $p_{T,min}^{lead} = 7$ (bottom) GeV/c in central (left) and peripheral (right) Au+Au collisions at $\sqrt{s_{NN}} = 200$ GeV as a function of $p_{T,jet}$. The colored boxes around markers represent correlated systematic uncertainty, while gray-shaded areas represent shape systematic uncertainty. The boxes around unity represent global systematic uncertainties – normalization of the spectra (teal), T_{AA} (orange) and the PYHTIA p+p baseline (pink). The gray circles represent points biased by p_T^{lead} requirement. The purple dashed line represents the start of the region where the p_T^{lead} bias is small. The green squares (central, $p_{T,min}^{lead} = 5$ GeV/c only) represent ALICE results from Pb+Pb collisions at $\sqrt{s_{NN}} = 5.02$ TeV. Only points in the overlap $p_{T,jet}$ range are plotted and systematic errors of this measurement were added in quadrature.

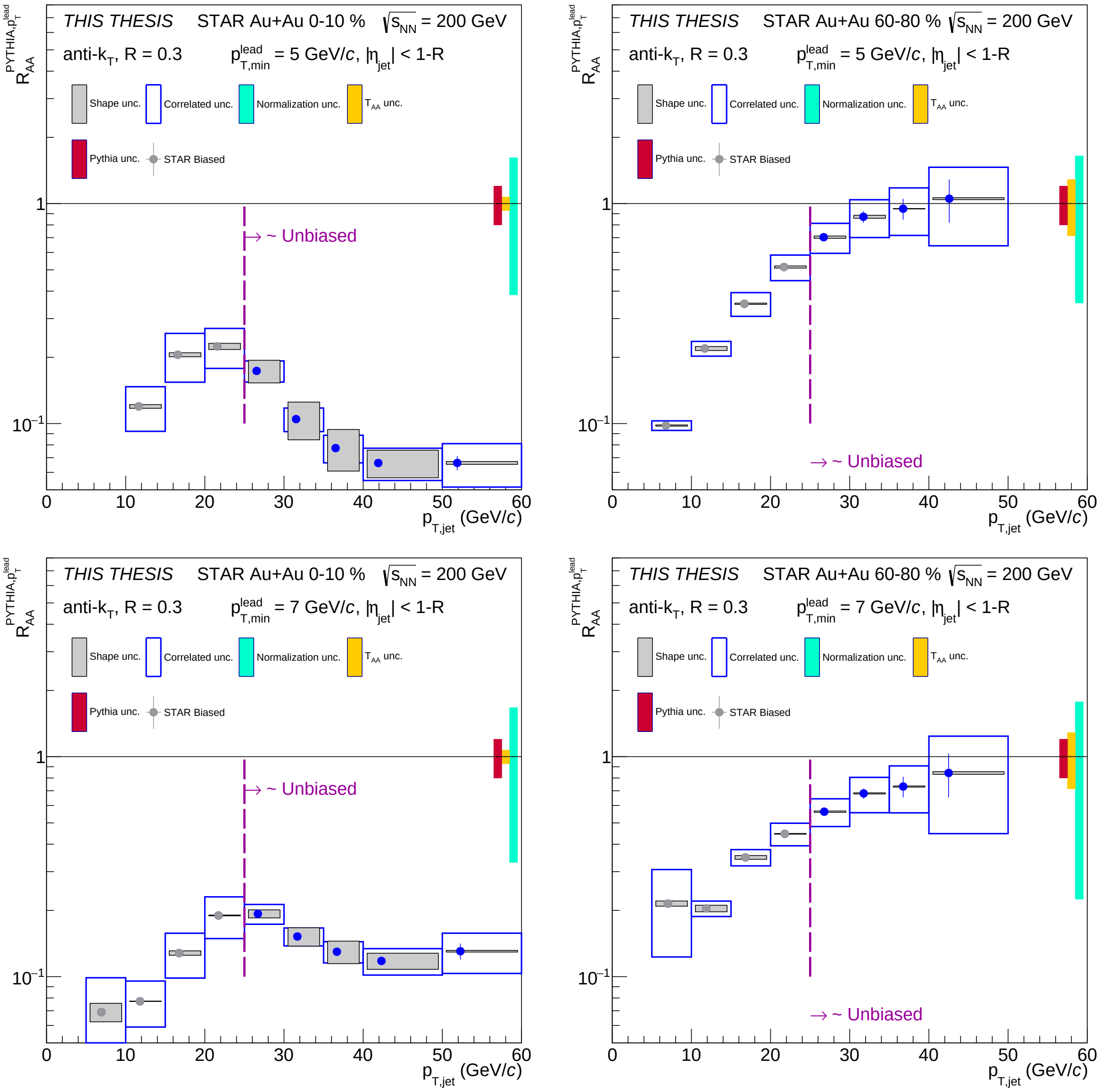

Figure 6.13: Double–biased nuclear modification factor $R_{\mathrm{AA}}^{\mathrm{PYTHIA},p_{\mathrm{T}}^{\mathrm{lead}}}$ (blue circles) of anti-k_{T} jets reconstructed with R = 0.3 and $p_{\mathrm{T,min}}^{\mathrm{lead}}$ = 5 (top) and $p_{\mathrm{T,min}}^{\mathrm{lead}}$ = 7 (bottom) GeV/c in central (left) and peripheral (right) Au+Au collisions at $\sqrt{s_{\mathrm{NN}}} = 200$ GeV as a function of $p_{\mathrm{T,jet}}$. The colored boxes around markers represent correlated systematic uncertainty, while gray-shaded areas represent shape systematic uncertainty. The boxes around unity represent global systematic uncertainties – normalization of the spectra (teal), T_{AA} (orange) and the PYHTIA p+p baseline (pink). The gray circles represent points biased by $p_{\mathrm{T}}^{\mathrm{lead}}$ requirement. The purple dashed line represents the start of the region where the $p_{\mathrm{T}}^{\mathrm{lead}}$ bias is small.

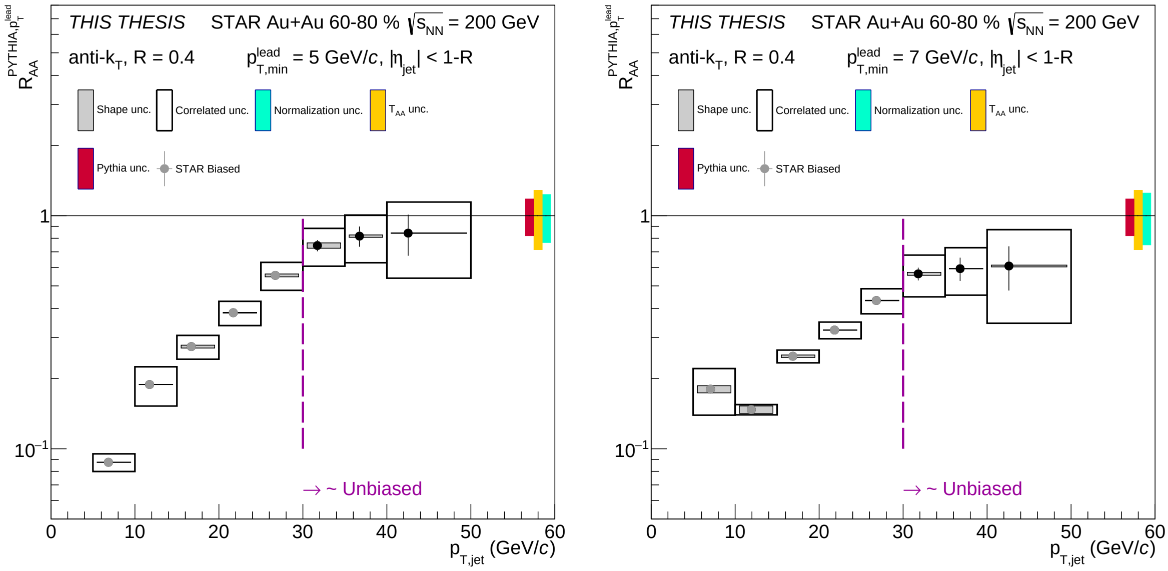

Figure 6.14: Double–biased nuclear modification factor $R_{AA}^{PYTHIA,p_T^{lead}}$ (black circles) of anti-k_T jets reconstructed with $R = 0.4$ and $p_{T,min}^{lead} = 5$ (left) and $p_{T,min}^{lead} = 7$ (right) GeV/c in peripheral Au+Au collisions at $\sqrt{s_{NN}} = 200$ GeV as a function of $p_{T,jet}$. The colored boxes around markers represent correlated systematic uncertainty, while gray-shaded areas represent shape systematic uncertainty. The boxes around unity represent global systematic uncertainties – normalization of the spectra (teal), T_{AA} (orange) and the PYHTIA $p+p$ baseline (pink). The gray circles represent points biased by p_T^{lead} requirement. The purple dashed line represents the start of the region where the p_T^{lead} bias is small.

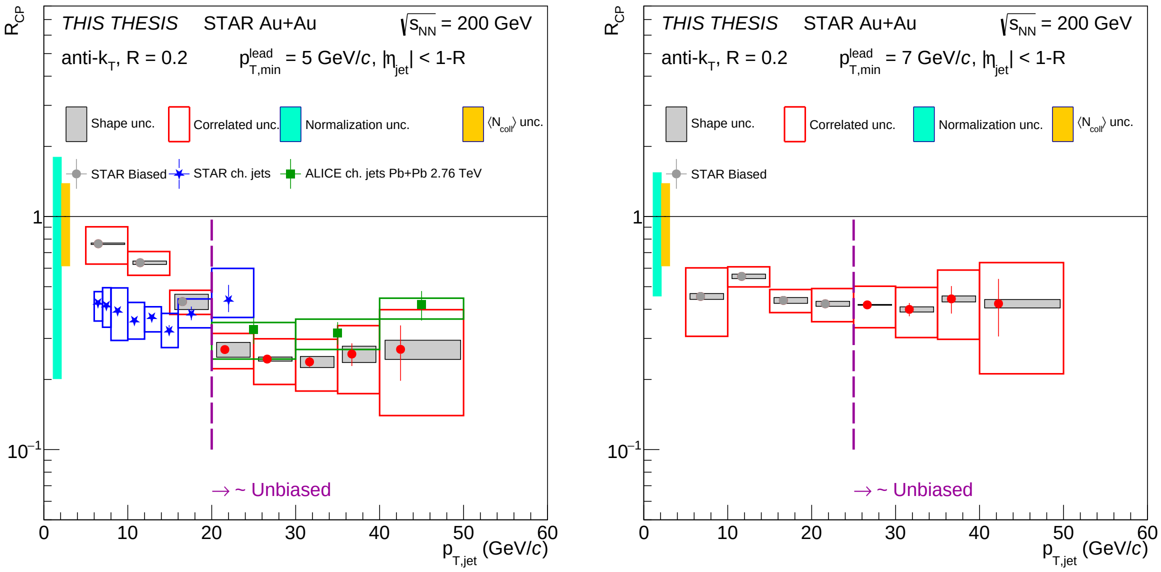

Figure 6.15: Nuclear modification factor R_{CP} (red circles) of anti-k_{T} jets reconstructed with $R = 0.2$ and $p_{\mathrm{T,min}}^{\mathrm{lead}} = 5$ (left) and $p_{\mathrm{T,min}}^{\mathrm{lead}} = 7$ (right) GeV/c in Au+Au collisions at $\sqrt{s_{\mathrm{NN}}} = 200$ GeV as a function of $p_{\mathrm{T,jet}}$. The colored boxes around markers represent correlated systematic uncertainty, while gray-shaded areas represent shape systematic uncertainty. The boxes around unity represent global systematic uncertainties – normalization of the spectra (teal) and T_{AA} (orange). The gray circles represent points biased by $p_{\mathrm{T}}^{\mathrm{lead}}$ requirement. The purple dashed line represents the start of the region where the $p_{\mathrm{T}}^{\mathrm{lead}}$ bias is small. The blue stars ($p_{\mathrm{T,min}}^{\mathrm{lead}} = 5$ GeV/c only) represent STAR data from charged-particle jet analysis in the same collision system and energy with systematic errors of this measurement being added in quadrature. This analysis does not report the "~Unbiased" region for R_{CP}. The green squares ($p_{\mathrm{T,min}}^{\mathrm{lead}} = 5$ GeV/c only) represent ALICE results from charged-particle jet analysis in Pb+Pb collisions at $\sqrt{s_{\mathrm{NN}}} = 2.76$ TeV. Only points in the overlap $p_{\mathrm{T,jet}}$ range are plotted and systematic errors of this measurement were added in quadrature.

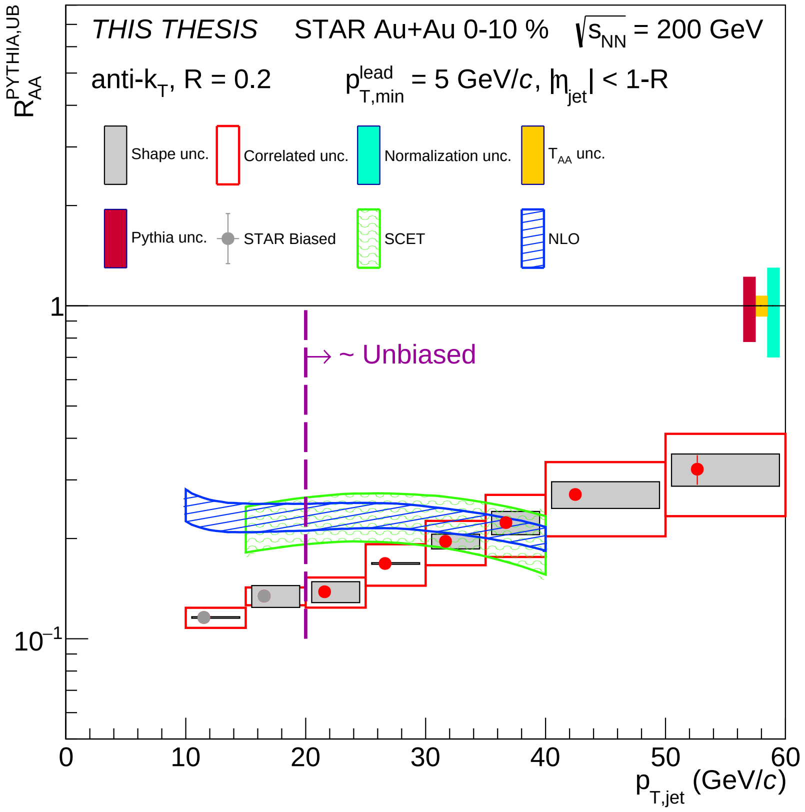

Figure 6.16: Nuclear modification factor $R_{AA}^{PYTHIA,p_T^{lead}}$ (red circles) of anti-k_T jets reconstructed with R = 0.2 and $p_{T,min}^{lead}$= 5 GeV/c in central Au+Au collisions at $\sqrt{s_{NN}}$ = 200 GeV as a function of $p_{T,jet}$. The colored boxes around markers represent correlated systematic uncertainty, while gray-shaded areas represent shape systematic uncertainty. The boxes around unity represent global systematic uncertainties – normalization of the spectra (teal), T_{AA} (orange) and the PYHTIA p+p baseline (pink). The gray circles represent points biased by p_T^{lead} requirement. The purple dashed line represents the start of the region where the p_T^{lead} bias is small. The blue area represents the NLO prediction and the green area represents the SCET model prediction (see text for details).

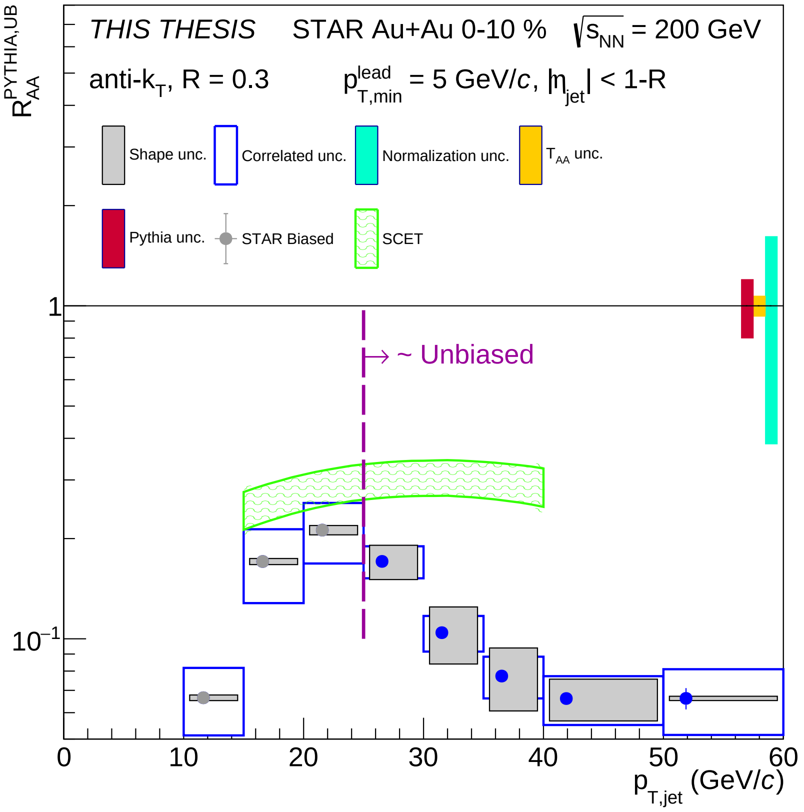

Figure 6.17: Nuclear modification factor $R_{AA}^{PYTHIA,p_T^{lead}}$ (blue circles) of anti-k_T jets reconstructed with $R = 0.3$ and $p_{T,min}^{lead} = 5$ GeV/c in central Au+Au collisions at $\sqrt{s_{NN}} = 200$ GeV as a function of $p_{T,jet}$. The colored boxes around markers represent correlated systematic uncertainty, while gray-shaded areas represent shape systematic uncertainty. The boxes around unity represent global systematic uncertainties – normalization of the spectra (teal), T_{AA} (orange) and the PYHTIA $p+p$ baseline (pink). The gray circles represent points biased by p_T^{lead} requirement. The purple dashed line represents the start of the region where the p_T^{lead} bias is small. The green area represents the SCET model prediction (see text for details).

Chapter 7

Service Task - TPC Tracking Efficiency Uncertainty

The STAR TPC is a remarkably versatile detector with impressive tracking capabilities. However, not every charged particle will be reconstructed as a track and such probability is represented by the tracking efficiency. The inefficiency can be caused by particles falling outside of the sensitive volume of the TPC before leaving enough hits, by hitting a dead sector within the volume, by passing through the central membrane of the TPC and by track overlaps and splitting. The TPC tracking efficiency depends on multiple factors, mainly on the particle p_{T} and the event centrality and also on its position with respect to the TPC and the PV and to a lesser extent on the particle species. The tracking efficiency is around 98 % for high-p_{T} tracks in low-multiplicity events and around 80 % in central Au+Au events and quickly decreases for tracks below $p_{\mathrm{T}} \approx 1$ GeV/c [180].

The nominal value of the tracking efficiency is determined by comparing particle spectra from real data and from simulation. Therefore, the quality of the simulation determines the uncertainty of the TPC tracking efficiency. The TPC tracking efficiency uncertainty has been the subject of debate for the entire duration of STAR operations. The original TPC overview document quotes the systematic uncertainty as 6 % [160] and early studies [195] support this claim and later efforts, for example [196, 197], reduced this uncertainty to 5 % or possibly even lower [198].

With increasing size of the datasets and the shift towards precision measurements, STAR results became less statistics-limited and the need to reduce the systematic errors obtained a high priority within STAR. The tracking efficiency uncertainty is a major source of the overall systematic uncertainty for nearly all measuremets at STAR and therefore a specialized task force has been established in 2020 with the goals of carefully and differentially estimating the tracking efficiency uncertainty and possibly suggesting improvements to the simulation software with hopes of reducing the uncertainty and therefore enabling the publication of higher-quality results. The author of this thesis was an active member of this group for almost three years, fulfilling his sevice task[1]. The efforts within the task force are still ongoing and an official publication is expected once the key analyses are finalized. The following sections (7.1 and 7.2) describe the analyses performed by the author. Since these analyses are very technical and included the development of the software for obtaining the tracking efficiency, only the highlights of the efforts are presented along with discussion of the findings. The final section 7.3 then summarizes the results of the other analyses performed within the task force. The task force focuses on several key

---

[1] Participation in a service task is mandatory for all PhD students who aim to obtain their degree by analyzing STAR data. The student usually has a minor (helper) role in a detector maintenance/design team or a software development team led by senior scientists and the typical length of a service task is around 6 months.

datasets, such as the 2014 Au+Au and 2017 p+p, aiming to create a universal set of techniques usable to determine the tracking efficiency uncertainty for all existing and future STAR datasets.

7.1 Single-Hit TPC Efficiency

Following the steps in [198], a single-hit TPC efficiency was obtained from the 2017 p+p collisions at $\sqrt{s_{\mathrm{NN}}} = 510$ GeV and from 2014 Au+Au collisions at $\sqrt{s_{\mathrm{NN}}} = 200$ GeV and from the corresponding embedding samples. Embedding as a technique is described in 5.4.1. For this study, private embedding was done by the author.

The left panel of Fig. 7.1 shows the ratio of number of tracks which have 44 hits in the TPC and number of tracks with all 45 hits as a function of the pad row, where the one hit is missing, in minimum bias p+p data and embedding. The events were selected with $V_z > 0$ for two cases of track pseudorapidity. The first case (black) are tracks with $-0.2 < \eta < -0.1$ and therefore this sample contains a high population of tracks which cross the central membrane of the TPC. Red color marks tracks which move away from the central membrane and therefore do not cross it. The results are inconclusive mainly due to statistical limitations of the embedding, but there are hints of disagreement between data and simulation, especially for tracks crossing the central membrane in the inner sector of the TPC (rows 5-7). The two data samples appear consistent with each other, not showing a significant effect of the central membrane.

The right panel of Fig. 7.1 shows the same situation in Au+Au collisions. The simulation underpredicts the single-hit inefficiency for all pad rows, clearly demonstrating the inability of the STAR simulation software to describe correctly the single-hit TPC efficiency in the high-multiplicity environment and therefore makes this study unfit for the determination of the TPC tracking efficiency uncertainty. These findings were presented to the STAR embedding experts as a motivation for further improvements of the simulation software.

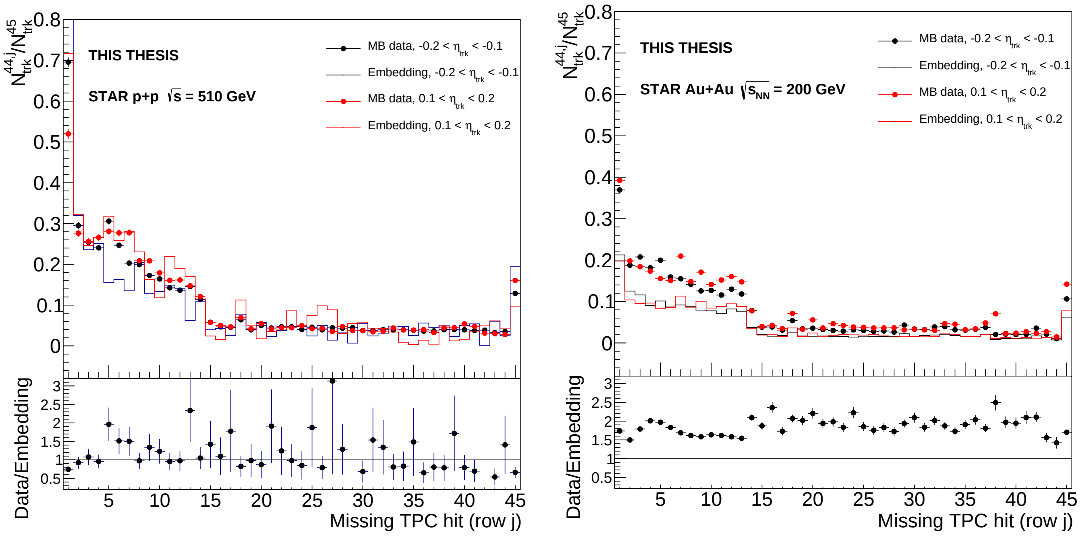

Figure 7.1: Ratio of the number of tracks with 44 TPC hits to the number of tracks with 45 TPC hits as a function of the pad row of the missing hit (upper panel) and the double ratio (lower panel) between data (markers) and the corresponding embedding sample (lines) for tracks likely crossing the TPC central membrane (black) in p+p collisions at $\sqrt{s_{\mathrm{NN}}} = 510$ GeV (left) and Au+Au collisions at $\sqrt{s_{\mathrm{NN}}} = 200$ GeV (right). The red color represents tracks which do not cross the membrane.

7.2 Cosmic Tracks

When there is an extended period during the STAR data taking operations without beam collisions, the STAR detector can be used to detect cosmic particles (usually muons). The study of cosmic tracks provides a unique way of obtaining the TPC tracking efficiency uncertainty. Figure 7.2 demonstrates the basic idea. A cosmic track enters the STAR TPC from above, creating a track in the upper part of the TPC, leaves the TPC active volume around the beam pipe and then re-enters the TPC in the lower part generating a second track. If we then select tracks which pass close to the center of the STAR detector and match the two tracks created by the cosmic particle together, we can obtain the TPC tracking efficiency by comparing the number of matched bottom tracks to the number of top tracks. The matching was done via χ^2 calculation using the track covariance matrix. The uncertainty is then again obtained by comparing the data with simulation. The main advantages of this analysis are the access to full-length tracks covering a large kinematic range ($0 < p_{\mathrm{T}} < 15$ GeV/c) and the emptiness of the detector, since it is very rare for two cosmic particles to enter the TPC within the time window given by the TOF (used as a cosmic trigger) timing resolution, making it a very clean technique. The inherent disadvantages are the inability to account for the effects of the event multiplicity and the bias caused by the preferred direction of the cosmic particles[2], which makes it unusable for fixed-target datasets[3].

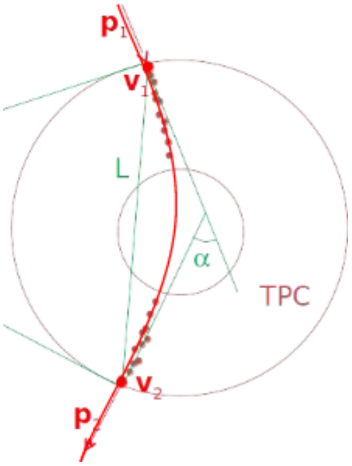

Figure 7.2: Illustration of the cosmic track technique described in the text. Cartoon made by Petr Chaloupka.

Figure 7.3 (left panel) shows the tracking efficiency as a function of cosmic track p_{T} and η from the year 2018 where one sector of the STAR iTPC was already installed. It can be seen that the efficiency quickly rises with p_{T}, reaching a plateau of about 87 % around 3 GeV/c, before slowly decreasing down to 75 % at high p_{T}. The η dependence is not clear, but the data suggest higher efficiency for low-p_{T} tracks at positive η than negative η, a trend that is reversed at high p_{T}. The right panel of Fig. 7.3 shows the same dependence for simulated muons. The overall efficiency is significantly lower, peaks around 1 GeV/c at 80 % and quickly decreases to a plateau at 60 %. There is no significant η dependence

---

[2] The cosmic muon intensity I as a function of the incident polar angle θ behaves as $I \propto \cos^n \theta$, where n depends on the lattitude, longitude and altitude of the detector, but generally $n \approx 2$.

[3] STAR has run several weeks in a fixed-targed configuration during the BES-II phase in order to complement the low-energy datasets from the standard collider configuration and to take full advantage of the forward upgrades.

observed in the simulated data. The discrepancies between data and simulation can be attributed to the inability of the simulation software to correctly reproduce the underlying cosmic track distributions and this has again been brought to the attention of the embedding team, since the development of the STAR simulation software lies beyond the scope of this task force. This analysis is still ongoing with the effect of the single iTPC sector being investigated in the 2019 data, where the iTPC has been fully installed and operational for the whole data taking period.

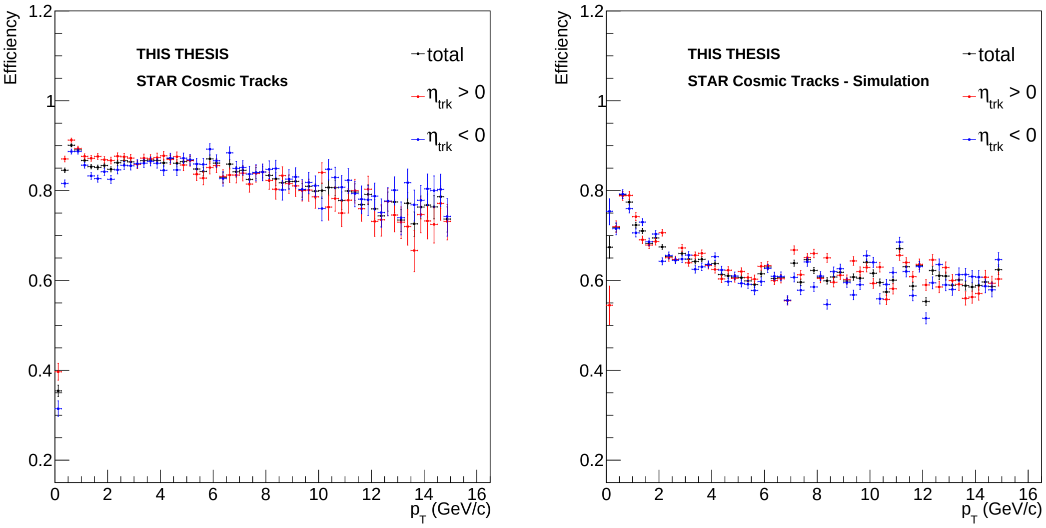

Figure 7.3: Tracking efficiency as a function of cosmic track p_T from year 2018 data (left) and simulation (right). Black points represent the total efficiency while blue markers represent efficiency for top tracks with negative η and red markers for top tracks with positive η.

7.3 Other Analyses

There are two additional efforts still ongoing within the tracking efficiency uncertainty task force. The first method is the reconstruction of three-pion vertices which emerge from a $K^{\pm} \rightarrow \pi^{\pm} + \pi^{\mp} + \pi^{\pm}$ decay. Since the TPC is able to also track the mother kaon, the ratio of the number of three-pion vertices with associated kaon track to the number of three-pion vertices without a corresponding kaon is dependent only on the TPC tracking efficiency. Therefore, by comparing the results from data and from embedding, one gets a systematic difference equal to the TPC tracking efficiency uncertainty. Figure 7.4 shows the spatial distribution of the three-pion decays inside the TPC and illustrates the possible decay scenarios. This approach yields very promising preliminary results, reducing the systematic uncertainty below 5 %, but since it is an ongoing task with no official results, final numbers cannot be quoted at the time of writing this thesis. The main disadvantage is that due to the limited TPC acceptance, the three-pion vertexes limit the maximum length of the tracks and therefore needs to be complemented by the cosmic track study. This method is also not well-suited for data from the fixed-target program.

The second method is based on the matching of tracks detected by another detector to the TPC tracks. For example, ALICE uses the matching of TPC tracks to their silicon-based Inner Tracking System (ITS). However, STAR has no such tracking system available for recent commonly-used datasets, except for the HFT Runs in 2014-2016. The new GMT detector, located at the outer edge of the TPC, can be used for

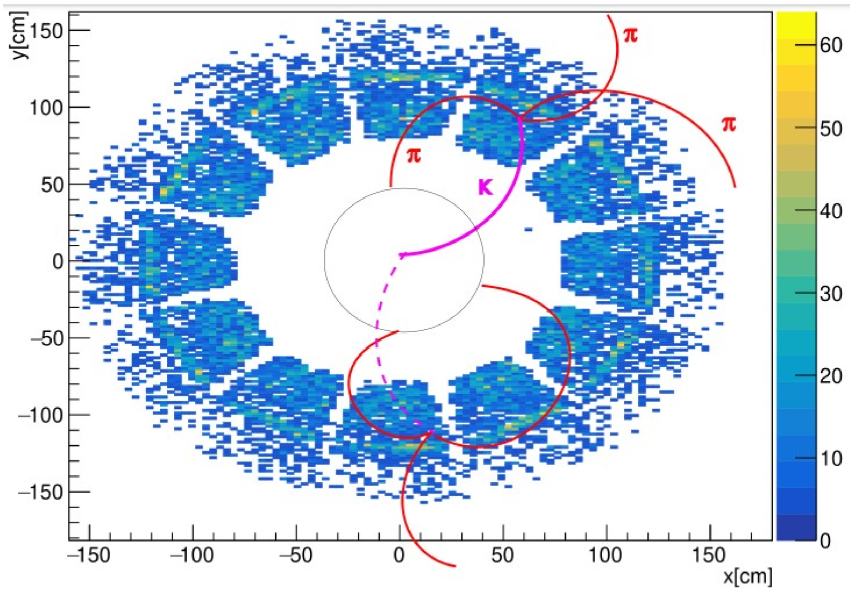

Figure 7.4: Spatial distribution of three-pion decays inside the TPC with illustration of two such possible decays. Red lines represent reconstructed pion tracks and magenta lines represent reconstructed (solid) and unreconstructed (dashed) kaon tracks. Made by Petr Chaloupka.

such purpose. Whenever there is a hit in the GMT with no corresponding TPC track, it is a result of the TPC tracking inefficiency. However, since the GMT simulation software is still not fully implemented within the STAR framework, much effort is still needed in this direction.

Chapter 8

Other Contributions

This chapter summarizes additional contributions by the author.

Contributions to Publications

The author was significantly involved in the publication process of the paper [199] in the role of Code QA member of the GodParent Committee (GPC). The GPC is responsible for internal discussion and preparation of each STAR analysis for publication. It is composed of several senior scientists, a PWG expert, the Principal Authors (PAs) and the Code QA person. The Code QA member (usually a senior PhD student) has the responsibility to review and understand the code used for the analysis, to check the code for errors and compatibility, and to fully reproduce all steps of the analysis from the selection of the dataset to the plotting of the figures presented in the final publication. In addition, the Code QA member also provides feedback regarding the documentation of the analysis code and (optionally) serves as another reviewer of the paper draft.

This paper presents results of the analysis of charged particle and jet production in various event activity (EA) classes of p+Au collisions at $\sqrt{s_{\mathrm{NN}}} = 200$ GeV at STAR in search for jet quenching in small-system collisions. This is an important complementary measurement to the jet quenching measurements in Au+Au collisions, such as the one presented in this thesis.

The event activity was determined from the signal recorded by the BBC forward detector. In MB collisions, the low-EA class represents the 30 % of events with the lowest recorded BBC signal and the high-EA class represents the 30 % of events with the highest BBC signal. In HT-triggered events, the BBC signal distribution is skewed compared to MB events and the same EA class cut–off values correspond to 19% and 42% of events, respectively. This behavior is analogous to the centrality difference between MB and HT events observed in Au+Au collisions (Fig. 5.27, discussed in Sec. 5.8). Figure 8.1 shows that the charged particle production in low-EA events is comparable to that in p+p collisions and increases with larger EA. This is in contrast with the results of hard-scale measurement, shown in Fig. 8.2, where the production of high-p_{T} dijets decreases with increasing EA.

This difference between soft- and hard-scale behavior warrants a question whether this can be a signal of jet quenching in high-EA p+Au events. Therefore, the paper also reports the ratios of dijet azimuthal separation $\Delta\phi$ (Fig. 8.3) and p_{T} imbalance A_{J} (Fig. 8.4) in high- and low-EA events. Within the precision of the measurement, no significant differences are observed in either case between the low- and high-EA classes, disfavoring the presence of jet quenching even in the highest 30% EA p+Au collisions at top RHIC energies.

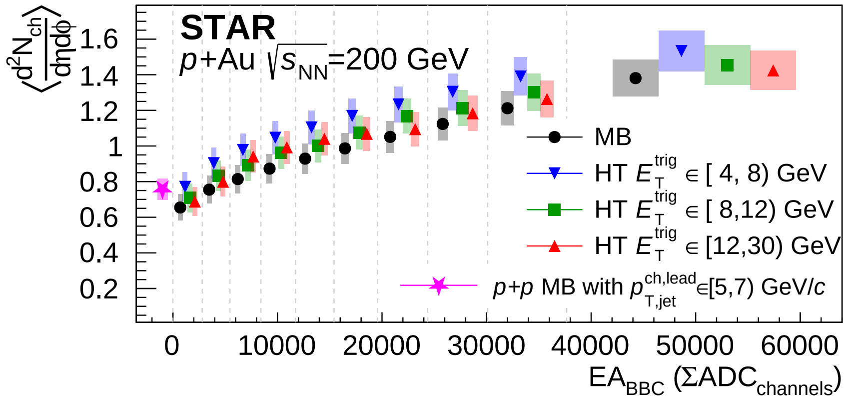

Figure 8.1: Charged particle yield as a function of event activity EA_{BBC} in p+Au collisions at $\sqrt{s_{\text{NN}}}$ = 200 GeV. Black circles represent values from MB events and other symbols correspond to HT events selected with different trigger transverse energy values. Markers are horizontally offset for visual clarity. The star marker is for p+p collisions at the same energy which contain a low-p_{T} jet [200], and is not associated with any specific EA value. The error bars represent statistical and the shaded boxes systematic uncertainties. Taken from [199].

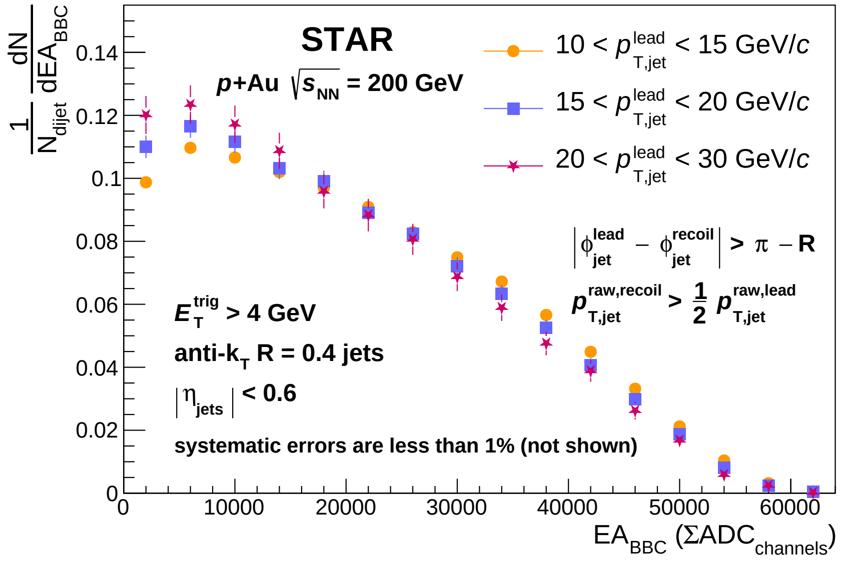

Figure 8.2: Trigger-normalized yield of dijets as a function of event activity EA_{BBC} in p+Au collisions at $\sqrt{s_{\text{NN}}}$ = 200 GeV. Orange circles, blue squares and purple stars represent data for different ranges of leading jet p_{T}. The error bars represent statistical uncertainty while the systematic uncertainty is less than 1 % and not shown. Taken from [199].

In addition, the author has also served in multiple minor roles. The author is one of the PAs of a paper which reports the first measurement of the total open charm cross section at STAR (curently within the GPC review), served two weeks of shifts (11 papers) converting existing STAR data to the HEPdata format – required for all publications, and served as a member of the institutional review teams for multiple STAR papers.

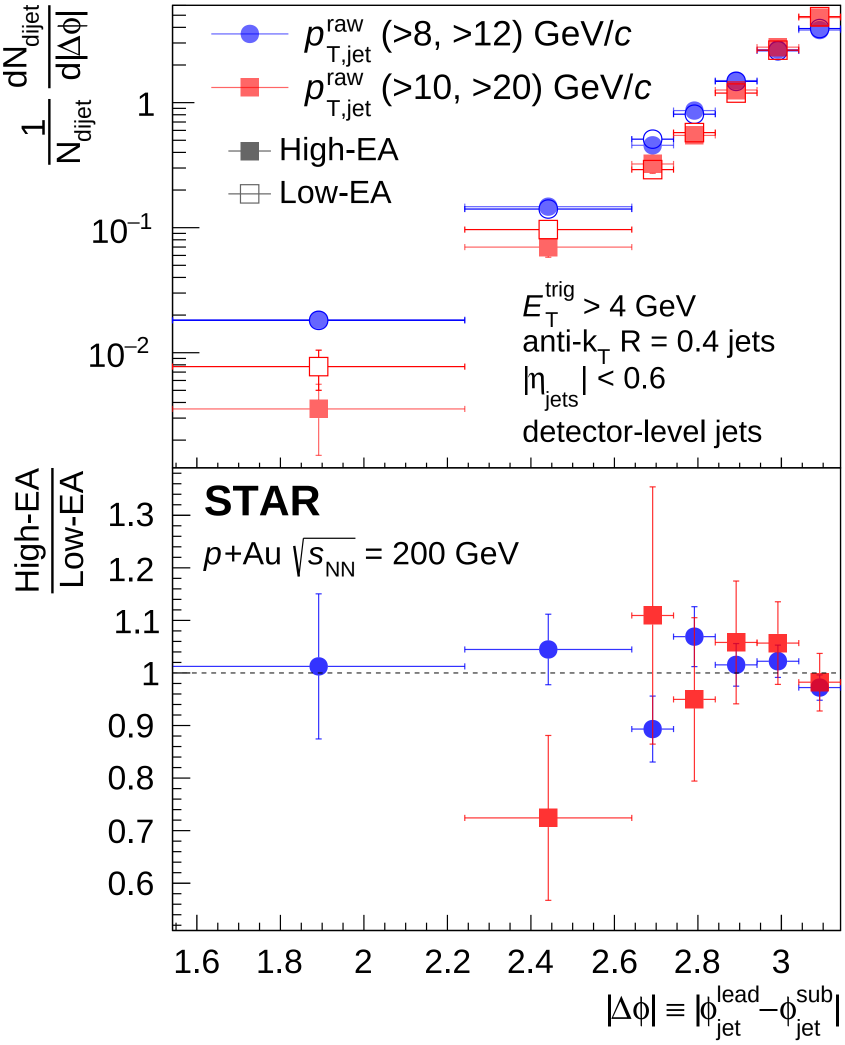

Figure 8.3: Distributions of the azimuthal separation $\Delta\phi$ (top panel) between the leading and sub-leading jets for high- (filled markers) and low-EA (empty markers) events. Circles represent the distributions for the lower $p_{\mathrm{T,jet}}^{\mathrm{raw}}$ requirement and squares represent the distributions for a higher $p_{\mathrm{T,jet}}^{\mathrm{raw}}$ requirement. Ratios between high-EA and low-EA events (bottom panel). Taken from [199].

Contributions to STAR Operations

The author has been an active contributor to the STAR collaboration, serving four weeks as a Detector Operator (DO) in the STAR control room. The DO's responsibilities include turning on and off the STAR detector subsystems or changing their status in order to ensure that they are working properly during data taking and to avoid any damage in case of planned or unexpected interruptions of the data taking. The author was also personally responsible for the training of two future DOs from FNSPE CTU. In addition, the author served three weeks of shifts as a Shift Crew, which has the responsibility to monitor QA plots which are filled in real–time during the STAR data taking runs and to search for and report any

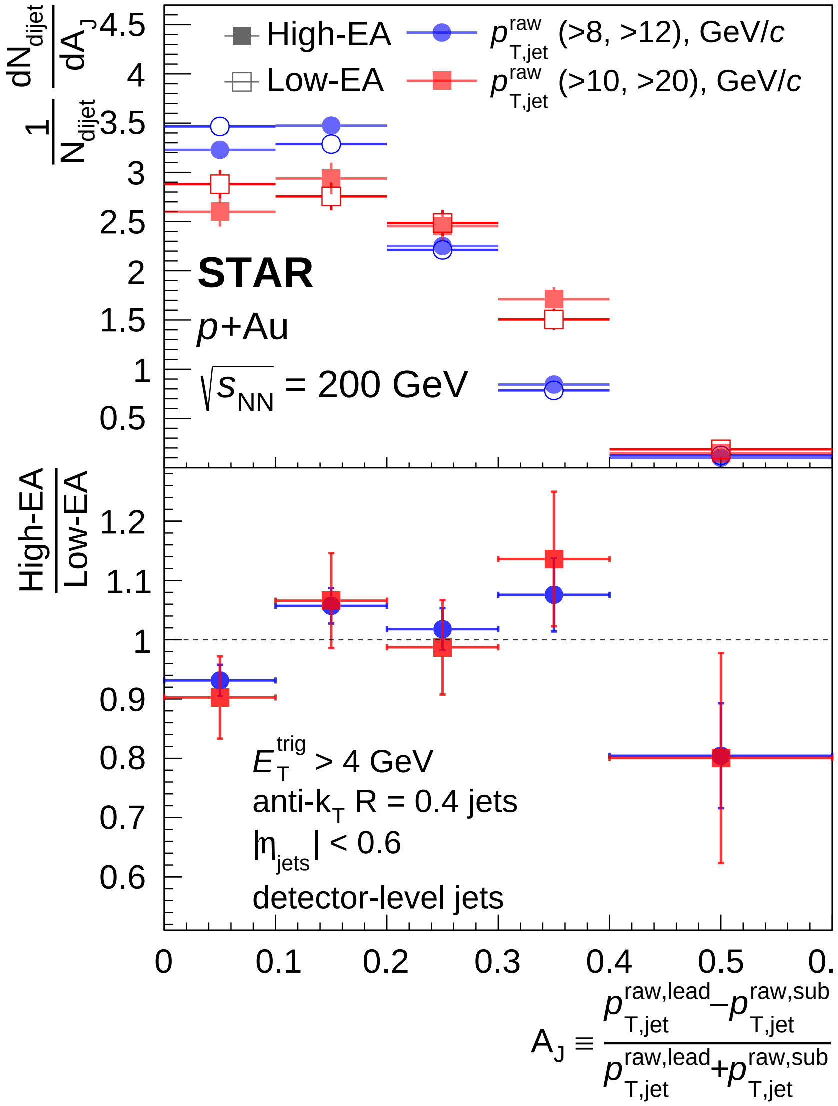

Figure 8.4: Distributions of the jet p_T imbalance A_J (top panel) for high- (filled markers) and low-EA (empty markers) events. Circles represent the distributions for the lower $p^{\rm raw}_{\rm T,jet}$ requirement and squares represent the distributions for a higher $p^{\rm raw}_{\rm T,jet}$ requirement. Ratios between high-EA and low-EA events (bottom panel). Taken from [199].

irregularities which may help identify problems with the STAR subsystems or the DAQ process.

Summary & Outlook

This thesis focuses on jets which serve as a final-state approximation of high-energy partons. Jet quenching in central nucleus–nucleus collisions at high energy has long been one of the key evidences of QGP formation, which has implications for the evolution of the entire universe. This thesis presents the first measurement of inclusive fully-reconstructed jet production in Au+Au collisions at $\sqrt{s_{\mathrm{NN}}} = 200$ GeV, significantly extending the transverse momentum reach of earlier measurement performed for charged-particle jets.

This analysis utilizes the large-statistics dataset recorded by the STAR experiment with a high-tower trigger, which offers unprecedented kinematic reach of the measurement. Jets combine the information from charged particles reconstructed by the TPC and from neutral particles detected by the BEMC. The BEMC energy is corrected for charged-particle track energy deposition via the hadronic correction. The addition of the BEMC information constitutes a major challenge to an already very complex analysis. The effects of the large and fluctuating background – especially in central events – are mitigated by subtracting the median background density and by imposing cuts on the jet area, neutral energy fraction and the leading hadron transverse momentum $p_{\mathrm{T}}^{\mathrm{lead}}$.

The residual background and detector effects are corrected by utilizing the simulation sample consisting of PYTHIA 6 p+p events embedded into STAR minimum-bias Au+Au collisions. The response matrix is constructed by matching particle- and detector-level jets with small angular separation. The iterative Bayesian unfolding method is used to obtain the fully-corrected jet spectra. A series of tests was performed to ensure the mathematical stability and physical correctness of the results, including the closure test. Two classes of systematic uncertainties – correlated and shape – were carefully estimated and are reported separately for the results. The biases introduced to the measurement by selecting events with the high-tower trigger are evaluated and a normalization factor is estimated from fitting the ratio of the fully-corrected spectra and the spectra from minimum-bias collisions.

The results of the analysis include the invariant p_{T} spectra of inclusive fully-reconstructed jets. The spectra are reported up to $p_{\mathrm{T,jet}} = 60$ GeV/c for anti-k_{T} jets reconstructed with $R = 0.2$ and $R = 0.3$ in central Au+Au collisions, essentially doubling the kinematic reach of previous STAR analysis of inclusive jets which include only charged particles. The spectra in peripheral Au+Au collisions are reported also for $R = 0.4$ and up to 50 GeV/c, again significantly extending the reach of the previous STAR results. The bias imposed on the spectra by requiring a high-p_{T} leading particle in the jets is carefully estimated by comparing spectra with different values of this $p_{\mathrm{T,min}}^{\mathrm{lead}}$ cut. It is found that the bias decreases with increasing $p_{\mathrm{T,jet}}$ and the region, where the bias of this cut becomes small starts at $p_{\mathrm{T,jet}} = 15$ GeV/c for small jets and $p_{\mathrm{T,jet}} = 30$ GeV/c for large jets, compatible with the PYTHIA 6 prediction for p+p collisions.

The PYTHIA 6 simulation is used as a p+p reference because the STAR inclusive jet cross section measurement in p+p collisions at $\sqrt{s} = 200$ GeV still awaits publication. This reference was used to calculate the nuclear modification factor R_{AA}, which reaches values $R_{\mathrm{AA}} \sim 0.2 - 0.3$ in central collisions, slightly increasing with $p_{\mathrm{T,jet}}$, for small jets at high $p_{\mathrm{T,jet}}$, confirming significant energy losses of these highly energetic partons in the QGP. This behavior is consistent with the inclusive jet measurement from Pb+Pb collisions at $\sqrt{s_{\mathrm{NN}}} = 5.02$ TeV at the LHC in the overlap $p_{\mathrm{T,jet}}$ region. There is a tension between the results of this thesis and the results of the STAR charged-particle jet analysis in the overlap $p_{\mathrm{T,jet}}$ region with low $p_{\mathrm{T}}^{\mathrm{lead}}$ bias. This tension can be resolved when taking into account the difference in jet constituents of the two analyses and the large systematic uncertainties of the measurements. The R_{AA} in peripheral Au+Au collisions is consistent with unity and with the previous STAR results. Two theoretical predictions incorporating jet quenching are compared to the results and both are compatible with the data within the uncertainties, further confirming the findings of this analysis. The results for larger jets are inconclusive mainly due to the large uncertainty of the spectra normalization.

The nuclear modification factor R_{CP}, which compares the (properly scaled) spectra from central and peripheral collisions is reported for jets reconstructed with $R = 0.2$. The ratio reaches values $R_{\mathrm{CP}} \sim 0.3$ at high $p_{\mathrm{T,jet}}$ with weak dependence on $p_{\mathrm{T,jet}}$ in the region where the $p_{\mathrm{T}}^{\mathrm{lead}}$ bias is small. This result is consistent within uncertainties with the results from charged-particle jet analyses at STAR and at ALICE, and once more agrees with our understanding of the physics of heavy-ion collisions.

The future of this analysis includes the precise determination of the normalization factor by calculating the equivalent minimum-bias events, which requires the presence of the trigger tower within the jets. A better description of the underlying-event background, achievable possibly by considering a mixed-event background subtraction or the application of machine-learning techniques could also lead to the extension of the analysis to larger jet radii.

The thesis also contains a chapter describing the work of the task force charged with improving the understanding of the STAR TPC tracking efficiency and its uncertainty, and to suggest improvements which would lead towards lowering this uncertainty. The author has performed two analyses as his service task, one focusing on determining the single-hit TPC efficiency and the other consisted of obtaining the tracking efficiency from cosmic particles passing through the STAR TPC volume. Both analyses generated valuable input for the simulation experts at STAR.

References

[1] J. Bjorken, *Energy Loss of Energetic Partons in Quark-Gluon Plasma: Possible Extinction of High p_{T} Jets in Hadron-Hadron Collisions*, *FERMILAB-Pub-82/59-THY* (1982) .

[2] STAR collaboration, *Transverse-Momentum and Collision-Energy Dependence of High-pT Hadron Suppression in Au+Au Collisions at Ultrarelativistic Energies*, *Physical Review Letters* **91** (2003) .

[3] STAR collaboration, *Disappearance of Back-To-Back High-p_T Hadron Correlations in Central Au+Au Collisions at $\sqrt{s_{NN}} = 200$ GeV*, *Physical Review Letters* **90** (2003) .

[4] M. Gyulassy, *The QGP Discovered at RHIC*, in *Structure and Dynamics of Elementary Matter*, W. Greiner, M. G. Itkis, J. Reinhardt and M. C. Güçlü, eds., (Dordrecht), pp. 159–182, Springer Netherlands, 2004.

[5] CMS collaboration, *Study of high-p_T charged particle suppression in PbPb compared to pp collisions at $\sqrt{s_{NN}}$=2.76 TeV*, *The European Physical Journal C* **72** (2012) .

[6] ALICE collaboration, *The ALICE experiment – A journey through QCD*, `2211.04384`.

[7] J. Dalton, *A new system of chemical philosophy*, vol. 1. R. Bickerstaff, Strand, London, 1808.

[8] J. J. Thomson, *XL. Cathode Rays*, *The London, Edinburgh, and Dublin Philosophical Magazine and Journal of Science* **44** (1897) 293 [`https://doi.org/10.1080/14786449708621070`].

[9] J. J. Thomson, *XXIV. On the structure of the atom: an investigation of the stability and periods of oscillation of a number of corpuscles arranged at equal intervals around the circumference of a circle; with application of the results to the theory of atomic structure* , *The London, Edinburgh, and Dublin Philosophical Magazine and Journal of Science* **7** (1904) 237 [`https://doi.org/10.1080/14786440409463107`].

[10] H. Geiger and E. Marsden, *On a diffuse reflection of the α-particles*, *Proceedings of the Royal Society London A* **82** (1909) 495.

[11] E. Rutherford, “The Development of the Theory of Atomic Structure.” Lecture, Cambridge University, 1936.

[12] N. Bohr, *On the Constitution of Atoms and Molecules. Pt.II*, *Philosophical Magazine* **26** (1913) 476.

[13] I. Štoll, *Dějiny fyziky*. Prometheus, 2009.

[14] J. Chadwick, *The existence of a neutron*, *Proceedings of the Royal Society London A* **136** (1932) 692.

[15] C. D. Anderson, *The Positive Electron*, *Physical Review* **43** (1933) 491.

[16] S. H. Neddermeyer and C. D. Anderson, *Note on the Nature of Cosmic-Ray Particles*, *Physical Review* **51** (1937) 884.

[17] F. L. Wilson, *Fermi's Theory of Beta Decay*, *American Journal of Physics* **36** (1968) 1150 [`https://pubs.aip.org/aapt/ajp/article-pdf/36/12/1150/11891052/1150_1_online.pdf`].

[18] H. Yukawa, *On the Interaction of Elementary Particles*, *Proc. of Phys.-Math. Soc. Jap.* **17** (1935) 48.

[19] C. M. G. Lattes, H. Muirhead, G. P. S. Occhialini and C. F. Powell, *Processes Involving Charged Mesons*, *Nature* **159** (1947) 694.

[20] V. V. Ezhela et al., *Particle physics: One hundred years of discoveries. An annotated chronological bibliography*. 1996.

[21] M. Gell-Mann, *A schematic model of baryons and mesons*, *Phys. Lett.* **8** (1964) 214.

[22] G. Zweig, *An SU(3) model for strong interaction symmetry and its breaking. Version 2*, pp. 22–101. CERN, 2, 1964.

[23] E. D. Bloom, D. H. Coward, H. DeStaebler, J. Drees, G. Miller, L. W. Mo et al., *High-Energy Inelastic $e - p$ Scattering at 6° and 10°*, *Phys. Rev. Lett.* **23** (1969) 930.

[24] M. Breidenbach, J. I. Friedman, H. W. Kendall, E. D. Bloom, D. H. Coward, H. DeStaebler et al., *Observed behavior of highly inelastic electron-proton scattering*, *Phys. Rev. Lett.* **23** (1969) 935.

[25] S. L. Glashow, J. Iliopoulos and L. Maiani, *Weak Interactions with Lepton-Hadron Symmetry*, *Phys. Rev. D* **2** (1970) 1285.

[26] J. J. Aubert, U. Becker, P. J. Biggs, J. Burger, M. Chen, G. Everhart et al., *Experimental Observation of a Heavy Particle J*, *Phys. Rev. Lett.* **33** (1974) 1404.

[27] J. E. Augustin, A. M. Boyarski, M. Breidenbach, F. Bulos, J. T. Dakin, G. J. Feldman et al., *Discovery of a Narrow Resonance in e^+e^- Annihilation*, *Phys. Rev. Lett.* **33** (1974) 1406.

[28] M. Kobayashi and T. Maskawa, *CP-Violation in the Renormalizable Theory of Weak Interaction*, *Progress of Theoretical Physics* **49** (1973) 652 [`https://academic.oup.com/ptp/article-pdf/49/2/652/5257692/49-2-652.pdf`].

[29] E288 collaboration, *Observation of a Dimuon Resonance at 9.5 GeV in 400-GeV Proton-Nucleus Collisions*, *Physical Review Letters* **39** (1977) .

[30] M. L. Perl, G. S. Abrams, A. M. Boyarski, M. Breidenbach, D. D. Briggs, F. Bulos et al., *Evidence for Anomalous Lepton Production in $e^+ - e^-$ Annihilation*, *Phys. Rev. Lett.* **35** (1975) 1489.

[31] PLUTO collaboration, *Evidence for gluon bremsstrahlung in e+e- annihilations at high energies*, *Physics Letters B* **86** (1979) 418.

[32] D0 collaboration, *Observation of the Top Quark*, *Phys. Rev. Lett.* **74** (1995) 2632.

[33] CDF collaboration, *Observation of Top Quark Production in $\overline{p}p$ Collisions with the Collider Detector at Fermilab*, *Phys. Rev. Lett.* **74** (1995) 2626.

[34] DONUT collaboration, *Observation of tau neutrino interactions*, *Physics Letters B* **504** (2001) 218.

[35] ATLAS collaboration, *Observation of a new particle in the search for the Standard Model Higgs boson with the ATLAS detector at the LHC*, *Phys. Lett. B* **716** (2012) 1.

[36] CMS collaboration, *Observation of a new boson at a mass of 125 GeV with the CMS experiment at the LHC*, *Phys. Lett. B* **716** (2012) 30.

[37] A. D. Sakharov, *Violation of CP in variance, C asymmetry, and baryon asymmetry of the universe*, *Phys. Usp.* **34** (1991) 392.

[38] Super Kamiokande collaboration, *Evidence for oscillation of atmospheric neutrinos*, *Physical Review Letters* **81** (1998) 1562.

[39] SNO collaboration, *Measurement of the Rate of $\nu_e + d -> p + p + e^-$ interactions produced by 8B Solar Neutrinos at the Sudbury Neutrino Observatory*, *Physical Review Letters* **87** (2001) .

[40] G. Hooft, *A planar diagram theory for strong interactions*, *Nuclear Physics B* **72** (1974) 461.

[41] ATLAS collaboration, *Determination of the strong coupling constant from transverse energy-energy correlations in multijet events at $\sqrt{s} = 13$ TeV with the ATLAS detector*, *Journal of High Energy Physics* **2023** (2023) .

[42] D. J. Gross and F. Wilczek, *Ultraviolet Behavior of Non-Abelian Gauge Theories*, *Phys. Rev. Lett.* **30** (1973) 1343.

[43] H. D. Politzer, *Reliable Perturbative Results for Strong Interactions?*, *Phys. Rev. Lett.* **30** (1973) 1346.

[44] E. V. Shuryak, *Quantum chromodynamics and the theory of superdense matter*, *Physics Reports* **61** (1980) 71.

[45] NA50 collaboration, *Anomalous J/ψ suppression in Pb-Pb interactions at 158 GeV/c per nucleon*, *Physics Letters B* **410** (1997) 337.

[46] BRAHMS collaboration, *Pseudorapidity Distributions of Charged Particles from Au+Au Collisions at the Maximum RHIC Energy, $\sqrt{s_{NN}} = 200$ GeV*, *Physical Review Letters* **88** (2002) .

[47] M. L. Miller, K. Reygers, S. J. Sanders and P. Steinberg, *Glauber Modeling in High-Energy Nuclear Collisions*, *Annual Review of Nuclear and Particle Science* **57** (2007) 205.

[48] STAR collaboration, *Centrality and transverse momentum dependence of D^0-meson production at mid-rapidity in Au+Au collisions at $\sqrt{s_{\rm NN}} =$ 200 GeV*, *Phys. Rev.* **C99** (2019) 034908 [`1812.10224`].

[49] C. Shen, “Sketch of relativistic heavy-ion collisions.” [online, cit. 9/7/2023], The Ohio State University, August, 2014.

[50] R. Hagedorn, *Statistical thermodynamics of strong interactions at high energies*, *Nuovo Cimento, Suppl.* **3** (1965) 147.

[51] R. Hagedorn, *On the hadronic mass spectrum*, *Nuovo Cimento A* **52** (1967) 1336.

[52] N. Cabibbo and G. Parisi, *Exponential hadronic spectrum and quark liberation*, *Physics Letters B* **59** (1975) 67.

[53] J. C. Collins and M. J. Perry, *Superdense Matter: Neutrons or Asymptotically Free Quarks?*, *Phys. Rev. Lett.* **34** (1975) 1353.

[54] F. Karsch, *Lattice QCD at High Temperature and Density*, 2001.

[55] U. Heinz and M. Jacob, *Evidence for a New State of Matter: An Assessment of the Results from the CERN Lead Beam Programme*, 2000.

[56] BRAHMS collaboration, *Quark-gluon plasma and color glass condensate at RHIC? The perspective from the BRAHMS experiment*, *Nuclear Physics A* **757** (2005) 1 .

[57] PHOBOS collaboration, *The PHOBOS perspective on discoveries at RHIC*, *Nuclear Physics A* **757** (2005) 28 .

[58] STAR collaboration, *Experimental and theoretical challenges in the search for the quark gluon plasma: The STAR Collaboration's critical assessment of the evidence from RHIC collisions*, *Nucl. Phys.* **A757** (2005) 102 [`nucl-ex/0501009`].

[59] PHENIX collaboration, *Formation of dense partonic matter in relativistic nucleus-nucleus collisions at RHIC: Experimental evaluation by the PHENIX Collaboration*, *Nuclear Physics A* **757** (2005) 184 .

[60] M. Luzum and P. Romatschke, *Conformal relativistic viscous hydrodynamics: Applications to RHIC results at* $\sqrt{s_{NN}}$ = 200 *GeV*, *Phys. Rev. C* **78** (2008) 034915.

[61] STAR collaboration, *Global* Λ *hyperon polarization in nuclear collisions*, *Nature* **548** (2017) 62.

[62] W. Busza, K. Rajagopal and W. van der Schee, *Heavy Ion Collisions: The Big Picture and the Big Questions*, *Annual Review of Nuclear and Particle Science* **68** (2018) 339.

[63] R. Pasechnik and M. Šumbera, *Phenomenological Review on Quark–Gluon Plasma: Concepts vs. Observations*, *Universe* **3** (2017) .

[64] S. Voloshin and Y. Zhang, *Flow study in relativistic nuclear collisions by Fourier expansion of azimuthal particle distributions*, *Z. Phys. C - Particles and Fields* **70** (1996) 665.

[65] R. Nouicer, *New state of nuclear matter: Nearly perfect fluid of quarks and gluons in heavy-ion collisions at RHIC energies*, *The European Physical Journal Plus* **131** (2016) .

[66] STAR collaboration, *Elliptic Flow in Au + Au Collisions at* $\sqrt{s_{\mathrm{NN}}} = 130\mathrm{GeV}$, *Phys. Rev. Lett.* **86** (2001) 402.

[67] STAR collaboration, *Azimuthal anisotropy in Au+Au collisions at* $\sqrt{s_{NN}}$ *= 200 GeV*, *Phys. Rev. C* **72** (2005) 014904 [`nucl-ex/0409033`].

[68] STAR collaboration, *Third harmonic flow of charged particles in Au + Au collisions at* $\sqrt{s_{NN}} = 200$ *GeV*, *Phys. Rev. C* **88** (2013) 014904.

[69] ALICE collaboration, *Higher harmonic flow coefficients of identified hadrons in Pb-Pb collisions at* $\sqrt{s_{NN}}$ *= 2.76 TeV*, *Journal of High Energy Physics* **2016** (2016) .

[70] CMS collaboration, *Observation of long-range, near-side angular correlations in proton-proton collisions at the LHC*, *Journal of High Energy Physics* **2010** (2010) .

[71] ATLAS collaboration, *Observation of Long-Range Elliptic Azimuthal Anisotropies in* $\sqrt{s} = 13$ *and 2.76 TeV pp Collisions with the ATLAS Detector*, *Phys. Rev. Lett.* **116** (2016) 172301.

[72] J. Rafelski and B. Müller, *Strangeness Production in the Quark-Gluon Plasma*, *Phys. Rev. Lett.* **48** (1982) 1066.

[73] NA57 collaboration, *Enhancement of hyperon production at central rapidity in 158 AGeV/c Pb-Pb collisions*, *Journal of Physics G: Nuclear and Particle Physics* **32** (2006) 427.

[74] STAR collaboration, *Enhanced strange baryon production in Au+Au collisions compared to* $p + p$ *at* $\sqrt{s_{NN}} = 200$ *GeV*, *Phys. Rev. C* **77** (2008) 044908.

[75] ALICE collaboration, *Multi-strange baryon production at mid-rapidity in Pb–Pb collisions at* $\sqrt{s_{NN}} = 2.76\ TeV$, *Physics Letters B* **728** (2014) 216.

[76] T. Matsui and H. Satz, *J/ψ suppression by quark-gluon plasma formation*, *Physics Letters B* **178** (1986) 416.

[77] CMS collaboration, *Measurement of nuclear modification factors of* $\Upsilon(1S)$, $\Upsilon(2S)$, *and* $\Upsilon(3S)$ *mesons in PbPb collisions at* $\sqrt{s_{NN}}$ *= 5.02 TeV*, *Physics Letters B* **790** (2019) 270.

[78] S. Digal, P. Petreczky and H. Satz, *Quarkonium feed down and sequential suppression*, *Phys. Rev. D* **64** (2001) 094015 [`hep-ph/0106017`].

[79] STAR collaboration, *Measurement of Sequential* Υ *Suppression in* Au + Au *Collisions at* $\sqrt{s_{NN}} = 200$ GeV *with the STAR Experiment*, *Phys. Rev. Lett.* **130** (2023) 112301.

[80] PHENIX collaboration, *Enhanced Production of Direct Photons in Au+Au Collisions at* $\sqrt{s_{NN}} =$ *200 GeV and Implications for the Initial Temperature*, *Physical Review Letters* **104** (2010) .

[81] ALICE collaboration, *Direct photon production in Pb-Pb collisions at* $\sqrt{s_{NN}}$ *= 2.76 TeV*, *Physics Letters B* **754** (2016) 235.

[82] Y. Aoki, G. Endrodi, Z. Fodor, S. D. Katz and K. K. Szabo, *The Order of the quantum chromodynamics transition predicted by the standard model of particle physics*, *Nature* **443** (2006) 675 [`hep-lat/0611014`].

[83] M. Buballa, *NJL model analysis of quark matter at large density*, *Phys. Rept.* **407** (2005) 205 [`hep-ph/0402234`].

[84] P. Braun-Munzinger and J. Wambach, *Colloquium: Phase diagram of strongly interacting matter*, *Rev. Mod. Phys.* **81** (2009) 1031.

[85] STAR collaboration, *An Experimental Exploration of the QCD Phase Diagram: The Search for the Critical Point and the Onset of De-confinement*, 2010.

[86] G. Odyniec (for the STAR collaboration), *Beam Energy Scan Program at RHIC (BES I and BES II) – Probing QCD Phase Diagram with Heavy-Ion Collisions*, *PoS* **CORFU2018** (2019) 151.

[87] P. Braun-Munzinger and J. Wambach, *Colloquium: Phase diagram of strongly interacting matter*, *Rev. Mod. Phys.* **81** (2009) 1031.

[88] K. Fukushima and T. Hatsuda, *The phase diagram of dense QCD*, *Reports on Progress in Physics* **74** (2010) 014001.

[89] R. Sahoo and T. K. Nayak, *Possible Early Universe Signals in Proton Collisions at the Large Hadron Collider*, *Current Science* **121** (2021) 1403.

[90] M. Voutilainen, "Jets at LHC." CTEQ Summer School 2016, Hamburg, Germany, 2016.

[91] CMS collaboration, "Jet Quenching Observed by CMS in Heavy-Ion Collisions." [online, cit. 9/8/2023], CERN, 2010.

[92] M. Cacciari, G. P. Salam and G. Soyez, *The anti-k_T jet clustering algorithm*, *Journal of High Energy Physics* **2008** (2008) 063.

[93] J. C. Collins, D. E. Soper and G. Sterman, *Factorization of Hard Processes in QCD*, 2004.

[94] H1, ZEUS collaboration, *Combined Measurement and QCD Analysis of the Inclusive e+- p Scattering Cross Sections at HERA*, *JHEP* **01** (2010) 109 [`0911.0884`].

[95] Y. L. Dokshitzer, *Calculation of the Structure Functions for Deep Inelastic Scattering and e+ e- Annihilation by Perturbation Theory in Quantum Chromodynamics.*, *Sov. Phys. JETP* **46** (1977) 641.

[96] V. N. Gribov and L. N. Lipatov, *Deep inelastic e p scattering in perturbation theory*, *Sov. J. Nucl. Phys.* **15** (1972) 438.

[97] G. Altarelli and G. Parisi, *Asymptotic freedom in parton language*, *Nuclear Physics B* **126** (1977) 298.

[98] M. R. Whalley, D. Bourilkov and R. C. Group, *The Les Houches Accord PDFs (LHAPDF) and Lhaglue*, 2005.

[99] D. de Florian and W. Vogelsang, *Resummed cross section for jet production at hadron colliders*, *Phys. Rev. D* **76** (2007) 074031.

[100] B. Andersson, G. Gustafson, G. Ingelman and T. Sjöstrand, *Parton fragmentation and string dynamics*, *Physics Reports* **97** (1983) 31.

[101] T. Sjöstrand, *The Pythia event generator: Past, present and future*, *Computer Physics Communications* **246** (2020) 106910.

[102] K. Olive, *Review of Particle Physics*, *Chinese Physics C* **38** (2014) 090001.

[103] L. Frankfurt, V. Guzey and M. Strikman, *Leading twist nuclear shadowing phenomena in hard processes with nuclei*, *Physics Reports* **512** (2012) 255–393.

[104] K. J. Eskola, P. Paakkinen, H. Paukkunen and C. A. Salgado, *EPPS16: nuclear parton distributions with LHC data*, *The European Physical Journal C* **77** (2017) .

[105] J. W. Cronin, H. J. Frisch, M. J. Shochet, J. P. Boymond, P. A. Piroué and R. L. Sumner, *Production of hadrons at large transverse momentum at 200, 300, and 400 GeV*, *Phys. Rev. D* **11** (1975) 3105.

[106] D. d'Enterria and B. Betz, *High-p(T) hadron suppression and jet quenching*, *Lect. Notes Phys.* **785** (2010) 285.

[107] D. d'Enterria, *Jet quenching*, *Landolt-Bornstein* **23** (2010) 471 [`0902.2011`].

[108] R. Baier, Y. Dokshitzer, A. Mueller, S. Peigné and D. Schiff, *Radiative energy loss and* $p\perp$*-broadening of high energy partons in nuclei*, *Nuclear Physics B* **484** (1997) 265.

[109] R. Feynman, R. Field and G. Fox, *Correlations among particles and jets produced with large transverse momenta*, *Nuclear Physics B* **128** (1977) 1.

[110] D. Krohn, J. Thaler and L.-T. Wang, *Jet Trimming*, *JHEP* **02** (2010) 084 [`0912.1342`].

[111] M. Dasgupta, A. Fregoso, S. Marzani and G. P. Salam, *Towards an understanding of jet substructure*, *JHEP* **09** (2013) 029 [`1307.0007`].

[112] G. P. Salam, *Towards Jetography*, *Eur. Phys. J. C* **67** (2010) 637 [`0906.1833`].

[113] G. P. Salam and G. Soyez, *A practical seedless infrared-safe cone jet algorithm*, *Journal of High Energy Physics* **2007** (2007) 086.

[114] G. C. Blazey, J. R. Dittmann, S. D. Ellis, V. D. Elvira, K. Frame, S. Grinstein et al., *Run II Jet Physics: Proceedings of the Run II QCD and Weak Boson Physics Workshop*, 2000.

[115] S. D. Ellis and D. E. Soper, *Successive combination jet algorithm for hadron collisions*, *Physical Review D* **48** (1993) 3160.

[116] M. Cacciari and G. P. Salam, *Dispelling the* N^3 *myth of the Kt jet-finder*, *Physics Letters B* **641** (2006) 57.

[117] Y. Dokshitzer, G. Leder, S. Moretti and B. Webber, *Better jet clustering algorithms*, *Journal of High Energy Physics* **1997** (1997) 001.

[118] M. Cacciari, G. P. Salam and G. Soyez, *FastJet user manual*, *The European Physical Journal C* **72** (2012) .

[119] X.-N. Wang, *Where Is the Jet Quenching in Pb+Pb Collisions at 158 AGeV*, *Physical Review Letters* **81** (1998) 2655.

[120] STAR collaboration, *Centrality dependence of high* p_T *hadron suppression in Au+Au collisions at* $\sqrt{s_{NN}}$ *= 130-GeV*, *Phys. Rev. Lett.* **89** (2002) 202301 [`nucl-ex/0206011`].

[121] STAR collaboration, *Evidence from d* + Au *Measurements for Final-State Suppression of High-p_T Hadrons in* Au + Au *Collisions at RHIC*, *Phys. Rev. Lett.* **91** (2003) 072304.

[122] Y. L. Dokshitzer, V. A. Khoze and S. I. Troian, *On specific QCD properties of heavy quark fragmentation ('dead cone')*, *J. Phys.* **G17** (1991) 1602.

[123] M. J. Tannenbaum, *How do quarks and gluons lose energy in the QGP?*, *Journal of Physics: Conference Series* **589** (2015) 012019.

[124] CMS collaboration, *Measurement of inclusive jet cross sections in pp and PbPb collisions at* $\sqrt{s_{NN}}$ = 2.76 *TeV*, *Phys. Rev. C* **96** (2017) 015202.

[125] T. Sjöstrand, S. Mrenna and P. Skands, *PYTHIA 6.4 physics and manual*, *Journal of High Energy Physics* **2006** (2006) .

[126] X.-N. Wang and M. Gyulassy, *HIJING: A Monte Carlo model for multiple jet production in p p, p A and A A collisions*, *Phys. Rev. D* **44** (1991) 3501.

[127] CMS collaboration, *Observation and studies of jet quenching in PbPb collisions at nucleon-nucleon center-of-mass energy = 2.76 TeV*, *Phys. Rev. C* **84** (2011) 024906 [`1102.1957`].

[128] ATLAS collaboration, *Observation of a Centrality-Dependent Dijet Asymmetry in Lead-Lead Collisions at* $\sqrt{s_{NN}}$ = 2.76 *TeV with the ATLAS Detector at the LHC*, *Physical Review Letters* **105** (2010) .

[129] STAR collaboration, *Dijet imbalance measurements in Au + Au and pp collisions at* $\sqrt{s_{NN}}$ = 200 *GeV at STAR*, *Phys. Rev. Lett.* **119** (2017) 062301 [`1609.03878`].

[130] CMS collaboration, *Measurement of inclusive jet production and nuclear modifications in pPb collisions at* $\sqrt{s_{\mathrm{NN}}}$ *= 5.02 TeV*, *Eur. Phys. J. C* **76** (2016) 372 [`1601.02001`].

[131] STAR collaboration, *Measurement of inclusive charged-particle jet production in Au + Au collisions at* $\sqrt{s_{NN}}$ = 200 *GeV*, *Phys. Rev. C* **102** (2020) 054913.

[132] A. Mukherjee and W. Vogelsang, *Jet production in (un)polarized pp collisions: Dependence on jet algorithm*, *Phys. Rev. D* **86** (2012) 094009.

[133] STAR collaboration, *Longitudinal double-spin asymmetry for inclusive jet and dijet production in pp collisions at* $\sqrt{s}$ = 510 GeV, *Phys. Rev. D* **100** (2019) 052005.

[134] Z. Chang, *Inclusive Jet Cross Section Measurements in pp Collisions at* $\sqrt{s}$ *= 200 and 510 GeV with STAR*, 2021.

[135] ALICE collaboration, *Measurements of inclusive jet spectra in pp and central Pb-Pb collisions at* $\sqrt{s_{\mathrm{NN}}}$ *= 5.02 TeV*, *Phys. Rev. C* **101** (2020) 034911 [`1909.09718`].

[136] CMS collaboration, *First measurement of large area jet transverse momentum spectra in heavy-ion collisions*, *JHEP* **05** (2021) 284 [`2102.13080`].

[137] ALICE collaboration, *Measurement of inclusive charged-particle jet production in pp and p-Pb collisions at* $\sqrt{s_{\mathrm{NN}}}$ = 5.02 *TeV*, `2307.10860`.

[138] CMS collaboration, *Studies of dijet transverse momentum balance and pseudorapidity distributions in pPb collisions at* $\sqrt{s_{\mathrm{NN}}} = 5.02$ *TeV*, *Eur. Phys. J. C* **74** (2014) 2951 [`1401.4433`].

[139] K. Zapp, *JEWEL 2.0.0: directions for use*, *The European Physical Journal C* **74** (2014) .

[140] I. P. Lokhtin and A. M. Snigirev, *A model of jet quenching in ultrarelativistic heavy ion collisions and high-*p_T *hadron spectra at RHIC*, *The European Physical Journal C* **45** (2006) 211.

[141] N. A. Grünwald (for the ALICE collaboration), *New measurements of inclusive jet suppression and jet* v_2 *in Pb–Pb collisions at* $\sqrt{s_{NN}} = 5.02$ *TeV with ALICE*, in *Quark Matter 2023*, (Houston, Texas, USA), 2023, https://indico.cern.ch/event/1139644/contributions/5539964/.

[142] STAR collaboration, *Measurement of in-medium jet modification using direct photon+jet and* π^0*+jet correlations in* $p + p$ *and central Au+Au collisions at* $\sqrt{s_{\mathrm{NN}}} = 200$ *GeV*, `2309.00156`.

[143] STAR collaboration, *Semi-inclusive direct photon+jet and* π^0*+jet correlations measured in* $p + p$ *and central Au+Au collisions at* $\sqrt{s_{\mathrm{NN}}} = 200$ *GeV*, `2309.00145`.

[144] ATLAS collaboration, *Measurements of the suppression and correlations of dijets in Pb+Pb collisions at* $\sqrt{s_{NN}} = 5.02$ *TeV*, *Phys. Rev. C* **107** (2023) 054908 [`2205.00682`].

[145] ATLAS collaboration, *Measurement of substructure-dependent jet suppression in* Pb + Pb *collisions at 5.02 TeV with the ATLAS detector*, *Phys. Rev. C* **107** (2023) 054909.

[146] JETSCAPE collaboration, *The JETSCAPE framework*, `1903.07706`.

[147] A. Majumder, *Incorporating space-time within medium-modified jet-event generators*, *Phys. Rev. C* **88** (2013) 014909.

[148] Y. He, T. Luo, X.-N. Wang and Y. Zhu, *Linear boltzmann transport for jet propagation in the quark-gluon plasma: Elastic processes and medium recoil*, *Phys. Rev. C* **91** (2015) 054908.

[149] STAR collaboration, *Differential measurements of jet substructure and partonic energy loss in Au+Au collisions at* $\sqrt{S_{NN}}$ *=200 GeV*, *Phys. Rev. C* **105** (2022) 044906 [`2109.09793`].

[150] STAR collaboration, *Search for the chiral magnetic effect with isobar collisions at* $\sqrt{s_{NN}}$*=200 GeV by the STAR Collaboration at the BNL Relativistic Heavy Ion Collider*, *Phys. Rev. C* **105** (2022) 014901 [`2109.00131`].

[151] W. Fisher, “Run Overview of the Relativistic Heavy Ion Collider.” [online, cit. 9/25/2023].

[152] sPHENIX collaboration, *sPHENIX: The next generation heavy ion detector at RHIC*, *J. Phys. Conf. Ser.* **832** (2017) 012012 [`1611.03003`].

[153] H. Hahn, E. Forsyth, H. Foelsche, M. Harrison, J. Kewisch, G. Parzen et al., *The RHIC design overview*, *Nuclear Instruments and Methods in Physics Research Section A: Accelerators, Spectrometers, Detectors and Associated Equipment* **499** (2003) 245.

[154] T. Kanesue et al., *The Commissioning of the Laser Ion Source for RHIC-EBIS*, in *Proc. 5th International Particle Accelerator Conference (IPAC’14), Dresden, Germany, June 15-20, 2014*, no. 5 in International Particle Accelerator Conference, (Geneva, Switzerland), pp. 1890–1892, JACoW, July, 2014, DOI.

[155] J. Alessi, E. Beebe, D. Graham, A. Kponou, A. Pikin, K. Prelec et al., *Design of an EBIS for RHIC*, in *Proceedings of the 2003 Particle Accelerator Conference*, vol. 1, pp. 89–91 Vol.1, 2003, DOI.

[156] A. Zelenski, J. Alessi, B. Briscoe, G. Dutto, H. Huang, A. Kponou et al., *Optically pumped polarized H- ion source for RHIC spin physics*, *Review of Scientific Instruments* **73** (2002) 888 [`https://pubs.aip.org/aip/rsi/article-pdf/73/2/888/11032706/888_1_online.pdf`].

[157] K. Walsch, "RHIC Gets Ready to Smash Gold Ions for Run 23." [online, cit. 2/10/2023].

[158] STAR collaboration, *The STAR detector magnet subsystem*, *Nucl. Instrum. Meth. A* **499** (2003) 633.

[159] K. Ackermann, N. Adams, C. Adler, Z. Ahammed, S. Ahmad, C. Allgower et al., *STAR detector overview*, *Nuclear Instruments and Methods in Physics Research Section A: Accelerators, Spectrometers, Detectors and Associated Equipment* **499** (2003) 624 .

[160] M. Anderson et al., *The STAR time projection chamber: A Unique tool for studying high multiplicity events at RHIC*, *Nucl. Instrum. Meth.* **A499** (2003) 659 [`nucl-ex/0301015`].

[161] STAR collaboration, *STAR Public Image Library*, 2001.

[162] H. Bichsel, *Comparison of Bethe-Bloch and Bichsel Functions*, *STAR Note* **SN0439** (2001) .

[163] STAR collaboration, *Light nuclei collectivity from* $\sqrt{s_{NN}}$*=3 GeV Au+Au collisions at RHIC*, *Physics Letters B* **827** (2022) 136941.

[164] M. Beddo, E. Bielick, T. Fornek, V. Guarino, D. Hill, K. Krueger et al., *The STAR Barrel Electromagnetic Calorimeter*, *Nuclear Instruments and Methods in Physics Research Section A: Accelerators, Spectrometers, Detectors and Associated Equipment* **499** (2002) 725.

[165] W. Llope, J. Zhou, T. Nussbaum, G. Hoffmann, K. Asselta, J. Brandenburg et al., *The STAR Vertex Position Detector*, *Nuclear Instruments and Methods in Physics Research Section A: Accelerators, Spectrometers, Detectors and Associated Equipment* **759** (2014) 23 .

[166] STAR collaboration, *The beam-beam counter: A local polarimeter at STAR*, *AIP Conf. Proc.* **980** (2008) 390.

[167] C. Adler, A. Denisov, E. Garcia, M. Murray, H. Stroebele and S. White, *The RHIC zero degree calorimeters*, *Nuclear Instruments and Methods in Physics Research Section A: Accelerators, Spectrometers, Detectors and Associated Equipment* **470** (2001) 488.

[168] F. Geurts et al., *Proposal for a Large Area Time of Flight System for STAR*, *STAR Note* **SN0621** (2004) .

[169] D. R. Beavis et al., *The STAR Heavy Flavor Tracker*, *STAR Note* **SN0600** (2011) .

[170] T. Huang, R. Ma, B. Huang, X. Huang, L. Ruan, T. Todoroki et al., *Muon identification with Muon Telescope Detector at the STAR experiment*, *Nuclear Instruments and Methods in Physics Research Section A: Accelerators, Spectrometers, Detectors and Associated Equipment* **833** (2016) 88.

[171] C. Allgower, B. Anderson, A. Baldwin, J. Balewski, M. Belt-Tonjes, L. Bland et al., *The STAR endcap electromagnetic calorimeter*, *Nuclear Instruments and Methods in Physics Research Section A: Accelerators, Spectrometers, Detectors and Associated Equipment* **499** (2003) 740.

[172] J. Adams et al., *The STAR Event Plane Detector*, *Nucl. Instrum. Meth. A* **968** (2020) 163970 [`1912.05243`].

[173] N. Ermakov, *The GMT detector alignment in the STAR experiment*, *Journal of Physics: Conference Series* **675** (2016) 042019.

[174] STAR collaboration, *A Proposal for STAR Inner TPC Sector Upgrade (iTPC)*, *STAR Note* **SN0619** (2015) .

[175] STAR collaboration, *The STAR Forward Calorimeter System and Forward Tracking System beyond BES-II*, *STAR Note* **SN0648** (2016) .

[176] O. D. Tsai, E. Aschenauer, W. Christie, L. E. Dunkelberger, S. Fazio, C. A. Gagliardi et al., *Development of a forward calorimeter system for the STAR experiment*, *Journal of Physics: Conference Series* **587** (2015) 012053.

[177] STAR/CBM collaboration, eTOF Group, *Physics Program for the STAR/CBM eTOF Upgrade*, 2016.

[178] A. Accardi et al., *Electron Ion Collider: The Next QCD Frontier: Understanding the glue that binds us all*, *Eur. Phys. J. A* **52** (2016) 268 [`1212.1701`].

[179] ePIC collaboration, "ePIC Wiki - Main Page." [online, cit. 10/19/2023].

[180] J. Rusňák, *Jet Reconstruction in Au+Au collisions at RHIC*, Ph.D. thesis, Faculty of Nuclear Sciences and Physical Engineering, Czech Technical University in Prague, 2017.

[181] R. Brun and F. Rademakers, *ROOT: An object oriented data analysis framework*, *Nucl. Instrum. Meth. A* **389** (1997) 81.

[182] M. Cacciari, G. P. Salam and G. Soyez, *The catchment area of jets*, *Journal of High Energy Physics* **2008** (2008) 005–005.

[183] R. Brun, F. Bruyant, M. Maire, A. C. McPherson and P. Zanarini, *GEANT 3: user's guide Geant 3.10, Geant 3.11; rev. version*. CERN, Geneva, 1987.

[184] E. Lesser, *Measurements of jet substructure in pp and Pb-Pb collisions at* $\sqrt{s_{\mathrm{NN}}} = 5.02$ *TeV with ALICE*, 2023.

[185] R. Lavička, *Ultra-Peripheral Collisions at ALICE – Looking inside lead ions*, Ph.D. thesis, Faculty of Nuclear Sciences and Physical Engineering, Czech Technical University in Prague, 2021.

[186] T. Adye, *Unfolding algorithms and tests using RooUnfold*, `1105.1160`.

[187] A. Höcker and V. Kartvelishvili, *SVD approach to data unfolding*, *Nuclear Instruments and Methods in Physics Research Section A: Accelerators, Spectrometers, Detectors and Associated Equipment* **372** (1996) 469 .

[188] G. D'Agostini, *Improved iterative Bayesian unfolding*, `1010.0632`.

[189] ALICE collaboration, *Measurement of charged jet suppression in Pb-Pb collisions at $\sqrt{s_{\rm NN}} = 2.76$ TeV*, *Journal of High Energy Physics* **2014** (2014) .

[190] I. Vitev and B.-W. Zhang, *Jet Tomography of High-Energy Nucleus-Nucleus Collisions at Next-to-Leading Order*, *Phys. Rev. Lett.* **104** (2010) 132001.

[191] STAR collaboration, *Longitudinal double-spin asymmetry and cross section for inclusive jet production in polarized proton collisions at $\sqrt{s} = 200$ GeV*, *Phys. Rev. Lett.* **97** (2006) 252001 [`hep-ex/0608030`].

[192] Y.-T. Chien, A. Emerman, Z.-B. Kang, G. Ovanesyan and I. Vitev, *Jet quenching from QCD evolution*, *Phys. Rev. D* **93** (2016) 074030.

[193] Y.-T. Chien and I. Vitev, *Towards the understanding of jet shapes and cross sections in heavy ion collisions using soft-collinear effective theory*, *Journal of High Energy Physics* **2016** (2016) .

[194] ATLAS collaboration, *Measurement of charged-particle spectra in Pb+Pb collisions at $\sqrt{s_{\rm NN}} = 2.76$ TeV with the ATLAS detector at the LHC*, *Journal of High Energy Physics* **2015** (2015) .

[195] M. Calderón de la Barca Sánchez, *Charged Hadron Spectra at $\sqrt{s_{NN}} = 130$ GeV*, Ph.D. thesis, Yale University, 2001.

[196] B. Choi, *Charged Hadron Spectra at $\sqrt{s_{NN}} = 130$ GeV*, Ph.D. thesis, University of Texas at Austin, 2002.

[197] STAR collaboration, *Systematic measurements of identified particle spectra in pp, d* + Au*, and* Au + Au *collisions at the STAR detector*, *Phys. Rev. C* **79** (2009) 034909.

[198] D. Kalinkin, *Tracking efficiency uncertainty for the STAR TPC*, *STAR Note* **SN0759** (2020) .

[199] STAR collaboration, *Event activity correlations and jet measurements in p+Au collisions at $\sqrt{s_{\rm NN}} = 200$ GeV*, `2404.08784`.

[200] STAR collaboration, *Underlying event measurements in p+p collisions at $\sqrt{s} = 200$ GeV at RHIC*, *Physical Review D* **101** (2020) .

List of Figures

List of Tables

Appendix A

Bad Run List

See Ch. 5 for details on bad run selection. Runs with the following IDs (360 in total) were excluded from the analysis:
15076108, 15077001, 15077003, 15077033, 15077042, 15077043, 15077044, 15077045, 15077046, 15077048, 15077049, 15077050, 15077051, 15077059, 15077061, 15077063, 15077067, 15079048, 15078001, 15078069, 15078071, 15078073, 15078074, 15078075, 15078103, 15078104, 15078107, 15078108, 15079041, 15080053, 15080054, 15080059, 15081015, 15081022, 15082016, 15082023, 15082030, 15082031, 15082052, 15082064, 15083019, 15083021, 15083023, 15083025, 15083027, 15083028, 15084002, 15084006, 15084009, 15084010, 15084011, 15084022, 15084025, 15084027, 15084028, 15084029, 15084030, 15084036, 15084064, 15086060, 15086076, 15087013, 15087042, 15087055, 15088003, 15088004, 15088005, 15088006, 15089009, 15089010, 15090068, 15092016, 15092017, 15092018, 15089023, 15089024, 15089025, 15089026, 15090006, 15092004, 15092005, 15092007, 15092008, 15092009, 15092011, 15092012, 15092013, 15096057, 15098015, 15098040, 15098041, 15101042, 15101045, 15101047, 15101049, 15101050, 15102008, 15102035, 15102040, 15103010, 15103014, 15103016, 15104004, 15104007, 15104039, 15104052, 15104059, 15107077, 15108021, 15108074, 15109005, 15110039, 15110040, 15110041, 15110042, 15110043, 15110058, 15111001, 15111002, 15111003, 15111004, 15111005, 15111006, 15111007, 15111008, 15111009, 15111010, 15111011, 15111012, 15111013, 15111014, 15111015, 15111016, 15114010, 15114011, 15114012, 15114013, 15114027, 15114028, 15117002, 15119042, 15119043, 15119056, 15121060, 15121061, 15122046, 15122047, 15122048, 15123034, 15125075, 15126002, 15126004, 15126006, 15126008, 15130036, 15132005, 15132006, 15133017, 15134053, 15135062, 15140026, 15142019, 15142020, 15142054, 15142055, 15142058, 15144036, 15146042, 15146043, 15146044, 15146045, 15146046, 15146064, 15146065, 15146066, 15146067, 15146068, 15146069, 15147022, 15147023, 15147024, 15147025, 15147026, 15147037, 15147038, 15147039, 15147040, 15149067, 15150057, 15156001, 15161037, 15162004, 15165008, 15165009, 15165055, 15166013, 15102015, 15102016, 15102018, 15102046, 15102047, 15102050, 15103019, 15103020, 15103021, 15103057, 15104013, 15104014, 15104062, 15105019, 15112049, 15118063, 15119025, 15121076, 15122063, 15126009, 15126010, 15126011, 15126012, 15126013, 15126015, 15126016, 15129006, 15130001, 15131049, 15133043, 15138069, 15144004, 15145021, 15146003, 15146004, 15146049, 15146050, 15146051, 15146052, 15146054, 15146055, 15146057, 15146058, 15147001, 15147002, 15147003, 15147004, 15147005, 15147006, 15147007, 15147008, 15147027, 15147028, 15147029, 15147030, 15147031, 15147032, 15147033, 15147041, 15147042, 15148003, 15148004, 15148005, 15148006, 15148007, 15148008, 15148009, 15148010, 15148011, 15149069, 15149073, 15150005, 15150027, 15150030, 15150031, 15150062, 15151042, 15152004, 15156008, 15157017, 15159054, 15161051, 15161066,

15161067, 15162047, 15162053, 15163022, 15163058, 15164048, 15164067, 15165039, 15095020, 15095021, 15097059, 15098001, 15098002, 15098003, 15098005, 15098036, 15100100, 15100101, 15100102, 15100103, 15101020, 15101022, 15102021, 15102024, 15102026, 15103026, 15103028, 15103030, 15104016, 15104017, 15104018, 15104068, 15105002, 15105006, 15105033, 15105072, 15106001, 15108018, 15108019, 15109039, 15109040, 15110032, 15114058, 15115088, 15120011, 15121062, 15121077, 15121078, 15122003, 15122004, 15122006, 15122008, 15122010, 15122011, 15124044, 15122045, 15125003, 15126017, 15126018, 15126019, 15126021, 15126022, 15126023, 15146059, 15146060, 15146061, 15146062, 15147009, 15147010, 15147011, 15147012, 15147013, 15147014, 15147015, 15150059, 15151050, 15154003, 15159035, 15161022, 15162031, 15166045

Appendix B

Bad Tower List

See Ch. 5 for details on tower selection. In total, 822 towers with the following IDs were excluded from the analysis:
31, 34, 35, 38, 95, 96, 106, 113, 114, 134, 139, 157, 160, 175, 193, 200, 214, 220, 224, 257, 266, 267, 282, 286, 287, 296, 315, 317, 319, 340, 365, 371, 380, 389, 395, 405, 410, 420, 426, 433, 474, 483, 484, 504, 506, 520, 529, 533, 541, 555, 560, 561, 562, 580, 582, 584, 585, 600, 615, 617, 633, 635, 637, 638, 643, 649, 650, 653, 657, 671, 673, 674, 677, 693, 708, 749, 757, 759, 775, 776, 779, 783, 790, 793, 796, 799, 803, 810, 812, 813, 814, 817, 822, 825, 832, 837, 840, 844, 846, 848, 853, 857, 859, 873, 875, 887, 893, 897, 899, 903, 916, 924, 939, 940, 946, 953, 954, 956, 972, 979, 980, 989, 993, 996, 997, 999, 1005, 1012, 1014, 1016, 1017, 1020, 1023, 1026, 1027, 1028, 1039, 1040, 1042, 1044, 1045, 1046, 1048, 1055, 1056, 1057, 1059, 1062, 1064, 1078, 1080, 1081, 1083, 1084, 1090, 1100, 1101, 1102, 1103, 1104, 1122, 1124, 1125, 1127, 1128, 1130, 1132, 1137, 1141, 1142, 1143, 1144, 1145, 1146, 1147, 1148, 1149, 1150, 1151, 1152, 1153, 1154, 1155, 1156, 1157, 1158, 1159, 1160, 1161, 1162, 1163, 1164, 1165, 1166, 1167, 1168, 1169, 1170, 1171, 1172, 1173, 1174, 1175, 1176, 1177, 1178, 1179, 1180, 1181, 1182, 1183, 1184, 1185, 1186, 1187, 1188, 1189, 1190, 1191, 1192, 1193, 1194, 1195, 1196, 1197, 1198, 1199, 1200, 1201, 1202, 1203, 1204, 1205, 1206, 1207, 1208, 1209, 1210, 1211, 1212, 1213, 1214, 1215, 1216, 1217, 1218, 1219, 1220, 1221, 1224, 1232, 1237, 1238, 1239, 1240, 1244, 1250, 1257, 1258, 1259, 1260, 1262, 1274, 1279, 1280, 1284, 1288, 1293, 1294, 1298, 1300, 1304, 1307, 1308, 1312, 1313, 1325, 1329, 1335, 1337, 1340, 1341, 1348, 1353, 1354, 1366, 1369, 1375, 1376, 1378, 1388, 1394, 1405, 1407, 1408, 1409, 1434, 1436, 1439, 1440, 1448, 1475, 1480, 1486, 1537, 1567, 1574, 1588, 1592, 1597, 1599, 1612, 1619, 1620, 1654, 1668, 1679, 1701, 1702, 1705, 1720, 1728, 1740, 1745, 1753, 1759, 1762, 1765, 1766, 1773, 1781, 1786, 1789, 1807, 1856, 1860, 1866, 1877, 1878, 1879, 1901, 1920, 1938, 1945, 1984, 2000, 2032, 2040, 2059, 2073, 2077, 2080, 2092, 2093, 2097, 2104, 2120, 2128, 2129, 2140, 2160, 2162, 2168, 2175, 2176, 2177, 2192, 2195, 2196, 2197, 2200, 2202, 2214, 2215, 2216, 2217, 2222, 2223, 2240, 2243, 2260, 2278, 2299, 2303, 2305, 2309, 2310, 2311, 2312, 2339, 2340, 2357, 2366, 2386, 2390, 2391, 2392, 2409, 2415, 2417, 2419, 2420, 2439, 2445, 2458, 2459, 2478, 2479, 2497, 2500, 2535, 2539, 2540, 2559, 2560, 2579, 2580, 2582, 2589, 2590, 2591, 2592, 2596, 2598, 2609, 2610, 2611, 2612, 2619, 2629, 2630, 2631, 2632, 2637, 2639, 2649, 2650, 2651, 2652, 2669, 2670, 2671, 2672, 2678, 2689, 2690, 2691, 2692, 2709, 2710, 2711, 2712, 2715, 2717, 2718, 2719, 2729, 2730, 2731, 2732, 2738, 2749, 2753, 2754, 2755, 2756, 2773, 2774, 2775, 2776, 2781, 2782, 2782, 2783, 2784, 2793, 2794, 2795, 2796, 2801, 2802, 2803, 2804, 2813, 2814, 2815, 2816, 2820, 2821, 2822, 2822, 2823, 2824, 2834, 2835, 2836, 2841, 2842, 2843, 2844, 2858, 2865, 2874, 2880, 2890, 2918, 2929, 2961, 2969, 2973, 2974, 2975, 2976, 2977, 2978, 2981, 2982, 2983, 2984, 2985, 2986, 2987, 2988, 2989, 2990, 2991,

2992, 2993, 2994, 2995, 2996, 2997, 2998, 2999, 3000, 3001, 3002, 3003, 3004, 3005, 3006, 3007, 3008, 3009, 3010, 3011, 3012, 3013, 3014, 3015, 3016, 3017, 3018, 3019, 3020, 3021, 3022, 3023, 3024, 3025, 3026, 3027, 3028, 3029, 3030, 3031, 3032, 3033, 3034, 3035, 3036, 3037, 3038, 3039, 3040, 3041, 3042, 3043, 3044, 3045, 3046, 3047, 3048, 3049, 3050, 3051, 3052, 3053, 3054, 3055, 3056, 3057, 3058, 3059, 3060, 3070, 3071, 3079, 3098, 3099, 3100, 3139, 3146, 3186, 3218, 3220, 3240, 3263, 3288, 3298, 3299, 3300, 3316, 3320, 3328, 3329, 3337, 3339, 3349, 3350, 3351, 3352, 3354, 3355, 3356, 3360, 3362, 3369, 3370, 3371, 3372, 3377, 3378, 3379, 3380, 3381, 3382, 3383, 3384, 3385, 3386, 3387, 3388, 3397, 3399, 3403, 3405, 3410, 3417, 3418, 3419, 3420, 3425, 3425, 3426, 3426, 3427, 3427, 3428, 3428, 3432, 3433, 3433, 3434, 3434, 3435, 3435, 3436, 3436, 3438, 3445, 3445, 3446, 3446, 3447, 3447, 3448, 3448, 3452, 3452, 3454, 3454, 3455, 3455, 3456, 3456, 3469, 3473, 3479, 3487, 3493, 3494, 3495, 3498, 3499, 3514, 3516, 3518, 3534, 3555, 3580, 3584, 3588, 3589, 3594, 3595, 3596, 3599, 3600, 3603, 3611, 3616, 3668, 3670, 3678, 3679, 3690, 3692, 3700, 3717, 3718, 3720, 3725, 3738, 3739, 3757, 3769, 3777, 3780, 3800, 3838, 3840, 3880, 3897, 3984, 4006, 4013, 4017, 4018, 4019, 4020, 4037, 4038, 4039, 4040, 4053, 4057, 4058, 4059, 4060, 4077, 4078, 4079, 4080, 4097, 4098, 4099, 4100, 4117, 4118, 4119, 4120, 4124, 4137, 4138, 4139, 4140, 4157, 4158, 4159, 4160, 4171, 4175, 4177, 4178, 4179, 4180, 4217, 4220, 4223, 4259, 4279, 4288, 4300, 4312, 4318, 4331, 4350, 4355, 4357, 4369, 4400, 4405, 4437, 4438, 4458, 4459, 4469, 4479, 4495, 4496, 4497, 4498, 4499, 4500, 4519, 4520, 4539, 4557, 4560, 4563, 4579, 4618, 4657, 4677, 4678, 4684, 4717, 4737, 4763, 4768, 4783

Appendix C

Systematic Uncertainty

The figures in this chapter contain the summary of the systematic uncertainty of all reported jet spectra, except R = 0.2 jets with $p_{\mathrm{T,min}}^{\mathrm{lead}}$ = 5 GeV/c, which is presented in the main text (Chapter 5). Note that the last $p_{\mathrm{T,jet}}$ bin in peripheral collisions and first bin for spectra with $p_{\mathrm{T,min}}^{\mathrm{lead}}$ = 9 GeV/c are dominated by statistical fluctuations and the corresponding bins are not reported in the thesis.

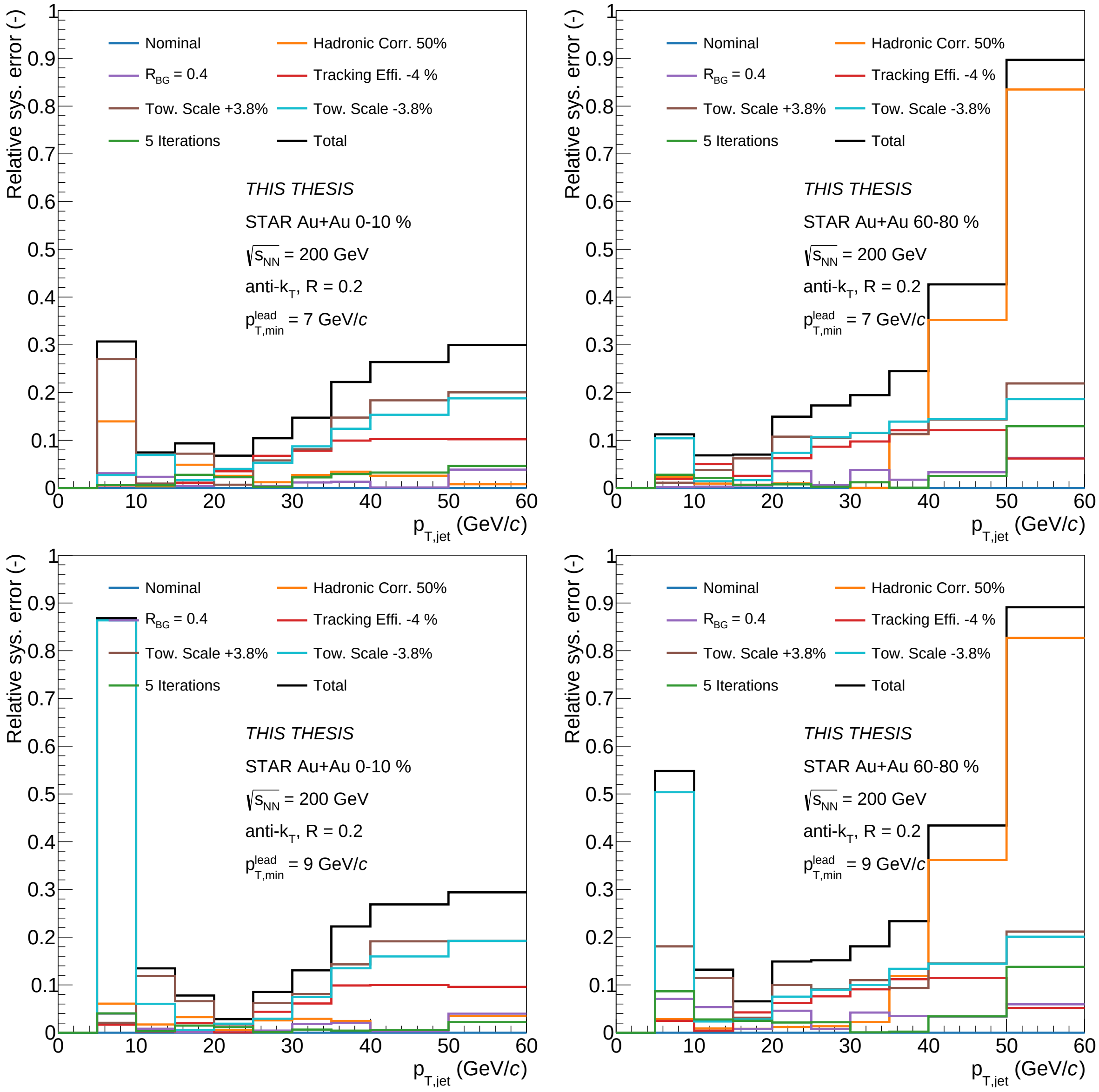

Figure C.1: Contributions to the total systematic error from various sources (different colors). The black line represents the total uncertainty obtained by adding the sources in quadrature. Jets were reconstructed with $R = 0.2$ and $p_{\mathrm{T,min}}^{\mathrm{lead}} = 7$ GeV/c (top) and $p_{\mathrm{T,min}}^{\mathrm{lead}} = 9$ GeV/c (bottom) in central (left) and peripheral (right) Au+Au collisions at $\sqrt{s_{\mathrm{NN}}} = 200$ GeV.

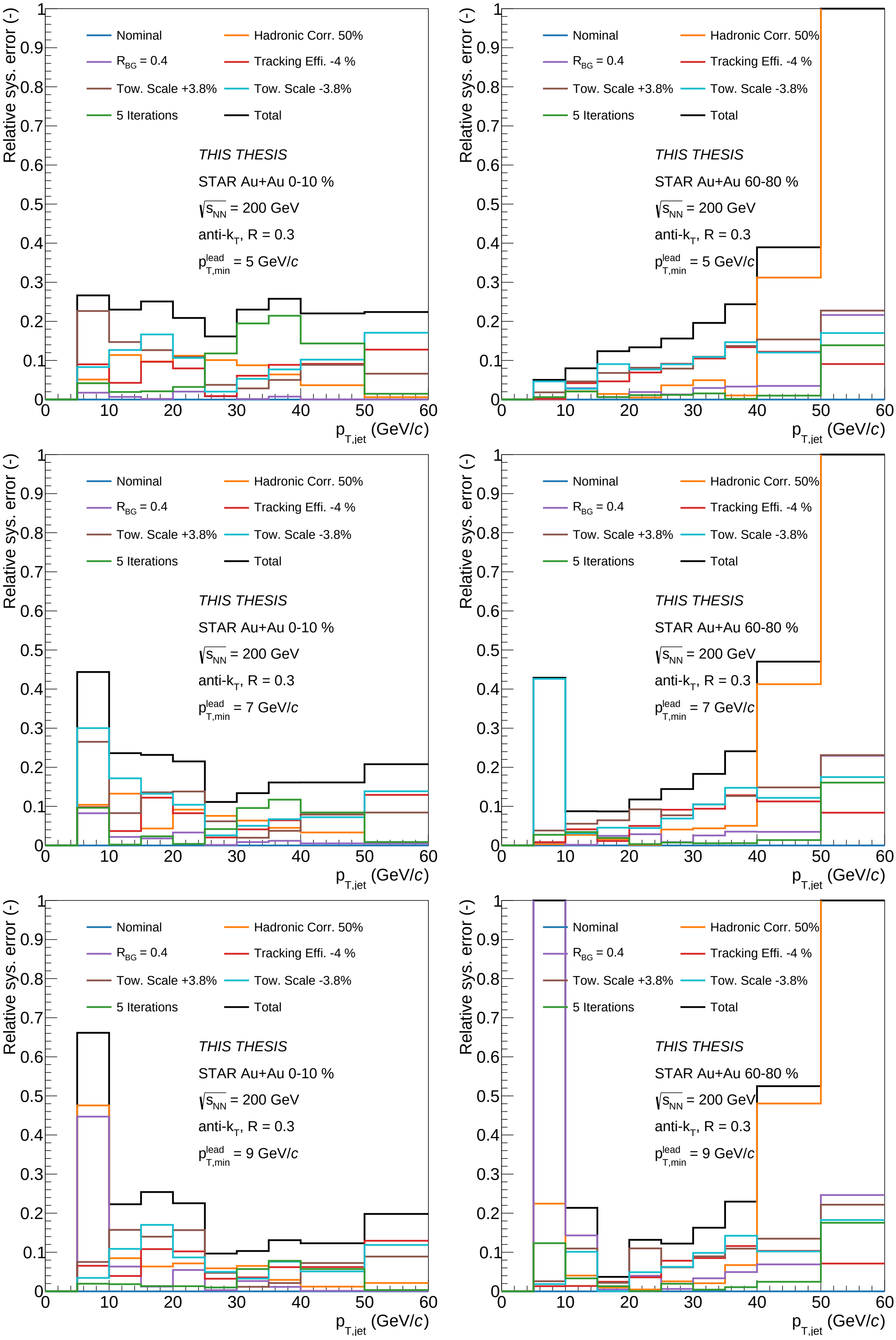

Figure C.2: Contributions to the total systematic error from various sources (different colors). The black line represents the total uncertainty obtained by adding the sources in quadrature. Jets were reconstructed with $R = 0.3$ and $p_{\mathrm{T,min}}^{\mathrm{lead}} = 5$ GeV/c (top) and $p_{\mathrm{T,min}}^{\mathrm{lead}} = 7$ GeV/c (middle) and $p_{\mathrm{T,min}}^{\mathrm{lead}} = 9$ GeV/c (bottom) in central (left) and peripheral (right) Au+Au collisions at $\sqrt{s_{\mathrm{NN}}} = 200$ GeV.

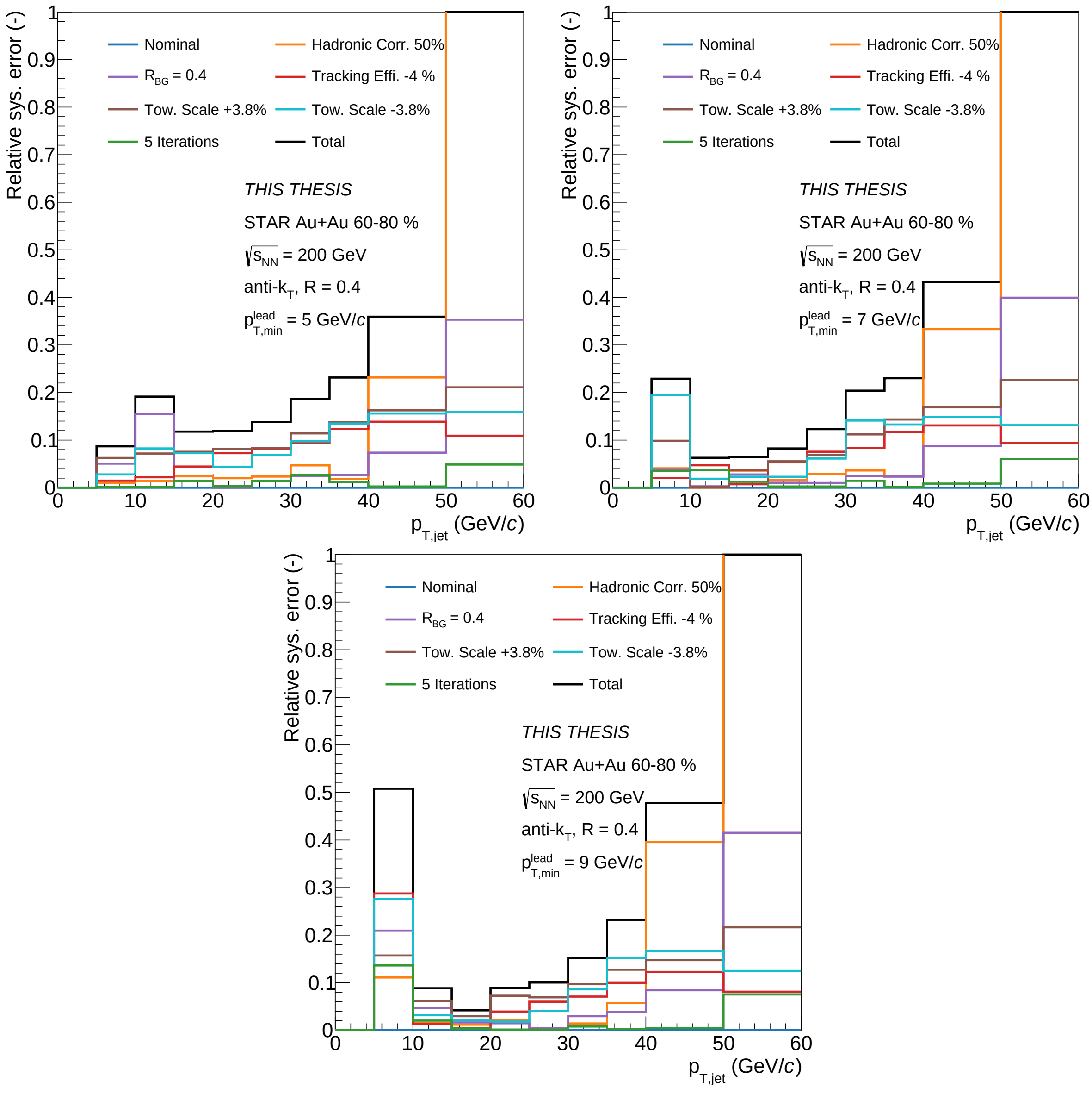

Figure C.3: Contributions to the total systematic error from various sources (different colors). The black line represents the total uncertainty obtained by adding the sources in quadrature. Jets were reconstructed with R = 0.4 and $p_{\mathrm{T,min}}^{\mathrm{lead}}$ = 5 GeV/c (top,left) and $p_{\mathrm{T,min}}^{\mathrm{lead}}$ = 7 GeV/c (top,right) and $p_{\mathrm{T,min}}^{\mathrm{lead}}$ = 9 GeV/c (bottom) in peripheral Au+Au collisions at $\sqrt{s_{\mathrm{NN}}}$ = 200 GeV.

Appendix D

Additional Results

Figures D.1–D.6 show the nuclear modification factors $R_{\mathrm{AA}}^{\mathrm{PYTHIA,UB}}$ and $R_{\mathrm{AA}}^{p_{\mathrm{T}}^{\mathrm{lead}}}$ for jets reconstructed with $p_{\mathrm{T,min}}^{\mathrm{lead}}$= 9 GeV/$c$ as a function of $p_{\mathrm{T,jet}}$and centrality. The R_{AA} reaches values around 0.2 – 0.3 in central collisions and values around 0.8 in peripheral Au+Au collisions at high–$p_{\mathrm{T,jet}}$, where the $p_{\mathrm{T}}^{\mathrm{lead}}$ bias is expected to be negligible.

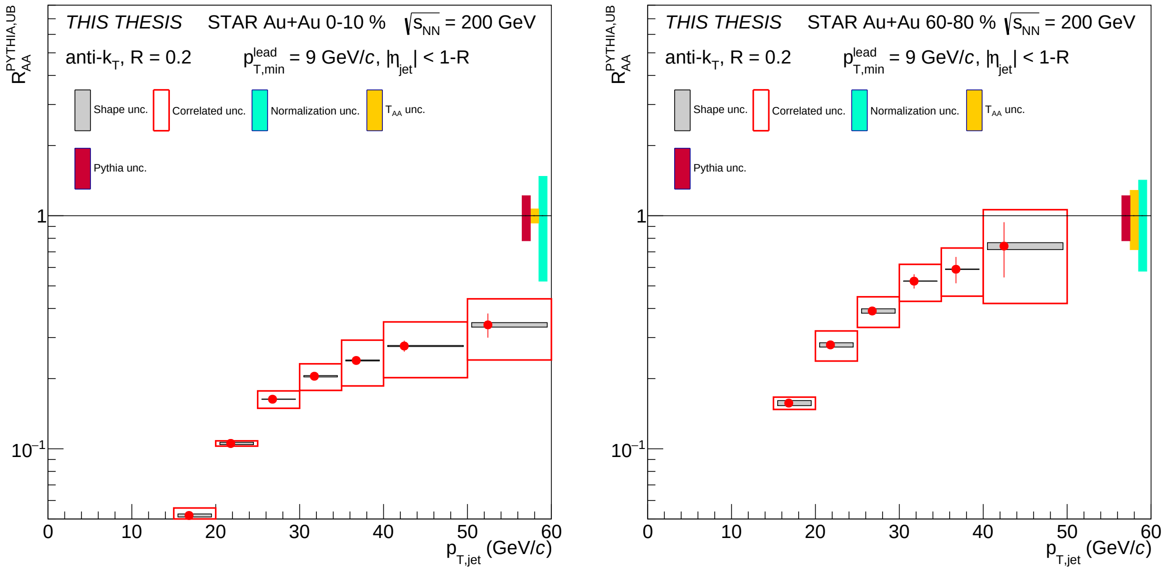

Figure D.1: Biased nuclear modification factor $R_{\mathrm{AA}}^{\mathrm{PYTHIA,UB}}$ (red circles) of anti-k_{T} jets reconstructed with R = 0.2 and $p_{\mathrm{T,min}}^{\mathrm{lead}}$= 9 GeV/$c$ in central (left) and peripheral (right) Au+Au collisions at $\sqrt{s_{\mathrm{NN}}}$ = 200 GeV. The colored boxes around markers represent correlated systematic uncertainty, while gray-shaded areas represent shape systematic uncertainty. The boxes around unity represent global systematic uncertainties - normalization of the spectra (teal), T_{AA} (orange) and the PYHTIA p+p baseline (pink).

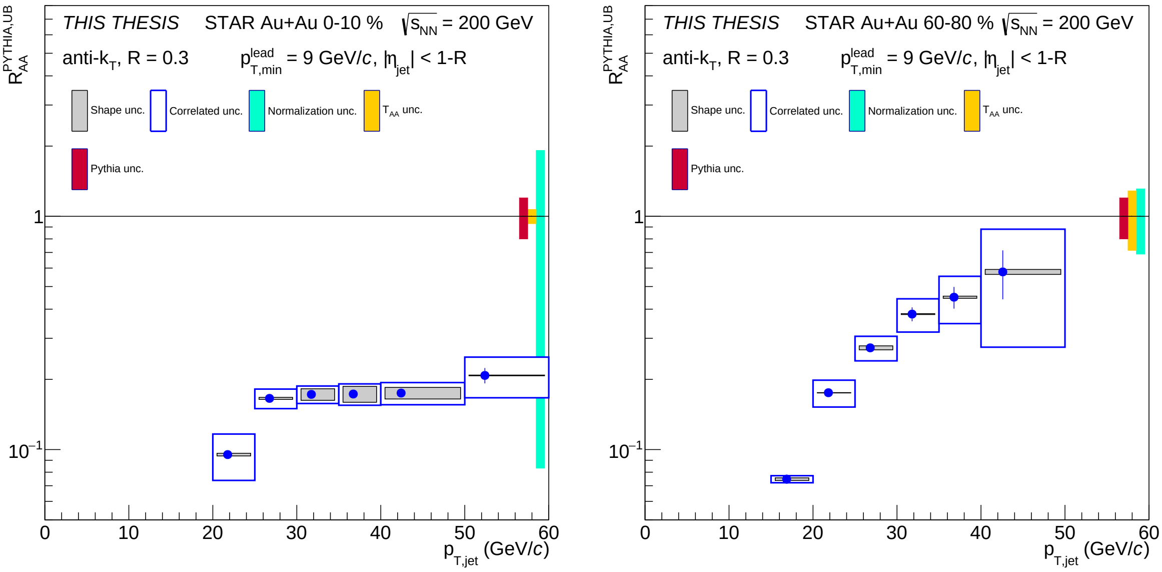

Figure D.2: Biased nuclear modification factor $R_{\mathrm{AA}}^{\mathrm{PYTHIA,UB}}$ (blue circles) of anti-k_{T} jets reconstructed with $R = 0.3$ and $p_{\mathrm{T,min}}^{\mathrm{lead}} = 9$ GeV/c in central (left) and peripheral (right) Au+Au collisions at $\sqrt{s_{\mathrm{NN}}} = 200$ GeV. The colored boxes around markers represent correlated systematic uncertainty, while gray-shaded areas represent shape systematic uncertainty. The boxes around unity represent global systematic uncertainties - normalization of the spectra (teal), T_{AA} (orange) and the PYHTIA p+p baseline (pink).

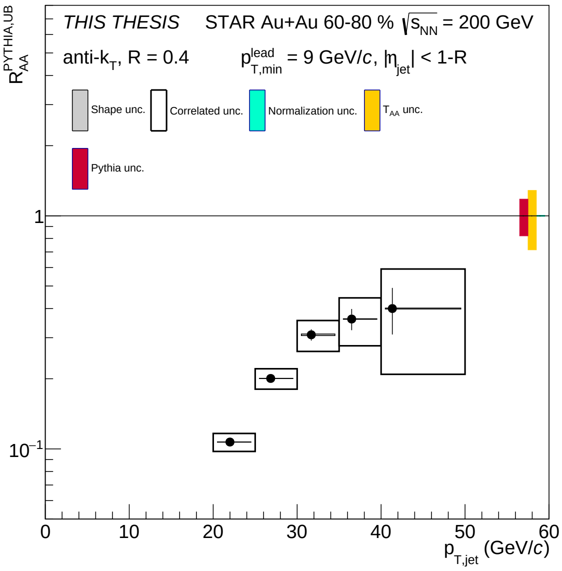

Figure D.3: Biased nuclear modification factor $R_{\mathrm{AA}}^{\mathrm{PYTHIA,UB}}$ (black circles) of anti-k_{T} jets reconstructed with $R = 0.4$ and $p_{\mathrm{T,min}}^{\mathrm{lead}} = 9$ GeV/c in peripheral (Au+Au collisions at $\sqrt{s_{\mathrm{NN}}} = 200$ GeV. The colored boxes around markers represent correlated systematic uncertainty, while gray-shaded areas represent shape systematic uncertainty. The boxes around unity represent global systematic uncertainties - normalization of the spectra (teal), T_{AA} (orange) and the PYHTIA p+p baseline (pink).

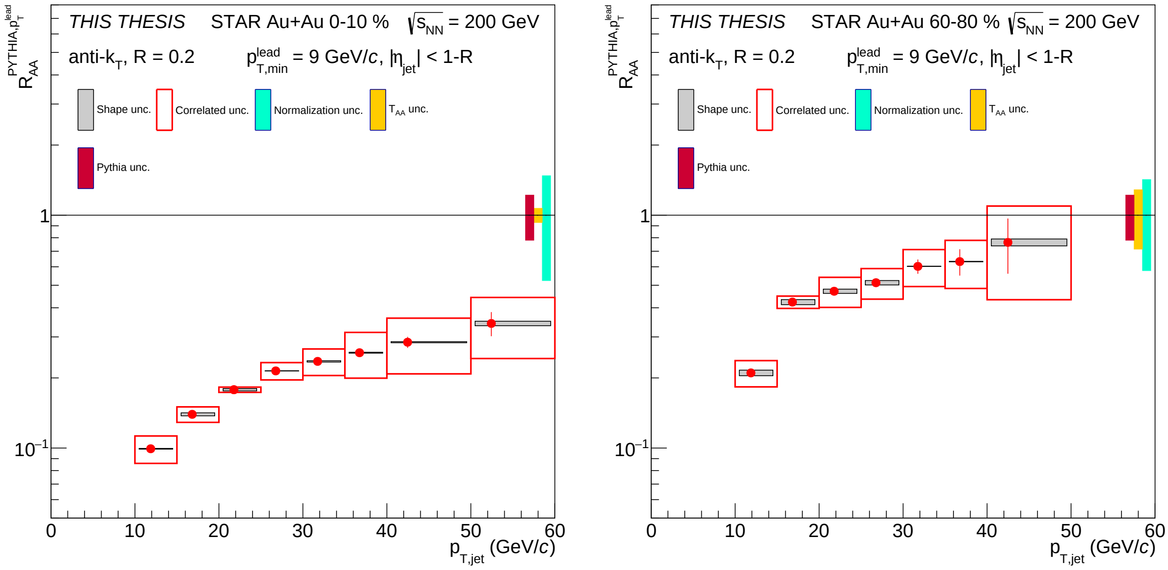

Figure D.4: Double–biased nuclear modification factor $R_{\mathrm{AA}}^{\mathrm{PYTHIA},p_{\mathrm{T}}^{\mathrm{lead}}}$ (red circles) of anti-k_{T} jets reconstructed with $R = 0.2$ and $p_{\mathrm{T,min}}^{\mathrm{lead}} = 9$ GeV/c in central (left) and peripheral (right) Au+Au collisions at $\sqrt{s_{\mathrm{NN}}} = 200$ GeV. The colored boxes around markers represent correlated systematic uncertainty, while gray-shaded areas represent shape systematic uncertainty. The boxes around unity represent global systematic uncertainties - normalization of the spectra (teal), T_{AA} (orange) and the PYHTIA p+p baseline (pink).

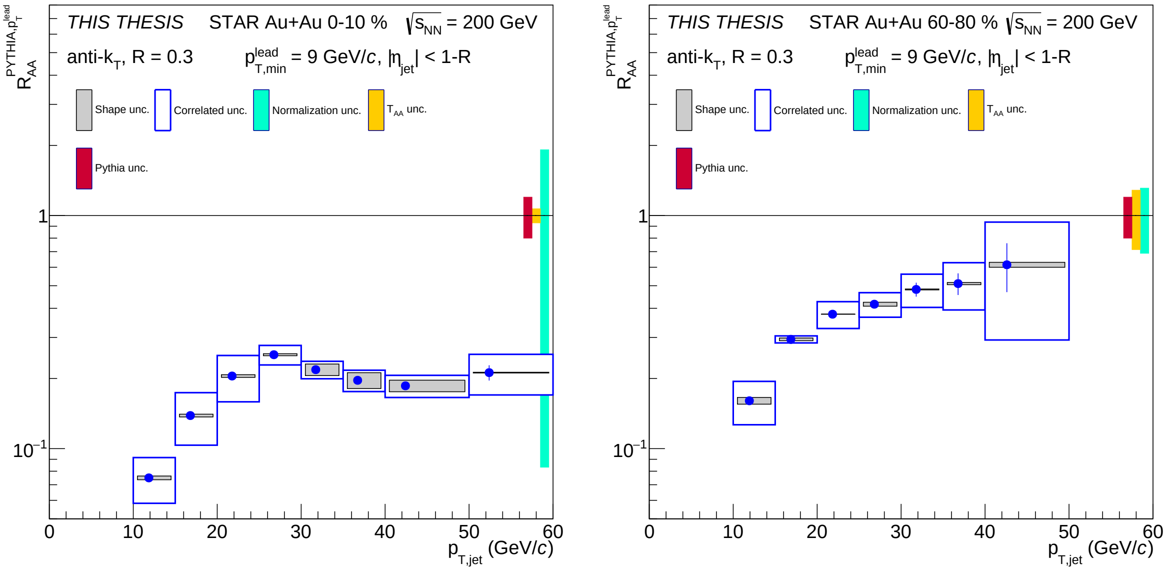

Figure D.5: Double–biased nuclear modification factor $R_{AA}^{PYTHIA,p_T^{lead}}$ (blue circles) of anti-k_T jets reconstructed with R = 0.3 and $p_{T,min}^{lead}$= 9 GeV/c in central (left) and peripheral (right) Au+Au collisions at $\sqrt{s_{NN}}$ = 200 GeV. The colored boxes around markers represent correlated systematic uncertainty, while gray-shaded areas represent shape systematic uncertainty. The boxes around unity represent global systematic uncertainties - normalization of the spectra (teal), T_{AA} (orange) and the PYHTIA p+p baseline (pink).

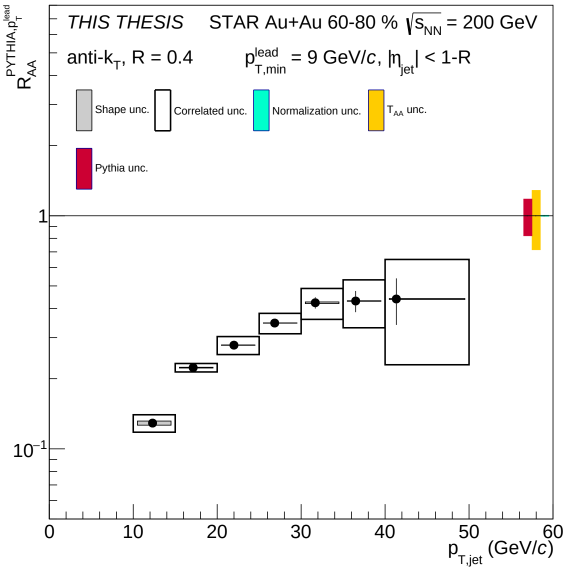

Figure D.6: Double–biased nuclear modification factor $R_{AA}^{PYTHIA,p_T^{lead}}$ (black circles) of anti-k_T jets reconstructed with R = 0.4 and $p_{T,min}^{lead}$= 9 GeV/c in peripheral Au+Au collisions at $\sqrt{s_{NN}}$ = 200 GeV. The colored boxes around markers represent correlated systematic uncertainty, while gray-shaded areas represent shape systematic uncertainty. The boxes around unity represent global systematic uncertainties - normalization of the spectra (teal), T_{AA} (orange) and the PYHTIA p+p baseline (pink).

List of Acronyms

AGS	Alternating Gradient Synchrotron
ALICE	A Large Ion Collider Experiment
ATHENA	A Totally Hermetic Electron-Nucleus Apparatus
ATLAS	A Toroidal LHC ApparatuS
BBC	Beam-Beam Counter
BCE	Before Common Era
BEMC	Barrel ElectroMagnetic Calorimeter
BES	Beam Energy Scan
BNL	Brookhaven National Laboratory
BRAHMS	Broad RAnge Hadron Magnetic Spectrometers
BSMD	Barrel Shower Maximum Detector
C/A	Cambridge/Aachen (algorithm)
CBM	Compressed Baryonic Matter (experiment)
CDF	Collider Detector at Fermilab
CERN	European Commission for Nuclear Research[1]
CMS	Compact Muon Solenoid
CNM	Cold Nuclear Matter
CP	Charge-Parity (symmetry)
CTU	Czech Technical University in Prague
DAQ	Data Acquisition
DCA	Distance of Closest Approach
DGLAP	Dokshitzer-Gribov-Lipatov-Altarelli-Parisi (equation)
DIS	Deep Inelastic Scattering

---

[1] From French: Conseil Européen pour la Recherche Nucléaire

DO	Detector Operator
DONUT	Direct Observation of the NU Tau (collaboration)
EA	Event Activity
EBIS	Electron Beam Ion Source
ECCE	The EIC Comprehensive Chromodynamics Experiment
EEMC	Endcap ElectroMagnetic Calorimeter
EIC	The Electron-Ion Collider
EPD	Event Plane Detector
ePIC	electron-Proton/Ion Collider (experiment)
ESMD	Endcap Shower Maximum Detector
eTOF	endcap Time Of Flight (detector)
FAIR	Facility for Antiproton and Ion Research
FCS	Forward Calorimeter System
FF	Fragmentation Function
FNSPE	Faculty of Nuclear Sciences and Physical Engineering
FST	Forward Silicon Tracker
FTS	Forward Tracking System
GEM	Gas Electron Multiplier (technology)
GMT	GEM Chambers to Monitor the TPC Tracking Calibrations
GPC	GodParent Committee
HERA	Hadron Electron Ring Accelerator
HFT	Heavy Flavor Tracker
HIJING	Heavy Ion Jet INteraction Generator
HT	High Tower (trigger)
iTPC	inner Time Projection Chamber
ITS	Inner Tracking System
JETSCAPE	Jet Energy-loss Tomography with a Statistically and Computationally Advanced Program Envelope
LBT	Linearized Boltzmann Transport (model)
LINAC	LINear ACcelerator
LION	Laser Ion Source

LIS	Laser Ion Source (concept)
LPM	Landau-Pomeranchuk-Migdal (regime)
LHAPDF	Les Houches Accord PDFs (library)
LHC	Large Hadron Collider
LO	Leading Order (calculation)
lQCD	lattice QCD (calculation)
MB	Minimum Bias (trigger)
MC	Monte Carlo (method)
MWPC	Multi Wire Proportional Chamber
MTD	Muon Telescope Detector
NEF	Neutral Energy Fraction
NLL	Next-to-Leading Logarithm (calculation)
(N)NLO	(Next-to-)Next-to-Leading Order (calculation)
NP	Non-Perturbative (calculation)
nPDF	nuclear Parton Distribution Function
NY	New York (state)
PA	Principal Author
PhD	Doctor of Philosophy[2]
PID	Particle IDentification
PDF	Parton Distribution Function
PETRA	Positron-Electron Tandem Ring Accelerator
PHENIX	The Pioneering High Energy Nuclear Interaction eXperiment
POWHEG	POsitive Weight Hardest Emission Generator
pQCD	perturbative QCD (calculation)
PV	Primary Vertex
PWG	Physics Working Group
PYQUEN	PYthia QUENched (model)
QA	Quality Assurance (of data)
QCD	Quantum ChromoDynamics
QED	Quantum ElectroDynamics

---

[2] From Latin: Philosophiae Doctor

QGP	Quark-Gluon Plasma
RF	RadioFrequency (technology)
RHIC	The Relativistic Heavy-Ion Collider
SCET	Soft Collinear Effective Theory
SLAC	Stanford Linear Accelerator Center
SM	Standard Model (of particle physics)
SISCone	Seedless Infrared-Safe Cone (algorithm)
SPS	Super Proton Synchrotron
sTGC	small-strip Thin Gas Chamber
STAR	The Solenoidal Tracker at RHIC
SVD	Singular Value Decomposition (method)
TOF	Time Of Flight (detector)
TPC	Time Projection Chamber
UE	Underlying Event
USA	United States of America
VPD	Vertex Position Detector
ZDC	Zero Degree Calorimeter

Published Papers

PROCEEDINGS OF SCIENCE

Measurement of open-charm hadron production in Au+Au collisions at $\sqrt{s_{\rm NN}}$ = 200 GeV with the STAR experiment

Robert Licenik[*][†]
Nuclear Physics Institute, Czech Academy of Sciences, 250 68 Rez, Czech Republic
E-mail: `licenik@ujf.cas.cz`

In ultrarelativistic heavy-ion collisions at RHIC energies, charm quarks are predominantly produced in initial hard partonic scatterings. Therefore, they experience the entire evolution of the hot and dense medium produced in these collisions, known as the Quark-Gluon Plasma (QGP). The STAR experiment is capable of studying the production of charm quarks and their interactions with the QGP through the reconstruction of the hadronic decays of $\rm D^0$, $\rm D^\pm$, $\rm D_s^\pm$ and $\Lambda_c^\pm$ hadrons. These measurements are possible thanks to the excellent track pointing resolution of the Heavy Flavor Tracker (HFT). In these proceedings, we present recent results on open-charm hadron measurements in Au+Au collisions at $\sqrt{s_{\rm NN}} = 200$ GeV. In particular, we discuss the nuclear modification factors of $\rm D^\pm$ and $\rm D^0$ mesons, which provide insights into the energy loss mechanism of charm quarks in the QGP, and the $\rm D^0$ elliptic and triangular flow coefficients, that probe the charm quark transport in the QGP. We also present the $\rm D_s^\pm/D^0$ and $\Lambda_c^\pm/\rm D^0$ yield ratios as a function of transverse momentum and collision centrality that help us better understand the charm quark hadronization process in heavy-ion collisions. Finally, we show the rapidity-odd directed flow of $\rm D^0$ mesons, which is sensitive to the initial tilt of the QGP bulk and can also probe the effects of the initial magnetic field in heavy-ion collisions.

European Physical Society Conference on High Energy Physics - EPS-HEP2019 -
10-17 July, 2019
Ghent, Belgium

---

[*] Speaker.
[†] For the STAR Collaboration

1. Introduction

A hot and dense medium of deconfined quarks and gluons (usually referred to as the Quark-Gluon Plasma - QGP) is created during the ultrarelativistic collisions of heavy nuclei at the Relativistic Heavy Ion Collider (RHIC) and at the Large Hadron Collider (LHC) [1, 2]. At RHIC, charm quarks are produced in such high-energy collisions predominantly through initial hard partonic scatterings, owing to their large mass. This makes the charm quarks a very valuable probe of the QGP, since they experience the entire evolution of the medium and their number is conserved throughout this process. The interactions between the charm quarks and the QGP can be studied by measuring observables related to the yields and anisotropies of charmed hadrons, such as D^0 (unless stated otherwise, D^0 denotes combined results from D^0 and $\overline{\mathrm{D}^0}$), $\mathrm{D}^\pm$, $\mathrm{D}_\mathrm{s}^\pm$ mesons and $\Lambda_\mathrm{c}^\pm$ baryon. The measurement of the nuclear modification factor R_{AA}, defined as the ratio of the yield of a given particle species in nucleus-nucleus (A+A) to the yield from proton-proton (p+p) collisions scaled by the mean number of binary collisions $\langle N_{\mathrm{coll}} \rangle$, can provide insights into the charm quark energy loss mechanism inside the medium. The so-called dead cone effect is expected to cause less energy loss for the heavy quarks compared to light-flavor quarks [3].

In these proceedings, we will discuss the R_{AA} of D^0 and $\mathrm{D}^\pm$ mesons. We will also present the recent measurements of the D^0 azimuthal anisotropy coefficients v_2 and v_3, representing the elliptic and triangular flow, respectively. Studying modification of the $\Lambda_\mathrm{c}^\pm/\mathrm{D}^0$ and $\mathrm{D}_\mathrm{s}^\pm/\mathrm{D}^0$ yield ratios can help us understand the effects of the coalescence mechanism [4, 5, 6] during the charm quark hadronization. Finally, we will present the results from the measurement of the rapidity-odd directed flow v_1 of D^0 and $\overline{\mathrm{D}^0}$ mesons, which is sensitive to the initial tilt of the QGP bulk [7] and could possibly also probe the effects of the initial electromagnetic field [8] generated during heavy-ion collisions. These measurements were conducted by the Solenoidal Tracker at RHIC (STAR) experiment utilizing the STAR Heavy Flavor Tracker (HFT).

2. Experimental Setup

The STAR experiment has a full azimuthal coverage and a pseudorapidity acceptance of $|\eta| < 1$. The Time Projection Chamber (TPC [9]) serves as the main tracking device at STAR and is also capable of identifying charged particles with momentum up to 1 GeV/c via the mean ionization energy loss (dE/dx) measurement. The particle identification is extended up to $p_{\mathrm{T}} = 3$ GeV/c by measuring the particle velocity with the Time-of-Flight detector (TOF [10]). The most important addition in the STAR heavy-flavor program was the HFT, a high-resolution 4-layer silicon detector, which is capable of achieving a track pointing resolution of 40 μm for kaons with momentum of 1 GeV/c [11]. It allows direct topological reconstruction of open-charm-hadron decays with a significant suppression of the combinatorial background. The open-charm hadrons which are used for the analyses presented in these proceedings were reconstructed in their most probable decay channels into charged hadrons [12]. For these analyses, about 900 million minimum-bias Au+Au collisions at $\sqrt{s_{\mathrm{NN}}} = 200$ GeV recorded by the STAR experiment during its run in year 2014 and/or about 1 billion events from year 2016 were used.

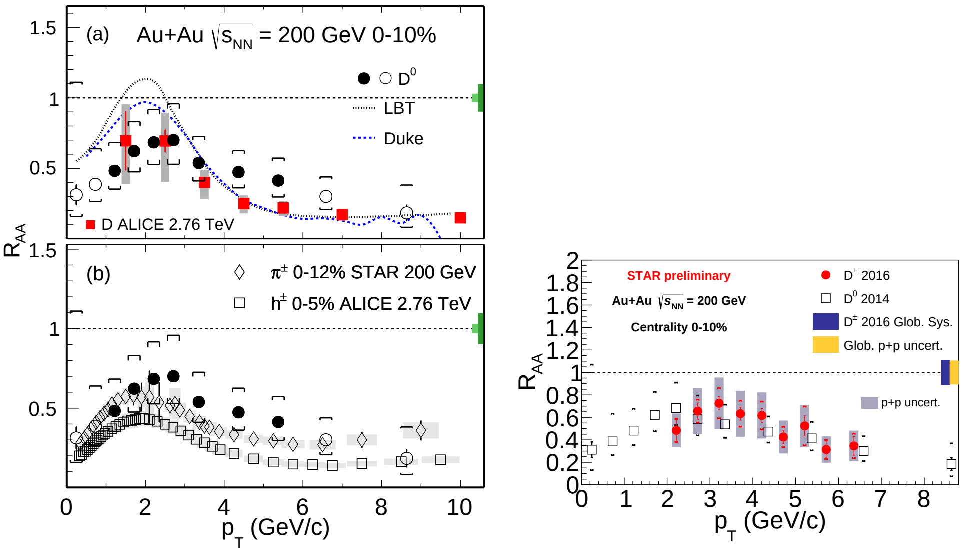

Figure 1: Left: The D^0 R_{AA} (circles) as a function of p_T in 0-10 % most central Au+Au collisions at $\sqrt{s_{NN}} = 200$ GeV [18]. Data are compared to (a) results from ALICE (squares) and the LBT and Duke models (dashed lines), and (b) light-flavor hadrons from STAR (diamonds) and ALICE (squares). Right: The D$^{\pm}$ R_{AA} (circles) as a function of p_T in 0-10 % most central 200 GeV Au+Au collisions. The error bars and boxes/gray bands represent statistical and systematic uncertainties, respectively. The p+p reference is taken from STAR combined D^0 and D* measurement [19].

3. Results

The left panel of Fig. 1 shows the nuclear modification factor R_{AA} of D^0 mesons as a function of p_T in central Au+Au collisions. The data from 2014 show significant suppression of D^0 production at high p_T (> 4 GeV/c), indicating large charm quark energy loss inside the QGP medium. The overall behavior is well described by the Linearized Boltzmann Transport (LBT [13]) and Duke [14] models, which include both collisional and medium-induced radiative energy losses and collective motion of the charm quarks inside the medium. The data are consistent with ALICE results from a combined D meson measurement [15] and the light-flavor hadrons at RHIC [16], while being less suppressed than light-flavor hadrons at the LHC [17] at intermediate p_T. The right panel of Fig. 1 shows that a very similar behavior is also observed in the D$^{\pm}$ production (from 2016 data), where the $R_{AA}(p_T)$ is consistent with that of D^0 mesons within uncertainties.

STAR has also measured the elliptic (v_2) and triangular (v_3) flow coefficients of D^0 mesons in Au+Au collisions at $\sqrt{s_{NN}} = 200$ GeV. The left panel of Fig. 2 shows the combined results from 2014 and 2016 data on STAR v_2/n_q as a function of $(m_T - m_0)/n_q$, where m_0 is the particle rest mass, $m_T = \sqrt{m_0^2 + p_T^2}$ and n_q is the number of constituent quarks, from semi-central collisions. These results improve the precision of the published results [20] and show that the charm quarks follow a similar trend as the light-flavor quarks [21]. As seen in the right panel of Fig. 2, the triangular flow of D^0 mesons, when scaled by n_q, is consistent with the light-flavor hadrons, although

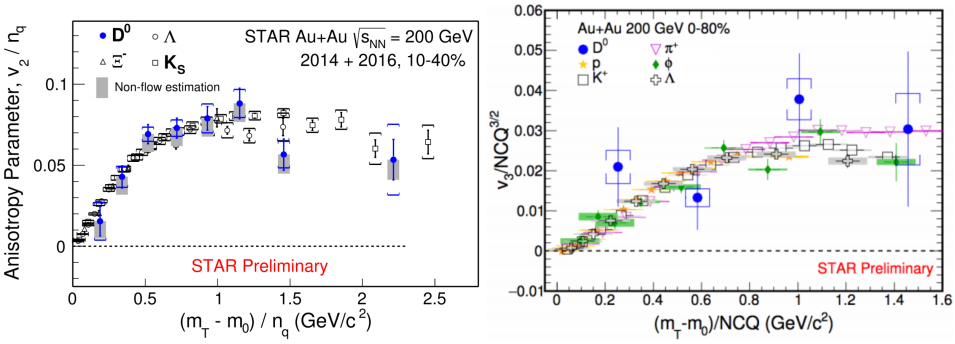

Figure 2: Left: The elliptic flow coefficient v_2 scaled by the number of constituent quarks n_q for D^0 mesons (full circles) and light-flavor hadrons as a function of $(m_\mathrm{T} - m_0)/n_q$ in the 10-40 % most central Au+Au collisions at $\sqrt{s_\mathrm{NN}} = 200$ GeV. Right: The triangular flow coefficient v_3 scaled by the number of constituent quarks $\mathrm{NCQ}^{\frac{3}{2}}$ for D^0 mesons (full circles) and light flavor hadrons as a function of $(m_\mathrm{T} - m_0)/\mathrm{NCQ}$ in the 0-80 % most central Au+Au collisions at $\sqrt{s_\mathrm{NN}} = 200$ GeV. The error bars and brackets represent statistical and systematic uncertainties, respectively.

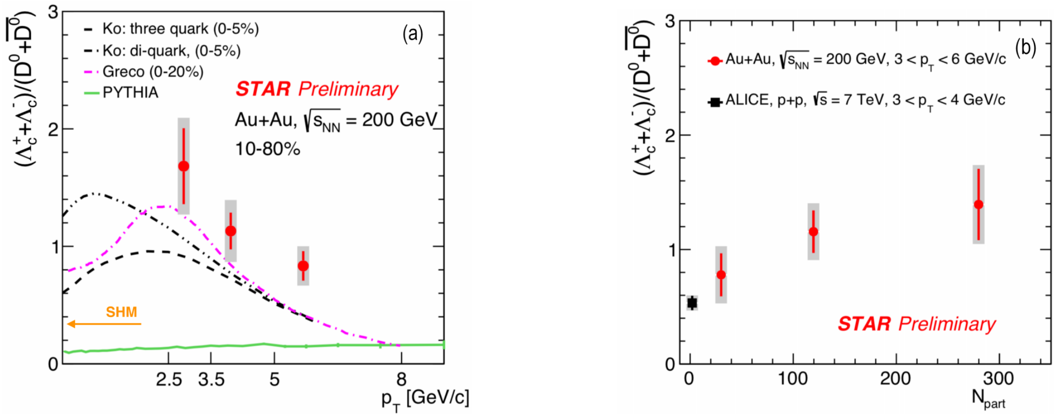

Figure 3: The $\Lambda_\mathrm{c}^\pm/\mathrm{D}^0$ ratio (circles) as a function of (a) p_T in the 10-80 % centrality class of Au+Au collisions at $\sqrt{s_\mathrm{NN}} = 200$ GeV (years 2014+2016), compared to Ko (0-5 %) and Greco (0-20 %) models and PYTHIA p+p reference, and (b) N_part for $3 < p_\mathrm{T} < 6$ GeV/c in Au+Au collisions at $\sqrt{s_\mathrm{NN}} = 200$ GeV. The error bars and gray bands represent statistical and systematic uncertainties, respectively.

the uncertainty of this measurement is larger. Both the v_2 and v_3 results indicate that the charm quarks show similar collectivity as light-flavor quarks and that they may thermalize in the medium.

Figure 3 shows the $\Lambda_\mathrm{c}^\pm/\mathrm{D}^0$ yield ratio as a function of p_T and centrality. The $\Lambda_\mathrm{c}^\pm$ baryon production is significantly enhanced compared to D^0 in Au+Au collisions and the magnitude of the enhancement increases from peripheral to central collisions. The p_T dependence of the enhancement is qualitatively described by models (Ko [5], Greco [22]), which take into account coalescence during charm quark hadronization, while the data are in significant disagreement with the PYTHIA p+p baseline.

The $\mathrm{D}_\mathrm{s}^\pm/\mathrm{D}^0$ ratio as a function of p_T in central and semi-central Au+Au collisions (from year

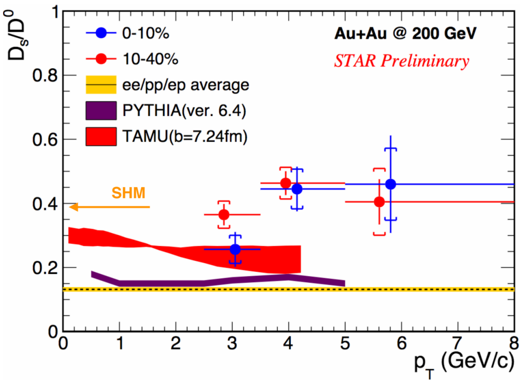

Figure 4: The $D_S^{\pm}/D^0$ ratio as a function of p_T in the 0-10 and 10-40 % centrality classes of Au+Au collisions at $\sqrt{s_{NN}}$ = 200 GeV, compared to elementary collisions average, TAMU model and PYTHIA p+p reference. The error bars and boxes represent statistical and systematic uncertainties, respectively.

2014), as seen in Fig. 4, shows a significant enhancement with respect to the PYTHIA p+p prediction and also to the average from e+e, e+p and p+p collisions [23]. While the TAMU model [6], which includes coalescence, predicts an enhancement of the $D_S^{\pm}/D^0$ ratio, it still underpredicts the data. Together with the $\Lambda_C^{\pm}$ results, the $D_S^{\pm}$ results support the idea of charm quark hadronization via coalescence. After measuring the D^0 production cross-section down to zero p_T, extrapolating the $D^{\pm}$ and $D_S^{\pm}$ production using Levy fits and calculating the $\Lambda_C^{\pm}$ production cross-section using the $\Lambda_C^{\pm}/D^0$ ratio, we conclude that the total charm quark cross section per binary nucleon-nucleon collision at mid-rapidity in Au+Au collisions at $\sqrt{s_{NN}} = 200$ GeV ($d\sigma^{c\bar{c}}/dy|_{y=0} = 152 \pm 13 \pm 29$ μb) is consistent with the result from p+p collisions at the same energy ($d\sigma^{c\bar{c}}/dy|_{y=0} = 130 \pm 30 \pm 26$ μb). Given the suppression of the D^0 yield at low p_T (Fig. 1) and the enhancements of $\Lambda_c^{\pm}$ and $D_s^{\pm}$, this suggests that the charm quark distribution among different hadron species during hadronization is significantly modified in the presence of the QGP.

The final result presented in these proceedings is the rapidity-odd component of the D^0 meson directed flow (v_1) shown in Fig. 5 [24]. The v_1 exhibits a negative slope for both D^0 and $\overline{D^0}$ mesons with the magnitude being significantly larger than that of kaons. This behavior is consistent with the hydrodynamical prediction [7], which takes into account the different longitudinal profiles of the charm quark production and the QGP bulk. The splitting between v_1 of D^0 and $\overline{D^0}$ as a result of charm quark and antiquark interaction with the initial electromagnetic field as predicted in [8] has not been observed within uncertainties.

4. Summary

The STAR experiment has extensively studied the production of open-charm hadrons, utilizing large data samples of Au+Au collisions at $\sqrt{s_{NN}} = 200$ GeV and the excellent pointing resolution of the HFT. Both the nuclear modification factors of $D^{\pm}$ and D^0 mesons show a significant suppression at high transverse momentum, indicating large charm quark energy loss in the QGP, comparable to light-flavor hadrons. The measurements of D^0 elliptic and triangular flow coefficients, which

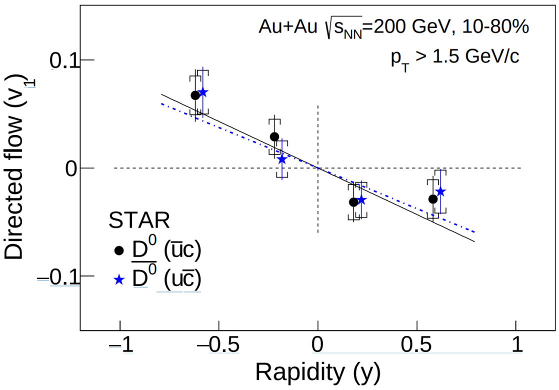

Figure 5: The D^0 directed flow coefficient v_1 as a function of rapidity y for particles with $p_T > 1.5$ GeV/c in the 10-80 % most central Au+Au collisions at $\sqrt{s_{NN}} = 200$ GeV. The lines represent linear fits to the data. The error bars and boxes represent statistical and systematic uncertainties, respectively.

follow the number-of-constituent-quarks scaling, indicate significant collective motion of charm quarks inside the medium and suggest that the charm quarks may achieve thermal equilibrium with the QGP at RHIC. The $\Lambda_c^{\pm}/D^0$ and $D_s^{\pm}/D^0$ ratios are significantly enhanced in Au+Au collisions compared to their p+p baselines and favor models which include coalescence during the charm quark hadronization. The results on the total charm cross-section confirm significant modification of charm hadrochemistry during hadronization. The measurement of the rapidity-odd component of the directed flow shows a large negative slope for both D^0 and $\overline{D^0}$ mesons, supporting the hydrodynamical prediction with a tilted QGP bulk, while the role of the initial electromagnetic field remains inconclusive.

Acknowledgments

This paper and the presentation at the EPS-HEP2019 conference were supported by the project LTT18002 of the Ministry of Education, Youth and Sport of the Czech Republic.

References

[1] STAR collaboration, *Experimental and theoretical challenges in the search for the quark gluon plasma: The STAR Collaboration's critical assessment of the evidence from RHIC collisions*, *Nucl. Phys.* **A757** (2005) 102 [`nucl-ex/0501009`].

[2] B. Muller, J. Schukraft and B. Wyslouch, *First Results from Pb+Pb collisions at the LHC*, *Ann. Rev. Nucl. Part. Sci.* **62** (2012) 361 [`1202.3233`].

[3] Y. L. Dokshitzer, V. A. Khoze and S. I. Troian, *On specific QCD properties of heavy quark fragmentation ('dead cone')*, *J. Phys.* **G17** (1991) 1602.

[4] Y. Oh, C. M. Ko, S. H. Lee and S. Yasui, *Heavy baryon/meson ratios in relativistic heavy ion collisions*, *Phys. Rev.* **C79** (2009) 044905 [`0901.1382`].

[5] S. H. Lee, K. Ohnishi, S. Yasui, I.-K. Yoo and C.-M. Ko, Λ_c *enhancement from strongly coupled quark-gluon plasma*, *Phys. Rev. Lett.* **100** (2008) 222301 [`0709.3637`].

[6] M. He, R. J. Fries and R. Rapp, $\mathbf{D_s}$*-Meson as Quantitative Probe of Diffusion and Hadronization in Nuclear Collisions*, *Phys. Rev. Lett.* **110** (2013) 112301 [`1204.4442`].

[7] S. Chatterjee and P. Bożek, *Large directed flow of open charm mesons probes the three dimensional distribution of matter in heavy ion collisions*, *Phys. Rev. Lett.* **120** (2018) 192301 [`1712.01189`].

[8] S. K. Das, S. Plumari, S. Chatterjee, J. Alam, F. Scardina and V. Greco, *Directed Flow of Charm Quarks as a Witness of the Initial Strong Magnetic Field in Ultra-Relativistic Heavy Ion Collisions*, *Phys. Lett.* **B768** (2017) 260 [`1608.02231`].

[9] M. Anderson et al., *The Star time projection chamber: A Unique tool for studying high multiplicity events at RHIC*, *Nucl. Instrum. Meth.* **A499** (2003) 659 [`nucl-ex/0301015`].

[10] F. Geurts et al., *Proposal for a Large Area Time of Flight System for STAR*, *STAR Note* **SN0621** (2004) .

[11] G. Contin et al., *The STAR MAPS-based PiXeL detector*, *Nucl. Instrum. Meth.* **A907** (2018) 60 [`1710.02176`].

[12] PARTICLE DATA GROUP collaboration, *Review of Particle Physics*, *Phys. Rev.* **D98** (2018) 030001.

[13] S. Cao, T. Luo, G.-Y. Qin and X.-N. Wang, *Linearized Boltzmann transport model for jet propagation in the quark-gluon plasma: Heavy quark evolution*, *Phys. Rev.* **C94** (2016) 014909 [`1605.06447`].

[14] Y. Xu, J. E. Bernhard, S. A. Bass, M. Nahrgang and S. Cao, *Data-driven analysis for the temperature and momentum dependence of the heavy-quark diffusion coefficient in relativistic heavy-ion collisions*, *Phys. Rev.* **C97** (2018) 014907 [`1710.00807`].

[15] ALICE collaboration, *Transverse momentum dependence of D-meson production in Pb-Pb collisions at* $\sqrt{s_{\rm NN}} = 2.76$ *TeV*, *JHEP* **03** (2016) 081 [`1509.06888`].

[16] STAR collaboration, *Energy dependence of* $\pi^{\pm}$*, p and anti-p transverse momentum spectra for Au+Au collisions at* $\sqrt{s_{\rm NN}} = 62.4$ *and 200-GeV*, *Phys. Lett.* **B655** (2007) 104 [`nucl-ex/0703040`].

[17] ALICE collaboration, *Centrality Dependence of Charged Particle Production at Large Transverse Momentum in Pb–Pb Collisions at* $\sqrt{s_{\rm NN}} = 2.76$ *TeV*, *Phys. Lett.* **B720** (2013) 52 [`1208.2711`].

[18] STAR collaboration, *Centrality and transverse momentum dependence of* D^0*-meson production at mid-rapidity in Au+Au collisions at* $\sqrt{s_{\rm NN}} =$ 200 *GeV*, *Phys. Rev.* **C99** (2019) 034908 [`1812.10224`].

[19] STAR collaboration, *Measurements of* D^0 *and* D^* *Production in* $p+p$ *Collisions at* $\sqrt{s} = 200$ *GeV*, *Phys. Rev.* **D86** (2012) 072013 [`1204.4244`].

[20] STAR collaboration, *Measurement of* D^0 *Azimuthal Anisotropy at Midrapidity in Au+Au Collisions at* $\sqrt{s_{\rm NN}} = 200$ *GeV*, *Phys. Rev. Lett.* **118** (2017) 212301 [`1701.06060`].

[21] STAR collaboration, *Centrality dependence of charged hadron and strange hadron elliptic flow from* $\sqrt{s_{\rm NN}} = 200$*-GeV Au + Au collisions*, *Phys. Rev.* **C77** (2008) 054901 [`0801.3466`].

[22] S. Plumari, V. Minissale, S. K. Das, G. Coci and V. Greco, *Charmed Hadrons from Coalescence plus Fragmentation in relativistic nucleus-nucleus collisions at RHIC and LHC*, *Eur. Phys. J.* **C78** (2018) 348 [`1712.00730`].

[23] M. Lisovyi, A. Verbytskyi and O. Zenaiev, *Combined analysis of charm-quark fragmentation-fraction measurements*, *Eur. Phys. J.* **C76** (2016) 397 [`1509.01061`].

[24] STAR COLLABORATION collaboration, *First observation of the directed flow of* D^0 *and* $\overline{D^0}$ *in* $\mathrm{Au+Au}$ *collisions at* $\sqrt{s_{NN}} = 200$ GeV, *Phys. Rev. Lett.* **123** (2019) 162301.

PROCEEDINGS OF SCIENCE

Measurement of inclusive jet production in Au+Au collisions at $\sqrt{s_{\mathrm{NN}}}$ = 200 GeV by the STAR experiment

---

Robert Licenik (for the STAR Collaboration)[a,*]

[a] *Nuclear Physics Institute, Czech Academy of Sciences,*
250 68, Rez, Czech Republic

E-mail: `licenik@ujf.cas.cz`

The STAR Collaboration reports the measurement of inclusive jet production in central (0-10%) and peripheral (60-80%) Au+Au collisions at $\sqrt{s_{\mathrm{NN}}}$ = 200 GeV, using both charged-particle and fully-reconstructed jets. Jet reconstruction is carried out using the anti-k_{T} algorithm with resolution parameters R = 0.2, 0.3 and 0.4. Yield suppression of charged-particle jets is observed for central Au+Au collisions relative to both peripheral Au+Au collisions and a vacuum baseline utilizing PYTHIA 6 simulations. The magnitude of the suppression is similar to that measured at the LHC and can be described by theoretical calculations. No evidence of significant medium-induced jet broadening is observed, based on comparison of jet spectra at varying R. The yield suppression, when expressed as the jet transverse momentum shift corresponding to energy loss, is consistent in magnitude with coincidence measurements at RHIC based on direct-photon and hadron triggers. There is an indication of larger energy loss observed at the LHC.

HardProbes2020
1-6 June 2020
Austin, Texas

---

[*] Speaker

https://pos.sissa.it/

PoS(HardProbes2020)123

The Quark-Gluon Plasma (QGP) created in high-energy heavy-ion collisions is opaque to jets (jet quenching) [1], a phenomenon that was first observed at RHIC via suppression of high transverse momentum (p_T) hadron yields and correlations [2]. Such measurements only provide limited insight into jet quenching mechanisms and dynamics, and more detailed measurements with reconstructed jets are required. While charged-particle and fully-reconstructed inclusive jet productions have been extensively studied in Pb+Pb collisions at the LHC ([3–5]), these proceedings focus on inclusive jet production in heavy-ion collisions at RHIC. We discuss recently reported measurements of charged-particle jets in Au+Au collisions by the STAR Collaboration [6], together with a new analysis to measure fully-reconstructed jets which is expected to have greater kinematic reach and improved systematic precision. The analysis uses data from the STAR detector [7], a large-acceptance system utilizing a solenoidal magnetic field, a Time Projection Chamber (TPC) [8] for charged-particle tracking and momentum reconstruction, and the Barrel Electromagnetic Calorimeter (BEMC) [9], which measures energy deposited by neutral particles and provides online triggers. STAR offers a full azimuthal coverage within pseudorapidity acceptance $|\eta| < 1$. The charged-jet analysis utilizes a dataset for Au+Au collisions at $\sqrt{s_\mathrm{NN}} = 200$ GeV with $L_\mathrm{int} = 70\ \mu\mathrm{b}^{-1}$, recorded in 2011 with a Minimum-Bias trigger. The fully-reconstructed jet analysis uses Au+Au collisions at $\sqrt{s_\mathrm{NN}} = 200$ GeV recorded in 2014 using a High-Tower trigger, which requires at least ~ 4 GeV in one BEMC tower.

Details of the charged-particle jet analysis, based on charged-particle tracks measured in the TPC, are found in [6]. The fully-reconstructed jet analysis also utilizes BEMC clusters (3x3 adjacent towers), corrected for hadronic energy deposition. The cluster transverse energy is limited to $0.2 < E_\mathrm{T} < 30.0$ GeV. The combinatorial background in both analyses is removed by imposing a cut on the leading hadron transverse momentum $p_\mathrm{T,lead}$. However, this cut also biases the fragmentation of the surviving jet population. This bias is measured by varying the $p_\mathrm{T,lead}$ cut and results are presented for the unbiased region.

Figure 1 shows charged-particle (left) and fully-reconstructed (right) jet distributions as a function of $p_\mathrm{T,jet}^\mathrm{reco}$ ($= p_\mathrm{T,jet}^\mathrm{raw} - \rho \cdot A$, where A is the jet area and ρ is the median background energy density, calculated event-wise) for $R = 0.4$ and various values of the $p_\mathrm{T,lead}$ cut in central Au+Au collisions at $\sqrt{s_\mathrm{NN}} = 200$ GeV. It can be seen that the $p_\mathrm{T,lead}$ cut significantly suppresses the combinatorial background, especially at low $p_\mathrm{T,jet}^\mathrm{reco}$. The distributions from the fully-reconstructed-jet analysis also indicate its extended kinematic reach, but corrected results are a work in progress. In the following we only show corrected results from the charged-particle jet analysis. Corrections are applied for the smearing effects of combinatorial background and instrumental effects using the SVD and Bayesian unfolding methods (details in [6]).

Figure 2 shows charged-particle jet R_CP, the scaled ratio of yields in central to peripheral collisions, which exhibits a similar level of suppression to charged hadrons at RHIC [10] and LHC energies [11] and to charged-particle jets at the LHC at higher $p_\mathrm{T,jet}$ [3], with weak $p_\mathrm{T,jet}^\mathrm{ch}$ dependence. Figure 3 shows charged-particle jet $R_\mathrm{AA}^\mathrm{PYTHIA}$, the yield suppression for central Au+Au collisions compared to pp baseline calculated by PYTHIA 6 (Perugia 2012, further tuned by STAR [12]). Calculations based on jet quenching models [13–16], shown in the various colored lines and shaded regions, are consistent with the measured value of $R_\mathrm{AA}^\mathrm{PYTHIA}$.

Figure 4 shows the transverse momentum shift $-\Delta p_\mathrm{T,jet}$, corresponding to yield suppression

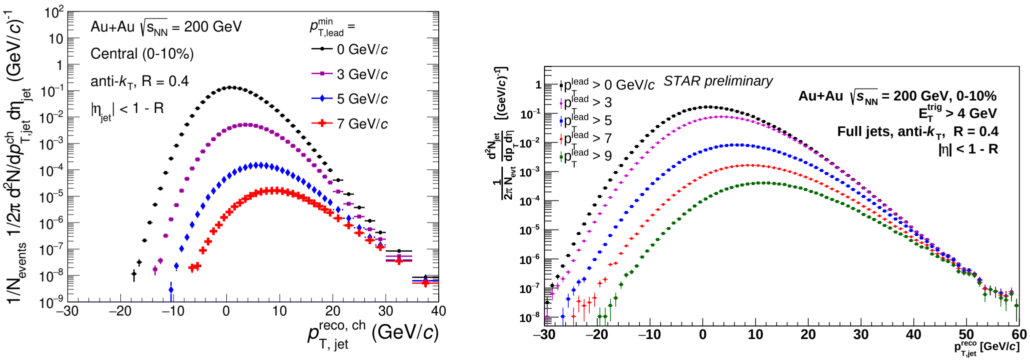

Figure 1: Uncorrected distribution of charged-particle [6] (left) and fully-reconstructed (right) jets as a function of $p^{\text{reco}}_{\text{T,jet}}$ in 0-10% Au+Au collisions at $\sqrt{s_{\text{NN}}}$ = 200 GeV. Different colors represent different values of the $p_{\text{T,lead}}$ cut.

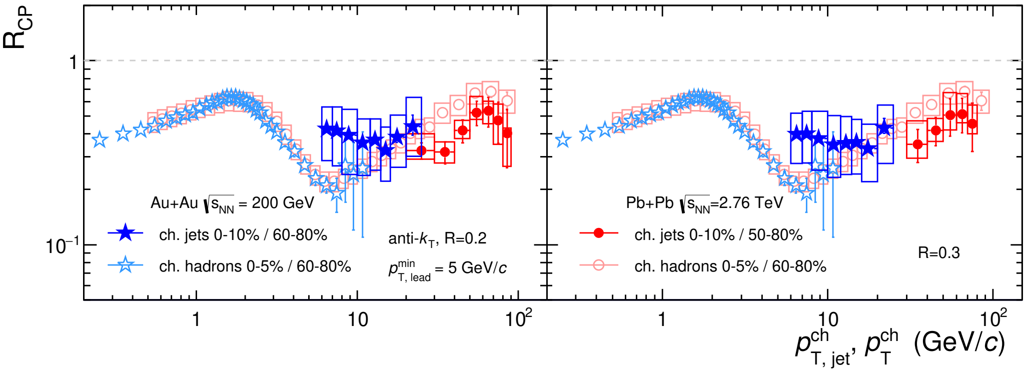

Figure 2: R_{CP} of charged-particle jets reconstructed with R = 0.2 and 0.3 and $p_{\text{T,lead}}$ > 5 GeV/c (solid stars) [6]. Also shown are similar suppression measurements with jets at the LHC [3] and inclusive charged hadrons at RHIC [10] and the LHC [11].

[17], from neutral trigger+jet coincidence measurements at RHIC (red and blue points), inclusive jet measurement (green, this analysis) and charged hadron+jet coincidence measurements at RHIC and the LHC (black points). Results are consistent between channels at RHIC, and indicate smaller jet energy loss at RHIC than at the LHC (though the *relative* shift appears larger at RHIC).

The ratio of inclusive jet cross-sections at different R and fixed $p_{\text{T,jet}}$ measures the jet transverse energy profile. We do not observe any modification of transverse jet profile compared to *pp* collision reference in peripheral or central collisions [6]. Dispersion of the model predictions is larger in this observable than in the $R^{\text{PYTHIA}}_{\text{AA}}$, which implies strong physical motivation to improve systematic uncertainties and study fully-reconstructed jets.

This work is supported by the project LTT18002 of the Ministry of Education, Youth and Sport of the Czech Republic.

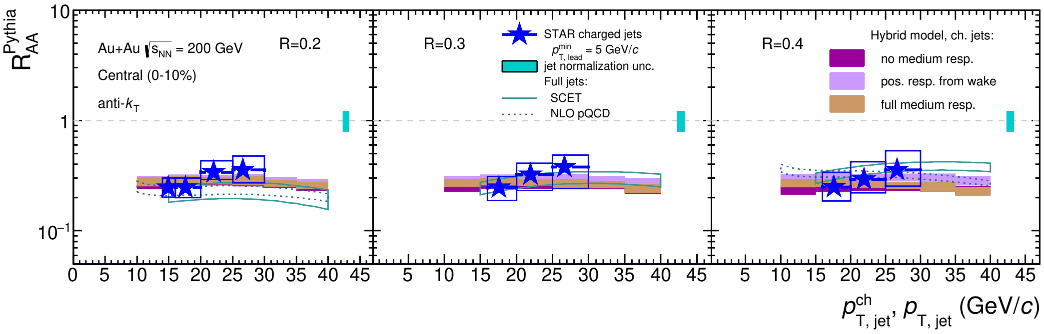

Figure 3: R_{AA}^{PYTHIA} as a function $p_{T,jet}^{ch}$ of charged-particle jets at STAR reconstructed with R = 0.2, 0.3 and 0.4, and $p_{T,lead}$ > 5 GeV/c [6]. Bands represent theory predictions.

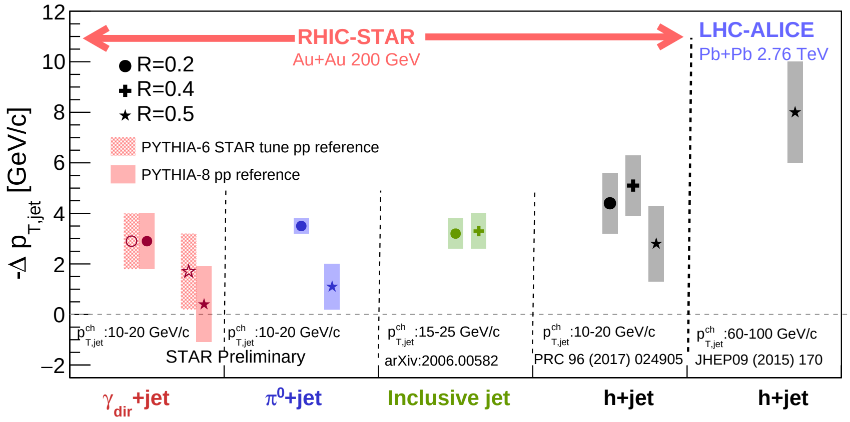

Figure 4: Transverse momentum shift $-\Delta p_{T,jet}$ from this analysis (middle) compared to various semi-inclusive jet results at RHIC and LHC energies (references in figure).

References

[1] W. Busza, K. Rajagopal and W. van der Schee, *Heavy ion collisions: The big picture and the big questions*, *Annual Review of Nuclear and Particle Science* **68** (2018) 339–376.

[2] STAR collaboration, *Evidence from d* + Au *measurements for final-state suppression of high-p_T hadrons in* Au + Au *collisions at RHIC*, *Phys. Rev. Lett.* **91** (2003) 072304.

[3] ALICE collaboration, *Measurement of charged jet suppression in Pb-Pb collisions at* $\sqrt{s_{NN}}$ *= 2.76 TeV*, *Journal of High Energy Physics* **2014** (2014) .

[4] ATLAS collaboration, *Measurement of the nuclear modification factor for inclusive jets in Pb+Pb collisions at* $\sqrt{s_{NN}}$ = 5.02 *TeV with the ATLAS detector*, *Physics Letters B* **790** (2019) 108–128.

[5] CMS collaboration, *Measurement of inclusive jet cross sections in pp and PbPb collisions at* $\sqrt{s_{NN}} = 2.76$ *TeV*, *Phys. Rev. C* **96** (2017) 015202.

[6] STAR collaboration, J. Adam, L. Adamczyk, J. R. Adams, J. K. Adkins, G. Agakishiev, M. M. Aggarwal et al., *Measurement of inclusive charged-particle jet production in Au+Au collisions at* $\sqrt{s_{NN}}$*=200 GeV*, 2020.

[7] K. Ackermann, N. Adams, C. Adler, Z. Ahammed, S. Ahmad, C. Allgower et al., *STAR detector overview*, *Nuclear Instruments and Methods in Physics Research Section A: Accelerators, Spectrometers, Detectors and Associated Equipment* **499** (2003) 624 .

[8] M. Anderson et al., *The STAR time projection chamber: A Unique tool for studying high multiplicity events at RHIC*, *Nucl. Instrum. Meth.* **A499** (2003) 659 [`nucl-ex/0301015`].

[9] M. Beddo, E. Bielick, T. Fornek, V. Guarino, D. Hill, K. Krueger et al., *The STAR Barrel Electromagnetic Calorimeter*, *Nuclear Instruments and Methods in Physics Research Section A: Accelerators, Spectrometers, Detectors and Associated Equipment* **499** (2002) 725.

[10] STAR collaboration, *Transverse-momentum and collision-energy dependence of high-*p_T *hadron suppression in* Au + Au *collisions at ultrarelativistic energies*, *Phys. Rev. Lett.* **91** (2003) 172302.

[11] ATLAS collaboration, *Measurement of charged-particle spectra in Pb+Pb collisions at* $\sqrt{s_{\mathrm{NN}}} = 2.76$ *TeV with the ATLAS detector at the LHC*, *Journal of High Energy Physics* **2015** (2015) .

[12] STAR collaboration, *Longitudinal double-spin asymmetry for inclusive jet and dijet production in pp collisions at* $\sqrt{s} = 510$ GeV, *Phys. Rev. D* **100** (2019) 052005.

[13] I. Vitev and B.-W. Zhang, *Jet tomography of high-energy nucleus-nucleus collisions at next-to-leading order*, *Phys. Rev. Lett.* **104** (2010) 132001.

[14] Y.-T. Chien, A. Emerman, Z.-B. Kang, G. Ovanesyan and I. Vitev, *Jet quenching from qcd evolution*, *Phys. Rev. D* **93** (2016) 074030.

[15] Y.-T. Chien and I. Vitev, *Towards the understanding of jet shapes and cross sections in heavy ion collisions using soft-collinear effective theory*, *Journal of High Energy Physics* **2016** (2016) .

[16] J. Casalderrey-Solana, D. C. Gulhan, J. G. Milhano, D. Pablos and K. Rajagopal, *Angular structure of jet quenching within a hybrid strong/weak coupling model*, *Journal of High Energy Physics* **2017** (2017) .

[17] STAR collaboration, *Measurements of jet quenching with semi-inclusive hadron+jet distributions in Au + Au collisions at* $\sqrt{s_{NN}} = 200$ *GeV*, *Phys. Rev. C* **96** (2017) 024905.

RECENT RESULTS OF INCLUSIVE JET PRODUCTION IN Au+Au COLLISIONS AT $\sqrt{s_{\mathrm{NN}}} = 200$ GeV BY THE STAR EXPERIMENT

R. Licenik (for the STAR Collaboration), licenik@ujf.cas.cz, Nuclear Physics Institute of the Czech Academy of Sciences, Prague, Czech republic

INTRODUCTION

Jets are an excellent probe of the Quark-Gluon Plasma (QGP) - an exotic state of matter created in high-energy nucleus-nucleus collisions. They are created at the very early stage in the collision during hard parton-parton scatterings, which means that they experience the entire evolution of the system. In addition, their production cross section in proton-proton collisions is calculable by perturbative Quantum Chromodynamics. The modification of jet production as the result of parton interactions with the QGP medium (jet quenching) was first studied via suppression of high-transverse momentum (high-p_{T}) hadrons [1], which provided a clear evidence of QGP formation in Au+Au collisions at top RHIC energies. Since then, detailed measurements with reconstructed jets have been carried out in Pb+Pb collisions at the LHC [2, 3, 4]. These proceedings focus on the recently reported results of inclusive charged-particle jet production in Au+Au collisions at $\sqrt{s_{\mathrm{NN}}} = 200$ GeV by the STAR experiment at RHIC [5] and also on the ongoing analysis of fully-reconstructed jets, which is expected to bring extended kinematic reach and improved precision.

DATASET AND ANALYSIS

The analysis uses the STAR detector [6], a multi-purpose large-acceptance system utilizing a solenoidal magnetic field. Charged-particle tracks and their momenta are reconstructed in the Time Projection Chamber (TPC) [7]. The Barrel Electromagnetic Calorimeter [8] is used to measure the energy deposited by neutral particles and also provides online triggers. The STAR detector offers a full azimuthal coverage within pseudorapidity range $|\eta| < 1$. The dataset for the charged-particle jet analysis amounts to ~ 6 μb^{-1} of Au+Au collisions at $\sqrt{s_{\mathrm{NN}}} = 200$ GeV recorded with the minimum-bias trigger in year 2011, while the fully-reconstructed jet analysis uses a 5.2 nb^{-1} dataset of Au+Au collisions at the same energy recorded in 2014 using the High-Tower trigger, requiring a signal threshold of ~ 4 GeV in a single BEMC tower. Charged-particle jets are reconstructed from TPC tracks (see [5] for analysis details), while fully-reconstructed jets also include the energy from BEMC clusters (3×3 towers), corrected for hadronic energy deposition. The clusters' transverse energy was limited to $0.2 < E_{\mathrm{T}} < 30.0$ GeV. Jets are reconstructed using the anti-k_{T} algorithm [9] with resolution parameters $R = 0.2, 0.3, 0.4$. The combinatorial-jet background in both analyses is suppressed by imposing a cut on the transverse momentum of the hardest particle ($p_{\mathrm{T,lead}}$) in a jet. However, this cut also introduces a bias into the fragmentation of the surviving jet population. This bias is estimated by varying the $p_{\mathrm{T,lead}}$ cut and physics results are discussed in the unbiased region.

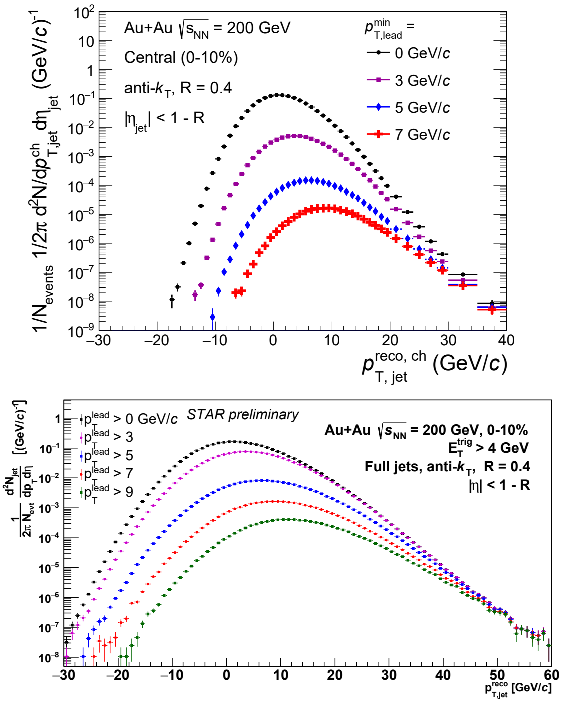

Fig. 1. Uncorrected distributions of charged-particle [5] (top) and fully-reconstructed (bottom) jets as a function of $p_{\mathrm{T,jet}}^{\mathrm{reco}}$ in 0-10 % Au+Au collisions at $\sqrt{s_{\mathrm{NN}}} = 200$ GeV. Different colors represent different values of $p_{\mathrm{T,lead}}$.

RESULTS

Figure 1 shows the charged-particle (top) and fully-reconstructed (bottom) jet distributions as a function of $p_{\mathrm{T,jet}}^{\mathrm{reco}} = p_{\mathrm{T,jet}}^{\mathrm{raw}} - \rho \cdot A$, where $p_{\mathrm{T,jet}}^{\mathrm{raw}}$ is the raw jet p_{T} given by the jet finder, A is the jet area and ρ is the median background energy density (calculated event-wise), for $R = 0.4$ in central Au+Au collisions. It can be seen that the $p_{\mathrm{T,lead}}$ cut significantly reduces the combinatorial background, especially at low $p_{\mathrm{T,jet}}^{\mathrm{reco}}$. The distributions also indicate the extended kinematic reach of the fully-reconstructed-jet analysis. However, since this analysis is a work in progress, we only show corrected results from the charged-particle jet analysis. Corrections are applied for the smearing effects of the high-multiplicity environment and instrumental effects using the SVD and Bayesian unfolding methods (details in [5]).

Figure 2 shows charged-particle jet R_{CP}, the scaled ratio of yields in central to peripheral collisions, which exhibits a similar level of suppression as charged hadrons at RHIC [10] and LHC energies [11] and as charged-particle jets at the LHC at higher $p_{\mathrm{T,jet}}^{\mathrm{ch}}$ [2], with weak $p_{\mathrm{T,jet}}^{\mathrm{ch}}$ dependence. Figure 3 shows charged-

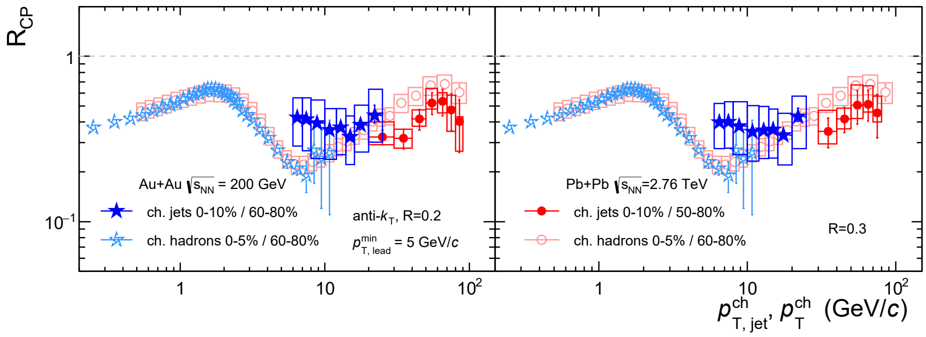

Fig. 2. R_{CP} of charged-particle jets reconstructed with $R = 0.2$ (left) and 0.3 (right) and $p_{\mathrm{T,lead}} > 5$ GeV/c (solid stars) [5]. Also shown are measurements of R_{CP} for charged-particle jets at the LHC (solid circles) [2] and inclusive charged hadrons at RHIC (open stars) [10] and the LHC (open circles) [11].

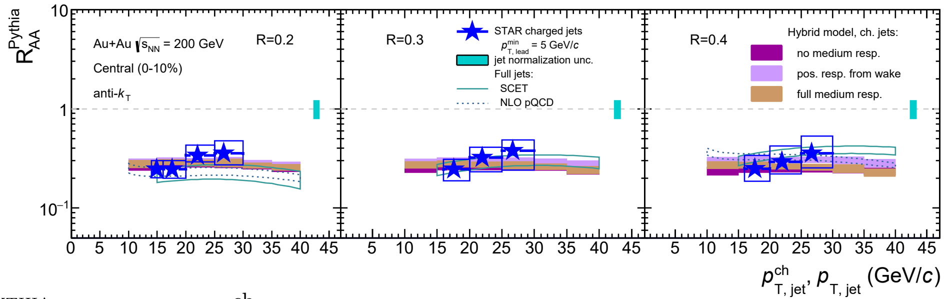

Fig. 3. $R_{\mathrm{AA}}^{\mathrm{PYTHIA}}$ as a function of $p_{\mathrm{T,jet}}^{\mathrm{ch}}$ for charged-particle jets at STAR reconstructed with $R = 0.2$ (left), 0.3 (middle) and 0.4 (right), and $p_{\mathrm{T,lead}} > 5$ GeV/c [5]. Bands represent theory calculations [13, 14, 15, 16].

particle jet $R_{\mathrm{AA}}^{\mathrm{PYTHIA}}$, which measures the yield suppression for central Au+Au collisions compared to p+p baseline calculated by PYTHIA 6 (Perugia 2012, further tuned by STAR [12]). Calculations based on jet quenching models are largely consistent with the measured value of $R_{\mathrm{AA}}^{\mathrm{PYTHIA}}$ within uncertainties, which motivates more precise measurements to distinguish among them.

CONCLUSIONS

We have discussed the recently reported results of charged-particle jet production in Au+Au collisions at $\sqrt{s_{\mathrm{NN}}} = 200$ GeV by the STAR experiment. The R_{CP} shows large suppression, consistent with similar measurement at the LHC and also with charged hadron results at RHIC and the LHC. The $R_{\mathrm{AA}}^{\mathrm{PYTHIA}}$ also shows large suppression consistent with models incorporating jet-quenching mechanisms. The ongoing fully-reconstructed jet analysis is expected to increase the kinematic reach and precision of STAR inclusive jet measurements.

ACKNOWLEDGMENT: This work is supported by the project LTT18002 of the Ministry of Education, Youth and Sport of the Czech Republic.

REFERENCES

1. STAR Collaboration, Phys. Rev. Lett. **91**, 072304 (2003).
2. ALICE Collaboration, J. High Energy Phys. **30**, 013 (2014).
3. ATLAS Collaboration, Phys. Lett. **B 790**, 108 (2019).
4. CMS Collaboration, Phys. Rev. **C 96**, 015202 (2017).
5. STAR Collaboration, arXiv:2006.00582 [nucl-ex].
6. K. Ackermann et al., Nucl. Instrum. Meth. **A 499**, 624 (2003).
7. M. Anderson et al., Nucl. Instrum. Meth. **A 499**, 659 (2003).
8. M. Beddo et al., Nucl. Instrum. Meth. **A 499**, 725 (2003).
9. M. Cacciari et al., J. High Energy Phys. **04**, 063 (2008).
10. STAR Collaboration, Phys. Rev. Lett. **91**, 172302 (2003).
11. ATLAS Collaboration, J. High Energy Phys. **09**, 050 (2015).
12. STAR Collaboration, Phys. Rev. **D 100**, 052005 (2019).
13. I. Vitev, B.-W. Zhang, Phys. Rev. Lett. **104**, 132001 (2010).
14. Y.-T. Chien et al., Phys. Rev. **D 93**, 074030 (2016).
15. Y.-T. Chien, I. Vitev, J. High Energy Phys. **05**, 023 (2016).
16. J. Casalderrey-Solana et al., J. High Energy Phys. **03**, 135 (2017).